

## INFORMATION TO USERS

This manuscript has been reproduced from the microfilm master. UMI films the text directly from the original or copy submitted. Thus, some thesis and dissertation copies are in typewriter face, while others may be from any type of computer printer.

**The quality of this reproduction is dependent upon the quality of the copy submitted.** Broken or indistinct print, colored or poor quality illustrations and photographs, print bleedthrough, substandard margins, and improper alignment can adversely affect reproduction.

In the unlikely event that the author did not send UMI a complete manuscript and there are missing pages, these will be noted. Also, if unauthorized copyright material had to be removed, a note will indicate the deletion.

Oversize materials (e.g., maps, drawings, charts) are reproduced by sectioning the original, beginning at the upper left-hand corner and continuing from left to right in equal sections with small overlaps.

Photographs included in the original manuscript have been reproduced xerographically in this copy. Higher quality 6" x 9" black and white photographic prints are available for any photographs or illustrations appearing in this copy for an additional charge. Contact UMI directly to order.

ProQuest Information and Learning  
300 North Zeeb Road, Ann Arbor, MI 48106-1346 USA  
800-521-0600

UMI<sup>®</sup>



**UNIVERSIT OF ALBERTA**

**ATTACHMENT OF FINE GAS BUBBLES ONTO A SOLID SURFACE  
AND ELECTROKINETICS OF GAS BUBBLES**

by

**CHUN YANG** ©

A thesis submitted to the Faculty of Graduate Studies and Research in partial fulfillment  
of the requirements for the degree of **DOCTOR OF PHILOSOPHY**

in

**DEPARTMENT OF MECHANICAL ENGINEERING**

EDMONTON, ALBERTA

SPRING 2000



National Library  
of Canada

Acquisitions and  
Bibliographic Services

395 Wellington Street  
Ottawa ON K1A 0N4  
Canada

Bibliothèque nationale  
du Canada

Acquisitions et  
services bibliographiques

395, rue Wellington  
Ottawa ON K1A 0N4  
Canada

*Your file Votre référence*

*Our file Notre référence*

The author has granted a non-exclusive licence allowing the National Library of Canada to reproduce, loan, distribute or sell copies of this thesis in microform, paper or electronic formats.

The author retains ownership of the copyright in this thesis. Neither the thesis nor substantial extracts from it may be printed or otherwise reproduced without the author's permission.

L'auteur a accordé une licence non exclusive permettant à la Bibliothèque nationale du Canada de reproduire, prêter, distribuer ou vendre des copies de cette thèse sous la forme de microfiche/film, de reproduction sur papier ou sur format électronique.

L'auteur conserve la propriété du droit d'auteur qui protège cette thèse. Ni la thèse ni des extraits substantiels de celle-ci ne doivent être imprimés ou autrement reproduits sans son autorisation.

0-612-60043-2

**Canada**

# UNIVERSITY OF ALBERTA

## LIBRARY RELEASE FORM

NAME OF AUTHOR: **CHUN YANG**

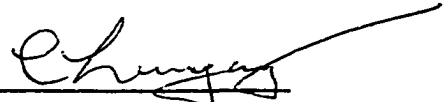
TITLE OF THESIS: **ATTACHMENT OF FINE GAS BUBBLES  
ONTO A SOLID SURFACE AND  
ELECTROKINETICS OF GAS BUBBLES**

DEGREE: **DOCTOR OF PHILOSOPHY**

YEAR THIS DEGREE GRANTED: **2000**

Permission is hereby granted to the University of Alberta Library to reproduce single copies of this thesis and to lend or sell such copies for private, scholarly, or scientific research purposes only.

The author reserves all other publication and other rights in association with the copyright in the thesis, and except as herein before provided, neither the thesis nor any substantial portion thereof may be printed or otherwise reproduced in any material form whatever without the author's prior written permission.



607C, Michener Park

Edmonton, AB T6H 5A1

Canada

November 3, 1999

# UNIVERSITY OF ALBERTA

## FACULTY OF GRADUATE STUDIES AND RESEARCH

The undersigned certify that they have read, and recommend to the Faculty of Graduate Studies and Research for acceptance, a thesis entitled **ATTACHMENT OF FINE GAS BUBBLES ONTO A SOLID SURFACE AND ELECTROKINETICS OF GAS BUBBLES** submitted by **CHUN YANG** in partial fulfillment of the requirements for the degree of **DOCTOR OF PHILOSOPHY**.



---

**Dr. D. Li**



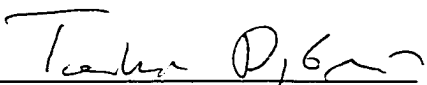
---

**Dr. J. H. Masliyah**




---

**Dr. J. D. Dale**



---

**Dr. T. Dabros**



---

**Dr. L. W. Kostiuk**



---

**Dr. M. Elimelech**

October 19, 1999

## **DEDICATION**

In memory of my lovely and respectful grandpa Zhongqi Yang  
who inspired me of curiosity about the grand nature and pursuit in the harmony science.

## **ABSTRACT**

Study of bubble attachment onto a solid surface (collector) is of fundamental importance to particle hydrodynamics and interfacial science. Interests in this subject stem from its relevance to flotation processes used extensively in many separation processes such as mineral extraction, potable water and wastewater treatment, and bitumen recovery. Despite decades of operation, questions (e.g., selective flotation) still remain regarding mechanisms behind bubble attachment process. In light of this, the attachment of fine bubbles onto model collector surfaces was quantitatively investigated using a well-controlled experimental system that is analogous to bubble-particle attachments in real flotation processes. Such an approach allows elucidation of the effects of colloidal forces on bubble attachment as well as the roles of hydrodynamics and gravity in bubble transport and capture.

This thesis presents results of both experimental investigation and theoretical modeling. On the experimental side, the well-established impinging jet technique is extended to the study of bubble attachment onto solid substrates. The experimental system is designed in such a way that fine bubbles (either Hydrogen or Oxygen bubbles) generated by electrodes are carried by flowing solution to go through a capillary tube and to impinge onto a collector surface. Thorough experiments were carried out to investigate bubble attachment under a wide range of hydrodynamic and physicochemical conditions. Moreover, as no commercial instrument was available for measuring the zeta potential of gas bubbles – which is an important parameter for quantifying the electrostatic double layer interaction, an electrophoresis apparatus was therefore devised



for such a purpose.

On the theoretical side of this study, an Eulerian based approach was used to derive a bubble transport equation that includes contributions from hydrodynamic convection, Brownian diffusion, migration under gravitational buoyancy force and *DLVO* colloidal forces (e.g., the van der Waals and electrical double layer interactions). It was found that the theoretical predictions are generally in reasonable agreement with the corresponding experimental data of bubble attachment to methylated glass, suggesting validation of the bubble transport model. However, the proposed model failed to predict bubble attachment onto untreated glass at low Reynolds numbers. Several possible mechanisms are suggested to account for such a discrepancy.

## ACKNOWLEDGEMENTS

Many wonderful people, directly or indirectly, supported and inspired me to complete this thesis. I would like to express my thanks to my parents, my wife and my son for their unwavering and unconditional love and support. Although they may not technically know anything about colloidal transport phenomenon, they definitely know how to love and support someone who does it. I appreciate their sacrifices for allowing me to pursue my dream. I also wish to thank Mr. Albert Enn for his consistent help and love to my family.

I am indebted to my supervisor Dr. Dongqing Li, who always gives me confidence in my abilities, shows me by his own example that studying interfacial phenomena is fun, gives me uncountable words of advice, and has provided me opportunities of involving a wide spectrum of research projects. I also wish to thank my supervisor Dr. Jacob H. Masliyah for his direct support and guidance to this thesis research. He always encourages me and believes in me to independently conduct research. I am impressed with his sharp insights into physical phenomena and I have learnt a lot from his supervision. Last but not least, I would like to specifically acknowledge Dr. Tadeusz Dabros, who was one of the inventors of the impinging jet technique used in this study. He has made many original contributions that can be reflected from this thesis. Undoubtedly, without his supervision, it is impossible for me to finish this work.

Meanwhile, I would like to extend my appreciation to the external member of my examining committee Dr. Menachem Elimelech, for his time and consideration of this thesis and the members of my supervisory committee: Dr. Doug J. Dale and Dr. Tom W. Forest for their interest, effort, and suggestions.

I am grateful to the personnel support and facilities provided by Syncrude Canada Ltd.– Edmonton Research Center. Specifically, I am in deep gratitude to Dr. Jan Czarnecki who is my contact in Syncrude and gives me innumerable guidance and help

for me. I also wish to thank my friend Dr. Anthony Yeung for his friendship, help in preparation of this thesis, stimulating discussion and sharing ideas of research. To all other colleagues in our colloidal and interfacial science group at Syncrude, Shawn Taylor, Kevin Moran, Alex Wu, Isabelle Laroche, and Zhian (Joe) Zhou, thank you all for many valuable talking and words of encouragement. In addition, I appreciate the wonderful working environment created by my office mate, Carla Tosto and the following people who work in the same laboratory: Peter Abel, Allen Yeung, Tom Tran, Betty Fung, Razaul Haque, and Richard Maslanko.

Finally, I am also grateful to the University of Alberta for awarding me the Doctoral Dissertation Fellowship and the Andrew Stewart Memorial Graduate Prize during the period of this research.

# TABLE OF CONTENTS

<b>Chapter 1</b>	<b>Introduction</b>	1
1.1	Introduction and Motivation	1
1.2	Objectives of This Study	3
1.3	Thesis Outline	4
1.4	Literature Review	6
1.4.1	Bubble-Particle Interaction and Attachment	6
1.4.2	Deposition of Colloidal Particles	8
1.4.3	The Impinging Jet Technique	10
<b>Chapter 2</b>	<b>Fluid Flow Fields in the Impinging Jet Flow Region</b>	13
2.1	Introduction	13
2.2	Governing Equations	13
2.3	Stream Function – Vorticity Method	15
2.4	Boundary Conditions	17
2.5	Numerical Method	21
2.6	Simulation Results and Discussion	24
2.7	Stagnation Point Flow Patterns and Flow Intensity of the Impinging Jet Flow	25
<b>Chapter 3</b>	<b>Bubble Transport Equation for Impinging Jet System</b>	58
3.1	Introduction	58
3.2	Mass Conservation Equation	58
3.3	General Expression for Mass Flux	59
3.4	Bubble Velocity	60
3.5	Bubble Diffusion Coefficient	62
3.6	External Body Forces	63
3.7	Colloidal Surface Forces	63

	3.7.1	van der Waals Interaction	64
	3.7.2	Electrostatic Double Layer ( <i>EDL</i> ) Interaction	67
	3.8	Bubble Transport Equation	74
	3.9	Boundary Conditions	76
	3.10	Validity of Application of the Mass Transport Equation to Fine gas Bubbles	77
<b>Chapter 4</b>		<b>Theoretical Results for Bubble Attachment</b>	<b>83</b>
	4.1	Introduction	83
	4.2	Limiting Analytical Solutions to Mass Transfer Equation	83
	4.3	Numerical Method for Solving Bubble Transport Equation	87
	4.4	Numerical Model Validation	90
	4.5	Numerical Analyses of Bubble Attachment	92
	4.5.1	Effect of van der Waals Interaction	93
	4.5.2	Effect of Hydrodynamic Conditions and Bubble Size	94
	4.5.3	Effect of Gravitational Forces	95
	4.5.4	Effect of Electrostatic Double Layer Interaction	95
	4.5.5	Application of Bubble Transport Equation to Fine Gas Bubbles Attachment onto a Large Solid Particle	98
	4.6	Summary	100
<b>Chapter 5</b>		<b>Experimental Method for Bubble Attachment Studies</b>	<b>114</b>
	5.1	Overview	114
	5.2	The Impinging Jet System	114
	5.3	Experimental Procedure	116
	5.5.1	Preparation and Characterization of Glass Collector Surfaces	116
	5.5.2	Determination of Zeta-Potentials of Fine Bubbles and Collector Surfaces	119
	5.5.3	Impinging Jet Experimental Test	119
	5.4	Bubble Attachment Data Analyses	122

<b>Chapter 6</b>	<b>Measurement of the Zeta-Potential of Fine Bubbles</b>	131
6.1	Introduction	131
6.1.1	Background and Objectives	131
6.1.2	Review of Bubble Zeta-Potential Measurements	133
6.1.3	Proposed Approach for the Present Study	136
6.2	Electrophoresis Method	136
6.2.1	Electrophoresis, Electrophoretic Mobility, and Zeta-Potential	136
6.2.2	Electrokinetic Equations	138
6.2.2.1	Smoluchowski Equation	139
6.2.2.2	Improved Theories of Electrophoresis	141
6.2.3	Coupled Phenomena Involved in Electrophoresis Measurement	142
6.2.3.1	Electroosmotic Flow and Stationary Level	142
6.2.3.2	Temperature Rise during Measurement	145
6.2.3.3	Mass Transfer and Hydrodynamic Behavior of a Microbubble	147
6.2.3.4	Error Estimate for Electrophoresis Measurement	150
6.3	Experimental	151
6.3.1	Equipment Configuration	151
6.3.1.1	Electrophoresis System	152
6.3.1.2	Positioning and Motion Control System	153
6.3.1.3	Optical Video-Image System	153
6.3.2	Calibration of the Cell Depth	153
6.3.3	Determination of the Stationary Level	154
6.3.4	Experimental Procedure	157
6.4	Results and Discussion	158
6.4.1	pH Effect	160
6.4.2	Electrolyte Concentration Effect	161

	6.4.3	Metal Ions Effect	162
	6.4.4	Zeta-Potential of Bubbles in Syncrude Process Water	163
	6.5	Summary	164
<b>Chapter 7</b>		<b>Bubble Attachment Results for Model Collector Surfaces</b>	181
	7.1	Introduction	181
	7.2	Collector Surface Preparation and Characterization	182
	7.3	Bubble Generation and Characterization	184
	7.4	Bubble Attachment onto Methylated Glass Collectors	186
	7.4.1	Effect of Hydrodynamic Conditions	186
	7.4.2	Effect of Electrolyte Concentration	187
	7.4.3	Effect of Solution pH	188
	7.4.4	Effect of Metal Ions	189
	7.5	Bubble Attachment: Comparison between Experiments Theoretical Predictions	191
	7.6	Remarks on Bubble Attachment to Untreated/Methylated Glass Collectors	197
	7.7	Deviation of Theory from Experiment at Low Reynolds Numbers	199
	7.8	Summary	204
<b>Chapter 8</b>		<b>Conclusions and Recommendations</b>	227
	8.1	Contributions Made by This Study	227
	8.2	Recommendations for Future Work	230
<b>Bibliography</b>			234
<b>Appendix A1</b>		<b>Numerical Schemes for Solving Flow Fields in the Impinging Jet Flow Region Using the Stream Function – Vorticity Method</b>	244
	A1.1	Stream Function Equation	244
	A1.2	Vorticity Equation	246

<b>Appendix A2</b>	<b>Thickness of Viscous Boundary Layer in the Impinging Jet Flow Region</b>	251
<b>Appendix A3</b>	<b>An Expression for the Dependence of the Sherwood Number on the Peclet Number in the Impinging Jet Flow Region</b>	255
<b>Appendix A4</b>	<b>Electroosmotic Flow Inside Rectangular Electrophoresis Cells</b>	261
A4.1	Electrostatic Double Layer Field in Rectangular Geometry	261
A4.2	Electroosmotic Flow Field in a Rectangular Cell	265
<b>Appendix A5</b>	<b>Proof of Validity of the Poisson – Boltzmann Equation for the Electroosmotic Flow in a Rectangular Electrophoresis Cell</b>	270



## LIST OF TABLES

<b>Table 4.1</b>	Results of mass transfer rate of fine gas bubbles attachment onto a large solid particle by using the bubble transport equation (4.1).	102
<b>Table 6.1</b>	Calibration results for the cell depth.	166
<b>Table 7.1</b>	Measured contact angles for the untreated and methylated glass collectors using captive bubble method.	207
<b>Table 7.2</b>	Zeta-potentials of the bubbles and the collectors.	208
<b>Table A1.1</b>	Coefficients expressed in general equation (A1.1)	250
<b>Table A3.1</b>	Application of equation (A3.7) to the particle concentration maximum (shown in Figure A3.1) in the presence of gravity and van der Waals ( <i>VDW</i> ) forces only.	259

## LIST OF FIGURES

<b>Figure 2.1</b>	Geometric configuration of the impinging jet cell.	28
<b>Figure 2.2a</b> <b>Figure 2.2b</b>	Computational domain I. Computational domain II.	29
<b>Figure 2.3</b>	Illustration of a portion of the finite-difference grid.	30
<b>Figure 2.4a</b>	Numerical simulation of stream function profiles in the impinging jet flow region for $Re = 1$ .	31
<b>Figure 2.4b</b>	Numerical simulation of stream function profiles in the impinging jet flow region for $Re = 10$ .	32
<b>Figure 2.4c</b>	Numerical simulation of stream function profiles in the impinging jet flow region for $Re = 100$ .	33
<b>Figure 2.4d</b>	Numerical simulation of stream function profiles in the impinging jet flow region for $Re = 1000$ .	34
<b>Figure 2.5a</b>	Numerical simulation of radial velocity distributions in the impinging jet flow region for $Re = 1$ .	35
<b>Figure 2.5b</b>	Numerical simulation of radial velocity distributions in the impinging jet flow region for $Re = 10$ .	36
<b>Figure 2.5c</b>	Numerical simulation of radial velocity distributions in the impinging jet flow region for $Re = 100$ .	37
<b>Figure 2.5d</b>	Numerical simulation of radial velocity distributions in the impinging jet flow region for $Re = 1000$ .	38
<b>Figure 2.6a</b>	Numerical simulation of axial velocity distributions in the impinging jet flow region for $Re = 1$ .	39
<b>Figure 2.6b</b>	Numerical simulation of axial velocity distributions in the impinging jet flow region for $Re = 10$ .	40
<b>Figure 2.6c</b>	Numerical simulation of axial velocity distributions in the impinging jet flow region for $Re = 100$ .	41
<b>Figure 2.6d</b>	Numerical simulation of axial velocity distributions in the impinging jet flow region for $Re = 1000$ .	42

<b>Figure 2.7a</b>	Numerical simulation of stream function profiles in the impinging jet flow region for $Re = 1$ . Calculations based on the computational domain II.	43
<b>Figure 2.7b</b>	Numerical simulation of stream function profiles in the impinging jet flow region for $Re = 10$ . Calculations based on the computational domain II.	44
<b>Figure 2.7c</b>	Numerical simulation of stream function profiles in the impinging jet flow region for $Re = 100$ . Calculations based on the computational domain II.	45
<b>Figure 2.7d</b>	Numerical simulation of stream function profiles in the impinging jet flow region for $Re = 1000$ . Calculations based on the computational domain II.	46
<b>Figure 2.8a</b>	Comparison of velocity profiles at the tube exit for two different computational domains ( $Re = 1$ ).	47
<b>Figure 2.8b</b>	Comparison of velocity profiles at the tube exit for two different computational domains ( $Re = 10$ ).	48
<b>Figure 2.8c</b>	Comparison of velocity profiles at the tube exit for two different computational domains ( $Re = 100$ ).	49
<b>Figure 2.8d</b>	Comparison of velocity profiles at the tube exit for two different computational domains ( $Re = 1000$ ).	50
<b>Figure 2.9</b>	Dependence of the dimensionless intensity of the stagnation point flow, $\bar{\alpha}$ , on the Reynolds number, $Re$ .	51
<b>Figure 2.10a</b>	Dependence of the axial $v_z$ and the reduced radial $v_r/r$ velocity components on the coordinate $z$ for $Re = 1$ .	52
<b>Figure 2.10b</b>	Dependence of the axial $v_z$ and the reduced radial $v_r/r$ velocity components on the coordinate $z$ for $Re = 10$ .	53
<b>Figure 2.10c</b>	Dependence of the axial $v_z$ and the reduced radial $v_r/r$ velocity components on the coordinate $z$ for $Re = 100$ .	54
<b>Figure 2.10d</b>	Dependence of the axial $v_z$ and the reduced radial $v_r/r$ velocity components on the coordinate $z$ for $Re = 1000$ .	55

<b>Figure 2.11</b>	Dependence of the calculated reduced axial velocity component $(-v_z/z^2)$ as $z \rightarrow 0$ on the coordinate $r$ for various Reynolds numbers.	56
<b>Figure 2.12</b>	Dependence of the reduced radial velocity component $(v_r/r)$ as $z \rightarrow 0$ on the coordinate, $r$ , for various Reynolds numbers.	57
<b>Figure 3.1</b>	Diagram illustrating the basic features of the impinging jet system.	81
<b>Figure 3.2</b>	Universal hydrodynamic correction coefficients for a spherical particle diffusion and motion near a plane.	82
<b>Figure 4.1</b>	Calculated Sherwood number, $Sh$ , versus Peclet number, $Pe$ , for different gravity numbers, $Gr$ .	103
<b>Figure 4.2</b>	Comparison of numerical prediction of Sherwood number, $Sh$ , for latex particle deposition with experimental results obtained by Dabros and van de Ven.	104
<b>Figure 4.3</b>	Comparison of numerical prediction of Sherwood number, $Sh$ , for oil droplets deposition with experimental results obtained by Sanders et al.	105
<b>Figure 4.4</b>	Calculated Sherwood number, $Sh$ , versus Peclet number, $Pe$ , for different adhesion numbers, $Ad$ , with a fixed gravity number $Gr = 10^5$ .	106
<b>Figure 4.5</b>	Normalized bubble attachment flux, $j_o/n_\infty$ , versus bubble radius, $a_p$ , for different Reynolds numbers, $Re$ , with the <i>EDL</i> interaction.	107
<b>Figure 4.6a</b>	Calculated Sherwood number, $Sh$ , versus Peclet number, $Pe$ , for different gravity numbers, $Gr$ , under combined effects of the repulsive van der Waals ( $Ad = -0.1$ ) interaction and the <i>EDL</i> interaction ( $DI = 1000$ , $\tau = 1000$ , and $Da = 2$ ).	108
<b>Figure 4.6b</b>	Dimensionless bubble-collector interaction force profile corresponding to Figure 4.6a.	109
<b>Figure 4.7a</b>	Calculated Sherwood number, $Sh$ , versus Peclet number, $Pe$ , for different <i>EDL</i> parameters, $DI$ , under combined effects of the repulsive van der Waals ( $Ad = -0.1$ ) interaction and the <i>EDL</i> interaction ( $\tau = 1000$ and $Da = 2$ ).	110
<b>Figure 4.7b</b>	Dimensionless bubble-collector interaction force profile corresponding to Figure 4.7a.	111

<b>Figure 4.8a</b>	Calculated Sherwood number, $Sh$ , versus Peclet number, $Pe$ , for different <i>EDL</i> ionic strength, $\tau$ , under combined effects of the repulsive van der Waals ( $Ad = -0.1$ ) interaction and the <i>EDL</i> interaction ( $\tau = 1500$ and $Da = 2$ ).	112
<b>Figure 4.8b</b>	Dimensionless bubble-collector interaction force profile corresponding to Figure 4.8a.	113
<b>Figure 5.1</b>	Schematic of experimental setup for the performing laboratory-scale bubble attachment measurements.	124
<b>Figure 5.2</b>	Typical bubble attachment pattern on a glass surface.	125
<b>Figure 5.3a</b>	Calibration of the flowmeter for the low flow rate region.	126
<b>Figure 5.3b</b>	Calibration of the flowmeter for the high flow rate region.	127
<b>Figure 5.4</b>	Schematic diagram of chemical structures for untreated and methylated glass surfaces, proposed by Araujo et al. (1995).	128
<b>Figure 5.5</b>	Schematic of experimental setup for contact angle measurement.	129
<b>Figure 5.6</b>	An image used for determination of bulk bubble number concentration.	130
<b>Figure 6.1</b>	Structure of the <i>EDL</i> formed at a surface of potential; The lower curve representing strong adsorption within the Stern layer.	167
<b>Figure 6.2</b>	Schematic diagram representing charge distributions around a negatively charged particle.	168
<b>Figure 6.3</b>	(a) Velocity distributions in X-Y cross section of the rectangular electrophoretic cell (b) Geometric configuration of the electrophoresis cell and Cartesian coordinate system for evaluation of electroosmotic flow in the rectangular cell	169
<b>Figure 6.4</b>	Temperature rise of solution during electrophoretic measurements due to Ohmic heating.	170
<b>Figure 6.5</b>	Schematic of experimental setup for measurement of the zeta-potential of fine bubbles using microelectrophoresis technique.	171
<b>Figure 6.6</b>	Measured particle velocity distributions.	172

<b>Figure 6.7</b>	Measured zeta-potential of fine bubbles dispersed in a $10^{-4}$ M NaCl solution.	173
<b>Figure 6.8</b>	Comparison of the bubble zeta-potentials in a $10^{-2}$ M NaCl solution measured from this study with the data reported by Li and Somasundaran (1991).	174
<b>Figure 6.9</b>	Measured zeta-potential of fine bubbles versus solution pH for different concentrations of the NaCl solution.	175
<b>Figure 6.10</b>	Measured zeta-potential of fine bubbles versus solution pH in a $10^{-2}$ M NaCl solution with addition of $CaCl_2$ .	176
<b>Figure 6.11</b>	Measured zeta-potential of fine bubbles versus solution pH in a $10^{-2}$ M NaCl solution with addition of $AlCl_3$ .	177
<b>Figure 6.12</b>	Bubble zeta-potential in Syncrude Canada Ltd. process water with addition of $CaSO_4$ .	178
<b>Figure 6.13</b>	Bubble zeta-potential in synthetic water for different pH values.	179
<b>Figure 6.14</b>	Bubble zeta-potential in synthetic water with addition of $CaSO_4$ .	180
<b>Figure 7.1a</b>	Surface roughness of the untreated glass scanned by AFM.	209
<b>Figure 7.1b</b>	Surface roughness of the methylated glass scanned by AFM.	210
<b>Figure 7.2</b>	Bubble size distributions in a 0.01 M NaCl solution for various Reynolds numbers.	211
<b>Figure 7.3</b>	Experimental results of the normalized bubble attachment density on the methylated glass versus time for different Reynolds numbers (Re), while keeping both solution concentration and pH constant.	212
<b>Figure 7.4</b>	Experimental results of the normalized bubble attachment density on the methylated glass versus time for different solution concentrations with fixed Reynolds number (Re) and solution pH.	213
<b>Figure 7.5</b>	Experimental results of the normalized bubble attachment density on the methylated glass versus time for different solution pH's with fixed Reynolds number (Re) and solution concentration.	214

<b>Figure 7.6</b>	Experimental results of the normalized bubble attachment density on the methylated glass versus time with effect of different levels of $CaCl_2$ concentration, while keeping Reynolds number ( $Re$ ) and solution $pH$ constant.	215
<b>Figure 7.7</b>	Experimental results of the normalized bubble attachment density on the methylated glass versus time with effect of different metal ions, while keeping Reynolds number ( $Re$ ) and solution $pH$ constant.	216
<b>Figure 7.8</b>	Schematic diagram showing the van der Waals interaction for the methylated glass /water/ air system.	217
<b>Figure 7.9</b>	Calculated effective Hamaker constant for the methylated glass /water/air system.	218
<b>Figure 7.10</b>	Variation of the normalized bubble attachment flux onto methylated glass surfaces with the Reynolds number for different concentrations of the solution.	219
<b>Figure 7.11a</b>	Variation of the normalized bubble attachment flux onto methylated glass surfaces with the Reynolds number. Solid symbols represent experimentally measured flux; Open symbols are calculated bubble attachment flux with bubble size distribution corrections.	220
<b>Figure 7.11b</b>	Variation of the normalized bubble attachment flux onto methylated glass surfaces with the Reynolds number. Solid lines represent solutions to bubble transport equation based on a uniform bubble size; Solid symbols represent measured flux; Open symbols are calculated bubble attachment flux with bubble size distribution corrections.	221
<b>Figure 7.12</b>	Normalized bubble attachment flux onto methylated glass surfaces versus $NaCl$ solution concentration with a fixed Reynolds number $Re=200$ . Solid symbols represent measured flux; Solid line is the calculated mean attachment flux with bubble size distribution correction.	222
<b>Figure 7.13</b>	Normalized bubble attachment flux onto methylated glass surfaces versus $NaCl$ solution $pH$ with a fixed Reynolds number $Re=200$ . Solid symbols represent measured flux; Solid line is the calculated mean attachment flux with bubble size distribution correction.	223

<b>Figure 7.14</b>	Normalized bubble attachment flux onto untreated glass surfaces versus the Reynolds number for fixed solution concentration and pH value. Solid symbols represent measured flux; Solid line is the calculated mean attachment flux with bubble size distribution correction.	224
<b>Figure 7.15a</b>	(i) Scanned image for bubble attachment on the untreated glass surface (top view); (ii) Configuration of bubble attachment on the untreated glass surface (side view)	225
<b>Figure 7.15b</b>	(i) Scanned image for bubble attachment on the methylated glass surface (top view); (ii) Configuration of bubble attachment on the methylated glass surface (side view)	226
<b>Figure A2.1</b>	Dependence of the hydrodynamic boundary-layer thickness, $\delta_v$ , on the Reynolds number, $Re$ in the impinging jet flow region (the radius of the capillary tube is chosen as $R = 1325 \mu m$ ).	254
<b>Figure A3.1</b>	Effect of the Peclet number, $Pe$ , on computational particle concentration distributions under positive gravity force ( $Gr > 0$ ) in the absence of the <i>EDL</i> interaction.	250



## NOMENCLATURE

<i>a</i>	half height of electrophoresis cell, [m]
<i>a<sub>o</sub></i>	particle radius, [m]
<i>a<sub>p</sub></i>	bubble radius, [m]
A	cross-sectional area of rectangular electrophoresis cell or bubble surface area, [m <sup>2</sup> ]
<i>Ad</i>	dimensionless adhesion number, [ $A_{132}/(6kT)$ ]
<i>A<sub>ij</sub></i>	Hamaker constant for the van der Waals interaction between phase i and phase j across vacuum, [J]
<i>A<sub>132</sub></i>	Hamaker constant for the van der Waals interaction between phase 1 (a bubble) and phase 2 (collector surface) separated by medium 3 (an aqueous solution), [J]
<i>b</i>	half depth of electrophoresis cell, [m]
<i>c</i>	solution mole ionic concentration (M or mol/L)
$\Delta c$	concentration difference between bubble surface and bulk solution, [M]
<i>c<sub>o</sub></i>	experimentally determined bubble bulk number concentration, [m <sup>-3</sup> ]
<i>c<sub>v,f</sub></i>	constant-volume specific heat capacity of solution, [JKg <sup>-1</sup> K <sup>-1</sup> ]
<i>Ca</i>	capillary number, [ $\mu_f U_p / \gamma_{lv}$ ]
$\underline{\underline{D}}$	bubble diffusion coefficient tensor, [m <sup>2</sup> s <sup>-1</sup> ]
<i>D<sub>∞</sub></i>	bulk bubble diffusion coefficient, [m <sup>2</sup> s <sup>-1</sup> ]
<i>D</i>	ion diffusion coefficient, [m <sup>2</sup> s <sup>-1</sup> ]
<i>Da</i>	dimensionless <i>EDL</i> asymmetry parameter, [ $(\zeta_c - \zeta_p)^2 / (2\zeta_c \zeta_p)$ ]
<i>DI</i>	dimensionless <i>EDL</i> parameter, [ $(4\pi\epsilon_o\epsilon_r a_p \zeta_c \zeta_p) / (kT)$ ]
<i>e</i>	elementary charge, [ $1.602 \times 10^{-19}$ C]
<i>E, <math>\underline{E}</math></i>	electric field strength or vector, [V m <sup>-1</sup> ]
<i>f</i>	friction factor

$f_1, f_2, f_3, f_4$	dimensionless universal hydrodynamic correction coefficients
$F, \underline{F}$	force or force vector, [N]
$F_r, F_z$	force components, [N]
$F_{Col}$	colloidal force, [N]
$F_{Ex}$	external force, [N]
$F_G$	gravitational force, [N]
$F_{VDW}$	van der Waals interaction force, [N]
$\bar{F}_z$	dimensionless normal (axial) component force, [ $F_z a_p / (kT)$ ]
$g, \underline{g}$	gravitational acceleration or vector, [ $m s^{-2}$ ]
$Gr$	dimensionless gravity number, [ $(2 \Delta\rho g a_p^3) / (9\mu_r D_\infty)$ ]
$h$	separation gap between bubble and collector, [ $h = z - a_p$ ] [m]
$\bar{h}$	dimensionless separation gap between bubble and collector, [ $h/a_p$ ]
$\Delta\bar{h}_i$	nonuniform mesh size in physical domain
$H_o$	dimensionless separation distance between capillary exit and collector
$j, \underline{j}$	bubble mass transfer flux and its vector, [ $m^{-2} s^{-1}$ ]
$j_o$	bubble attachment flux, [ $m^{-2} s^{-1}$ ]
$\bar{j}_o$	normalized bubble attachment flux, [ $m s^{-1}$ ]
$j_r, j_z$	bubble mass transfer flux components, [ $m^{-2} s^{-1}$ ]
$\bar{j}_r, \bar{j}_z$	dimensionless bubble mass transfer flux components, [ $(j_i a_p) / (D_\infty n_\infty)$ , ( $i=r, n$ ) ]
$\bar{J}_o$	calculated normalized bubble attachment mean flux with correction for bubble size distributions, [ $m s^{-1}$ ]
$k$	Boltzmann constant, [ $1.381 \times 10^{-23} JK^{-1}$ ]
$K$	electric conductivity of solution, [ $\Omega^{-1} m^{-1}$ ]
$i$	Electric current going through electrophoresis cell, [A]

$M$	mole concentration, [mol/L]
$n$	bubble number concentration, [ $\text{m}^{-3}$ ]
$n_{io}$	bulk number concentration of type-i ions, [ $\text{m}^{-3}$ ]
$n_o$	ion number concentration of bulk solution, [ $\text{m}^{-3}$ ]
$n_t$	bubble attachment density, [ $\text{m}^{-2}$ ]
$\bar{n}_t$	normalized bubble attachment density, [m]
$n_\infty$	bubble number concentration in the bulk, [ $\text{m}^{-3}$ ]
$\bar{n}$	dimensionless bubble number concentration, [ $n/n_\infty$ ]
$N$	grid number for numerical calculation
$N_A$	molar numbers of ions transfer from the bulk to bubble surface, [mol]
$N_A$	Avogadro's constant, [ $6.023 \times 10^{23}$ ]
$N_t$	number of attached bubbles
$N(t)$	number of bubbles passing through a central section of capillary exit over a time interval $\Delta t$
$p$	pressure, [ $\text{N m}^{-2}$ ]
$\bar{p}$	dimensionless pressure, [ $p/(\rho_f V^2)$ ]
$p(a_{pi})$	bubble size distribution intensity function
$Pe$	Peclet number, [ $2\alpha a_p^3/D_\infty$ ] for bubble attachment or [ $U_b a_p/D$ ] for ion mass transfer (adsorption)
$Q$	volumetric flow rate, [ $\text{m}^3 \text{s}^{-1}$ ]
$Q$	heat gain inside electrophoresis cell due to Ohmic heating, [J]
$r$	radial cylindrical coordinate
$r_c$	radius of the section area at tube exit for determining bubble bulk number concentration, [m]
$\bar{r}$	dimensionless radial cylindrical coordinate, [ $r/R$ or $r/a_p$ ]
$R$	radius of capillary tube or cylindrical coordinator, [m]
$R$	Electric resistance of solution filled in electrophoresis cell, [ $\Omega$ ]

$R$	gas constant, [8.314 JK <sup>-1</sup> mol <sup>-1</sup> ]
$Re$	Reynolds number, [ $\rho_f V R / \mu_f$ ]
$Sc$	Schmidt number, [ $\mu_f / (\rho_f D_\infty)$ ]
$Sh$	Sherwood number, [ $j_o a_p / (D_\infty n_\infty)$ ] for bubble attachment or [ $\alpha_A a_p / D$ ] for ion mass transfer (adsorption)
$t$	time, [s]
$\Delta t$	time interval, [s]
$T$	absolute temperature, [K]
$\Delta T$	temperature rise, [K]
$\underline{u}$	bubble velocity vector, [ms <sup>-1</sup> ]
$u_g$	bubble velocity due to buoyancy effect, [ms <sup>-1</sup> ]
$u_{os}$	electroosmotic velocity induced at cell wall, [ms <sup>-1</sup> ]
$u_r$	bubble velocity component along direction of cylindrical coordinator $r$ , [ms <sup>-1</sup> ]
$u_z$	fluid velocity component along direction of cylindrical coordinator $z$ , [ms <sup>-1</sup> ]
$u(x, y)$	electroosmotic velocity distributions inside electrophoresis cell, [ms <sup>-1</sup> ]
$u_b(r)$	bubble velocity distributions at the tube exit, [ms <sup>-1</sup> ]
$U_b$	bubble terminal velocity inside electrophoretic cell, [ms <sup>-1</sup> ]
$U_o$	particle settling velocity, [ms <sup>-1</sup> ]
$U_p$	characteristic bubble velocity, [ms <sup>-1</sup> ]
$v_e$	local electroosmotic velocity, [ms <sup>-1</sup> ]
$v_E$	electrophoretic velocity, [ms <sup>-1</sup> ]
$v_{OB}(y)$	particle velocity distributions inside electrophoresis cell, [ms <sup>-1</sup> ]
$v_{OM}(y)$	electroosmotic velocity distributions inside electrophoresis cell, [ms <sup>-1</sup> ]

$v_r$	fluid velocity component along direction of cylindrical coordinator $r$ , [ms <sup>-1</sup> ]
$\bar{v}_r$	dimensionless fluid velocity component, [ $v_r/V$ ]
$v_z$	fluid velocity component along direction of cylindrical coordinator $z$ , [ms <sup>-1</sup> ]
$\bar{v}_z$	dimensionless fluid velocity component, [ $v_z/V$ ]
$v(r)$	fluid velocity distributions at the capillary tube exit, [ ms <sup>-1</sup> ]
$V$	average velocity at capillary tube exit, [ ms <sup>-1</sup> ]
$V_E$	electrophoretic mobility, [ $v_E/E$ ]
$V_{Col}$	colloidal interaction potential between a sphere and a flat plate, [J]
$V_{EDL}$	electrostatic double layer interaction potential, [J]
$V_{VDW}$	van der Waals interaction potential, [J]
$W$	energy input into electrophoresis cell by Ohmic heating, [J]
$Wb$	Webber number, [ $\rho_f U_p^2 a_p / \gamma_{lv}$ ]
$x$	x-coordinate, [m]
$X$	dimensionless x-coordinate
$y$	y-coordinate, [m]
$Y$	dimensionless y-coordinate
$y_o$	location of stationary level inside electrophoresis cell, [m]
$\bar{y}$	dimensionless y-coordinate
$z$	axial coordinate, or valence of ions
$\bar{z}$	dimensionless axial coordinate, [ $z/R$ or $z/a_p$ ]
$z_i$	valence of type-i ions

### *Greek Symbols*

$\alpha$	dimensionless relaxation factor for numerical iteration or flow intensity of stagnation point flow, [ m <sup>-1</sup> s <sup>-1</sup> ]
----------	--

$\alpha_A$	mass transfer coefficient based on mole concentration, [m s <sup>-1</sup> ]
$\bar{\alpha}$	dimensionless flow intensity of stagnation point flow
$\bar{\beta}$	new dimensionless variable for numerically solving bubble transport equation
$\Delta \bar{\beta}$	uniform mesh size for $\bar{\beta}$ variable in transformed domain
$\gamma_{lv}$	interfacial tension between liquid phase and vapor (or air) phase, [J m <sup>-2</sup> ]
$\Gamma$	gamma function
$\Gamma_A$	Gibbs surface mass excess (or interfacial mole density), [mol m <sup>-2</sup> ]
$\delta$	location of “perfect sink” boundary condition for bubble interception, [m]
$\bar{\delta}$	dimensionless location of “perfect sink” boundary condition, [ $\delta/a_p$ ]
$\delta_v$	thickness of hydrodynamic boundary layer in the impinging jet region, [m]
$\varepsilon$	convergence criterion for numerical iteration
$\varepsilon_o$	permittivity of vacuum, [ $\varepsilon_o = 8.854 \times 10^{-12}$ C V <sup>-1</sup> m <sup>-1</sup> ]
$\varepsilon_r$	dimensionless or relative dielectric constant
$\eta$	particle capture efficiency or a new variable for numerical calculation
$\theta$	contact angle or cylindrical coordinator, [deg]
$\kappa$	Debye-Hückel parameter, [ $(e^2 \sum n_{io} z_i^2 / \varepsilon_o \varepsilon_r k T)^{0.5}$ m <sup>-1</sup> ]
$\lambda$	London characteristic wavelength or retardation parameter, [m]
$\lambda$	solution molar conductivity, [m <sup>2</sup> Ω <sup>-1</sup> mol <sup>-1</sup> ]
$\lambda$	characteristic wavelength, [m]
$\bar{\lambda}$	dimensionless retardation wavelength, [ $\lambda/a_p$ ]
$\mu_f$	fluid viscosity, [Pa s]
$\zeta$	zeta-potential, [V]
$\rho_e$	electrostatic charge density, [C m <sup>-3</sup> ]
$\rho_f$	liquid density, [kg m <sup>-3</sup> ]
$\rho_o$	particle density, [kg m <sup>-3</sup> ]

$\rho_p$	bubble density, [ kg m <sup>-3</sup> ]
$\Delta \rho = \rho_p - \rho_f$	density difference between bubble and liquid fluid phase, [ kg m <sup>-3</sup> ]
$\bar{\rho}$	dimensionless radial coordinate
$\tau$	dimensionless ionic strength, [ $\kappa a_p$ ]
$\phi(h)$	potential energy of interaction between two overlap flat double layers, [V]
$\varphi$	local potential in the <i>EDL</i> field, [V]
$\psi$	local electrostatic potential, [V]
$\psi$	stream function, [ m <sup>3</sup> s <sup>-1</sup> ]
$\psi_o$	surface potential, [V]
$\psi_\zeta$	Stem potential, [V]
$\bar{\psi}$	dimensionless stream function
$\zeta$	zeta-potential, [V]
$\bar{\omega}$	dimensionless vorticity
$\bar{\omega}^*$	ratio of dimensionless flow vorticity to dimensionless radial distance, [ $\bar{\omega}/r$ ]
$\nabla$	gradient operator
$\nabla^2$	Laplacian operator

# CHAPTER 1

## INTRODUCTION

### 1.1 Introduction and Motivation

Attachment of gas bubbles onto surfaces (referred to as collectors) is vital to the success of flotation processes that have been extensively used in many industrial and environmental separation processes, such as mineral extraction, bitumen recovery, petrochemical refining, potable water and wastewater treatment, food processing, and pulp and paper manufacturing. A fundamental understanding of the underlying mechanisms of bubble-collector interaction and attachment is essential to the process control and optimisation of the aforementioned technological processes.

From a theoretical perspective, the bubble attachment process can be quite complicated. For ease of understanding, such a process is conceptually divided into the following four stages: (i) At large distances from the collector, bubble transport in the bulk fluid is determined by convection and migration due to external forces such as buoyancy. (ii) As a bubble approaches the collector within a distance comparable to the bubble size, displacement of the fluid between the bubble and the collector becomes increasingly difficult due to additional hydrodynamic drag on the bubble (in contrast to the transport of a bubble in an unbounded, infinite fluid. The resulting reduction in bubble mobility is commonly referred to as the particle-wall hydrodynamic interaction. (iii) At even closer distances to the collector (1-100 nm), apart from the above-mentioned hydrodynamic interaction, the bubble's motion will be affected by at least two types of well-recognized colloidal forces: First, the universal van der Waals (*VDW*) interaction becomes significant within such a range. Second, interfaces in aqueous media are nearly always charged due to the adsorption of ionic surface-active molecules or the dissociation of ionizable surface sites. Therefore, a so-called electrostatic double layer (*EDL*) is formed near charged surfaces within a region of the order of the Debye length. The *EDL* interaction may develop at such a region. These two colloidal interactions form the basis



of the well-known Derjaguin-Landau-Verwey-Overbeek (*DLVO*) theory of colloidal stability. Further, other non-*DLVO* colloidal interactions may be important to bubble attachment under certain physicochemical conditions. These are short-range interactions (approximately 1-10 nm) which may include hydration (structural), steric, hydrophobic, and polymer bridging interactions. In addition, stochastic effects, such as discrete surface charges at the collector and bubble surfaces, surface heterogeneity and roughness, etc., may play pronounced roles at such separations. (iv) It has been recognized that before the bubble can be in physical contact with the collector, the liquid film between the bubble and the collector surface must rupture. The rupture of the liquid film takes place at the so-called critical film thickness, which is associated with the stability of the thin liquid film. To a large extent, such a process is dependent on the surface interaction forces between the bubble and the collector surface. If the thin film is broken, a three-phase contact line is created and a contact angle is formed, resulting in the bubble being in physical contact with the collector. This step involves many complex phenomena, some of which are even difficult to define. It becomes obvious that traditional continuum mechanics breaks down at such dimensions. No theory is available to quantitatively describe the physical processes at such a stage.

Strictly speaking, a rigorous study of the entire process of bubble attachment should take into account all phenomena involved in the above four stages. For simplicity, however, the present work will only focus on the transport of fine bubbles from a liquid flow onto a collector surface. Bubble attachment is considered to take place when bubbles can be brought close to the collector surface within an interception distance, which usually is in the same range as the so-called primary energy minimum (*PEM*). No attempt will be made to describe bubble attachment when and after the bubbles are in physical contact with the collector. Nevertheless, as stated above, the complex bubble attachment process is usually controlled by the simultaneous influences of convection, diffusion, colloidal and hydrodynamic interactions, and external body forces such as gravity. Therefore, the study of bubble attachment under controlled conditions can give insights into the dynamic nature of colloidal interactions operating between bubbles and collectors and the roles of hydrodynamics and gravitational forces in bubble transport and

capture. However, very little information is available on quantitatively describing the influences of these factors on the bubble attachment.

Flotation is a separation method based on the attachment of gas bubbles onto target particles as gas bubbles rise through a solution or suspension. The flotation technology was originally developed in the early years of this century for the beneficiation of mineral recovered. It is now extensively used in mineral processing, accounting for 95% of total amount of base metals recovery. Owing to its simplicity, reliability, and efficiency, the flotation process has been employed in the Clark Hot Water Process used for extraction of bitumen from the Athabasca Oil Sands in Alberta, Canada. In addition, such separation technique is also widely used to treat wastewater discharged by a wide variety of industrial processes, including urban sewage treatment, general metals-related manufacturing, and food processing. Despite many years of operation, questions still remain around regarding the dominant mechanisms behind the attachment of gas bubbles to particles. Specifically, it has been frequently reported in many industrial applications that some particles are floatable, while others are not. This phenomena is referred to as “selective flotation”, and has not yet been fully understood.

It is therefore of great importance, from both theoretical and practical perspectives, to fundamentally explore the governing mechanisms of the bubble attachment process.

## **1.2 Objectives of This Study**

The intention of this thesis was to develop an experimental technique that enables one to quantitatively and visually study the bubble attachment process. As pointed out earlier, the process of bubble attachment involves at least two basic steps: first, the bubble must somehow be brought close to the collector surface, and second, the liquid film (between the bubble and the collector surface) rupture must occur. It has been recognised that bubble transport is mainly driven by hydrodynamic and gravitational buoyancy forces. The liquid film rupture, or the stability of the thin liquid film, is largely controlled by the colloidal interaction forces between the bubble and the collector

surface. Both hydrodynamic and colloidal interaction forces are, in turn, governed by hydrodynamic and physicochemical conditions including flow intensity, bubble size, ionic strength, solution pH, and type of metal ions. Although the importance of hydrodynamic and physicochemical effects is well recognized, there have been relatively few controlled studies of such effects on bubble attachment. Hence, one of the main objectives of this thesis is to conduct a systematic investigation of fine bubble attachment onto a solid surface under various hydrodynamic flow intensities, ionic strengths, solution pH's, and types of metal ions. Another important goal of this study is to provide extensive experimental data that would enable validation and improvement of fundamental bubble attachment models. In addition, as no commercial instrument is available for measuring the zeta-potential of bubbles (needed for quantifying the *EDL* interaction), an apparatus is devised to carry out such measurements. In summary, the three objectives of this study are restated as follows:

1. Develop a technique that allows one to experimentally and theoretically study the kinetics of fine bubble attachment to a solid surface.
2. Conduct systematic bubble attachment experiments under a wide range of hydrodynamic and physicochemical conditions so that a significant amount of experimental data on the bubble attachment process can be accumulated.
3. Develop a reliable apparatus based microelectrophoresis method to measure the zeta-potentials of gas bubbles under a wide variety of solution conditions.

In general, this investigation is intended to bridge the gap between theory and experiment. Although this study is fundamental in nature, information extracted from the bubble attachment process can be of great importance to the development and improvement of aforementioned industrial applications.

### **1.3 Thesis Outline**

This thesis presents the first study of bubble attachment onto a solid surface under well-controlled conditions, allowing for assessment of the applicability of the existing theories on bubble attachment. This is accomplished by using a well-established impinging jet technique. A summary of the overall thesis is given below:

Chapter 1 serves as a general introduction to the background and motivation of this work. The research objectives are laid out, and a literature review of the current status is included. A brief description of the impinging jet technique is also given.

The theoretical parts of the thesis are mainly included in Chapters 2 to 4. In Chapter 2, a procedure is developed for CFD (computational fluid dynamics) simulation of the flow fields in the entire impinging jet cell. A detailed numerical scheme is given in Appendix A1. An expression for the stagnation flow pattern is proposed to approximate the velocity field near the stagnation point, where colloidal interactions are expected to play important roles in bubble attachment. Such an expression will simplify the bubble transport equation derived in Chapter 3. An Eulerian based approach is employed to derive the bubble transport equation that accounts for contributions from convection, Brownian diffusion, hydrodynamic interactions, gravity, as well as van der Waals and *EDL* interactions. In Chapter 4, analytical solutions to the bubble transport equation are first presented. A numerical method for solving the complete bubble transport equation is then described. A parametric study is conducted to examine the effects of the dimensionless groups  $Pe$ ,  $Gr$ ,  $Ad$ ,  $DI$ ,  $Da$ , and  $\tau$  on the bubble attachment rate,  $Sh$ .

The bubble attachment experiments are presented in Chapters 5 and 7. The impinging jet system is described in Chapter 5. General experimental procedures are also given in this chapter. Chapter 7 presents all experimental results of bubble attachment onto methylated and untreated glass collectors. These experimental observations are compared with theoretical predictions based on the proposed model. Discussions are then given on these results.

Chapter 6 can be considered a separated part that deals with the measurement of bubble zeta-potentials. In addition, other relevant work is presented in Appendices A4 and A5. Appendix A4 presents a rigorous theoretical description of the electroosmotic flow in a rectangular electrophoresis cell. In Appendix A5, a theoretical proof is provided to illustrate the validity of the application of the Poisson-Boltzmann equation to electroosmotic flows in an electrophoresis cell.

Finally, Chapter 8 summarizes the contributions of this dissertation and gives recommendations for future work on bubble attachment studies.

## **1.4 Literature Review**

### **1.4.1 Bubble-Particle Interaction and Attachment**

Many theoretical and experimental studies on bubble-particle interaction and attachment have been accomplished, and can be found in a proliferation of publications. Excellent reviews were provided by Schulze (1984) and Yoon (1991). In the past, most of existing theoretical analyses of air flotation were focussed on the capture of non-Brownian micron-sized particles by a single, large gas bubble (being of the order of millimeters in diameter). The “collection efficiency” is usually introduced to quantify the flotation rate. Such a collection efficiency, however, depends on complex processes (or steps) of the particle-bubble collision, interaction, attachment, and detachment, and hence it is characterized by too many interplay factors. To simplify the theoretical analysis, it is acceptable, to some extent, to treat each step separately. This means the particle-bubble collision, attachment and detachment can be evaluated independently. Each of these steps has been extensively studied in the literature. For example, different theories have been developed to predict the bubble-particle collision efficiency. The simplest theory, due to Smoluchowski (1917), completely neglects the hydrodynamics of bubble-particle interaction and assumes that the bubble and the particle exactly follow vertical trajectories. In this case, the bubble and particle will collide if their horizontal separation distance is less than the sum of their radii. A slightly more advanced theory by Yoon and Luttrell (1989) assumes that the falling particle exactly follows the streamlines of the rising bubble. Loewenberg and Davis (1994) have presented a model for calculating the collision efficiency, which accurately includes the hydrodynamics of the collision process as well as the effect of van der Waals interactions. Following the same approach, Nguyen-Van (1994) and Heindel and Bloom (1999) improved on this model to cover a wider range of hydrodynamic conditions. Recently, a more comprehensive model was developed by Leppinen (1999) to incorporate the exact hydrodynamics of bubble-particle interactions under influences of both the van der Waals and *EDL* interactions. However, in accordance with the theoretical analyses, the corresponding experimental results,

mostly based on column flotation technique, always exhibit the net effect of these steps. In practice, it is difficult to split the bubble-solid attachment process into the individual steps. This, to some extent, makes it difficult to directly compare experimental results with theoretical predictions.

The diffusion capture of Brownian particles has also been studied extensively. Acrivos and Taylor (1962) considered the capture of diffusing point particles by a rising sphere. Later, Spielman (1970) and Prieve and Ruckenstein (1974) developed expressions for predicting the capture rates of spherical Brownian particles under hydrodynamic flow conditions. Recently, attempts were made to consider the gravity-induced aggregation of particles, accounting for the existence of van der Waals attraction, Brownian motion, and the *EDL* and hydrodynamic interactions (Melik and Fogler, 1984; Wang and Wen, 1990). These analyses are based on the solution of the quasi-steady convective-diffusion equation in terms of the pair probability density. However, such studies are restricted to cases where gravity effects are weak in relation to Brownian motion (i.e., small Peclet numbers).

A number of experimental studies tackling bubble-particle interaction and attachment has been reported to account for the effects of solution electrolyte concentration and pH (Fukui and Yuu, 1980; Okada et al., 1990), the types of metal ions (Celik et al., 1998), hydrophobic surface forces (Yoon and Mao, 1996), and inertial hydrodynamic interaction (Dai, et al., 1998). Exclusively, column flotation techniques were used in these studies. Based on such flotation experiments, only bulk-averaged information regarding bubble-particle interaction is available, and the results represent the net effect of hydrodynamics and colloidal surface forces. Further, the hydrodynamic conditions created in these column flotation experiments are difficult to control and reproduce. The undergoing phenomena are often so complex that it is very difficult to find a unique interpretation of the results in terms of a comprehensive physical framework. Therefore, to gain insights into the basic mechanisms involved in the process of bubble-solid surface interaction and attachment, it is appropriate to analyze a related but simpler and better-defined system. Such a system will be described in Section 1.4.3.

### **1.4.2 Deposition of Colloidal Particles**

From a physical perspective, there is great similarity between bubble attachment and particle deposition. Deposition techniques are often used in research because they provide laboratory – scale models of surface coating (Luthi and Ricka, 1998), filtration (Elimelech, 1991), fouling (Chan et al., 1996), and contamination control processes (Riley and Carbonell, 1993a; 1993b). The relationship between deposition experiments and these processes is self-evident. As Swanton (1995) pointed out in an excellent review on the experimental studies of colloidal stability, deposition experiments can be classified as “flow techniques across a collector surface”. Flow techniques generally allow for more rigorous control of the hydrodynamics, and also provide information regarding individual particle-collector interaction rather than the bulk-averaged information that is available from column experiments.

Extensive studies of particle deposition have been accomplished both experimentally and theoretically. Excellent reviews on this subject were provided by Adamczyk and co-workers (1983; 1994). The two existing theoretical approaches for predicting the kinetics of particle deposition, which take into account hydrodynamic interactions and colloidal surface forces, can be generally classified into the Lagrangian and the Eulerian methods. The Lagrangian method, also called the limiting trajectory analysis, focuses on an individual particle’s motion along its trajectory under the combined actions of all relevant forces and torques (Zebel, 1965; Spielman and Goren, 1970; Spielman and Fitzpatrick, 1973). Although a simple approach, it is of limited use in cases where Brownian diffusion is significant (e.g., for colloidal particles), the particle-collector interaction energy barriers are high, or the flow patterns are complex around the collector surface. In order to overcome these disadvantages, a more comprehensive approach for studying particle deposition, based on the Eulerian method, was developed by Ruckenstein and Prieve (1973) and Spielman and Fitzpatrick (1974). Most importantly, the Eulerian method can give particle concentration distributions that not only reflect the combined effects of hydrodynamic flow and surface forces, but also provide insights into particle transfer processes. Hence, the Eulerian approach will be implemented in this work.

In the literature, there are numerous theoretical and experimental studies which deal with particle deposition onto collectors having various kinds of shapes including the rotating disc (Wnek et al., 1977; Dabros and Adamczyk, 1979; Prieve and Lin, 1980; Rajagopalan and Kim, 1981), the spherical collectors (Spielman and Cukor, 1973; Spielman and Fitzpatrick, 1973), the cylindrical collectors (Spielman and Fitzpatrick, 1973; Adamczyk and van de Ven, 1981), and the parallel and cylindrical channels (Bowen et al., 1976; Bowen and Epstein, 1979). The most widely used device in deposition experiments is the rotating disc, which, from a hydrodynamic perspective, can be categorized as a “stagnation point flow technique”. As the name implies, the collector surface of such a device is a disc that rotates at a constant angular velocity to create a diffusion boundary layer of constant thickness. Another advantage of the rotating disc is that its surface is uniformly accessible from a mass transfer point of view, i.e., the mass flux does not depend on the location over the collector surface. One of the shortcomings of such a technique is due to the movement of the collector surface: deposition cannot be observed directly, and evaluation of the coating density can only be accomplished once the experiment has been completed and the collector is removed and placed under a microscope. Other types of stagnation point flow techniques, such as the spherical collectors and the cylindrical collectors, essentially suffer similar drawbacks.

Another widely used deposition device is the parallel-plate channel, which avoids the shortcomings associated with the rotating disc technique. A complete theoretical analysis of particle deposition in the parallel-plate channel was made by Bowen et al. (1976). The theory that describes particle deposition in the parallel-plate channel is essentially similar to the theory developed for the rotating disc, except that it must take into account changes in the particle deposition density with distance. Later, Bowen and Epstein (1979) studied the deposition of silica particles from a laminar flow suspension through a parallel-glass channel. Using such a technique, Sjollem et al. (1988) developed a system in which deposition of microorganisms is followed with continuous, automatic, image analysis. More recently, Song and Elimelech (1995) presented a more comprehensive theory of particle deposition onto a permeable surface in a parallel-plate



channel. However, the use of this technique is generally limited to applications where low flow rates are desired.

Recently, due largely to advancements in numerical simulation methods and facilities, a great deal of information has emerged on the study of particle deposition in complex systems such as packed bed (Elimelech, 1991, 1993), crossflow membrane (Hong et al., 1997; Faibish et al., 1998; Alargova et al., 1998), and periodic arrays of cylindrical collectors (Li and Park, 1997). A more advanced theory with completely incorporating of physicochemical particle-particle interactions was developed for particle deposition in crossflow microfiltration (Huisman et al., 1999).

### **1.4.3 The Impinging Jet Technique**

Studying particle deposition with a technique that makes the process controllable and visually observable not only provides a better understanding of the underlying deposition mechanisms, but also can shed insight into the relevant technological process. The impinging jet technique is one such example. It was pioneered by Dabros and van de Ven (1983a), who initially studied deposition of latex particles onto a glass surface. A theoretical model was developed, and good agreement was found between theory and experiment. In a later paper, Dabros and van de Ven (1987) extended latex deposition experiments to a wider range of hydrodynamic flow conditions. Such a technique has subsequently been used extensively in many research laboratories for study of particle deposition under effects of surfactants (Adamczyk et al., 1986), the attractive *EDL* interaction (Adamczyk et al. 1989), polyelectrolytes (Varenes and van de Ven, 1988; Boluk and van de Ven, 1990), polymer adsorption (Dijt et al., 1990), etc. The impinging jet technique can also be used as a probe to characterize polymers (van de Ven and Kelemen, 1996), examine particle detachment (Varenes and van de Ven, 1987), and study deposition structure and ordering (Adamczyk et al., 1990) and deposition of oil droplets (Sanders et al., 1995). Further, new technologies have recently been incorporated into the impinging jet technique to allow for the study of sub-micron colloidal particles (Polverari and van de Ven, 1995; Bohmer et al., 1998). More recently, a comprehensive theoretical analysis of particle deposition in the impinging jet was

provided by Yang et al. (1998c). Another geometric configuration of the impinging jet system was also reported by Adamczyk et al. (1993; 1999).

In this study, the well-established impinging jet technique has been extended to observe and analyze bubble attachment behaviors under various hydrodynamic and physicochemical conditions. The advantages of the impinging jet technique are multifold: Such a technique allows one to directly observe the attachment process in the vicinity of the stagnation point where colloidal interactions are expected to play important roles and hydrodynamic conditions are well-defined and controlled. Moreover, the theoretical model of bubble attachment flux to the collector is greatly simplified in the stagnation region so that the experimental results can be directly compared with theoretical predictions. In particular, the bubble-solid surface attachment can be modeled directly based on the continuity equation without artificially splitting into several steps, as done in the analysis of flotation efficiency mentioned earlier. In addition, both hydrodynamic and physicochemical conditions are reproducible, and they can be independently controlled so that the effects of hydrodynamics and colloidal surface forces on the attachment process can be studied separately and over a wide range of conditions.

It seems that Harwot and van de Ven (1997) were the first to use the impinging jet technique to study deposition phenomena related to flotation processes. They investigated the deposition of carboxylated latex particles onto an air/water interface in the presence of calcium oleate to model de-inking flotation. The surfaces of carboxylated latex particles resemble those of ink particles, whereas the air/water interface is representative of a bubble in water. From a physical point of view, the attachment of gas bubbles onto a solid surface in the impinging jet is analogous to bubble-particle interaction and attachment occurring in the flotation process. The flow pattern created around the stagnation point is very similar to that at the front end part of a spherical collector (a solid particle) exposed to an induced uniform flow or settling due to gravity. In addition, the quantitative nature of the short-ranged colloidal forces involved in the

impinging jet experiments is essentially the same as that which acts during the flotation process of bubble-particle interaction and attachment.

## **CHAPTER 2**

# **FLUID FLOW FIELDS IN THE IMPINGING JET FLOW REGION**

### **2.1 Introduction**

As stated in the Introduction, i.e., Chapter 1, one of the most important advantages of the impinging jet technique is that fluid flow fields in the impinging region are controllable and describable. Therefore, the hydrodynamic conditions (in terms of the flow intensity or the Reynolds number) in the impinging region can be readily manipulated to examine their impact on bubble attachment. In this Chapter, laminar flow fields in the impinging region are characterized through numerically solving the continuity and Navier – Stokes equations. The detailed numerical schemes developed for solving these equations are provided in Appendix A.1. Specifically, since it has been well-documented in the literature that the flow field in the impinging region around the stagnation point follows stagnation flow patterns to be elaborated in section 2.6, an analytical expression for such flow patterns is therefore developed to simplify the bubble transport equation that will be derived in Chapter 3. Finally, the valid range of the expressions is discussed on the basis of a comparison of the stagnation flow patterns with numerical simulation results.

### **2.2 Governing Equations**

Due to its effective transport capabilities to enhance heat and mass transfer, impinging jet flow has found a wide variety of applications, such as spraying cooling (Graham and Ramadhyani, 1996; Nishio and Kim 1998), paper drying, jet cutting (Amano and Brandt, 1984), and electrodeposition used in manufacturing MEMS devices (Chen and Modi, 1999). During the last two decades, fluid flow in the impinging region has been extensively studied in the literature (Deshpande and Vaishnav, 1982; Law and Masliyah, 1984; Parneix et al., 1999). An excellent review was provided by Polat et al.

(1991). In this work, the problem under consideration is essentially a laminar jet flow exiting from a circular capillary tube and impinging on a flat surface, which should be very straightforward to solve numerically.

Figure 2.1 illustrates the geometric configuration of the impinging jet flow. Liquid flow is introduced from the bottom, going through a circular tube of radius  $R$ , and issuing at the tube exit with an average velocity,  $V$ . The separation distance between the impingement plate I and the tube exit is  $H_o$ . As it is an inherent feature of the impinging jet technique that the fluid flow is axisymmetric, the flow fields essentially can be described using a two-dimensional cylindrical coordinate system. The origin of the axisymmetric coordinate system is located at the stagnation point. The outflow region is chosen at a location of distance  $L$ . If one assumes a Newtonian, incompressible, laminar flow under a steady-state situation, the flow fields are governed by

Continuity equation

$$\frac{1}{r} \frac{\partial (rv_r)}{\partial r} + \frac{\partial v_z}{\partial z} = 0 \quad (2.1)$$

Navier – Stokes equations

$$v_r \frac{\partial v_r}{\partial r} + v_z \frac{\partial v_r}{\partial z} = -\frac{1}{\rho_f} \frac{\partial p}{\partial r} + \frac{\mu_f}{\rho_f} \left[ \frac{\partial}{\partial r} \left( \frac{1}{r} \frac{\partial}{\partial r} (rv_r) \right) + \frac{\partial^2 v_r}{\partial z^2} \right] \quad (2.2a)$$

$$v_r \frac{\partial v_z}{\partial r} + v_z \frac{\partial v_z}{\partial z} = -\frac{1}{\rho_f} \frac{\partial p}{\partial z} + \frac{\mu_f}{\rho_f} \left[ \frac{1}{r} \frac{\partial}{\partial r} \left( r \frac{\partial v_z}{\partial r} \right) + \frac{\partial^2 v_z}{\partial z^2} \right] \quad (2.2b)$$

In above equations,  $v_r$  and  $v_z$  are the velocity components along directions of the two cylindrical coordinates shown in Figure 2.1.  $p$  is the hydraulic pressure.  $\rho_f$  and  $\mu_f$  are respectively the density and viscosity of the liquid fluid. It should be mentioned here that regardless of changes in the pH value and ionic concentration of the solution in experiments, both  $\rho_f$  and  $\mu_f$  are assumed to be of the same values as pure water in all calculations.

Defining the impinging jet Reynolds number  $Re = \frac{\rho_f R V}{\mu_f}$  (here  $R$  is the radius of the capillary tube and  $V$  is the average velocity at the capillary tube exit plane.) and nondimensionalizing equations (2.1) and (2.2a,b) via the following dimensionless variables:

$$\bar{r} = \frac{r}{R} \qquad \bar{z} = \frac{z}{R} \qquad (2.3a)$$

$$\bar{v}_r = \frac{v_r}{V} \qquad \bar{v}_z = \frac{v_z}{V} \qquad \bar{p} = \frac{p}{\rho_f V^2} \qquad (2.3b)$$

one can obtain the nondimensionalized form of the continuity and Navier – Stokes equations as follows

$$\frac{1}{r} \frac{\partial (\bar{r} \bar{v}_r)}{\partial \bar{r}} + \frac{\partial \bar{v}_z}{\partial \bar{z}} = 0 \qquad (2.4)$$

$$\bar{v}_r \frac{\partial \bar{v}_r}{\partial \bar{r}} + \bar{v}_z \frac{\partial \bar{v}_r}{\partial \bar{z}} = -\frac{\partial \bar{p}}{\partial \bar{r}} + \frac{1}{Re} \left[ \frac{\partial}{\partial \bar{r}} \left( \frac{1}{\bar{r}} \frac{\partial}{\partial \bar{r}} (\bar{r} \bar{v}_r) \right) + \frac{\partial^2 \bar{v}_r}{\partial \bar{z}^2} \right] \qquad (2.5a)$$

$$\bar{v}_r \frac{\partial \bar{v}_z}{\partial \bar{r}} + \bar{v}_z \frac{\partial \bar{v}_z}{\partial \bar{z}} = -\frac{\partial \bar{p}}{\partial \bar{z}} + \frac{1}{Re} \left[ \frac{1}{\bar{r}} \frac{\partial}{\partial \bar{r}} \left( \bar{r} \frac{\partial \bar{v}_z}{\partial \bar{r}} \right) + \frac{\partial^2 \bar{v}_z}{\partial \bar{z}^2} \right] \qquad (2.5b)$$

In the literature, several approaches have been successfully developed to numerically solve above nonlinear partial differential equations (PDE) (Polat et al., 1991). Of these, the most straightforward is the stream function – vorticity method (Deshpande and Vaishnav, 1982; Dabros and van de Ven, 1983a) which will be described in the next section.

### 2.3 Stream Function – Vorticity Method

The major difficulty in numerically solving an incompressible flow problem is dealing with the pressure source term in the Navier – Stokes equations. For axisymmetric flow, such a problem can be avoided by introducing a so-called stream function – vorticity method, in which the pressure terms are eliminated.

By definition, the stream function  $\psi$  and the vorticity  $\omega$  are expressed, in dimensionless forms, as

$$\bar{v}_r = -\frac{1}{r} \frac{\partial \bar{\psi}}{\partial z} \quad \bar{v}_z = \frac{1}{r} \frac{\partial \bar{\psi}}{\partial r} \quad (2.6)$$

$$\bar{\omega} = \frac{\partial \bar{v}_r}{\partial z} - \frac{\partial \bar{v}_z}{\partial r} \quad (2.7)$$

Substituting equation (2.6) into equation (2.4) identically satisfies the continuity requirement. The velocity components in equation (2.7) that defines the vorticity can be replaced by the stream function:

$$\bar{\omega} = -\frac{\partial}{\partial z} \left( \frac{1}{r} \frac{\partial \bar{\psi}}{\partial z} \right) - \frac{\partial}{\partial r} \left( \frac{1}{r} \frac{\partial \bar{\psi}}{\partial r} \right) \quad (2.8)$$

Briefly, equations (2.5) can be converted into the stream function – vorticity equation, that is obtained through first differentiating equations (2.5a) and (2.5b) with respect to ‘ $\bar{z}$ ’ and ‘ $\bar{r}$ ’, respectively, and followed by subtracting the two resulting equations. Then the final stream function – vorticity equation takes the form:

$$\bar{r}^{-2} \left[ \frac{\partial}{\partial z} \left( \frac{\bar{\omega}}{\bar{r}} \frac{\partial \bar{\psi}}{\partial r} \right) - \frac{\partial}{\partial r} \left( \frac{\bar{\omega}}{\bar{r}} \frac{\partial \bar{\psi}}{\partial z} \right) \right] - \frac{1}{\text{Re}} \left[ \frac{\partial}{\partial z} \left( \bar{r}^{-3} \frac{\partial}{\partial z} \left( \frac{\bar{\omega}}{\bar{r}} \right) \right) + \frac{\partial}{\partial r} \left( \bar{r}^{-3} \frac{\partial}{\partial r} \left( \frac{\bar{\omega}}{\bar{r}} \right) \right) \right] = 0 \quad (2.9)$$

By introducing a variable  $\bar{\omega}^*$  defined as

$$\bar{\omega}^* = \frac{\bar{\omega}}{\bar{r}} \quad (2.10)$$

equations (2.8) and (2.9) can be further rewritten in general forms suitable for the numerical stream function – vorticity approach (Gosman et al., 1969); these are the stream function  $\bar{\psi}$  equation

$$-\frac{\partial}{\partial z} \left( \frac{1}{\bar{r}} \frac{\partial \bar{\psi}}{\partial z} \right) - \frac{\partial}{\partial r} \left( \frac{1}{\bar{r}} \frac{\partial \bar{\psi}}{\partial r} \right) - \bar{r} \bar{\omega}^* = 0 \quad (2.11)$$

and the modified vorticity  $\bar{\omega}^*$  equation

$$\bar{r}^{-2} \left[ \frac{\partial}{\partial z} \left( \bar{\omega}^* \frac{\partial \bar{\psi}}{\partial r} \right) - \frac{\partial}{\partial r} \left( \bar{\omega}^* \frac{\partial \bar{\psi}}{\partial z} \right) \right] - \frac{\partial}{\partial z} \left[ \bar{r}^{-3} \frac{\partial}{\partial z} \left( \frac{1}{\text{Re}} \bar{\omega}^* \right) \right] - \frac{\partial}{\partial r} \left[ \bar{r}^{-3} \frac{\partial}{\partial r} \left( \frac{1}{\text{Re}} \bar{\omega}^* \right) \right] = 0 \quad (2.12)$$

## 2.4 Boundary Conditions

In order to solve the flow fields given by the second-order, nonlinear, elliptic PDE's (i.e., equations (2.11) and (2.12)), one has to specify boundary conditions. The boundary conditions for the stream function are, by themselves, relatively straightforward. However, due to a difficulty in the definition of  $\bar{\omega}$  along some boundaries such as solid boundary and symmetric boundary, careful attention must be paid to the values of the modified vorticity at such boundaries. Generally speaking,  $\bar{\omega}$  on a solid surface is neither zero nor constant. From a vortex dynamics prospective,  $\bar{\omega}$  is usually generated from solid surface, and subsequently is gradually dissipated through diffusion and convection. Generally, the boundary restriction conditions for  $\bar{\omega}$  at the solid and symmetric boundaries have to be deduced in conjunction with other information such as no slip condition, definition of the stream function and vorticity, as well as the vorticity conservation equation. All such boundary conditions are essentially the same as those given by Deshpande and Vaishnav (1982) and Dabros and van de Ven (1983a). Figure 2.2a shows the computational domain I that is bounded by (1) the axis of symmetry OA; (2) the exit of the capillary tube CD; (3) the impingement (collector) solid surface OF; (4) the exit plane along the capillary wall DE; (5) the outflow boundary EF. These boundary conditions are outlined as follows.

(1) The axis of symmetry OA ( $\bar{r} = 0$ )

Along the symmetric axis OA,  $\bar{v}_r = 0$ ,  $\frac{\partial \bar{v}_z}{\partial r} = 0$ , and  $\bar{\psi} = \text{constant}$ . It can readily

be deduced that  $\bar{\omega} = 0$ . For simplicity, it is acceptable to set  $\bar{\psi} = 0$  along the axis of

symmetry. However,  $\bar{\omega} = \frac{\bar{\omega}}{r} \neq 0$  on the symmetric axis. Note that  $\bar{v}_z$  is finite along the

symmetric axis,  $\bar{r} = 0$ . From the definition of the stream function given by equation

(2.6), it is seen that  $\frac{\partial \bar{\psi}}{\partial r}$  approaches zero at the same rate as  $\bar{r}$  near the axis. It follows

that the  $\bar{\psi} \sim \bar{r}$  distribution is parabolic in the immediate vicinity of the axis; and



symmetry demands that the second term in the  $\bar{\psi} \sim \bar{r}$  expansion be the fourth order (i.e., an even power). Thus the expression

$$\bar{\psi} = \bar{\psi}_o + a(\bar{z})\bar{r}^2 + b(\bar{z})\bar{r}^4 \quad (2.13)$$

is valid in the region near the axis, where  $\bar{\psi}_o$  is the stream function at the axis and is set to zero, and both  $a(\bar{z})$  and  $b(\bar{z})$  are functions of  $\bar{z}$  only. Substituting this expression into equation (2.11), the value of  $\bar{\omega}^*$  at the symmetric axis, i.e.,  $\bar{r} = 0$ , can be found

$$\bar{\omega}^*(\bar{z})\Big|_{\bar{r}=0} = -8b(\bar{z}) - \frac{d^2 a(\bar{z})}{d\bar{z}^2} \quad (2.14)$$

Both  $a(\bar{z})$  and  $b(\bar{z})$  can be readily derived from equation (2.13) in terms of  $\bar{\psi}_1$  and  $\bar{\psi}_2$  that are values of the stream function  $\bar{\psi}$  at the grid points  $(\bar{r}_1, \bar{z})$  and  $(\bar{r}_2, \bar{z})$ , respectively in the neighborhood of the axis. They are

$$a(\bar{z}) = \frac{1}{\bar{r}_2 - \bar{r}_1} \begin{pmatrix} \bar{r}_2^{-2} & \bar{r}_1^{-2} \\ \bar{r}_1 & \bar{r}_2 \end{pmatrix} \begin{pmatrix} \bar{\psi}_1 \\ \bar{\psi}_2 \end{pmatrix} \quad (2.15a)$$

$$b(\bar{z}) = \frac{1}{\bar{r}_2 - \bar{r}_1} \begin{pmatrix} -\frac{1}{\bar{r}_1} \bar{r}_2^{-2} & \frac{1}{\bar{r}_2} \bar{r}_1^{-2} \end{pmatrix} \begin{pmatrix} \bar{\psi}_1 \\ \bar{\psi}_2 \end{pmatrix} \quad (2.15b)$$

(2) The exit of the capillary tube CD ( $\bar{z} = \bar{H}_o$ ,  $\bar{r} \leq 1$ )

Since the ratio of the length  $l$  to the radius  $R$  of the capillary tube used in the impinging jet experimental system is relative large ( $\frac{l}{R} \geq 30$ ), the velocity on this plane can, therefore, be assumed to have a parabolic, fully-developed profile expressed as

$$\bar{v}_r = 0 \quad \bar{v}_z = 2(\bar{r}^2 - 1) \quad (2.16)$$

When equations (2.16) are substituted into equations (2.6) and (2.7), the stream function and the vorticity become

$$\bar{\psi} = -\bar{r}^2 \left(1 - \frac{1}{2}\bar{r}^2\right) \quad (2.17a)$$

$$\bar{\omega}^* = -4 \quad (2.17b)$$

(3) The impingement (collector) solid surface OF ( $\bar{z} = 0, 0 \leq \bar{r} \leq \bar{L} = 10$ )

The no-slip boundary condition is applied at the impingement (collector) surface, resulting in  $\bar{v}_r = 0$  and  $\bar{v}_z = 0$ . According to the definition of the stream function given by equation (2.6),  $\bar{\psi}$  is a constant, which should be set to the same value as that assigned to the symmetric axis, i.e.,  $\bar{\psi} = 0$ . However, the value of  $\bar{\omega}^* = \frac{\bar{\omega}}{r}$  is unknown as yet. A

procedure is introduced in the following to approximate  $\bar{\omega}^*$ . Following Roache (1972), expanding  $\bar{\psi}_i$ , the stream function at a grid point nearest the wall, in a Taylor series with respect to the values of  $\bar{\psi}_w$  and  $\frac{\partial^n \bar{\psi}}{\partial \bar{z}^n}$  at the wall and truncating the expansion after

terms of order  $(\delta z)^4$  yield

$$\bar{\psi}_i = \bar{\psi}_w + \frac{\partial \bar{\psi}}{\partial \bar{z}} \Big|_w \delta \bar{z} + \frac{\partial^2 \bar{\psi}}{\partial \bar{z}^2} \Big|_w \frac{(\delta \bar{z})^2}{2} + \frac{\partial^3 \bar{\psi}}{\partial \bar{z}^3} \Big|_w \frac{(\delta \bar{z})^3}{6} + O((\delta \bar{z})^4) \quad (2.18)$$

In this equation, the first derivative is equal to zero, i.e.,

$$\frac{\partial \bar{\psi}}{\partial \bar{z}} \Big|_w = 0 \quad (2.19)$$

due to no-slip condition.

Near the wall, if the boundary layer assumption applied, i.e., if  $\frac{\partial \bar{v}_z}{\partial r} \ll \frac{\partial \bar{v}_r}{\partial \bar{z}}$ , then the

second derivative,  $\frac{\partial^2 \bar{\psi}}{\partial \bar{z}^2} \Big|_w$ , can be directly related to  $\bar{\omega}$  through equations (2.7) and

(2.8), i.e.,

$$\frac{\partial^2 \bar{\psi}}{\partial \bar{z}^2} \Big|_w = -r \bar{\omega}_w \quad (2.20)$$

According to the definition of the vorticity, its first derivative is given by

$$\frac{\partial \bar{\omega}}{\partial \bar{z}} \Big|_w = \frac{\partial}{\partial \bar{z}} \left( \frac{\partial \bar{v}_r}{\partial \bar{z}} - \frac{\partial \bar{v}_z}{\partial \bar{r}} \right) \Big|_w = \left( \frac{\partial^2 \bar{v}_r}{\partial \bar{z}^2} - \frac{\partial^2 \bar{v}_z}{\partial \bar{z} \partial \bar{r}} \right) \Big|_w \quad (2.21)$$

Similarly, from the definition of the stream function, the first term on the right hand side of equation (2.21) can be expressed as

$$\frac{\partial^2 \bar{v}_r}{\partial \bar{z}^2} \Big|_w = \frac{\partial^2}{\partial \bar{z}^2} \left( -\frac{1}{r} \frac{\partial \bar{\psi}}{\partial \bar{z}} \right) \Big|_w = -\frac{1}{r} \frac{\partial^3 \bar{\psi}}{\partial \bar{z}^3} \Big|_w \quad (2.22)$$

Using the continuity equation (2.1), the second term in the right hand of equation (2.21) is rewritten as

$$\frac{\partial^2 \bar{v}_z}{\partial \bar{z} \partial \bar{r}} \Big|_w = \frac{\partial}{\partial \bar{r}} \left( \frac{\partial \bar{v}_z}{\partial \bar{z}} \right) \Big|_w = \frac{\partial}{\partial \bar{r}} \left( -\frac{1}{r} \frac{\partial (r \bar{v}_r)}{\partial \bar{r}} \right) \Big|_w = 0 \quad (2.23)$$

Then, when equations (2.22) and (2.23) are substituted into equation (2.21), the third derivative,  $\frac{\partial^3 \bar{\psi}}{\partial \bar{z}^3} \Big|_w$ , simplifies to

$$\frac{\partial^3 \bar{\psi}}{\partial \bar{z}^3} \Big|_w = -r \frac{\partial \bar{\omega}}{\partial \bar{z}} \Big|_w \approx -r \frac{\bar{\omega}_i - \bar{\omega}_w}{\delta z} \quad (2.24)$$

Substituting equations (2.19), (2.2), and (2.24) back into the original Taylor series expansion, i.e., equation (2.18), and rearranging it lead to the following expression for  $\bar{\omega}^*$  at the impingement surface OF:

$$\bar{\omega}_w^* \Big|_{OF} = -\frac{3(\bar{\psi}_i - \bar{\psi}_w)}{r^2 (\bar{z}_i - \bar{z}_w)^2} - \frac{\bar{\omega}_i}{2} \quad (2.25)$$

where the subscripts  $w$  and  $i$  refer to the wall and first internal grid points, respectively (see Figure 2.2a).

(4) The exit plane along the capillary wall DE ( $\bar{z} = \bar{H}_o$ ,  $0 \leq \bar{r} \leq \bar{L} = 10$ )

Again, imposing the no-slip boundary condition on the exit plane DE leads to a constant stream function on the surface. Its value is calculated as  $\bar{\psi} = -0.5$ , which is derived from the expression for  $\bar{\psi}$  given by equation (2.17b) in the limit as  $\bar{r}$  approaches 1. Based on the same approach developed for boundary OF, the vorticity on the boundary DE is given by

$$\bar{\omega}_w|_{DE} = -\frac{3(\bar{\psi}_i - \bar{\psi}_w)}{r^2 (\bar{z}_i - \bar{z}_w)^2} - \frac{\bar{\omega}_i}{2} \quad (2.26)$$

(5) The outflow boundary EF

Regardless of the numerical method employed, there is always a difficulty in specifying the outflow boundary conditions as they normally are unknown until the numerical calculations have been executed. Fortunately, the flow conditions set at the outflow region usually have little influence on the solution of the Navier – Stokes equations. Specifically, for the present study, the sole purpose of evaluating the flow fields in the impinging region is to determine the flow conditions around the stagnation region where bubble attachment occurs. It is, therefore, expected that the flow boundary conditions imposed at the cell exit will have no significant effect on the stagnation region, at least for large Reynolds number processes ( $Re = 100 - 700$ ) that were used in the present experiments.

Here, it is assumed that the flow conditions at the outflow boundary are stable (Dabros and van de Ven, 1987). Such conditions are expressed as

$$\frac{\partial \bar{v}_r}{\partial r} = 0 \quad \frac{\partial \bar{v}_z}{\partial r} = 0 \quad (2.27)$$

Based on the definitions of the vorticity and the stream function, equation (2.27) becomes

$$\frac{\partial \bar{\omega}}{\partial r} = \frac{\partial}{\partial r} \left( \frac{\partial \bar{v}_r}{\partial z} - \frac{\partial \bar{v}_z}{\partial r} \right) = \frac{\partial}{\partial z} \left( \frac{\partial \bar{v}_r}{\partial r} \right) = 0 \quad (2.28)$$

and

$$\frac{\partial^2 \bar{\psi}}{\partial r^2} = 0 \quad (2.29)$$

## 2.5 Numerical Method

The flow equations (2.11) and (2.12), together with boundary conditions described above can now be solved numerically. A finite difference analysis based control - volume method (Patankar, 1980) is introduced to derive partial differential

equations into discrete, algebraic equations by integrating each governing differential equation over a control volume surrounding a typical grid point P (shown by dashed lines in Figure 2.3). The upwind scheme is employed to approximate the convection terms. Central difference scheme is used to deal with the diffusion terms. The resulting finite-difference equations express the values of variables ( $\bar{\psi}$  and  $\bar{\omega}$ ) at grid P in terms of their values at eight neighboring grids S, SE, E, etc. The detailed derivation of these equations is given Appendix 1.

Once the algebraic equations have been derived, a Gauss-Seidel method based iterative procedure was employed to solve these equations. To begin, an initial guess was made for the flow field and the boundary conditions were imposed. Then, the set of finite-difference equations was solved to evaluate the values of  $\bar{\psi}$  and  $\bar{\omega}$  for each grid point P in the whole computational domain. It should be kept in mind that the latest values of  $\bar{\psi}$  and  $\bar{\omega}$  were always chosen in the calculation. The boundary conditions were subsequently recomputed based on the latest available values of  $\bar{\psi}$  and  $\bar{\omega}$ . This computational procedure was continued until numerical convergence was achieved. The convergence criterion, defined as the maximum fractional change of the calculated value of  $\bar{\psi}$  or  $\bar{\omega}$  at each grid on successive iterations, is expressed as

$$\left| \frac{\bar{\phi}^n - \bar{\phi}^{n-1}}{\bar{\phi}^{n-1}} \right|_{\max} \leq \varepsilon \quad (2.30)$$

where  $\bar{\phi}$  can be either  $\bar{\psi}$  or  $\bar{\omega}$  and  $\varepsilon$  is chosen as  $10^{-5}$  and  $10^{-3}$  for the stream function and the vorticity, respectively. The subscript n and (n-1) represent the nth and the (n-1)th iterative value, respectively.

Realizing the nonlinearity of the vorticity equation (2.12), an under-relaxation iteration was chosen to avoid divergence. The under-relaxation scheme is expressed as

$$\bar{\phi} = \alpha \bar{\phi}^n + (1 - \alpha) \bar{\phi}^{n-1} \quad (2.31)$$

Here, the coefficient  $\alpha$ , termed the under-relaxation parameter, stands for a number between 0 and 1. Its optimum value has been found to be 0.78 and 1.0 for the vorticity and the stream function, respectively.

Noting that the vorticity at the tube lip is discontinuous, special consideration thus is needed. When solving the equations for a point with  $\bar{r} \leq 1$ , the vorticity value at the tube lip was assumed to be the same as the vorticity of the tube exit-velocity profile. For calculations at a point  $\bar{r} \geq 1$ , the vorticity value at the lip was obtained by calculating it as though the lip were a point on the exterior of the tube wall. For calculations at the points exactly under the lip, i.e.,  $\bar{r} = 1$ , an average of the two values obtained above was taken.

According to Polat et al. (1991), the impinging jet flow will retain its laminar nature until the Reynolds number reaches 1500. (In the literature, numerous studies even reported that the critical transit Reynolds number from laminar to turbulent flow status is as high as 2500.) As such, the calculations were performed for Reynolds number up to 1000 only. For each calculation, flow fields obtained from a previous Re were used as an initial guess for the iterative computations for a larger Re. Typically, the number of iterations required for a convergent numerical solution vary from a few hundred to a few thousand, depending upon Re and the number of grids chosen. In the specified computational domain I, a uniform grid system was constructed as  $101 \times 101$  along the directions of axial  $z$  and radial  $r$ .

To validate the numerical code, several numerical tests were run to ensure numerical accuracy of the results. The first set of tests was the convergence of the solution. For a specific case, the solution converged after certain number of iterations according to the criterion described above. An additional number of iterations was executed to ensure that the solution did not drift away. In the second set of tests, the grid-independence of the results was verified by repeating the same calculation for two sets of grid numbers,  $41 \times 51$  and  $101 \times 101$ . These tests yielded consistent results, which provided assurance for the validity of the numerical scheme.

Once the stream function and the vorticity were calculated, the velocity fields could be obtained from the stream function (based on equation (2.6)) using the central difference scheme.

## 2.6 Simulation Results and Discussion

Computations were performed for various values of  $Re$  ranging from 1 to 1000. A good depiction of a steady laminar flow field is given by a display of the streamlines. Four displays of streamlines for different Reynolds numbers are shown in Figures 2.4 (a - d). In these cases, the value of  $\overline{H}_o = 2$  and the parabolic exit-velocity profile were used. Due to symmetry, only half of the impinging region is displayed. The impinging jet exit is at the upper left-hand corner with the main flow moving from left to right. Figure 2.4a shows that at the low value of  $Re = 1$ , the flow is essentially creeping. When  $Re = 10$ , it can be observed from Figure 2.4b that secondary flow is generated and eddies can be seen just around the exit of the tube. By further increasing  $Re$  (e.g.,  $Re = 100$  or  $1000$ ), the eddy is pushed away from the symmetric axis and the flow issuing from the tube is restricted to a thin region close to the impingement wall. Similar flow patterns were obtained numerically by Dabros and van de Ven (1983a) and Deshpande and Vaishnav (1982) for low and high Reynolds numbers, respectively.

The corresponding radial and axial velocity distributions are displayed in Figures 2.5 (a - d) and Figures 2.6 (a - d), respectively. Essentially, these results are in accordance with those reported by Deshpande and Vaishnav (1982).

It should be pointed out that the expressions derived for  $\overline{\psi}$  and  $\overline{\omega}$ , given by equations (2.17a, b), are valid only when a parabolic, fully-developed velocity profile holds. An implicit assumption made herein is that the flow at the exit is not affected by the presence of the impingement surface. Of course, such an effect due to confined geometry is dependent on many factors such as the flow condition ( $Re$ ) and the separation distance between the exit of the tube and the impingement surface  $H_o$ . In order to evaluate this effect, a new computational domain  $\Pi$  (see Figure 2.2b) was, therefore,

constructed to perform numerical simulations. Instead of considering a parabolic, fully-developed velocity profile at the exit, a parabolic flow was assumed to have been fully-developed at some point before the exit, for instance  $\Delta \bar{z}_{DD'} = 3$ . Under the new computational domain II, all boundary conditions will retain the same as the old computational domain I except for the inner wall boundary. Using a similar approach developed for the impingement surface OF, boundary conditions along the inner wall of the tube DD' are given by

$$\bar{\psi} = -0.5 \quad (2.32a)$$

$$\bar{\omega}_w|_{DD'} = \frac{-\frac{6(\bar{\psi}_i - \bar{\psi}_w)}{(r_i - r_w)^2} - \frac{\bar{\omega}_i}{r_i}}{2 + \frac{r_i - r_w}{r_w} + \frac{(r_i - r_w)^2}{4r_w^2}} \quad (2.32b)$$

Numerical calculations based on the new computational domain II give rise to the stream function distributions under various Reynolds numbers as shown in Figures 2.7 (a – d). A comparison is made in Figures 2.8 (a – d) between the tube exit velocity profiles of the two different computational domains. It is found that for creeping flow of  $Re = 1$  (shown in Figure 2.8a), the parabolic velocity profile at the tube exit is distorted because of the presence of the impingement plate. As the Reynolds number goes up, however, Figures 2.8 (b – d) clearly show that the extent of such “distortion” becomes negligible. This suggests that for the separation distance between the tube exit and the impingement surface of  $\bar{H}_o = 2$ , the presence of the impingement surface in downstream has virtually no influence on the exit velocity profiles in upstream if the process is convection dominated.

## 2.7 Stagnation Point Flow Patterns and Flow Intensity of the Impinging Jet Flow

It was not the original intention of this study to only perform CFD simulation of the entire impinging jet flow. What is of more interest in the present study, however, is to find the flow field information near the stagnation point region where colloidal surface forces between a bubble and the collector surface are expected to play important roles in



bubble transport and attachment. Fortunately, stagnation flows have been well documented in fluid mechanics studies. In the present work, the flow patterns around the stagnation point region are assumed to take the forms

$$\bar{v}_r = \bar{\alpha} \bar{z} \bar{r} \qquad \bar{v}_z = -\bar{\alpha} \bar{z}^2 \qquad (2.33)$$

where  $\bar{\alpha}$  is a dimensionless constant, which characterizes the intensity of the stagnation flow. When equation (2.33) is substituted into the definition of the vorticity, equations (2.7) and (2.10), the following is sought

$$\bar{\omega} = \frac{\bar{\omega}}{r} = \bar{\alpha} \qquad (2.34)$$

near the stagnation point region.

It is noted that for the stagnation flow, the flow intensity  $\bar{\alpha}$  should be independent of both the radial  $\bar{r}$  and axial  $\bar{z}$  coordinates.  $\bar{\alpha}$ , however, is found to be strongly dependent upon the Reynolds number,  $Re$ , and the dimensionless separation distance between the capillary tube exit and the impingement (collector) surface  $\bar{H}_o$ . In this study, numerical simulation results of the flow field were used to evaluate  $\bar{\alpha}$ . More specifically, for a fixed  $\bar{H}_o = 2$  (which matches exactly the experimental cell geometry), values of  $\bar{\alpha}$  for different Reynolds numbers were obtained by fitting the stagnation flow patterns to the velocity distributions predicted from numerically solving equations (2.11) and (2.12). The determined correlation of  $\bar{\alpha}$  versus  $Re$  is shown in Figure 2.9. An empirical expression describing the curve displayed in Figure 2.9 was obtained by performing regression analyses, and it is expressed as

$$\bar{\alpha} = 5.3 Re^{0.5} - 8.13 \quad (Re \geq 5) \qquad (2.35)$$

This correlation, together with equation (2.33), will represent the stagnation flow fields to simplify the solution to the governing mass transfer equations that will be discussed in Chapter 3.

In order to evaluate the valid range of lateral distance where stagnation point flow patterns given by equation (2.33) can be used to describe the fluid flow in the impinging

region, a series of numerical runs were performed for various  $Re$  values. Selected results for the dependence of the axial  $-\bar{v}_z$  and the reduced radial  $\bar{v}_r/r$  velocity components on the axial coordinate  $\bar{z}$  are shown in Figures 2.10 (a - d). These results suggest that depending upon  $Re$ , the proposed stagnation flow patterns can give a good estimate of the flow fields around the stagnation point as long as  $\bar{z} = \frac{z}{R} \leq 0.1$ . This value corresponds to  $z \approx 130 \mu m$ , when the radius of the capillary tube used in the experiments is chosen as  $R = 1.325 \text{ mm}$ . On the other hand, where the effect of the radial coordinate  $\bar{r}$  is concerned, the reduced velocity components  $-\bar{v}_z/z^{-2}$  and  $\bar{v}_r/z$  versus  $\bar{r}$  are shown in Figure 2.11 and Figure 2.12, respectively. It can be seen from Figure 2.11 that in the limit  $\bar{r} \rightarrow 0$  the  $-\bar{v}_z/z^{-2}$  function indeed approaches a constant, or in other words, it becomes relatively independent of the radial coordinate  $\bar{r}$ . One can readily deduce that the upper limit of  $\bar{r}$  for which the  $-\bar{v}_z/z^{-2}$  function remains relatively unchanged is roughly 0.25; this value increases as the Reynolds number decreases. In addition, the results shown in Figure 2.12 demonstrate that when  $\bar{r} \leq 0.25$  the  $\bar{v}_r/z$  profile can be well described by a linear function, in accordance with equation (2.33). Hence, it can be concluded that the proposed flow patterns expressed by equation (2.33) can be used to characterize the flow fields in the impinging region around the stagnation point region where  $\bar{r} \leq 0.25$  and  $\bar{z} \leq 0.1$ .

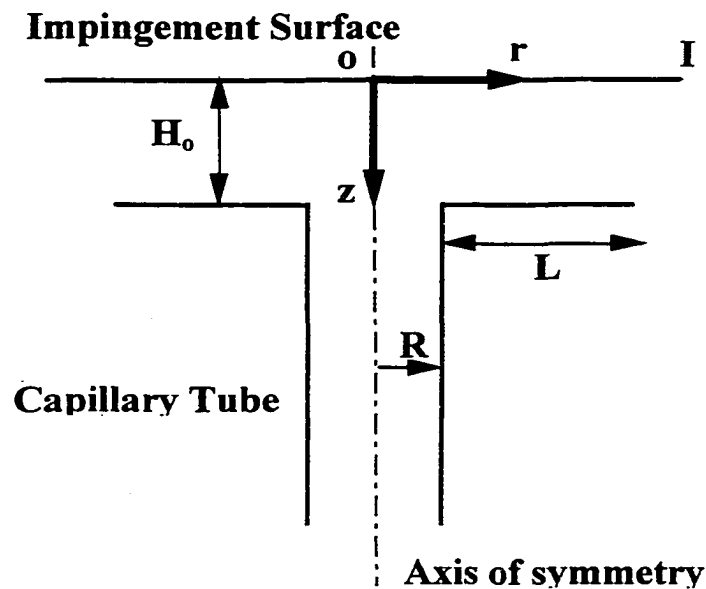


**Figure 2.1** Geometric configuration of the impinging jet cell. Flow jet enters a capillary tube of radius  $R$  and then impinges onto a collector surface  $I$  with a separation distance of  $H_0$ . The stagnation point  $O$ , located on the axis of symmetry and the impingement surface  $I$ , is the origin of the cylindrical coordinate system  $r$  and  $z$ .

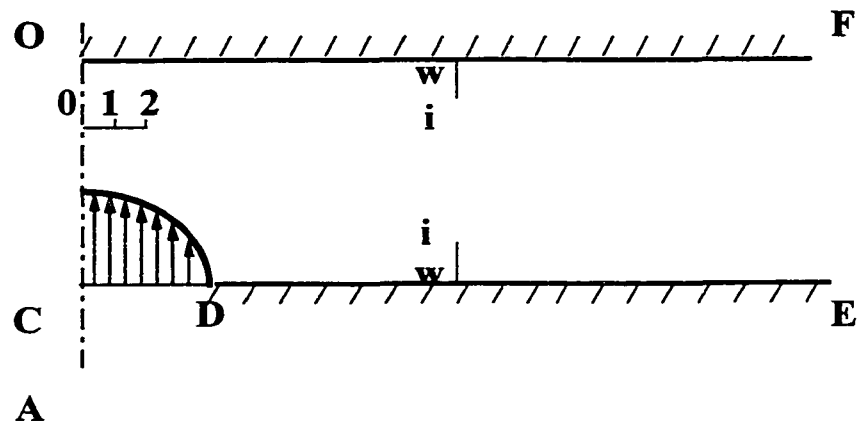


**Figure 2.2a** Computational domain I

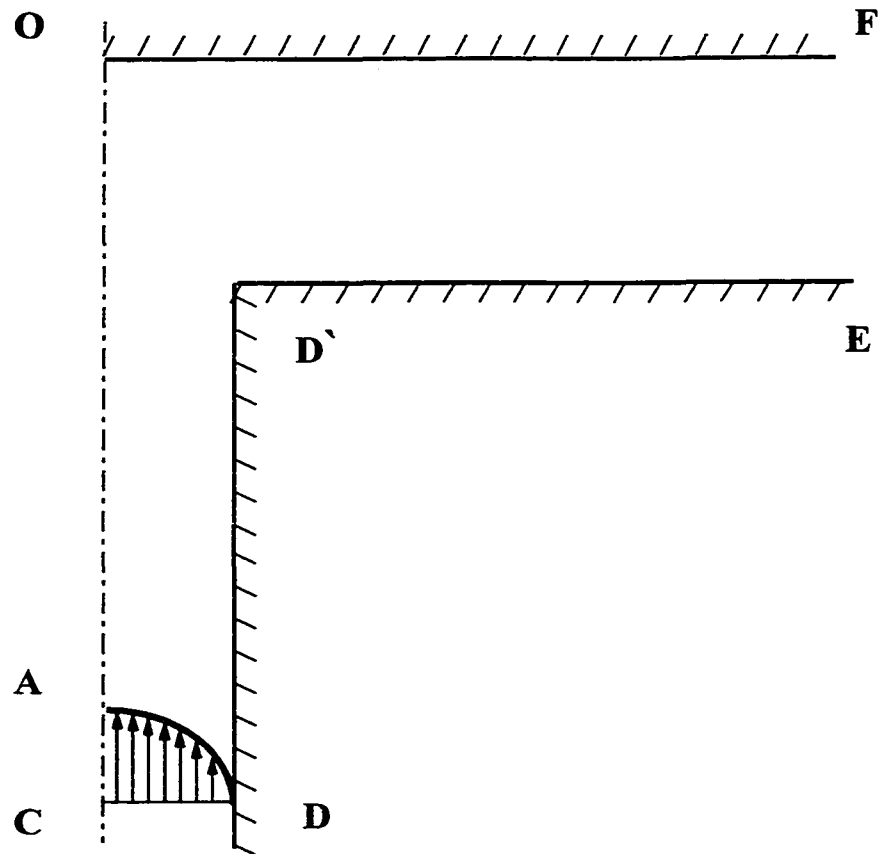


**Figure 2.2b** Computational domain II

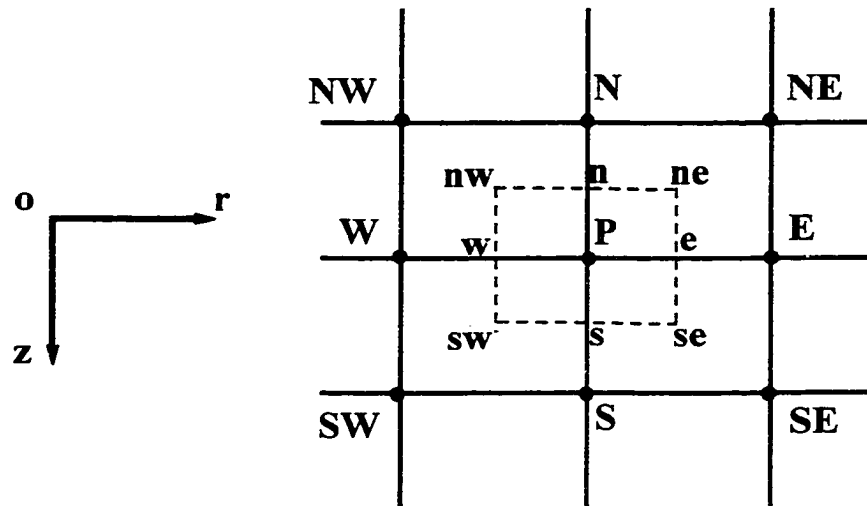


**Figure 2.3** Illustration of a portion of the finite – difference grid; the dotted lines enclose an elementary control volume used for derivation of conservation equations

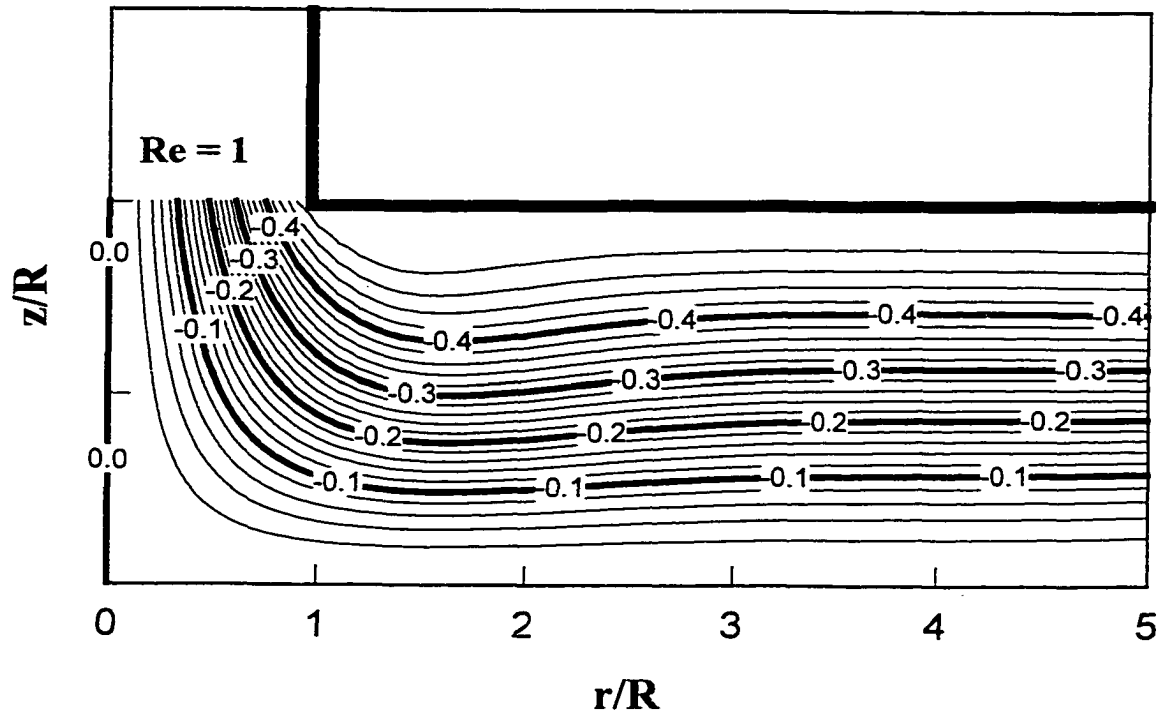


**Figure 2.4a** Numerical simulation of stream function profiles in the impinging jet flow region for  $Re = 1$

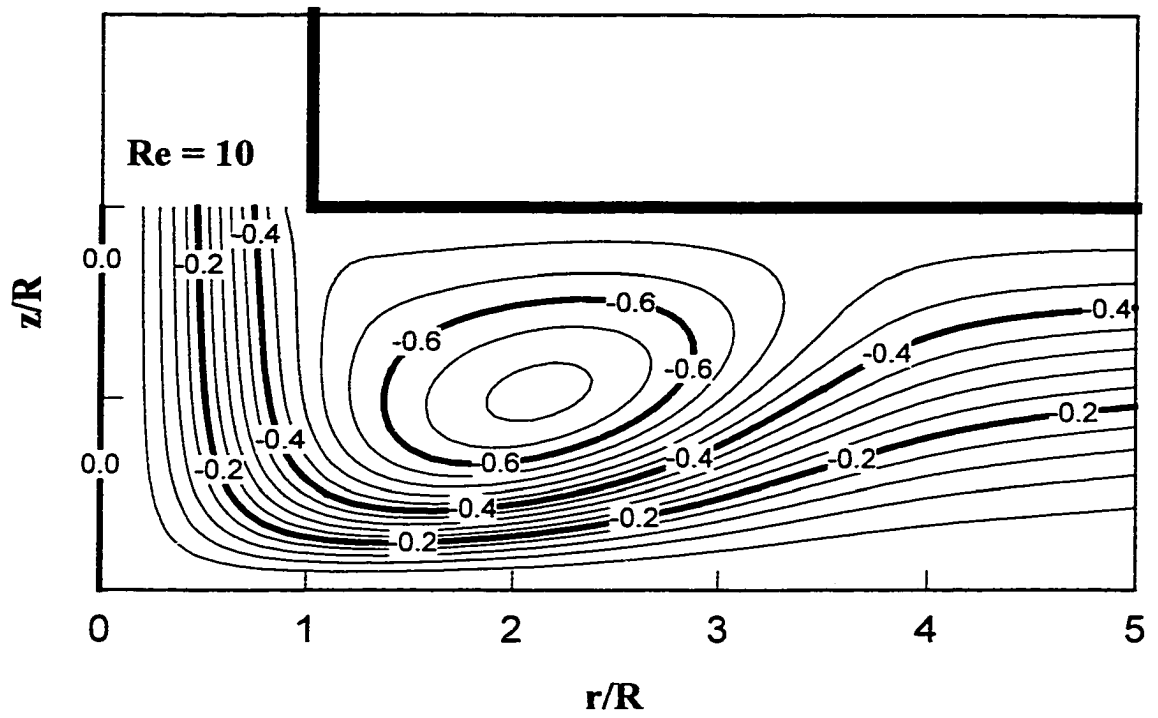


**Figure 2.4b** Numerical simulation of stream function profiles in the impinging jet flow region for  $Re = 10$

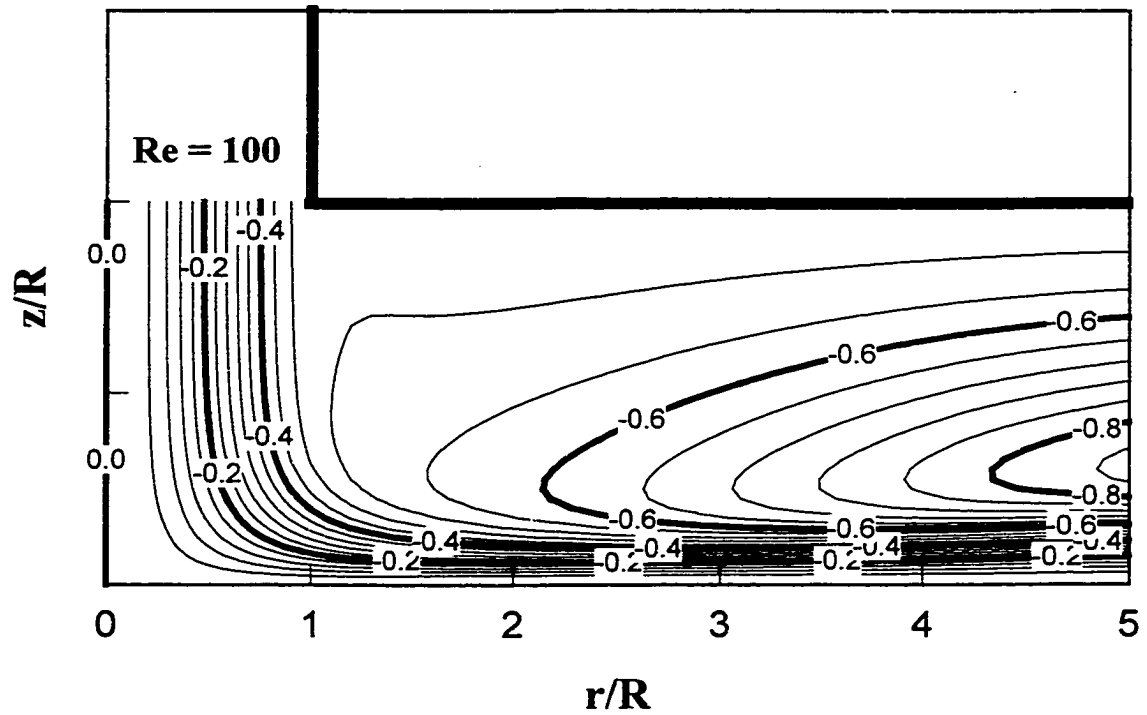


**Figure 2.4c** Numerical simulation of stream function profiles in the impinging jet flow region for  $Re = 100$



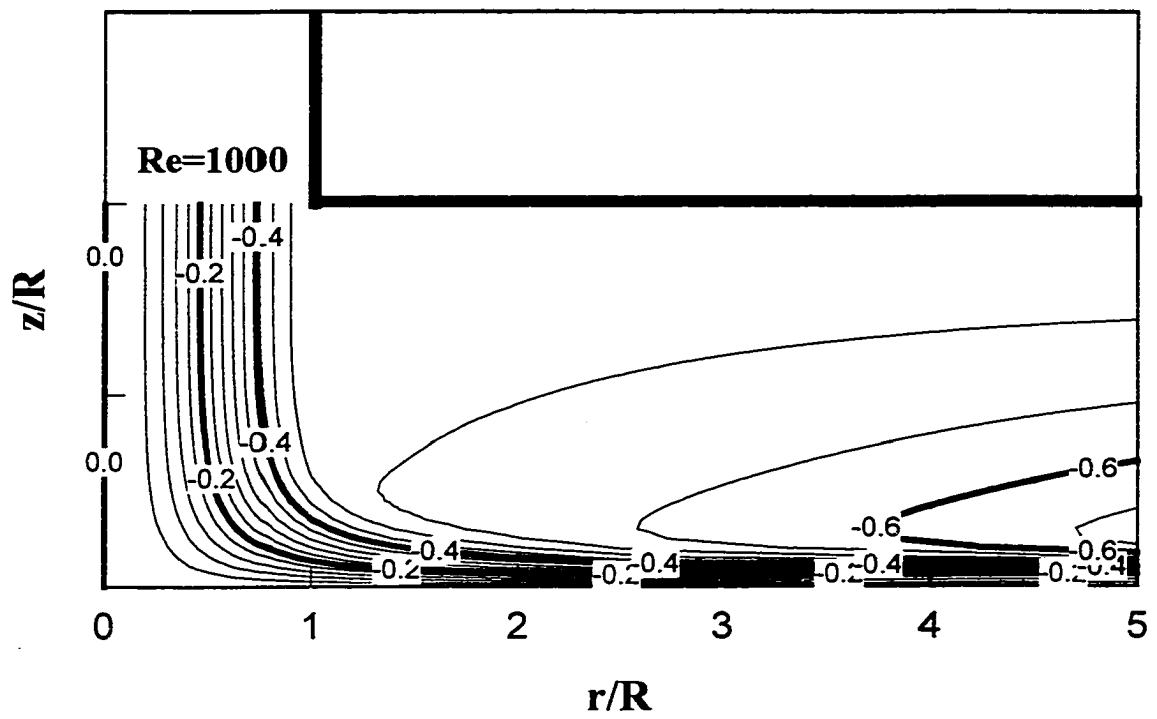


**Figure 2.4d** Numerical simulation of stream function profiles in the impinging jet flow region for  $Re = 1000$

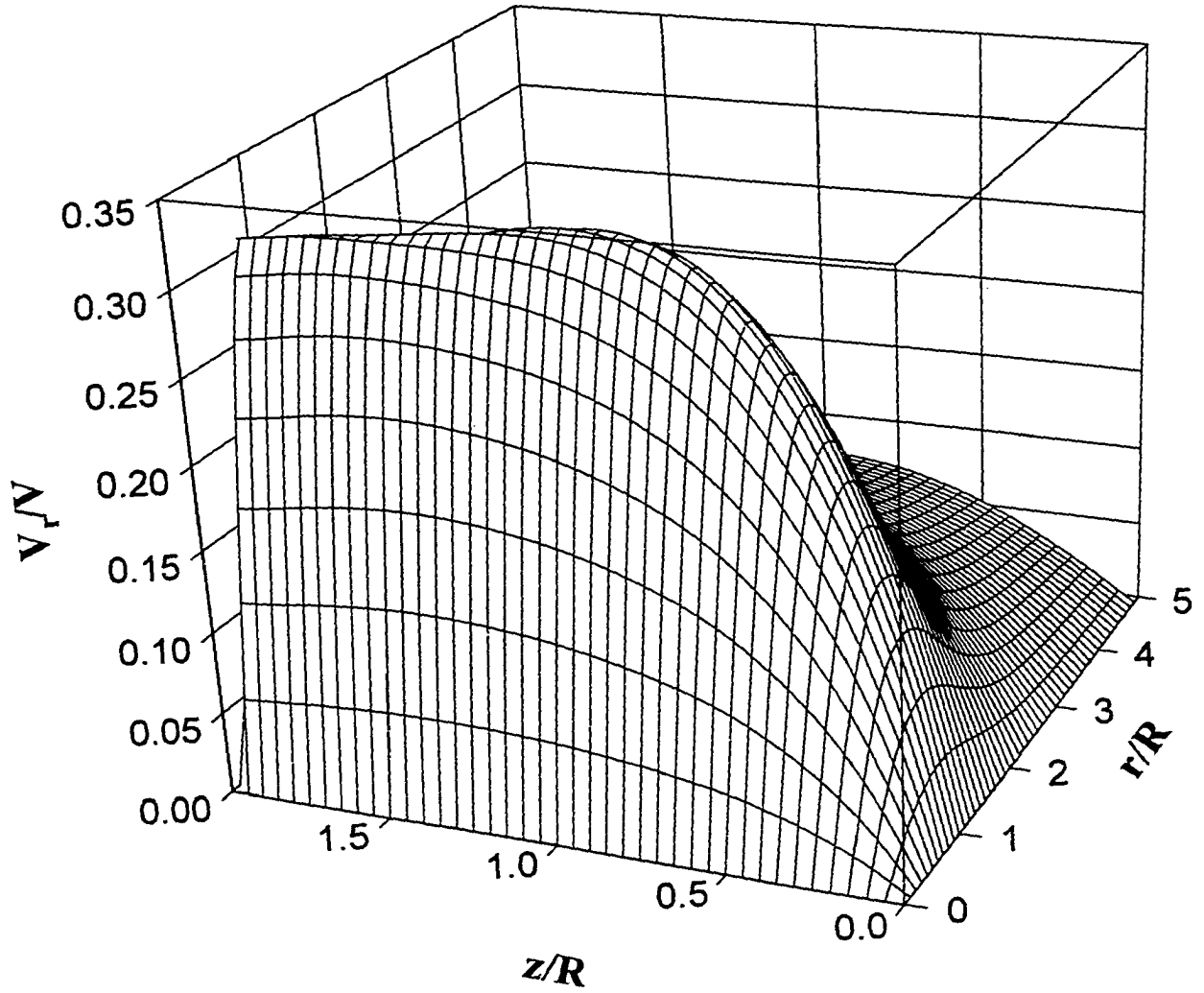


**Figure 2.5a** Numerical simulation of radial velocity distributions in the impinging jet flow region for  $Re = 1$

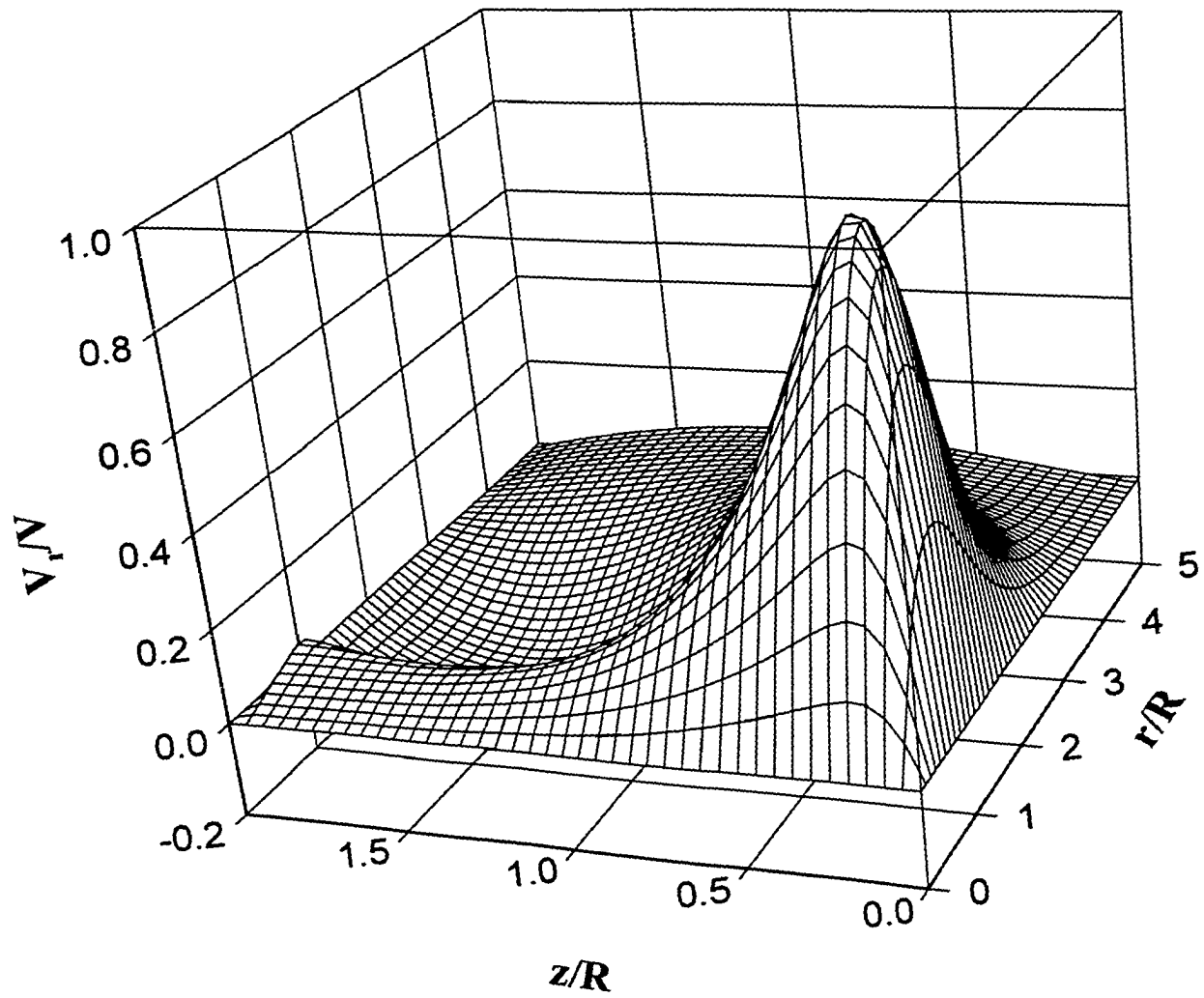


**Figure 2.5b** Numerical simulation of radial velocity distributions in the impinging jet flow region for  $Re = 10$

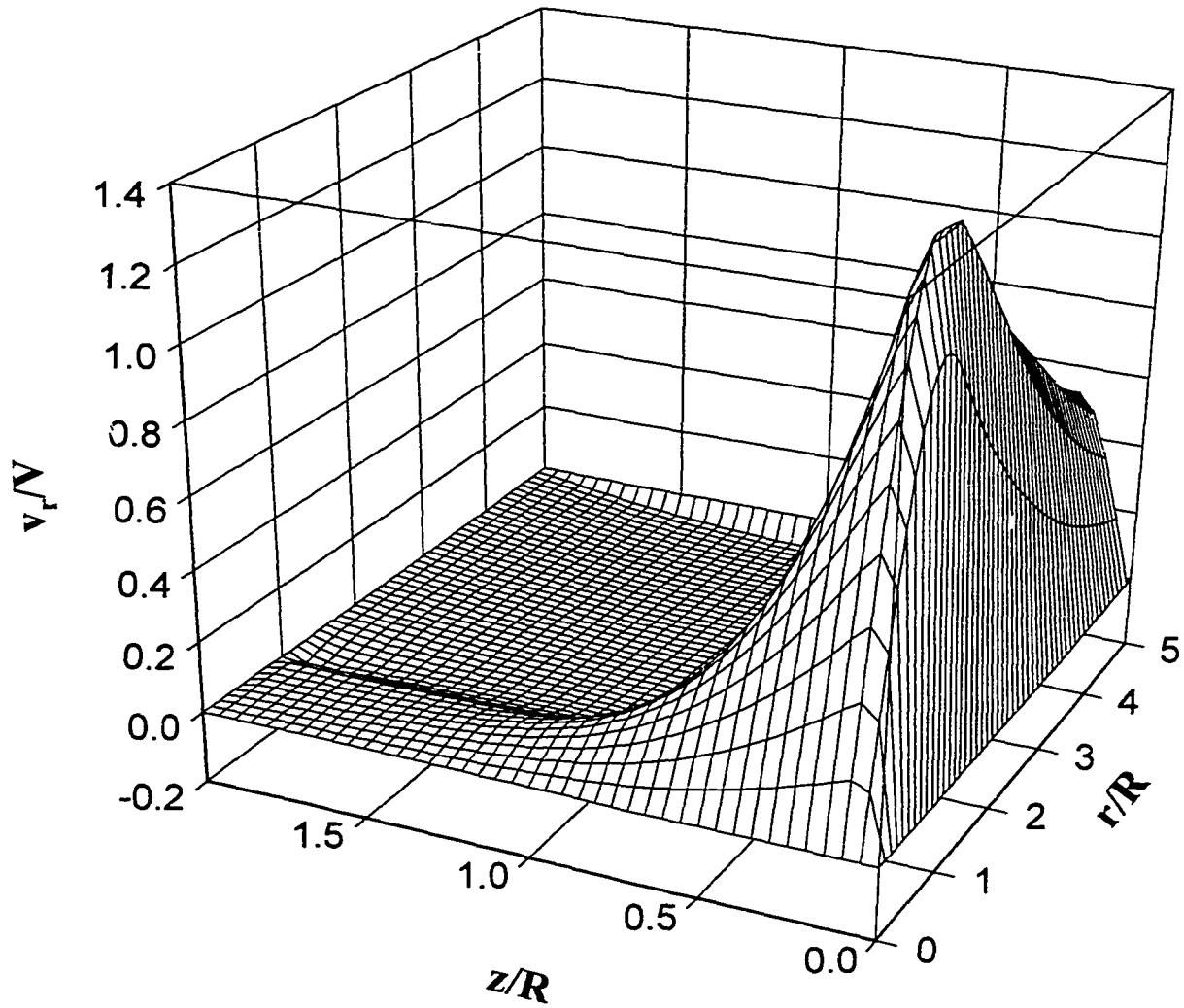


**Figure 2.5c** Numerical simulation of radial velocity distributions in the impinging jet flow region for  $Re = 100$

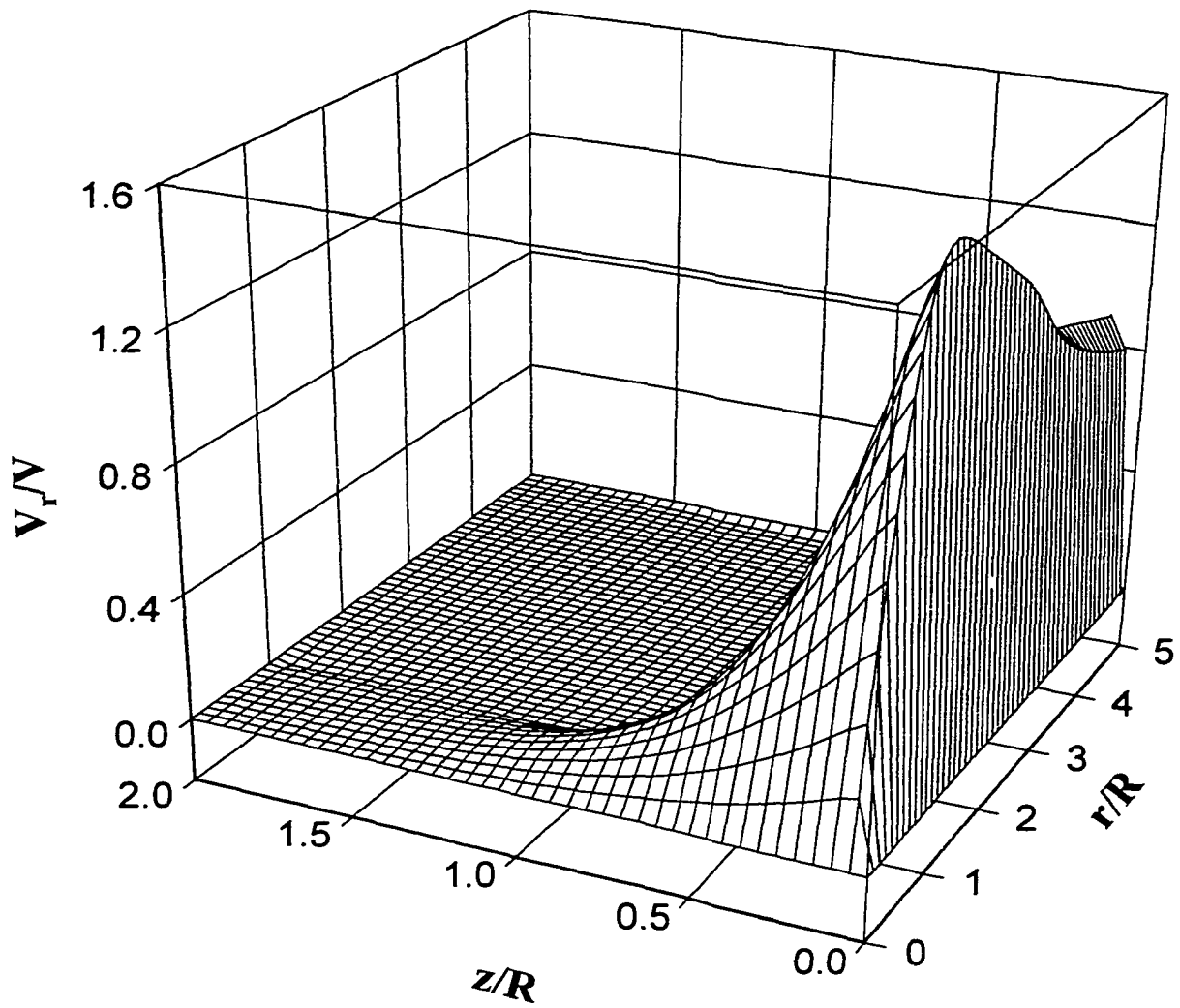


**Figure 2.5d** Numerical simulation of radial velocity distributions in the impinging jet flow region for  $Re = 1000$

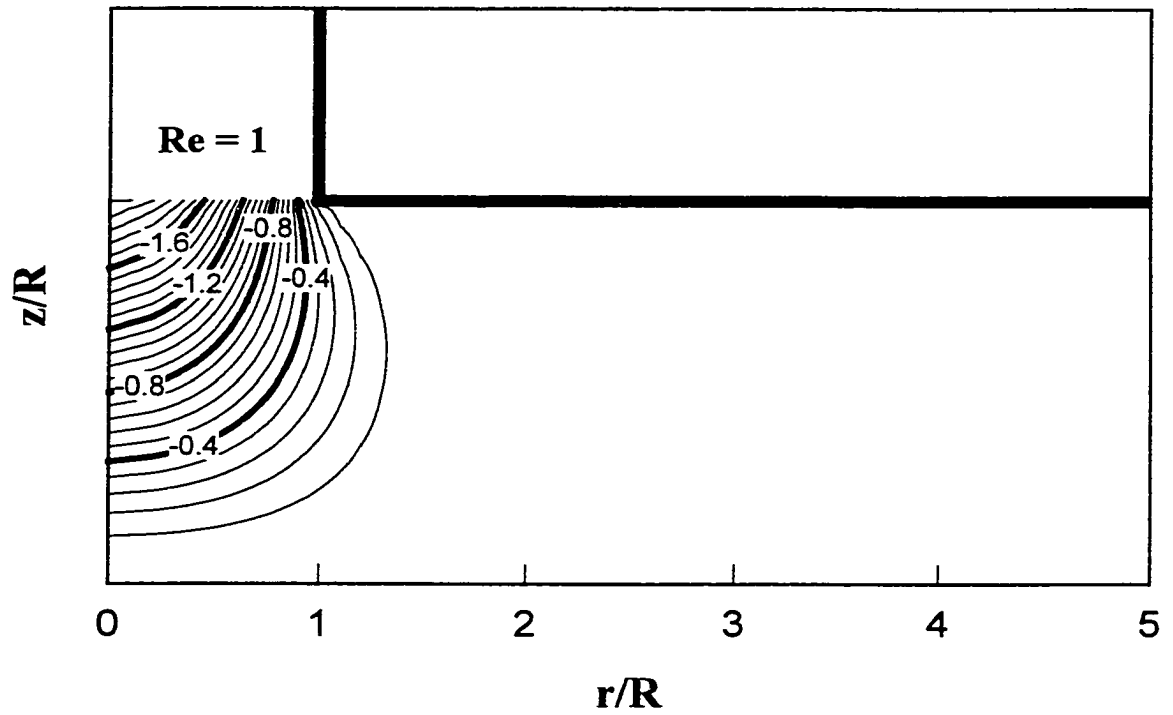


**Figure 2.6a** Numerical simulation of axial velocity distributions in the impinging jet flow region for  $Re = 1$

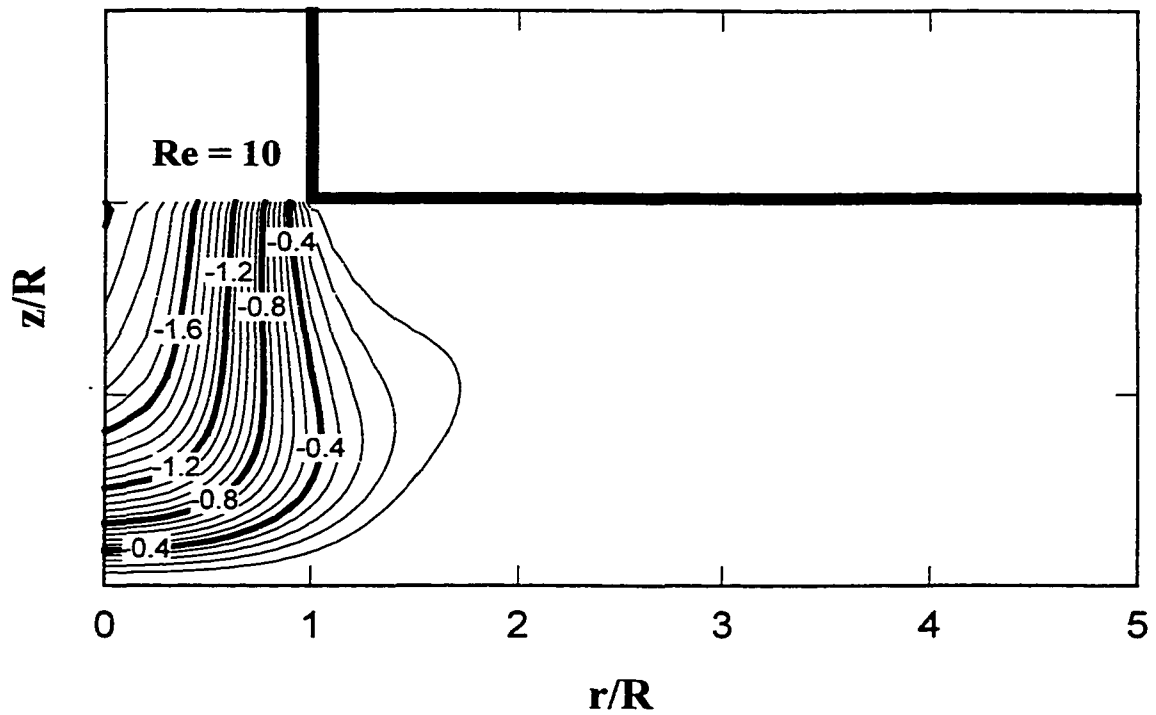


**Figure 2.6b** Numerical simulation of axial velocity distributions in the impinging jet flow region for  $Re = 10$

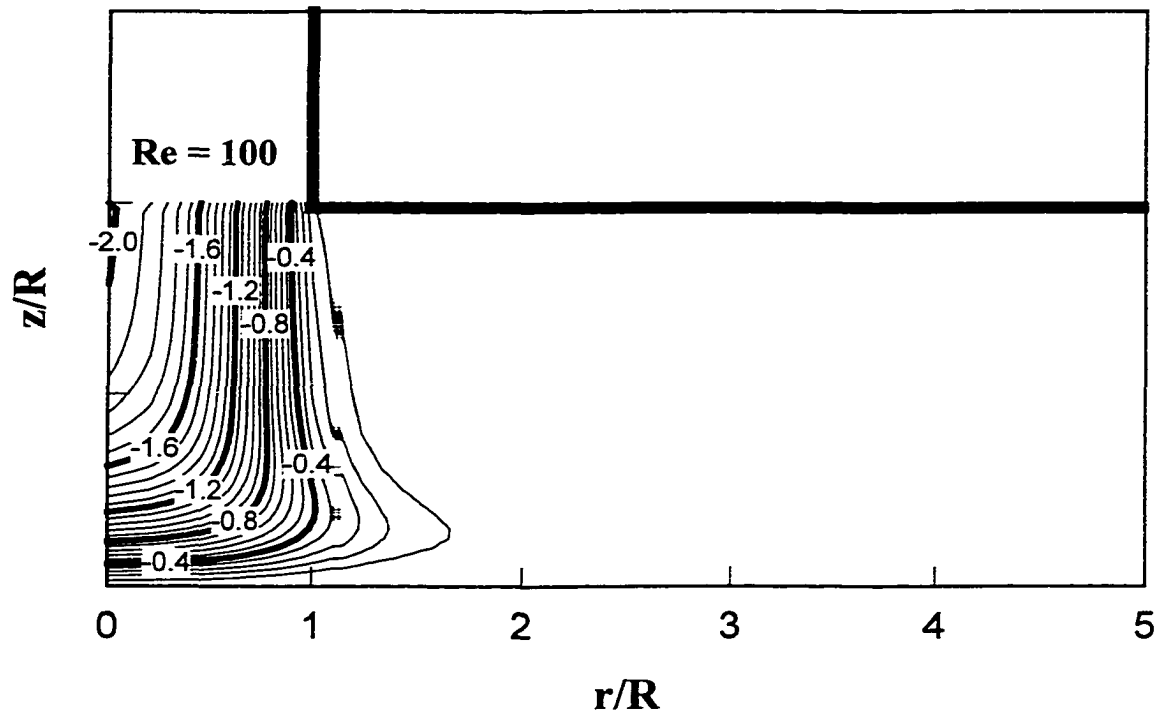


**Figure 2.6c** Numerical simulation of axial velocity distributions in the impinging jet flow region for  $Re = 100$



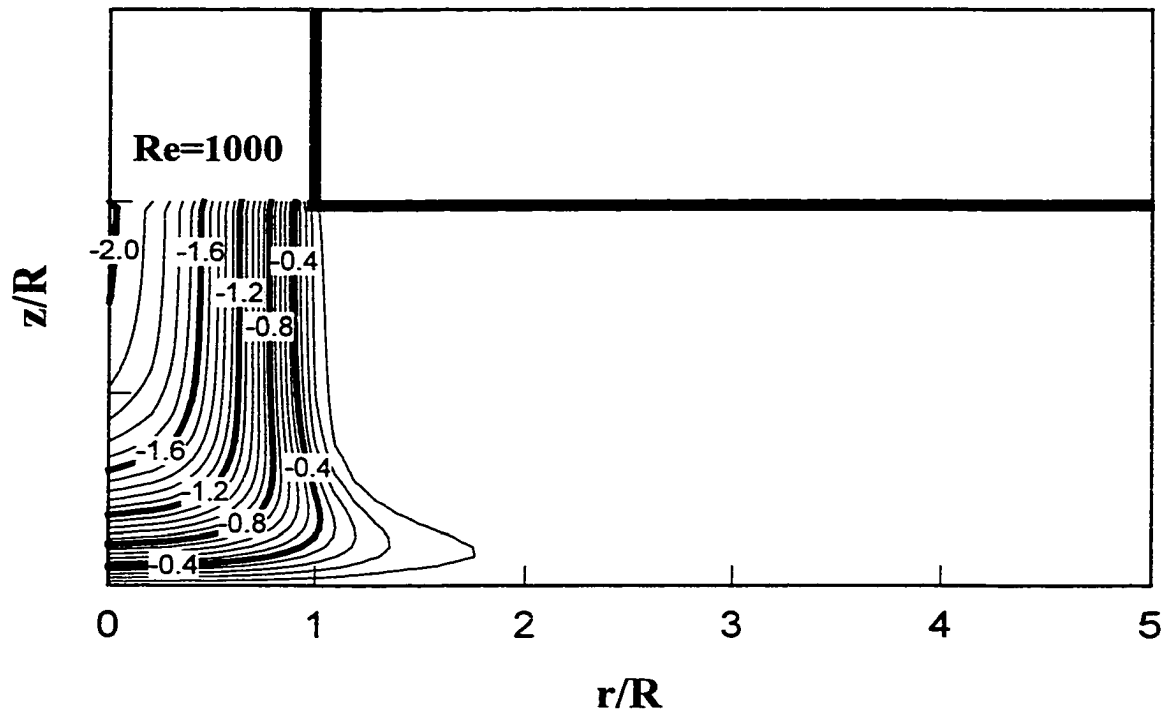


**Figure 2.6d** Numerical simulation of axial velocity distributions in the impinging jet flow region for  $Re = 1000$

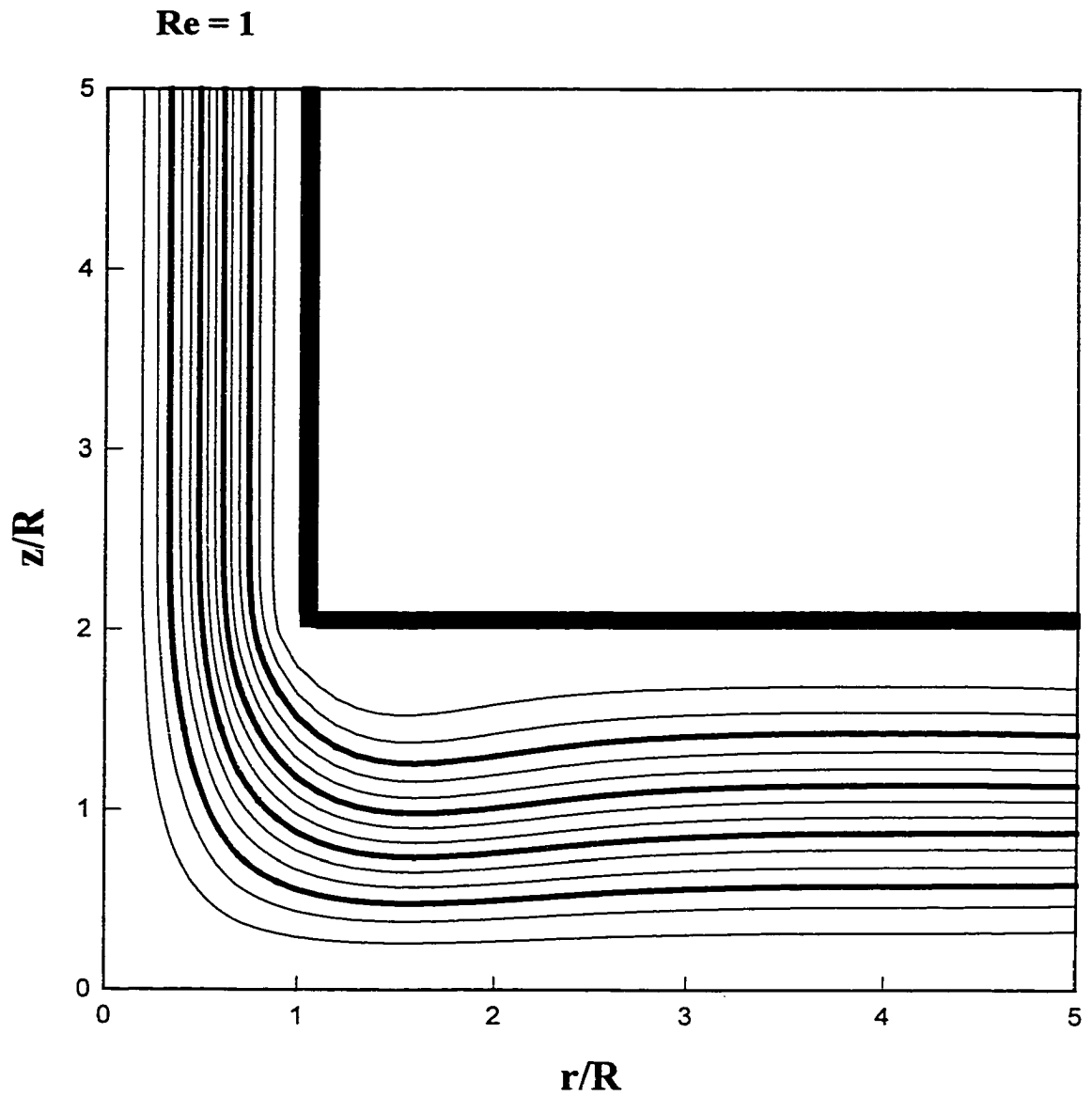


**Figure 2.7a** Numerical simulation of stream function profiles in the impinging jet flow region for  $Re = 1$ ; calculations based on the computational domain II

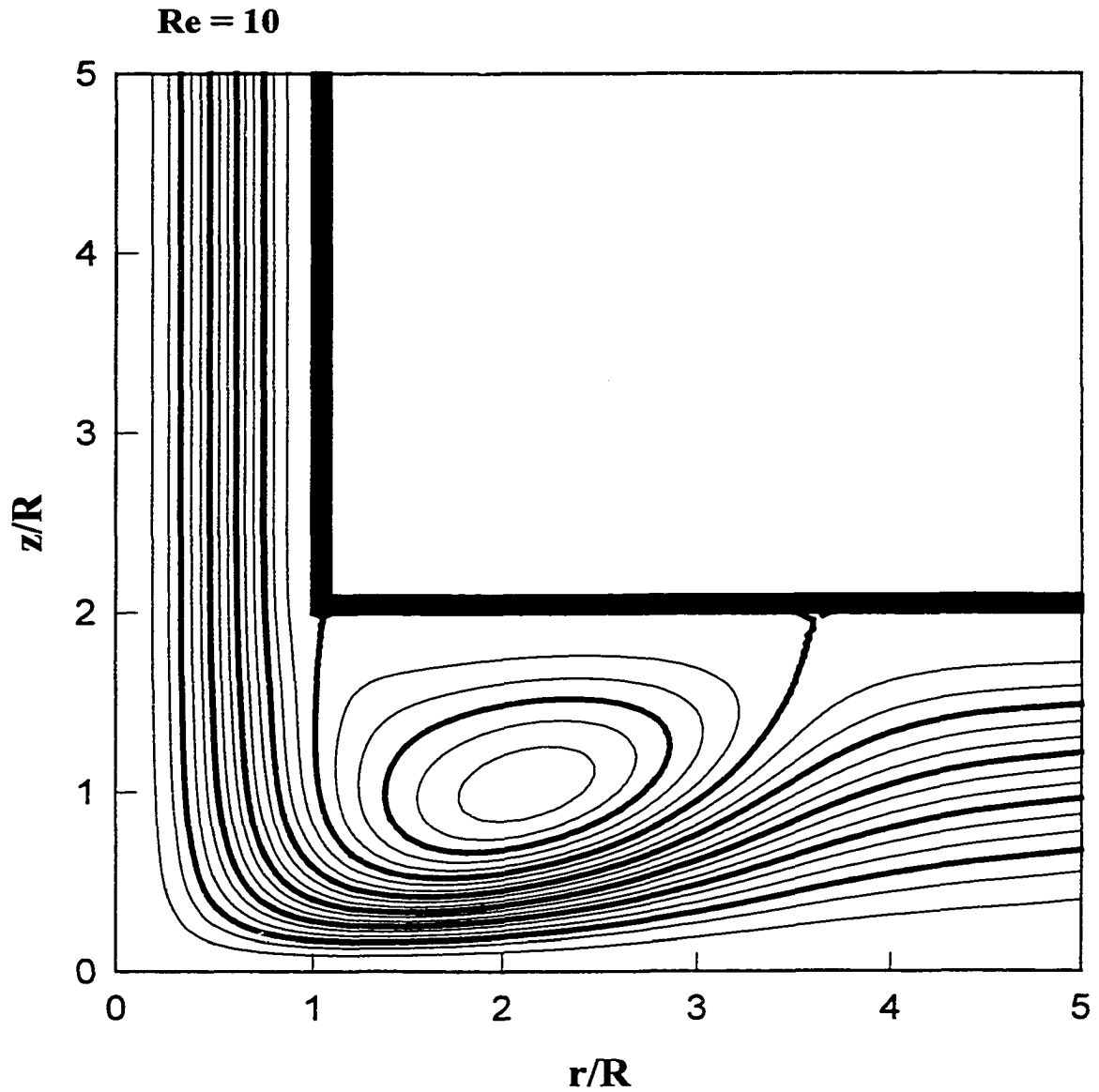


**Figure 2.7b** Numerical simulation of stream function profiles in the impinging jet flow region for  $Re = 10$ ; calculations based on the computational domain II

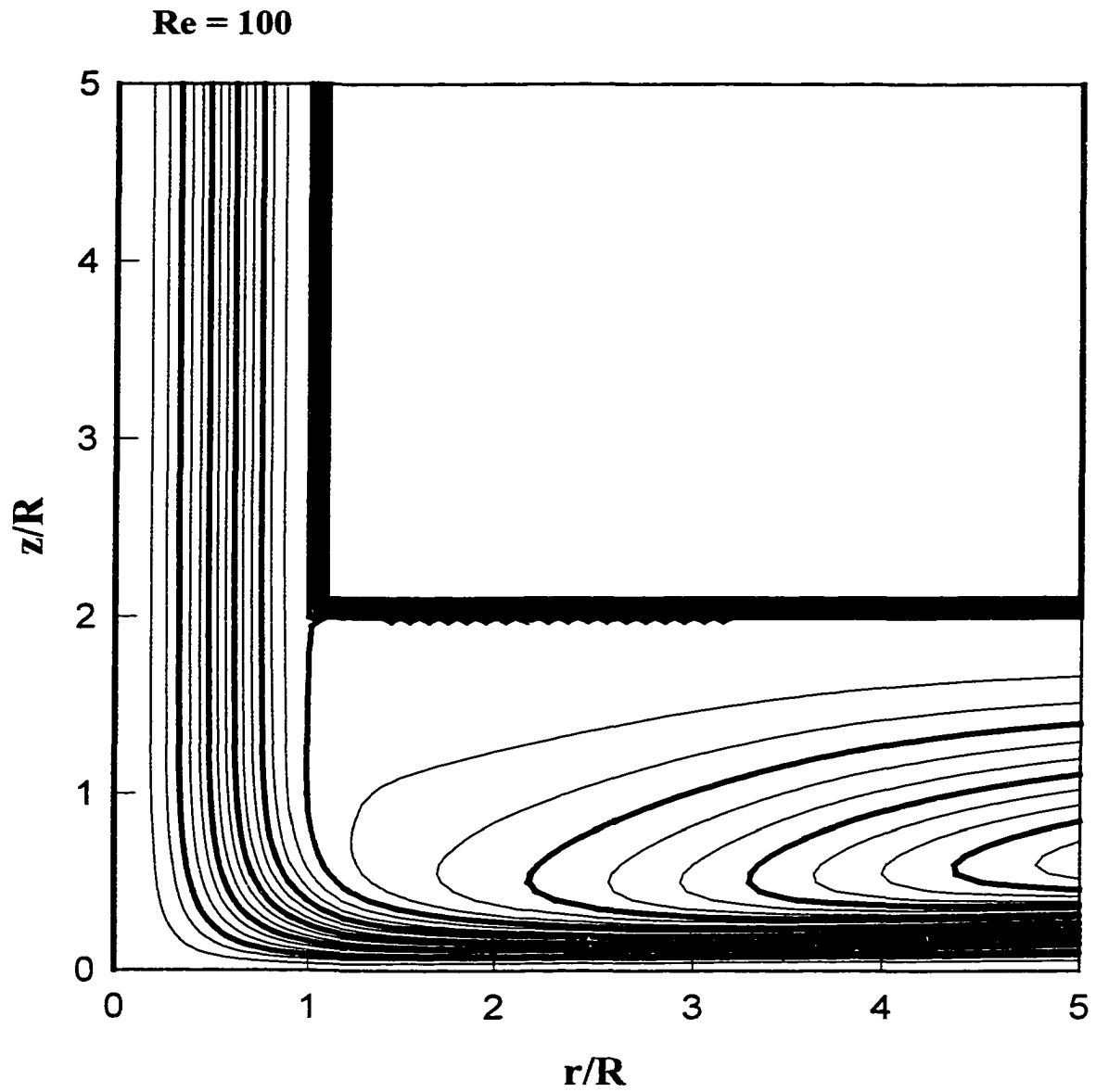


**Figure 2.7c** Numerical simulation of stream function profiles in the impinging jet flow region for  $Re = 100$ ; calculations based on the computational domain II

**Re = 1000**

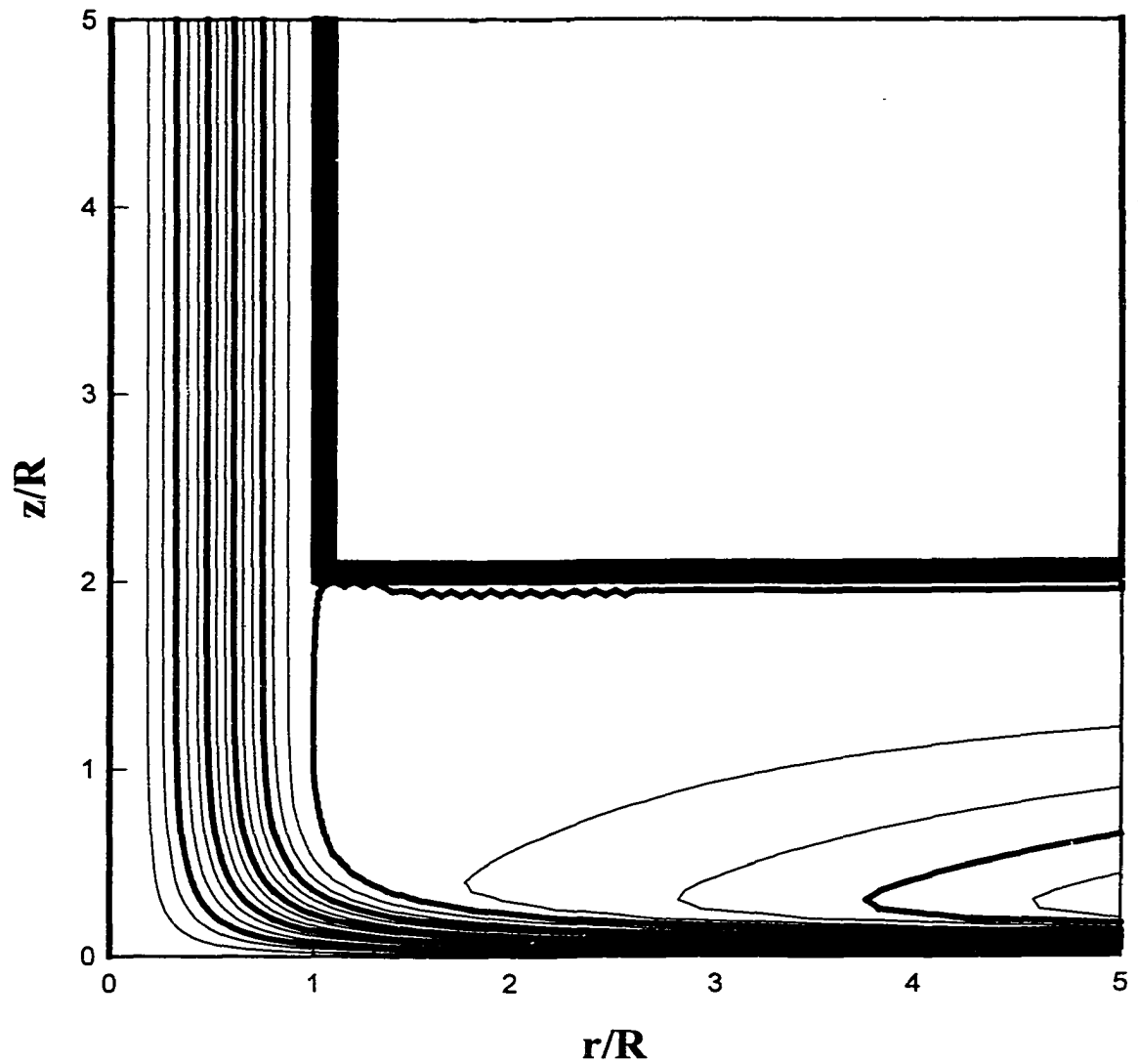


**Figure 2.7d** Numerical simulation of stream function profiles in the impinging jet flow region for  $Re = 1000$ ; calculations based on the computational domain II

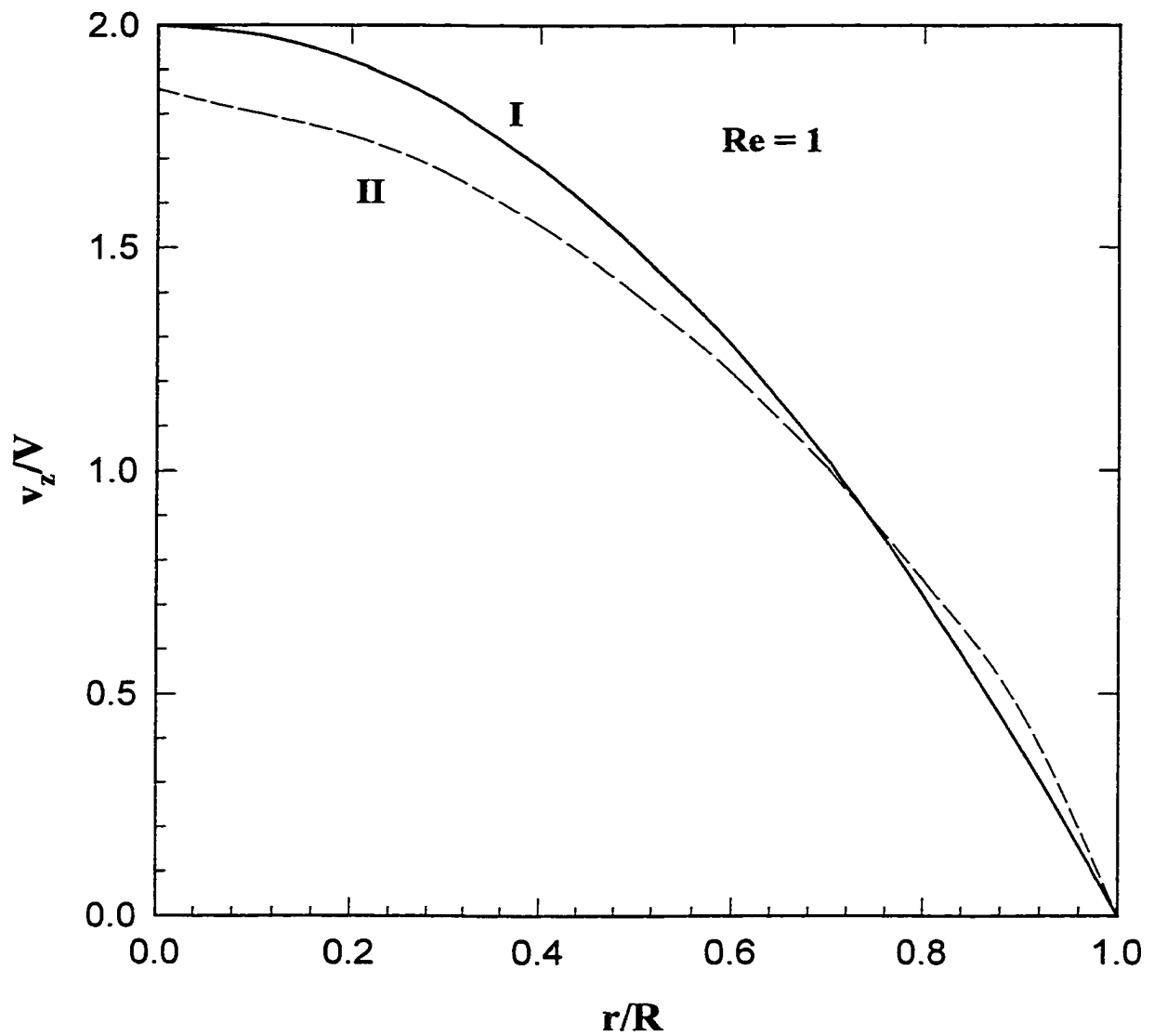


**Figure 2.8a** Comparison of velocity profiles at the tube exit for two different computational domains ( $Re = 1$ ); solid line -computational domain I; broken line - computational domain II

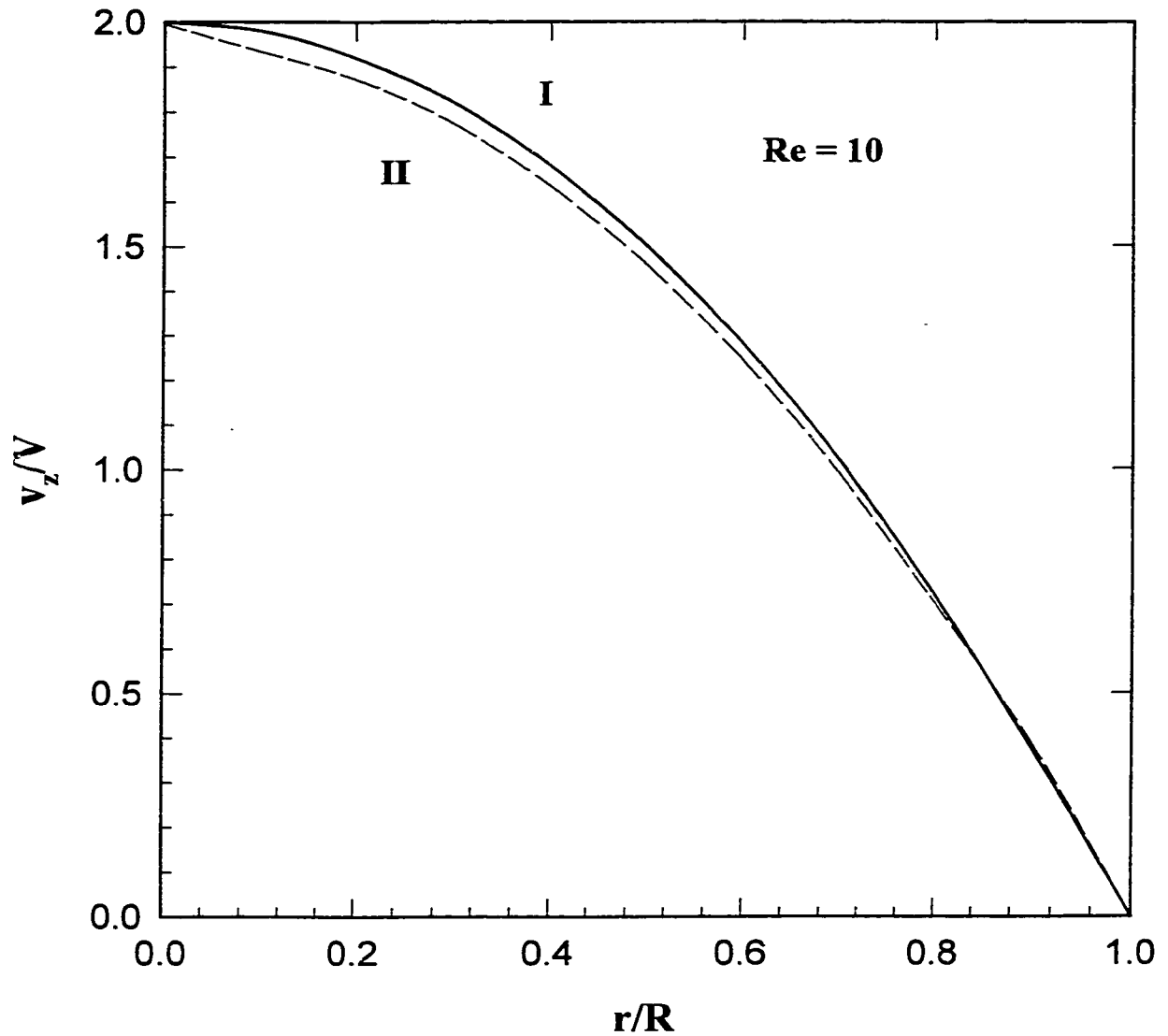


**Figure 2.8b** Comparison of velocity profiles at the tube exit for two different computational domains ( $Re = 10$ ); solid line - computational domain I; broken line - computational domain II

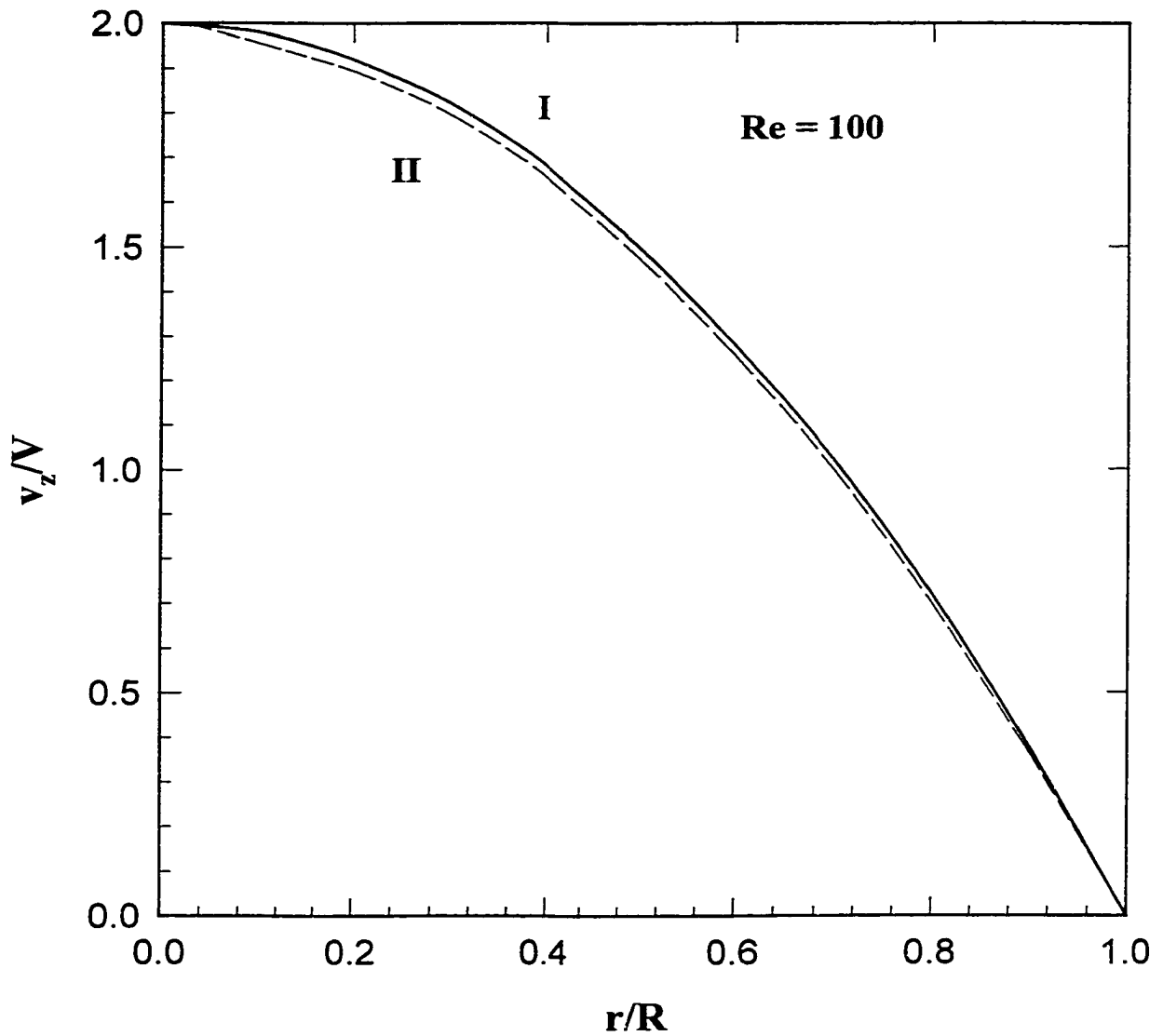


**Figure 2.8c** Comparison of velocity profiles at the tube exit for two different computational domains ( $Re = 100$ ); solid line - computational domain I; broken line - computational domain II



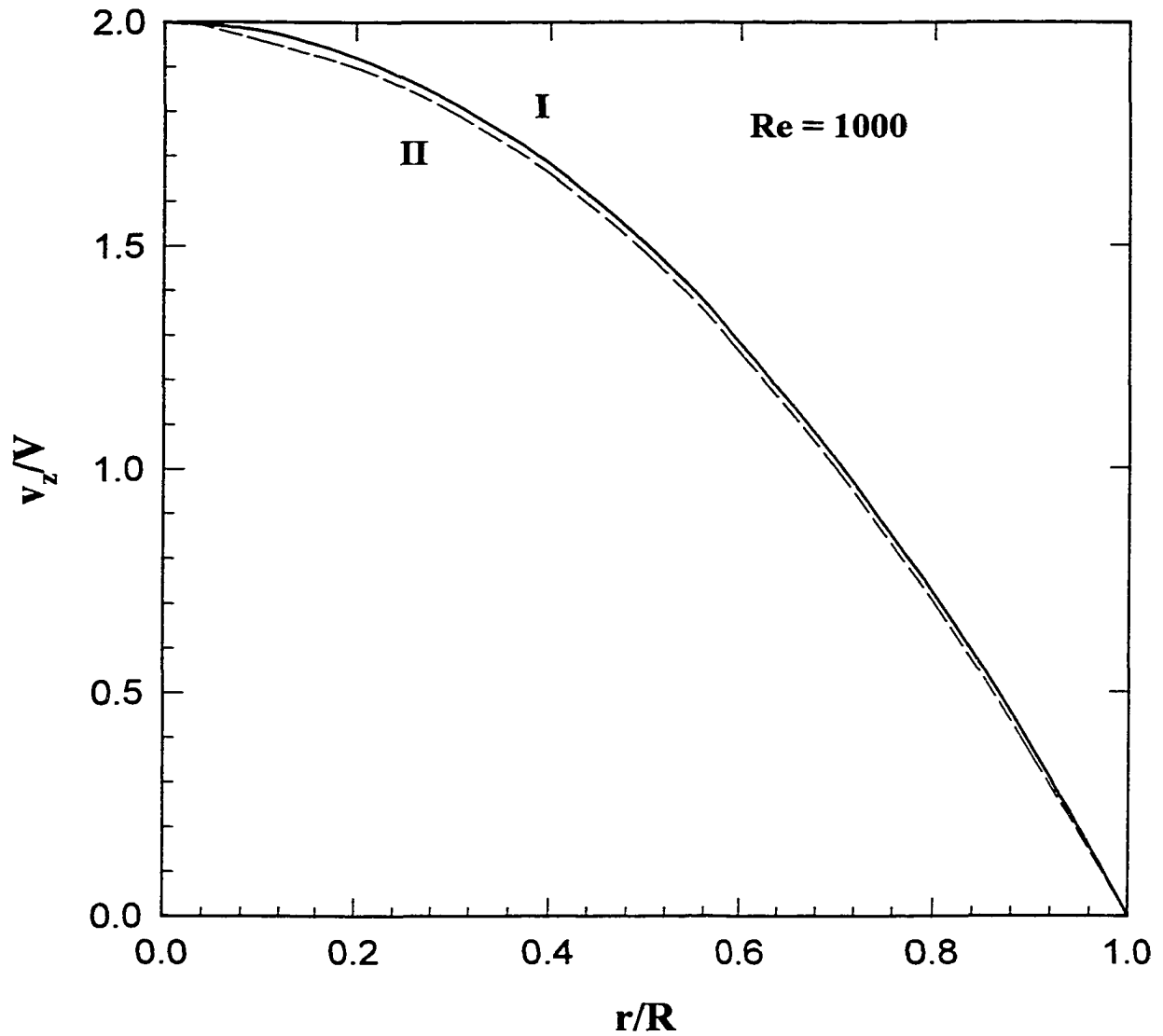


**Figure 2.8d** Comparison of velocity profiles at the tube exit for two different computational domains ( $Re = 1000$ ); solid line - computational domain I; broken line - computational domain II

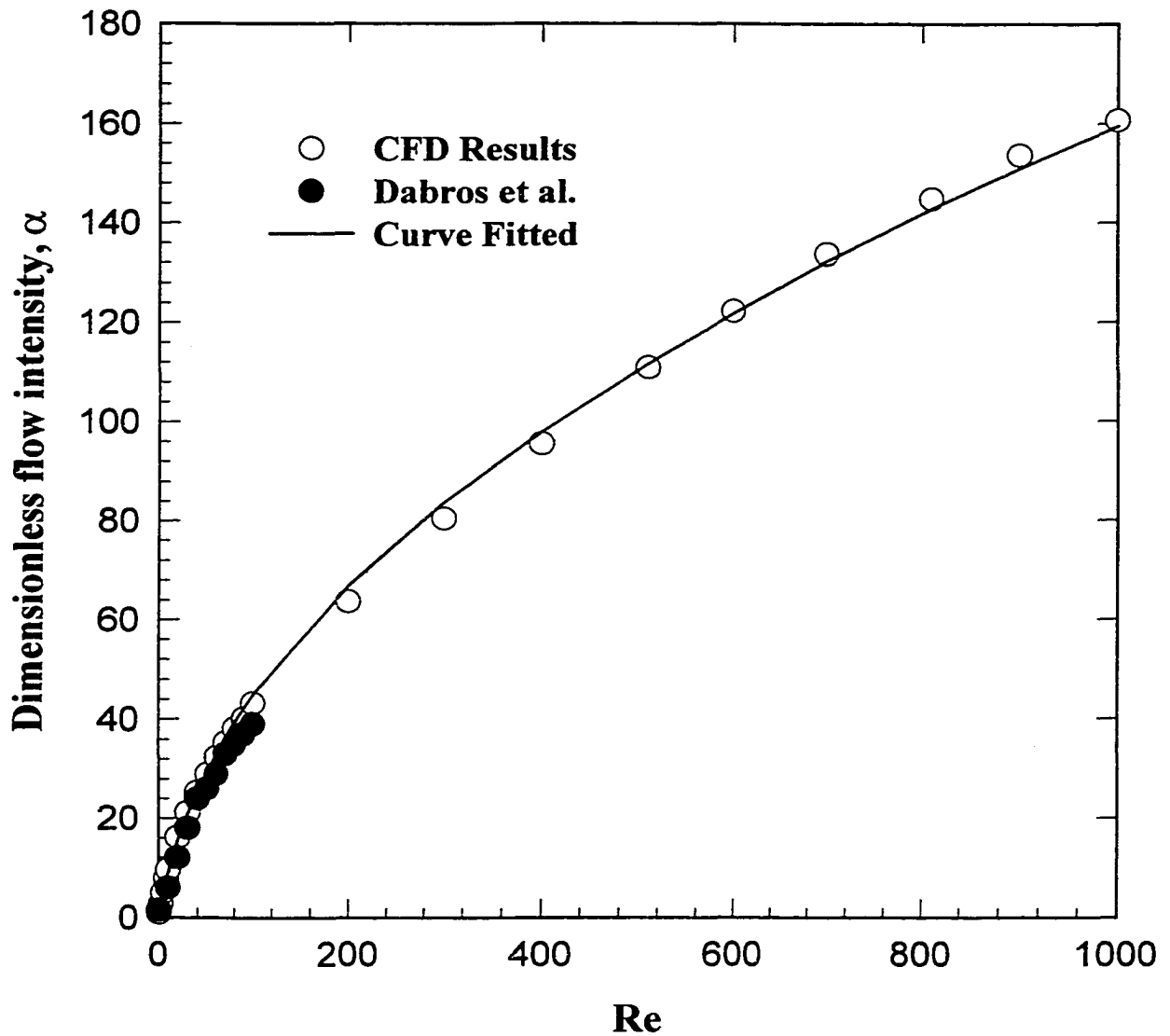


**Figure 2.9** Dependence of the dimensionless intensity of the stagnation point flow,  $\bar{\alpha}$ , on the Reynolds number,  $Re$ ; empty symbols show results of numerical simulations; solid symbols are quoted from Dabros et al. ; solid line represents regression analysis

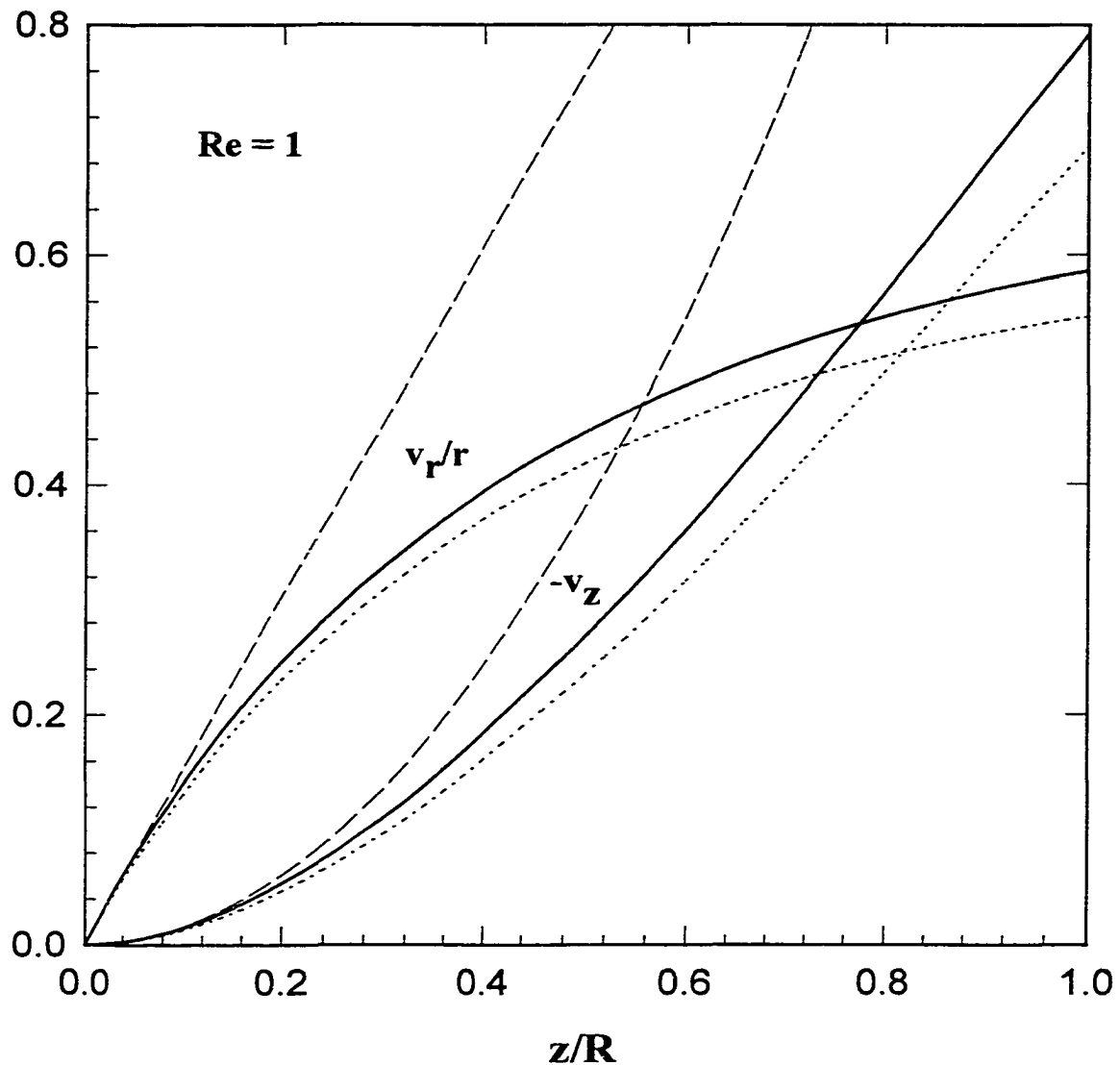


**Figure 2.10a** Dependence of the axial  $v_z$  and the reduced radial  $v_r/r$  velocity components on the coordinate  $z$  for  $Re = 1$ ; solid lines show numerical simulations obtained from grids  $j_r=2$ ; dotted lines are numerical simulations based on grids  $j_r=8$ ; dashed lines represent the analytical expressions for stagnation flow patterns given by equation (2.33)

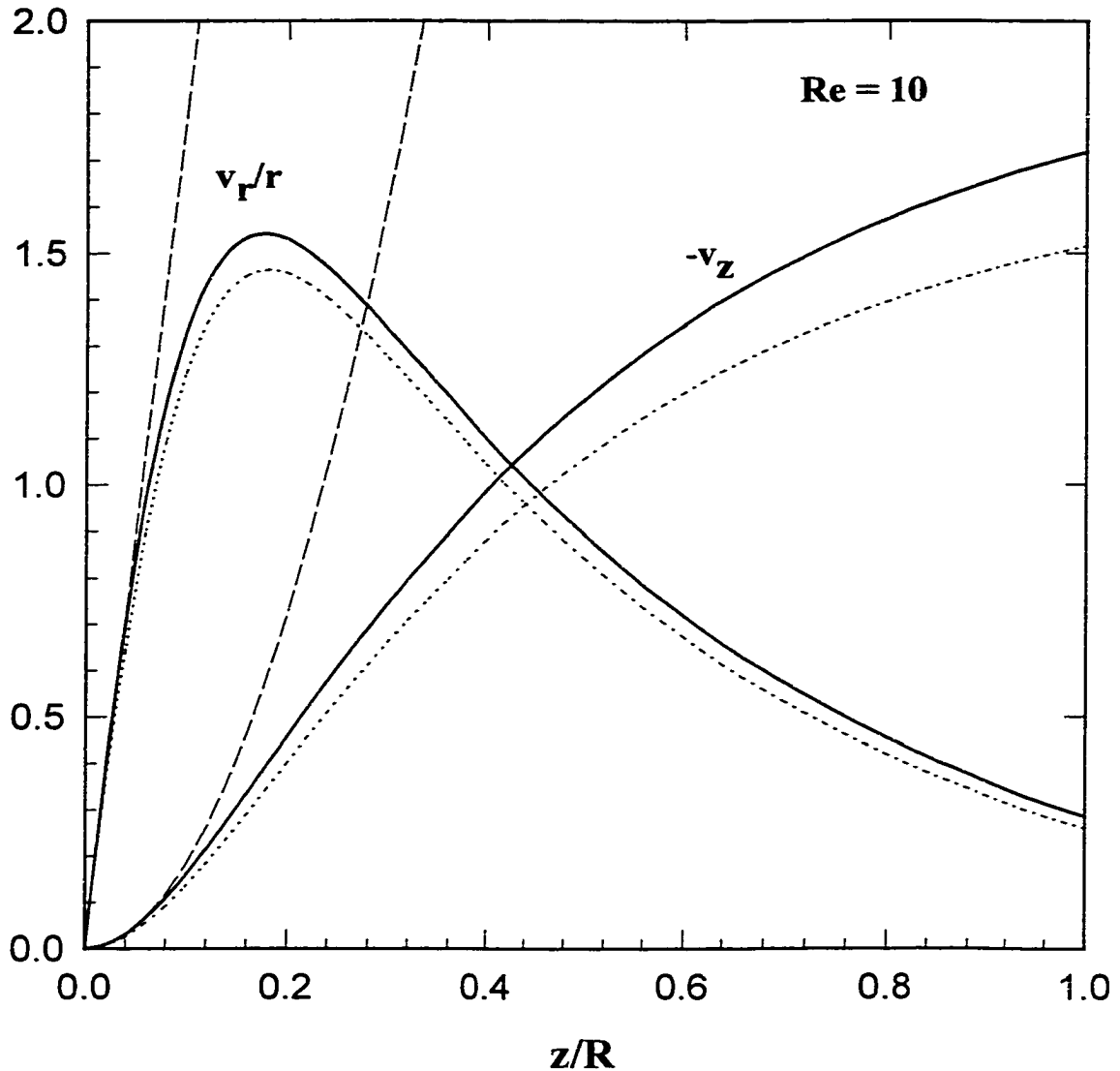


**Figure 2.10b** Dependence of the axial  $v_z$  and the reduced radial  $v_r/r$  velocity components on the coordinate  $z$  for  $Re = 1$ ; solid lines show numerical simulations obtained from grids  $j_r=2$ ; dotted lines are numerical simulations based on grids  $j_r=8$ ; dashed lines represent the analytical expressions for stagnation flow patterns given by equation (2.33)

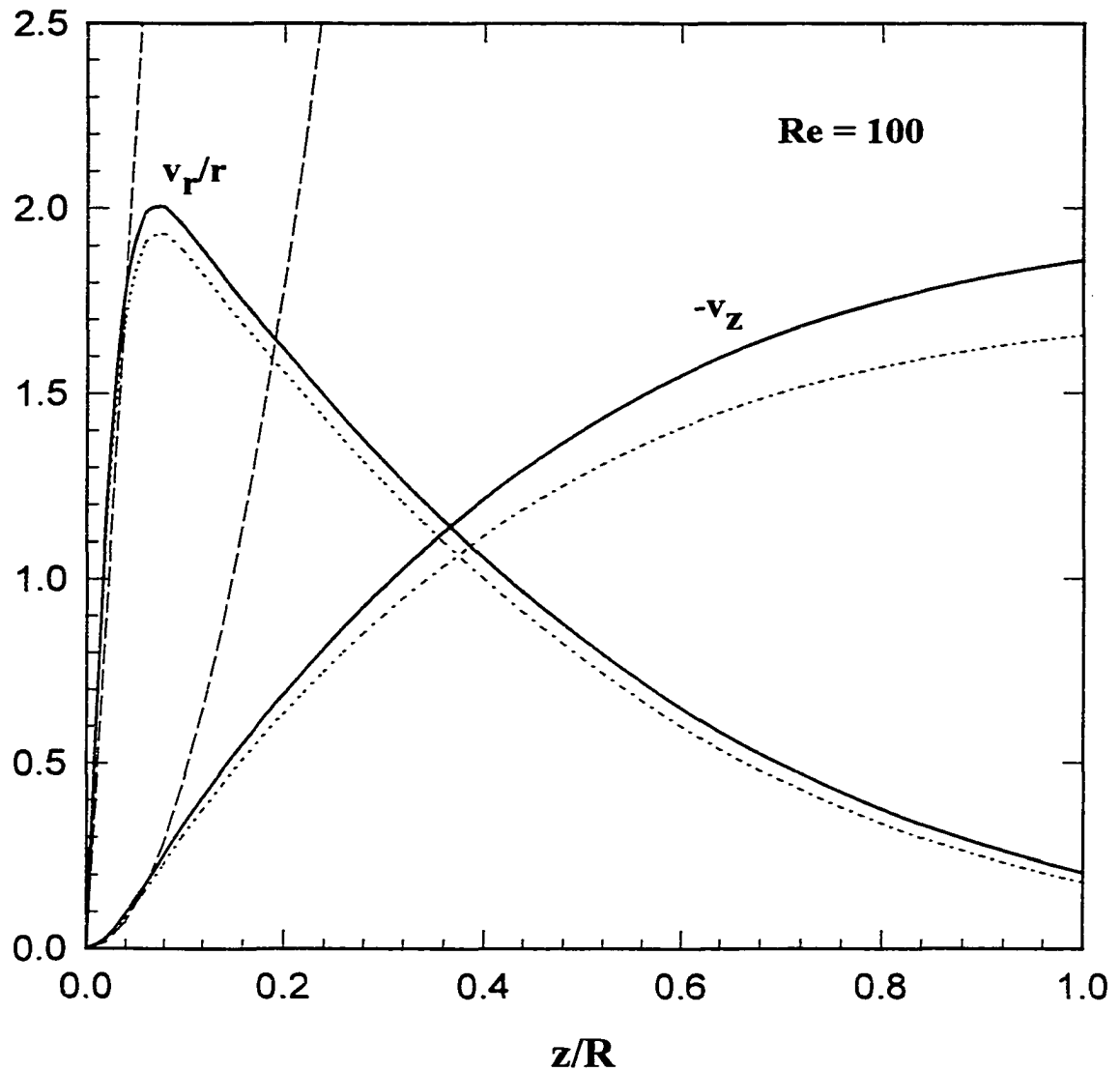


**Figure 2.10c** Dependence of the axial  $v_z$  and the reduced radial  $v_r/r$  velocity components on the coordinate  $z$  for  $Re = 100$ ; solid lines show numerical simulations obtained from grids  $j_r=2$ ; dotted lines are numerical simulations based on grids  $j_r=8$ ; dashed lines represent the analytical expressions for stagnation flow patterns given by equation (2.33)

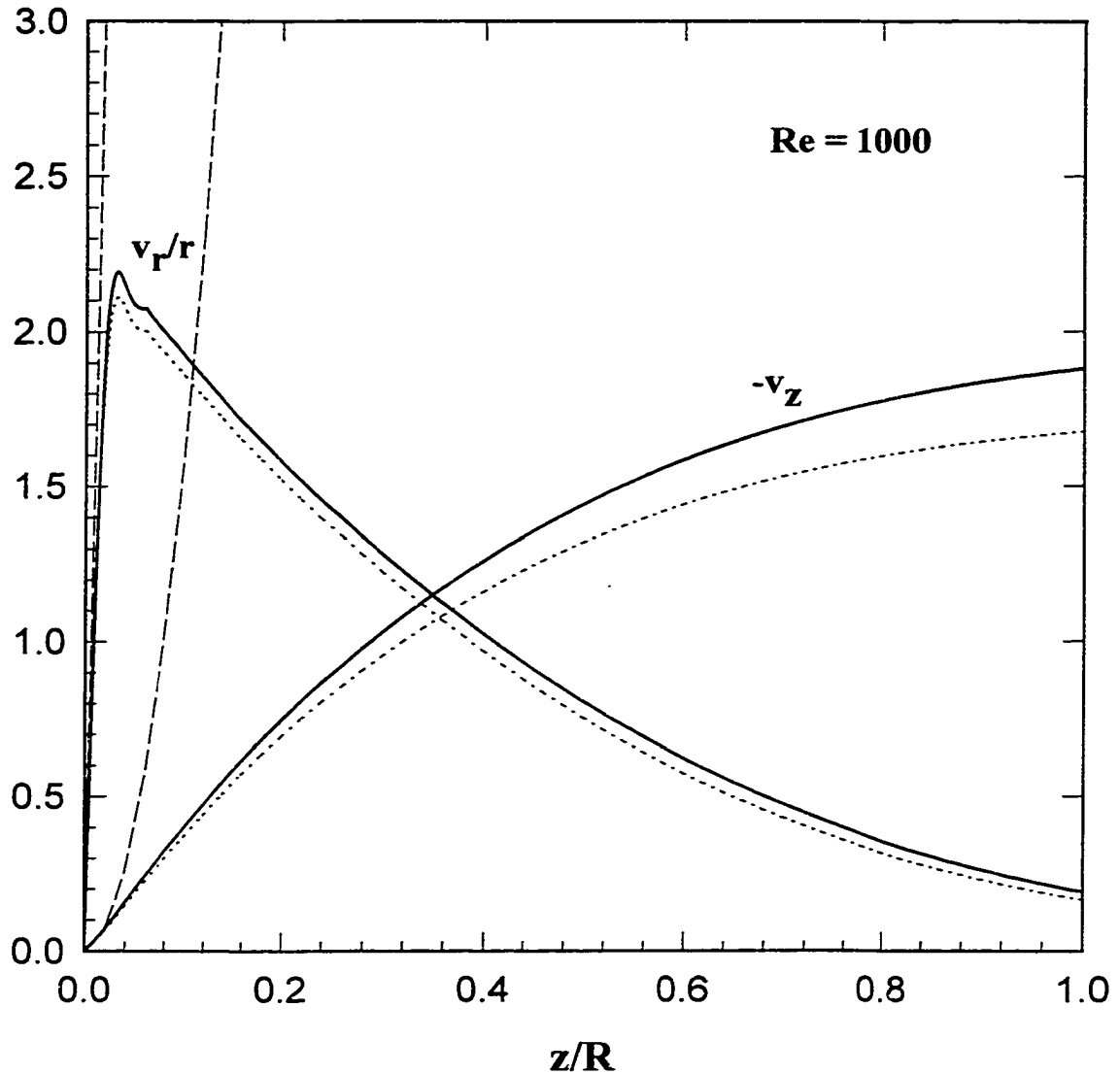


**Figure 2.10d** Dependence of the axial  $v_z$  and the reduced radial  $v_r/r$  velocity components on the coordinate  $z$  for  $Re = 1000$ ; solid lines show numerical simulations obtained from grids  $j_r=2$ ; dotted lines are numerical simulations based on grids  $j_r=8$ ; dashed lines represent the analytical expressions for stagnation flow patterns given by equation (2.33)

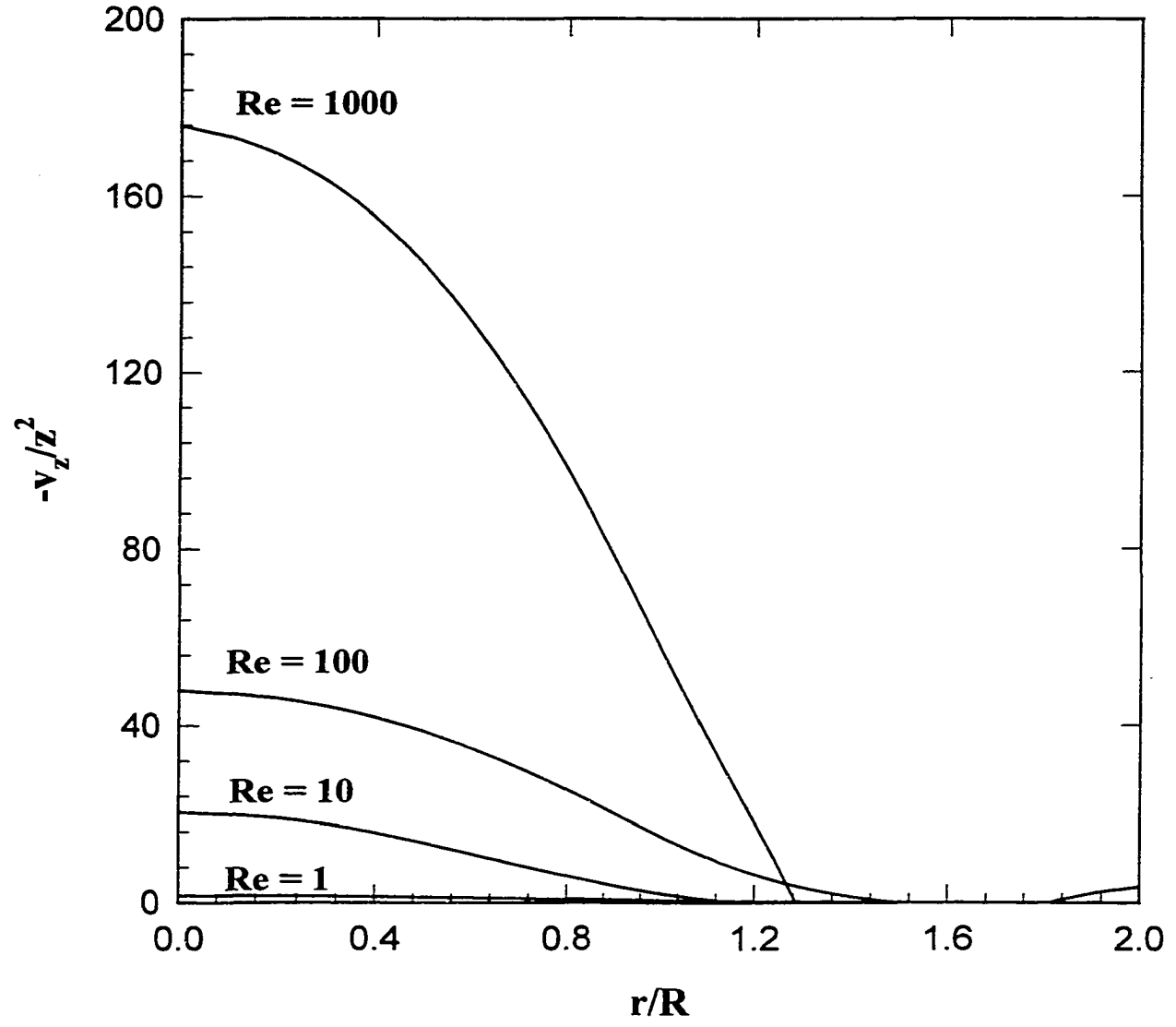


**Figure 2.11** Dependence of the calculated reduced axial velocity component ( $-v_z/z^2$ ) as  $z \rightarrow 0$  on the radial coordinate  $r$  for various Reynolds numbers

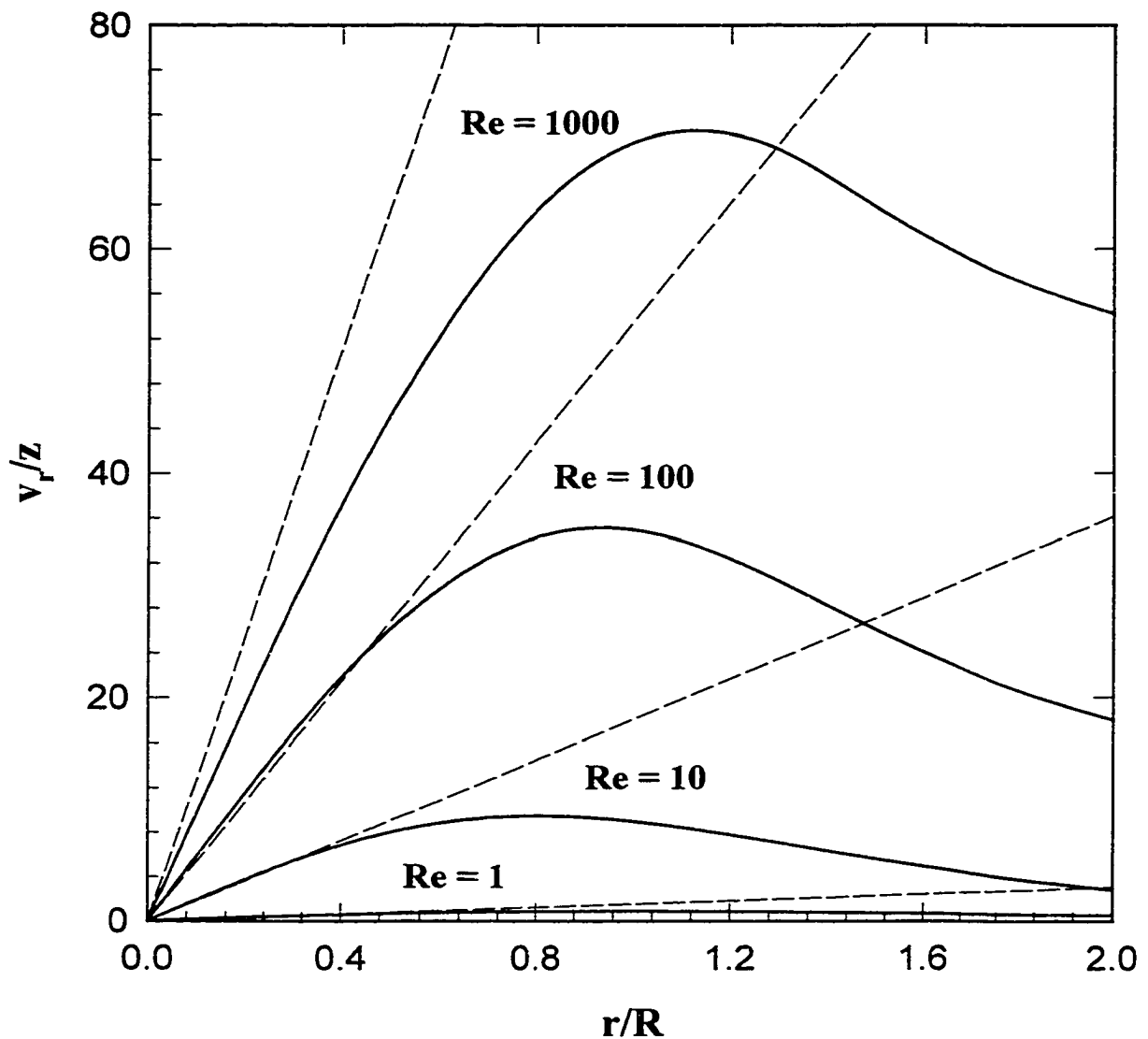


**Figure 2.12** Dependence of the reduced radial velocity component ( $v_r/r$ ) as  $z \rightarrow 0$  on the coordinate  $r$  for various Reynolds numbers; solid lines show numerical simulations; dashed lines represent the analytical expressions for stagnation flow patterns given by equation (2.33)



## CHAPTER 3

# BUBBLE TRANSPORT EQUATION FOR IMPINGING JET SYSTEM

### 3.1 Introduction

This chapter focuses on the modeling of bubble transport from the impinging flow jet onto a solid surface (Yang et al., 1998c). The Eulerian based approach is employed to derive bubble transport equation that includes influences of convection, Brownian diffusion, hydrodynamic interactions, gravity, as well as van der Waals and electrostatic double layer surface force interactions. The major emphasis is placed on a region around the stagnation point, where colloidal forces are expected to play important roles in bubble transport and attachment. Specifically, since the flow fields in this region follow the stagnation point flow patterns (expressed analytically by equation (2.33)), the bubble transport equation therefore can be greatly simplified to a second-order ordinary differential equation. Two widely used boundary conditions then are imposed to obtain numerical solutions of this equation. Although the presented model essentially shows no difference from models for deposition of solid particles and oil droplets in the impinging jet system developed by Dabros and van de Ven (1983, 1987) and Sanders et al. (1995), respectively, its specific applicability to fine bubbles is discussed in detail. In addition, since the hydrodynamic boundary layer concept is so important to description of the hydrodynamic features of impinging jet systems, a derivation of the thickness of the hydrodynamic boundary layer is, therefore, given in Appendix A.2 (Yang et al., 1999a).

### 3.2 Mass Conservation Equation

A simple schematic of the impinging jet system is illustrated in Figure 3.1. A more detailed description of such a system, used in experimental study of bubble attachment, will be provided in Chapter 5. To begin, consider a dilute suspension of spherical, non-interacting (i. e., interactions between fine bubbles are neglected) fine

bubbles suspended in a flowing jet characterized by the fluid velocity vector  $\underline{V}$  relative to a space-fixed frame of reference. The transfer of Brownian fine bubbles from flowing suspensions toward a collector surface in the impinging jet system is governed by the mass conservation equation, which, under the assumption of the absence of mass sources (e.g., coalescence of bubbles), takes the following form

$$\frac{\partial n}{\partial t} + \nabla \cdot \underline{j} = 0 \quad (3.1)$$

In this equation,  $n$  is the local number concentration of fine bubbles (i.e., the number of bubbles per unit volume),  $t$  is the time,  $\nabla$  is the gradient operator, and  $\underline{j}$  is the bubble mass transfer flux vector (number of bubbles per unit area per second).

Assuming further that the process reaches steady-state (which, in reality, occurs instantly when flow conditions are stable), the mass conservation equation is simplified to

$$\nabla \cdot \underline{j} = 0 \quad (3.2)$$

It should be noted that, due to axisymmetry of the impinging jet flow, the mass conservation equation can be described using a two-dimensional cylindrical coordinate system that is identical to the one used for description of the flow fields shown in Figure 2.1.

### 3.3 General Expression for Mass Flux

The bubble mass flux,  $\underline{j}$ , can be decomposed into contributions from fluid convection, diffusion, and migration under colloidal and external force fields. These contributions to the mass flux are expressed by the following convective diffusion equation or Fokker-Planck equation (van de Ven, 1989; Masliyah, 1994)

$$\underline{j} = \underline{u}n - \underline{D} \cdot \nabla n + \underline{D} \cdot \underline{F} \frac{n}{kT} \quad (3.3)$$

where  $\underline{u}$  is the bubble velocity,  $\underline{D}$  is the bubble diffusion coefficient tensor,  $kT$  represents thermal energy ( $k$  is the Boltzmann constant and  $T$  is the absolute temperature), and  $\underline{F}$  is the total force acting on a bubble.

In order to solve the mass conservation equation, one has to know the bubble velocity, determine the bubble mass diffusion coefficient, and specify all forces acting on a bubble. In general, the forces acting on a bubble may include external body forces  $\underline{F}_{Ex}$ , such as gravity, and colloidal surface forces  $\underline{F}_{Col}$ , such as van der Waals and electrostatic double layer (*EDL*) interactions.

$$\underline{F} = \underline{F}_{Ex} + \underline{F}_{Col} \quad (3.4)$$

### 3.4 Bubble Velocity

The bubble velocity is related to the fluid velocity; the latter can be obtained from numerically solving the continuity and Navier-Stokes equations as described in Chapter 2. Strictly speaking, the process involved in the impinging jet system, with bubble transport and attachment taking place, is a complex two-phase flow involving a suspension of bubbles entrained in a moving fluid. The solutions to the continuity and Navier-Stokes equations obtained in Chapter 2 should therefore be the case for undisturbed flow fields only. Application of such flow fields to the impinging jet situation means the effect due to the presence of fine bubbles is neglected. This assumption is valid only when the bubble concentration is below a certain level, which usually is recommended as 3 – 5% in the literature (Levich, 1962). In practice, the amount of fine bubbles generated in experiments was limited to 0.5 %  $v/v$  (volume to volume ratio). As such, the original two-phase flow problem can be safely treated as simple single-phase flow.

When a bubble moves in the vicinity of the collector surface, it experiences an increasing hydrodynamic drag (compared with the Stokes drag in an unbounded fluid) due to the drainage of the liquid between the bubble and the wall. Hence, the bubble velocity  $\underline{u}$  induced by fluid motion is, in general, different from the undisturbed fluid

velocity  $\underline{v}$  due to bubble-wall hydrodynamic interactions. Following van de Ven (1989) and Masliyah (1994), the relationships between  $\underline{u}$  and  $\underline{v}$  near the collector surface are given by

$$u_r = v_r f_3 \quad (3.5a)$$

$$u_z = v_z f_1 f_2 \quad (3.5b)$$

where  $f_1(z)$ ,  $f_2(z)$ , and  $f_3(z)$  are universal hydrodynamic functions accounting for the deviations from the Stokes drag formula due to the presence of the collector wall. They have been extensively studied in low Reynolds number fluid mechanics. Rigorous derivation of these functions was well documented in the literature by Brenner (1961), Goldman et al. (1967a), Goren (1970), and Goren and O'Neill (1971).

In general, the flow fields in the entire impinging region are obtained numerically as outlined in Chapter 2. With regard to bubble attachment, the region of most interest is that near the stagnation point ( $r = 0$ ), where colloidal surface forces between a bubble and the collector surface are expected to play an important role in bubble transport and attachment. In this region, the velocity components are approximated by the stagnation flow patterns given by equation (2.33). Replacing the fluid velocity  $\underline{v}$  in equation (3.5) by the stagnation point flow patterns, the bubble velocity can be expressed as

$$u_r(r, z) = \alpha r z f_3(z) \quad (3.6a)$$

$$u_z(z) = -\alpha z^2 f_1(z) f_2(z) \quad (3.6b)$$

where  $\alpha$  is the intensity of the stagnation flow, and is related to the dimensionless fluid intensity,  $\bar{\alpha}$ , defined in equation (2.33), through the following expression

$$\alpha = \bar{\alpha} \frac{V}{R^2} = \bar{\alpha} \frac{\mu_f Re}{\rho_f R^3} \quad (3.7)$$

where  $R$  is the radius of the capillary tube and  $V$  is the average velocity at the capillary tube exit. For the impinging jet system, the impinging jet Reynolds number,  $Re$ , is

$$\text{defined as } Re = \frac{\rho_f V R}{\mu_f}.$$

### 3.5 Bubble Diffusion Coefficient

Near the collector, hydrodynamic interactions also affect the bubble's diffusion coefficient (or diffusivity). The diffusion coefficient becomes dependent on the relative position and orientation between the bubble and the wall (i.e., it becomes a tensorial quantity). Again assuming a dilute suspension of spherical, non-interacting bubbles, the bubble diffusion coefficient components are formulated as (van de Ven, 1989; Masliyah, 1994)

$$\underline{\underline{D}} = \begin{pmatrix} D_{rr} & D_{r\bar{z}} \\ D_{\bar{z}r} & D_{\bar{z}\bar{z}} \end{pmatrix} = D_{\infty} \begin{pmatrix} d_{rr} & 0 \\ 0 & d_{\bar{z}\bar{z}} \end{pmatrix} \quad (3.8)$$

where  $D_{rr}(z) = D_{\infty}d_{rr} = D_{\infty}f_4(z)$  and  $D_{\bar{z}\bar{z}}(z) = D_{\infty}d_{\bar{z}\bar{z}} = D_{\infty}f_1(z)$ . Here,  $z$  represents the distance from the center of the bubble to the collector surface.  $D_{\infty}$  is the bubble Brownian diffusion coefficient in the bulk unbounded phase, and is determined from the Stokes-Einstein equation (van de Ven, 1989)

$$D_{\infty} = \frac{kT}{6\pi\mu_f a_p} \quad (3.9)$$

where  $\mu_f$  is the viscosity of the aqueous solution and  $a_p$  is the radius of the bubble.

Briefly, to introduce the hydrodynamic universal functions  $f_1(z)$  and  $f_4(z)$  (Goldman et al., 1967b) in equation (3.8) is to modify the bubble diffusion coefficients with consideration of hydrodynamic interaction between the bubble and the wall. The hydrodynamic universal functions  $f_1(z)$ ,  $f_2(z)$ ,  $f_3(z)$ , and  $f_4(z)$  have tabulated in the literature. In order to incorporate their values, as functions of the dimensionless separation distance between the bubbles and the collector surface, directly into subsequent numerical calculations, it is advantageous to curve fit each of these functions so that they could be expressed by empirical expressions. The results of these curve fits are given by Masliyah (1994) as follows:

$$f_1(\bar{h}) = 1.00 - 0.399 \exp(-0.14869\bar{h}) - 0.601 \exp(-1.2015\bar{h}^{0.92667}) \quad (3.10a)$$

$$f_2(\bar{h}) = 1.00 + 1.362 \exp(-1.3596\bar{h}) + 0.8764 \exp(-0.525\bar{h}^{0.56954}) \quad (3.10b)$$

$$f_3(\bar{h}) = 1.00 - 0.3752 \exp(-3.906\bar{h}) - 0.625 \exp(-3.105\bar{h}^{0.15}) \quad (3.10c)$$

$$f_4(\bar{h}) = 1.00 - 1.23122 \exp(-0.2734\bar{h}) + 0.8189 \exp(-0.175\bar{h}^{1.2643}) \quad (3.10d)$$

where  $\bar{h}$ , the dimensionless separation gap between a bubble and the collector surface, is defined as  $\bar{h} = \frac{z - a_p}{a_p}$ . Curves for each of the coefficients  $f_1(\bar{h})$ ,  $f_2(\bar{h})$ ,  $f_3(\bar{h})$ , and  $f_4(\bar{h})$  are shown in Figure 3.2.

### 3.6 External Body Forces

Generally, the external body forces acting on a bubble may include gravitational force, electrical force - if the charged bubble is subject to an external electric field, etc. As no external electric field was present in the experimental system, only gravitational body forces are considered, and the net gravity and buoyancy force is expressed by the following formula

$$\underline{F}_G = \frac{4}{3} \pi a_p^3 \Delta \rho \underline{g} \quad (3.11)$$

where  $\Delta \rho = \rho_p - \rho_f < 0$  is the density difference between the bubble  $\rho_p$  and the aqueous solution  $\rho_f$ .  $\underline{g}$  is the gravitational acceleration vector. In the impinging jet setup shown in Figure 3.1, bubbles are transported upward to the collector, indicating that the net gravitational force acts favorably to the attachment process.

Nondimensionalizing equation (3.11) with respect to the Brownian force,

$F_{Br} = \frac{kT}{a_p}$ , exerted on a sphere of radius  $a_p$ , it can be seen

$$\bar{F}_G = -Gr = \frac{4\pi}{3} \frac{\Delta \rho g a_p^4}{kT} = \frac{2}{9} \frac{\Delta \rho g a_p^3}{\mu_f D_\infty} \quad (3.12)$$

where  $Gr$  is the nondimensional gravity number. For bubbles the gravity number  $Gr$  is greater than zero.

### 3.7 Colloidal Surface Forces

When a fine bubble approaches the collector surface within a separation distance less than one micron, the bubble's motion is affected by at least two types of colloidal forces between the bubble and the collector surface through the aqueous phase, van der

Waals interaction force and electrostatic double layer interaction force. These two types of colloidal surface forces are widely recognized and well documented in the literature. They form the basis of the well-known *DLVO* theory of colloid stability, developed independently by Derjaguin and Landau in the USSR and Verwey and Overbeek in Netherlands. These two *DLVO* colloidal forces are considered in this study, and expressions for such interactions between a sphere and a flat surface will be given in the following.

In the literature, it usually quite straightforward to first derive the colloidal interaction potential  $V$  as a function of separation gap,  $h$ , between two interacting bodies. The corresponding colloidal interaction force,  $F_{Col}$ , is then related to the interaction potential,  $V_{Col}$ , by

$$F_{Col}(h) = -\frac{dV_{Col}(h)}{dh} \quad (3.13)$$

It is also noted here that these two colloidal forces which act between the bubble and the collector surface are always act along the axial direction (i.e., the normal direction of the collector). As such, the force can be treated as a scalar in the following expressions. In addition, for a dilute bubble suspension colloidal interactions between fine bubbles themselves are assumed to be negligible.

### 3.7.1 van der Waals Interaction

The universal attractive force between atoms and molecules, known as van der Waals interaction force, also operates between macroscopic objects and plays a very important role in bubble-solid interaction and attachment (Usui and Barouch, 1990). Physically, the interaction between macroscopic bodies arises from spontaneous electric and magnetic polarization, giving a fluctuating electromagnetic field within the media and in the gap between the bodies. There usually exists two methods for calculating van der Waals interaction force. The first approach, due mainly to Hamaker (Israelachvili, 1985) who developed the theory of van der Waals interaction between two macroscopic bodies of different geometries, is based on the assumption of pairwise additivity of all

individual intermolecular interactions. Although approximate, this approach captures the essential physics and provides insights into the van der Waals interaction. In the second method, Lifshitz (Israelachvili, 1985), on the basis of the continuity mechanics approach, derived a more rigorous expression for the van der Waals interaction between two semi-infinite media separated by a plane-parallel gap. The same treatment was later extended by Lifshitz and co-workers to deal with the case of two bodies separated by a third medium. In principle, the complex Lifshitz approach enables van der Waals interactions between any system of interest to be calculated. Direct measurements of van der Waals force between mica sheets (Israelachvili and Tabor, 1972) have confirmed the essential validity of the Lifshitz theory. However, proper application of this approach requires detailed knowledge of the dielectric constants and refractive indices of the interacting media over a wide frequency range, which normally are not available. Alternatively, one can still employ the old simple formula developed by Hamaker for description of van der Waals interaction. However, the Hamaker constant, a material dependent constant, is determined using the Lifshitz theory. Obviously, this treatment combines both approaches and is also valid in the framework of the Lifshitz theory. In particular, such a treatment is of great convenience to express van der Waals interaction for a heterogeneous system, i.e., media 1 and media 2 separated by a media 3.

For an undeformed sphere of radius  $a_p$  within a small separation gap  $h$  ( $h \ll a_p$ ) from a flat surface, van der Waals interaction potential can be formulated as (Mahanty and Ninham, 1976)

$$V_{VDW} = -\frac{A_{132} a_p}{6h} \quad (3.14)$$

where  $A_{132}$  is the Hamaker constant for the van der Waals interaction between phase 1 (spherical bubble) and phase 2 (flat plate) separated by medium 3 (aqueous solution).

It should be noted that the expression given by equation (3.14) is derived on the basis of an implicit assumption that the speed of electromagnetic wave propagation is infinite. In reality, the finite time of propagation of electromagnetic field causes a reduced correlation between dipolar oscillations in the interacting bodies and hence a



smaller van der Waals interaction; this is referred to as a retardation effect. It is fairly easy to modify the simple Hamaker approach to take into account the retardation effect by introducing a “characteristic wavelength”  $\lambda$  of the interaction, that usually takes on a value of 100 nm (Gregory, 1981; Israelachvili, 1985). Therefore, the modification of van der Waals interaction between a sphere and a flat plate, with consideration of the retardation effect, is given by Suzuki et al. (1969)

$$V_{VDW} = -\frac{A_{132} a_p}{6h} \frac{\lambda}{(\lambda + 11.116h)} \quad (3.15a)$$

or

$$F_{VDW} = -\frac{dV_{VDW}}{dh} = -\frac{A_{132} a_p}{6h^2} \frac{\lambda (\lambda + 22.232h)}{(\lambda + 11.116h)^2} \quad (3.15b)$$

Equation (3.15) can be nondimensionalized as

$$\bar{V}_{VDW} = \frac{V_{VDW}}{kT} = -Ad \frac{\bar{\lambda}}{h(\bar{\lambda} + 11.116\bar{h})} \quad (3.16a)$$

and

$$\bar{F}_{VDW} = \frac{F_{VDW}}{kT/a_p} = -Ad \frac{\bar{\lambda} (\bar{\lambda} + 22.232\bar{h})}{\bar{h}^2 (\bar{\lambda} + 11.116\bar{h})^2} \quad (3.16b)$$

where  $Ad = \frac{A_{132}}{6kT}$ ,  $\bar{\lambda} = \frac{\lambda}{a_p}$ , and  $\bar{h} = \frac{h}{a_p} = \frac{z - a_p}{a_p}$ .  $Ad$ , referred to as the adhesion

number, measures the strength of the van der Waals interaction.  $\bar{\lambda}$  is the dimensionless retardation wavelength.  $\bar{h}$  is the dimensionless separation gap between the sphere and the flat plate.

Following Gregory (1981), the Hamaker constant  $A_{132}$  can be written as

$$A_{132} = A_{12} + A_{33} - A_{13} - A_{23} \quad (3.17)$$

A useful approximation for Hamaker constants of different phases is the geometric mean assumption

$$A_{ij} \approx \sqrt{A_{ii} A_{jj}} \quad (3.18)$$

where  $A_{ii}$  is the Hamaker constant for two phases of the same material in vacuum.

With equation (3.18), equation (3.17) becomes

$$A_{132} \approx (\sqrt{A_{11}} - \sqrt{A_{33}})(\sqrt{A_{22}} - \sqrt{A_{33}}) \quad (3.19)$$

This expression indicates that, depending on the relative values of the individual Hamaker constant, the presence of a third medium may significantly reduce the van der Waals interaction. Since the Hamaker constant of gas phase 1 is at least three or four orders of magnitude lower than that of the liquid or solid phases, and in almost all cases,  $A_{22}$  (for solid) is greater than  $A_{33}$  (for water), the effective Hamaker constant  $A_{132}$  for a gas-water-solid system is negative. This suggests that the van der Waals interaction between a bubble and the collector surface across an aqueous solution considered in this study is repulsive in nature. The mechanisms of negative Hamaker constants and the conditions for repulsive van der Waals interactions were discussed in details by van Oss et al. (1990), and the subject was reviewed by Visser (1981).

### 3.7.2 Electrostatic Double Layer (*EDL*) Interaction

In addition to van der Waals interaction forces, the other type of colloidal surface forces included in the *DLVO* theory is due to electrostatic double layer (*EDL*) interaction between two charged interfaces. In essence, it can be viewed as Coulomb's electrostatic interaction between two charged surfaces across an aqueous solution.

It is experimentally evident that interfaces in an aqueous solution are nearly always charged for some reasons (such as the ionization of surface group, specific adsorption of ions, etc), and hence will attract oppositely charged counterions around them. The overall arrangement of the electrostatic charge on the charged interface, together with the redistribution of ions around it, is usually referred to as the electrostatic double layer (*EDL*) (Hunter, 1981; Masliyah, 1994). A widely accepted model for the *EDL* is due to Stern (Hunter, 1981). As a result of electrostatic attraction, some immobile counterions are located immediately adjacent to the charged surface to form the so-called Stern layer. Outside the Stern layer, the remaining mobile counterions are distributed more broadly in the diffuse layer, in which the motions of the ions is balanced by simultaneous influences of electrostatic attraction and random diffusion due to thermal excitation.

The interaction between two approaching charged surfaces is governed predominately by the overlap of the two diffuse layers. As such, the potential most relevant to the interaction is that at the boundary between the Stern and diffuse layers (i.e., the Stern potential), rather than the potential at the charged surface. Such boundary (the Stern plane) is generally considered to be at a distance of 0.3 to 0.5 *nm* from the charged surface, corresponding to the diameter of a hydrated counterion. There is no direct experimental method for determining the Stern potential, but there is good reason to believe (Lyklema, 1993) that the electrokinetic potential, or zeta-potential  $\zeta$ , is an adequate substitute, although this is still being debated. The electrokinetic potential is that at the plane of shear, between a particle and a fluid, when there is relative motion between them (Hunter, 1981; Lyklema, 1993). The well-known technique of particle electrophoresis, which will be discussed in details in Chapter 6, is the most common method for determining zeta-potentials.

The three major influences on the *EDL* interaction between two charged surfaces are the magnitude of the effective surface potential (generally assumed to be  $\zeta$ ), the geometric configurations of the two surfaces, and the extent of the diffuse layer. The extent of the diffuse layer (or the *EDL* thickness) that governs the range of the interaction can be quantified by the Debye-Hückel reciprocal length parameter. The Debye-Hückel parameter,  $\kappa$ , is defined as (Hunter, 1981)

$$\kappa = \left( \frac{e^2 \sum n_{i_0} z_i^2}{\epsilon_0 \epsilon_r kT} \right)^{1/2} \quad (3.20)$$

where  $e$  is the elementary charge ( $e = 1.602 \times 10^{-19} \text{ C}$ ),  $n_{i_0}$  is the bulk number concentration of type- $i$  ions,  $z_i$  is the valence of type- $i$  ions,  $\epsilon_0$  is the permittivity of vacuum ( $\epsilon_0 = 8.854 \times 10^{-12} \text{ C V}^{-1} \text{ m}^{-1}$ ),  $\epsilon_r$  is the dielectric constant or relative permittivity of the solution (for water  $\epsilon_r \approx 80$  at the room temperature  $T = 295.15 \text{ K}$ ),  $k$  is the Boltzmann constant ( $k = 1.381 \times 10^{-23} \text{ J K}^{-1}$ ), and  $T$  is the absolute temperature. Equation (3.20) shows that the *EDL* thickness,  $\kappa^{-1}$ , mainly depends on the aqueous

solution properties (e.g., the valence of ions,  $z_i$ , concentration,  $n_{i,o}$ , and the dielectric constant,  $\epsilon_r$ ) and as well, the temperature  $T$ .

Before calculating the *EDL* interaction between two charged surfaces, one has to know the electrostatic potential distributions within the aqueous solution inside the geometric configurations of the two surfaces. According to the Gouy-Chapman theory (Hunter, 1981), the potential distribution at any point in the system is governed by the Poisson-Boltzmann (P-B) equation

$$\nabla^2 \varphi = \frac{2n_o z e}{\epsilon_o \epsilon_r} \sinh\left(\frac{z e \varphi}{kT}\right) \quad (3.21)$$

where  $\nabla^2$  is the Laplacian operator and  $\varphi$  is the local potential. At this point, it should be pointed out that equation (3.21) is the simplified P-B equation for the case where the electrolyte solution is symmetric, i.e., in the bulk solution, the cations and anions have the same valence, which, mathematically is expressed as  $n_{-o} = n_{+o} = n_o$  and  $z_- = z_+ = z$  (here  $n_o$  is the ion number concentration of the bulk solution and  $z$  is the valence of ions and counterions). Owing to the Gouy-Chapman model (Hunter, 1981), it turns out that this symmetric treatment is applicable to most electrolytes.

By invoking the Debye-Hückel approximation for a case of low potentials (i.e.,  $\sinh\left(\frac{z e \varphi}{kT}\right) \approx \frac{z e \varphi}{kT}$ ) to linearize the P-B equation (3.21), Hogg, Healy, and Fuerstenau (1966) obtained an analytical solution to the linearized P-B equation (3.21) with constant potential boundary conditions for two parallel plates. They then formulated the potential energy of interaction,  $\phi(h)$ , between two flat double layers with a separation distance,  $h$ ,

$$\phi(h) = \frac{\epsilon_r \epsilon_o \kappa}{2} \left[ (\zeta_1^2 + \zeta_2^2) \left( 1 - \frac{\cosh(2\kappa h)}{\sinh(2\kappa h)} \right) + 2 \zeta_1 \zeta_2 \frac{1}{\cosh(2\kappa h)} \right] \quad (3.22)$$

where  $\zeta_1$  and  $\zeta_2$  are the zeta-potential of two flat plates, respectively. The interaction energy formulated here is defined as a change in free energy of the *EDL* system when two charged surface elements are brought from infinity to a specific separation distance,

$h$ . (Overbeek, 1990). Thermodynamically, since both temperature and pressure remain unchanged, such free energy is the generalized Gibbs free energy. Conventional concept of the Gibbs free energy, defined for a simple homogenous thermodynamic system, can not be applied here, because the system includes an electrostatic field. A more general discussion regarding the thermodynamics of the *EDL* was given by Sanfeld (1968), Overbeek (1990), and Hall (1991).

In addition to interactions between two flat plates, Hogg et al. (1966) calculated the *EDL* interaction potential of two spheres, of radii  $a_1$  and  $a_2$ , using the Derjaguin approach,

$$V_{EDL} = \frac{2\pi a_1 a_2}{a_1 + a_2} \int_0^\infty \phi(h) dh \quad (3.23)$$

where the *EDL* interaction between two spheres was assumed to be made up of contributions from infinitesimally small parallel rings, each of which was considered as a flat plate. When the expression for  $\phi(h)$ , given by equation (3.22), was substituted into equation (3.23), the integral was evaluated analytically as

$$V_{EDL} = \frac{2\pi \varepsilon_r \varepsilon_0 a_1 a_2 \zeta_1 \zeta_2}{(a_1 + a_2)} \left\{ \ln \left[ \frac{1 + \exp(-\kappa h)}{1 - \exp(-\kappa h)} \right] + \frac{(\zeta_1^2 + \zeta_2^2)}{2\zeta_1 \zeta_2} \ln[1 - \exp(-2\kappa h)] \right\} \quad (3.24)$$

where  $\zeta_1$  and  $\zeta_2$  are the zeta-potentials of the two spheres and  $h$  is the gap width between the spheres.

With equation (3.24), it is straightforward to derive the *EDL* interaction potential between a sphere and a flat plate by letting one sphere's radius be  $a_1 = a_p$  and the other's be infinite ( $a_2 \rightarrow \infty$ ):

$$V_{EDL} = 2\pi \varepsilon_r \varepsilon_0 a_p \zeta_p \zeta_c \left\{ \ln \left[ \frac{1 + \exp(-\kappa h)}{1 - \exp(-\kappa h)} \right] + \frac{(\zeta_p^2 + \zeta_c^2)}{2\zeta_p \zeta_c} \ln[1 - \exp(-2\kappa h)] \right\} \quad (3.25)$$

where  $\zeta_p$  and  $\zeta_c$  are the zeta-potentials of the sphere and the flat plate, respectively, and  $h$  is the separation distance between the sphere and the flat plate.

Acknowledging the relation between the interaction potential and the force given by equation (3.13), the *EDL* interaction force between a sphere and a flat plate therefore can be evaluated as

$$F_{EDL} = 4\pi \varepsilon_r \varepsilon_0 \kappa a_p \zeta_p \zeta_c \left[ \frac{\exp(-\kappa h)}{1 + \exp(-\kappa h)} - \frac{(\zeta_p - \zeta_c)^2 \exp(-2\kappa h)}{2\zeta_p \zeta_c (1 - \exp(-2\kappa h))} \right] \quad (3.26)$$

Equation (3.25) or equation (3.26) is usually called the *HHF* formula or approximation (following the names of Hogg, Healy, and Fuerstenau). Because of their simplicity, *HHF* formulae have been widely used in the literature to quantify the *EDL* interaction between a sphere and a flat plate. However, as suggested by Hogg et al. (1966), proper application of *HHF* formula is restricted to low values of zeta-potentials and a large value of  $\tau = \kappa a_p$ , since the Debye-Hückel linear approximation was used to solve the Poisson-Boltzmann (P-B) equation and the Derjaguin model was implemented to calculate interaction. The validity of the Debye-Hückel linear approximation, i.e.,

$$\sinh\left(\frac{ze\varphi}{kT}\right) \approx \frac{ze\varphi}{kT}, \text{ requires that } \left| \frac{ze\varphi}{kT} \right| \ll 1, \text{ which can be converted to values of } \zeta_p$$

and  $\zeta_c$  less than 25 mV. The second condition, i.e.,  $\tau = \kappa a_p \gg 1$ , enables that the Derjaguin integration model (expressed by equation (3.23)) can be used to calculate the *EDL* interaction between curved surfaces, such as sphere-sphere and sphere-wall interactions, on the basis of that between two flat surface elements. It has been shown by Verwey and Overbeek (1948) that the Derjaguin method gives a very good approximation provided the *EDL* thickness is small compared to the particle radius, i.e., for  $\tau = \kappa a_p > 10$ . Recently, numerical solutions of the complete non-linear Poisson-Boltzmann equation show that the *HHF* approximation is quite accurate even when  $\zeta_p$  and  $\zeta_c$  are up to 60 mV and  $\tau$  is as low as 5. A detailed discussion on the validity of the *HHF* expression was given by Chan and White (1980), Overbeek (1988), Carnie et al. (1994), and Warszynski and Adamczyk (1997).

In the literature, no general agreement exists on a quantitative description of the *EDL* interaction in dynamic attachment processes. The uncertainties originate from the choice of appropriate boundary conditions for the solution of the Poisson-Boltzmann equation. Specifically, there is not enough convincing experimental evidence regarding whether the interacting surfaces maintain a constant potential or a constant charge density for colloidal particles during the deposition process. As yet calculations of the *EDL* interaction in the literature are still exclusively made on the basis of two extreme cases: either constant potential or constant charge. Extensive discussions on this issue can be found elsewhere (Rajagopalan and Kim, 1981; Adamczyk et al., 1983; and Gregory, 1989). The reason the constant potential *HHF* approximation, which has a sound thermodynamics basis, is incorporated in the present model is solely due to its simplicity. From a physical point of view, the constant potential interaction is expected to be relevant to many real situations with large exchange of electrical current (or ions) taking place in a very short time (compared with Brownian particle collision time). It seems that further justification, specifically from an experimental point of view, is needed to clarify this issue.

In addition, it is noted that since the Boltzmann distribution is used to solve electric potential profiles, the *EDL* interaction model presented is, therefore, valid only within the framework of equilibrium thermodynamics. Strictly speaking, this is not the case for particle deposition or bubble attachment where the colloidal interactions essentially are of dynamic nature. In principle, as was pointed out by Warszynski and van de Ven (1990, 1991), the distributions of ions is described by the general convective diffusion equation (i.e., a combination of equations (3.2) and (3.3)). Thus, the interaction between a charged moving sphere and a charged stationary flat plate in a hydrodynamic situation becomes a complex coupled problem governed simultaneously by the Poisson equation, the general convective diffusion equation, and the equation of motion. As a result, on the one hand, the *EDL* interaction has to be reformulated to account for the combined hydrodynamic and electrokinetic interactions. The effect of hydrodynamic flow on the *EDL* interaction can be characterized using the Peclet number, physically representing the relative importance of the convection to diffusion. It is defined as

$Pe = u\kappa^{-1}/D$ , where  $u$  is the ion velocity,  $\kappa^{-1}$  is the *EDL* thickness that normally may be taken as 10 nm, and  $D$  is ion diffusion coefficient. In the impinging jet system, the appropriate ion velocity is of the order of  $\alpha(\kappa^{-1})^2$ . Assuming a reasonable value of  $\alpha = 1.0 \times 10^7 s^{-1} m^{-1}$  (Dabros and van de Ven, 1983) and  $D = 1.0 \times 10^{-10} m^2 s^{-1}$  (van de Ven, 1989),  $Pe$  is estimated to be of the order  $10^{-7}$ . This suggests that under the present situation, the perturbation of Boltzmann distribution, due to the presence of the hydrodynamic flow, is so small that the hydrodynamic convection effect on the *EDL* interaction is negligible. On the other hand, the hydrodynamic interactions, or more accurately,  $f_1(z)$ ,  $f_2(z)$ ,  $f_3(z)$  and  $f_4(z)$ , require modification; this is referred to as the electroviscous effects. Analyses made by Warszynski and van de Ven (1990, 1991) show that the particle mobility in the vicinity of the wall is a complex function of particle size, Debye length, zeta potential, etc. Specifically, for the gas bubbles where  $\kappa a_b$  is very large (at least several hundred), it is expected that the electroviscous effect is very weak (less than 2%). Only the electroviscous correction to  $f_1(z)$  was provided. No modification accounting for electroviscous effects for the functions  $f_2(z)$ ,  $f_3(z)$  and  $f_4(z)$  are available in the literature. Nevertheless, for simplicity, all these dynamic-related coupling effects are neglected.

Again, using the same nondimensionalizing approach as for van der Waals interaction, the nondimensional form of the *EDL* interaction potential can be expressed as

$$\bar{V}_{EDL} = \frac{V_{EDL}}{kT} = \frac{Dl}{2} \left\{ \ln \left[ \frac{1 + \exp(-\tau \bar{h})}{1 - \exp(-\tau \bar{h})} \right] + (Da + 1) \ln [1 - \exp(-2\tau \bar{h})] \right\} \quad (3.27)$$

and the nondimensional form of the *EDL* interaction force is

$$\bar{F}_{EDL} = \frac{F_{EDL}}{kT/a_p} = Dl \tau \left[ \frac{\exp(-\tau \bar{h})}{1 + \exp(-\tau \bar{h})} - Da \frac{\exp(-2\tau \bar{h})}{1 - \exp(-2\tau \bar{h})} \right] \quad (3.28)$$

where the dimensionless groups shown in these equations are defined as

$$Dl = \frac{4\pi \epsilon_o \epsilon_r a_p \zeta_c \zeta_p}{kT} \quad (3.29a)$$



$$\tau = \kappa a_p \quad (3.29b)$$

$$Da = \frac{(\zeta_c - \zeta_p)^2}{2\zeta_c \zeta_p} \quad (3.29c)$$

$DI$  is the dimensionless double layer parameter characterizing the strength of the *EDL* interaction;  $Da$  is the double layer asymmetry parameter representing the portion of the *EDL* interaction arising from the difference in  $\zeta$ -potential of the spherical particle and that of the flat collector surface;  $\tau$  is the ratio of the particle radius,  $a_p$ , to the *EDL* thickness,  $\kappa^{-1}$ , and is also called the dimensionless ionic strength since, as shown in equation (3.20), it is largely dependent upon the solution properties such as the ion number concentration, the valence of ions, and the dielectric constant of the solution.

### 3.8 Bubble Transport Equation

Once the bubble velocity (equation (3.6)), the bubble mass diffusion coefficient (equations (3.8) and (3.9)), and the total forces acting on a bubble (equations (3.12), (3.16) and (3.28)) are known, the bubble mass flux, given by the Fokker-Planck equation (3.3), can be expressed in an explicit form

$$j_r = \alpha r z f_3 n - D_\infty f_4 \frac{\partial n}{\partial r} + \frac{D_\infty f_4}{kT} F_r n \quad (3.30a)$$

$$j_z = -\alpha z^2 f_1 f_2 n - D_\infty f_1 \frac{\partial n}{\partial z} + \frac{D_\infty f_1}{kT} F_z n \quad (3.30b)$$

where  $F_r$  and  $F_z$  are the force components (including gravity force and colloidal forces discussed in Sections 3.8 and 3.9) along the directions of the cylindrical coordinates  $r$  and  $z$ , respectively.

Because of experimental conditions, the radial diffusion of bubbles in the stagnation point region can be neglected, and hence  $\frac{\partial n}{\partial r} = 0$ . If assuming zero radial components for the colloidal and external forces, i.e.,  $F_r = 0$ , the above equations are nondimensionalized to

$$\bar{j}_r = \frac{1}{2} f_3 Pe \bar{n} \bar{r} \bar{z} \quad (3.31a)$$

$$\bar{j}_z = -\frac{1}{2} f_1 f_2 Pe \bar{n} \bar{z}^2 - f_1 \frac{d\bar{n}}{d\bar{z}} + f_1 \bar{F}_z \bar{n} \quad (3.31b)$$

where  $\bar{j}_i$  is the dimensionless bubble mass flux ( $\bar{j}_i = \frac{a_p j_i}{D_\infty n_\infty}$  ( $i=r, z$ )),  $\bar{r}$  and  $\bar{z}$  are the nondimensional coordinates ( $\bar{r} = \frac{r}{a_p}$ ,  $\bar{z} = \frac{z}{a_p}$ ),  $\bar{n}$  is the dimensionless bubble number concentration ( $\bar{n} = \frac{n}{n_\infty}$ , where  $n_\infty$  is the number concentration of bubble in the bulk phase),  $Pe$  is the Peclet number representing the ratio of convection to diffusion in mass transfer ( $Pe = \frac{2\alpha a_p^3}{D_\infty}$ ), and  $\bar{F}_z$  denotes the dimensionless normal component of the forces acting on a bubble ( $\bar{F}_z = \frac{F_z}{kT/a_p}$ ).

Recalling all forces acting on a bubble have been defined in equations (3.12), (3.16) and (3.28), the net axial force  $\bar{F}_z$ , therefore, can be explicitly formulated as

$$\begin{aligned} \bar{F}_z &= \bar{F}_G + \bar{F}_{VDW} + \bar{F}_{EDL} \\ &= -Gr - Ad \frac{\bar{\lambda} (\bar{\lambda} + 22.232\bar{h})}{\bar{h}^2 (\bar{\lambda} + 11.116\bar{h})^2} + Dl \tau \left[ \frac{\exp(-\tau\bar{h})}{1 + \exp(-\tau\bar{h})} - Da \frac{\exp(-2\tau\bar{h})}{1 - \exp(-2\tau\bar{h})} \right] \end{aligned} \quad (3.32)$$

Finally, it is possible to rewrite the mass conservation equation (3.2) by substituting in equations (3.31a) and (3.31b)

$$(1 + \bar{h}) Pe f_3(\bar{h}) \bar{n} = \frac{d}{d\bar{h}} \left\{ f_1(\bar{h}) \left[ \frac{d\bar{n}}{d\bar{h}} + \frac{1}{2} (1 + \bar{h})^2 Pe f_2(\bar{h}) \bar{n} - \bar{F}_z(\bar{h}) \bar{n} \right] \right\} \quad (3.33)$$

where  $\bar{h} = \frac{z - a_p}{a_p}$  is the dimensionless separation between a bubble and the collector surface.

### 3.9 Boundary Conditions

Equation (3.33) is subject to the following boundary conditions:

$$\bar{n} = 1 \quad \text{as } \bar{h} \rightarrow \infty \quad (3.34a)$$

$$\bar{n} = 0 \quad \text{at } \bar{h}_o = \bar{\delta} = \frac{\delta}{a_p} \quad (3.34b)$$

The first condition given by equation (3.34a) is obvious; it denotes that as the separation distance  $\bar{h}$  is far away from the collector surface, the bubble number concentration,  $n$ , should be equal to  $n_\infty$  in the bulk phase. The second condition, referred to as “perfect sink” approximation, has been extensively used to model particle deposition (Prieve and Ruckenstein, 1974; Spielman, 1977; Adamczyk et al., 1983; Elimelech, 1991). The hypothetical situation described by this condition states that all particles are irreversibly captured by the collector surface once they have reached a certain separation distance  $\bar{\delta}$ , which is usually taken as the location of the primary energy minimum (*PEM*). The location of the *PEM* is typically at about 1.0 - 5.0 *nm* from the collector surface, and it is often deeper than 20 *kT* due to attractive colloidal forces such as van der Waals interactions. In analogy to particle deposition analysis, bubble attachment is considered to occur when a bubble could arrive at such an interception distance  $\bar{\delta}$ . As such, the present model essentially deals with bubble transport under the influences of gravity and hydrodynamic forces as well as colloidal surface forces from the bulk phase to a separation distance  $\bar{\delta}$ , beyond which the process involves many complex phenomena which may be difficult to define.

Obviously, one is unlikely to find analytical solutions to equation (3.33) due to its mathematical complexity. In practice, equation (3.33), together with boundary conditions (3.34a) and (3.34b), are solved numerically. The numerical procedures will be discussed in the next chapter.

### 3.10 Validity of Application of the Mass Transport Equation to Fine Gas Bubbles

In principle, the mass transport equation (i.e., equation (3.33)) derived in the previous section is quite general, and is applicable to describing deposition of colloidal particles (e.g., solid particles, oil droplets) onto a solid surface in the impinging jet system. To explore its applicability to fine bubbles, the following additional conditions must be satisfied.

#### (i) Bubble has to retain a spherical shape

The assumption of spherical bubbles is implemented throughout the entire model development in this chapter. It has been well recognized that the bubble shape may be deformed due to either fluid inertia or viscous forces which act on the bubble. When the viscous force is dominant, the deformation of the bubble shape can be best characterized by the capillary number,  $Ca = \frac{\mu_f U_p}{\gamma_{lv}}$ , which physically represents the ratio of the viscous force to the interfacial tension force (here  $U_p$  is the relative bubble-fluid velocity, and  $\gamma_{lv}$  is the interfacial tension which is taken as  $72.7 \text{ mJ m}^{-2}$  for completely mobile air-water interface at  $20^\circ \text{C}$ ). In the impinging jet system, the appropriate relative bubble-fluid velocity is of order  $\alpha a_p^2$ . Taking the upper bound of the laminar flow intensity  $\alpha$  to be of order  $1.0 \times 10^7 \text{ s}^{-1} \text{ m}^{-1}$  (equation (3.7)), one can readily calculate the capillary number to be of order  $Ca = 0.01$  for a bubble of radius  $a_p = 50 \mu\text{m}$ . On the other hand, when the inertia effect is significant, the bubble deformation is controlled by the Weber number,  $Wb = \frac{\rho_f U_p^2 a_p}{\gamma_{lv}}$ , which measures the ratio of the inertia force to the interfacial tension force. In a similar manner, the Weber number can be estimated to be of order  $Wb = 1.0 \times 10^{-4}$ . Therefore, one can conclude that both viscous and inertia forces are small compared to interfacial forces, and therefore the bubbles should always remain nearly spherical and undeformed in the present conditions.

**(ii) The hydrodynamic boundary layer should be thicker than the bubble diffusion boundary layer**

The derivation of the mass transport equation is based on prespecified hydrodynamic conditions. It can be shown (see Appendix A.2) that for an axisymmetric stagnation-point flow, the laminar hydrodynamic boundary-layer thickness,  $\delta_v$ , is approximately given by (Yang, et al., 1999a)

$$\delta_v = 4.8R Re^{-0.5} \quad (3.35)$$

where  $R$  is the radius of the capillary and  $Re$  is the impinging jet flow Reynolds number, defined as  $Re = \rho_f V R / \mu_f$  ( $V$  is the mean fluid velocity in the capillary). Equation (3.35) shows that, given a  $Re$ , the hydrodynamic boundary layer is constant; this is an important feature of the impinging jet flow. Depending on the Reynolds number, the hydrodynamic boundary-layer thickness typically varies between a few hundred microns to millimeters. For example, when the Reynolds number varies from 100 to 1000, the corresponding hydrodynamic boundary thickness falls from 640 to 200  $\mu m$ . On the other hand, it is difficult to quantitatively estimate the thickness of the bubble diffusion boundary layer, since the bubble concentration profile is quite complex in the vicinity of the wall due to hydrodynamic and colloidal interactions (Yang et al., 1998c). Simple geometrical interpretation of the diffusion boundary layer does not hold anymore. Nevertheless, as suggested by Adamczyk (1989), for micron-sized particles, the diffusion boundary layer thickness is of order 1 to 10  $\mu m$  for moderate flow rates, which is very thin compared to the hydrodynamic boundary-layer thickness. In particular, for the case considered here, because of the large value of the Schmidt number for gas bubbles in aqueous solutions ( $Sc = \mu_f / \rho_f D_\infty$ ), the bubble diffusion boundary layer should be even thinner. Thus, the condition that the hydrodynamic boundary layer is much thicker than the bubble diffusion boundary layer is fulfilled.

**(iii) The Stokes law can be applied to the bubble motion**

In section 3.3, the Stokes law conditions are applied to the bubble motion. Two assumptions are implicitly made in the application of the Stokes law: First, the Reynolds

number based on the gas bubble should be small, i.e.,  $Re_p = \rho_f U_p a_p / \mu_f < 1$ . Following the same approach used to estimate the capillary number and the Weber number, the typical bubble Reynolds number can be calculated to be of order  $Re_p = 0.1$  (here, the bubble radius is chosen to be  $50 \mu m$ ). Secondly, the no-slip boundary condition must be satisfied at the bubble surface. This condition opens the old “Pandora Box” regarding a bubble’s motion in a liquid, namely, whether the Rybczynski-Hadamard formula or the Stokes drag formula is confirmed by experiments (Levich, 1962). This subject has attracted the attention of scientists for decades (Griffith, 1962; Leal, 1992; Graciaa, et al., 1995). According to Leal (1992), with diameters over  $1 mm$ , fine bubbles in purified water obey the Rybczynski-Hadamard formula, suggesting no tangential stress acting on the bubble surface. It is not clear what the transition criterion is with respect to the bubble size, below which bubbles will follow the Stokes drag formula. Nonetheless, based on all evidences provided in the literature (Levich, 1962; Leal, 1992; Nguyen, 1998), there is no doubt that small bubbles below  $100 \mu m$  in diameter, as created in the impinging jet system, can certainly be treated as rigid spheres, i.e., objects satisfying no-slip boundary conditions.

**(iv) Choice of the separation distance  $\bar{\delta}$  should be physically meaningful and be shorter than the critical rupture thickness of thin liquid film as well**

This condition is associated with the “perfect sink” boundary condition, i.e., equation (3.34b). Physically, the boundary condition means that once a bubble has arrived at such separation distance, the bubble will no longer be part of the solution. In other words, the bubble is irreversibly captured by the collector surface and permanent attachment is achieved. Therefore, to make the “perfect sink” boundary condition valid, the separation distance  $\bar{h}_o = \bar{\delta}$  specified in equation (3.34b) usually should be chosen around the location of the primary energy minimum (*PEM*) where attractive interactions are present. In this study, computations were performed to estimate the influence of the separation distance  $\bar{\delta}$  on the attachment results. It was found that the results are insensitive to the choice of  $\bar{\delta}$  when  $\bar{\delta}$  is less than 0.001. Therefore, in the numerical

calculations,  $\bar{\delta}$  was chosen to be 0.0005. For a bubble radius of 10  $\mu m$ , this  $\bar{\delta}$  value corresponds to 5  $nm$ , which falls within the proximity of the primary energy minimum well in most situations.

On the other hand, it is well-known that the bubble attachment process is related to the drainage of the thin liquid film between the bubble and the collector surface. If the thin liquid film is unstable due to attractive forces and/or both buoyancy and hydrodynamic forces exerted on the bubble by the fluid flow, the thin liquid film will keep thinning until the film thickness reaches the so-called critical rupture thickness. Once the film breaks, a three-phase contact line is created. When radial hydrodynamic forces are not very strong, tangential forces caused by interfacial tension between gas bubble and liquid and physical or chemical heterogeneity of the surface such as surface roughness will render the bubbles immobile. In the literature, the value of the critical rupture thickness is reported in the range of 30 – 200  $nm$ , depending on the surface characteristics of the solid surface and the aqueous solution. Obviously such critical rupture thickness is much larger than the separation distance  $\bar{\delta}$  chosen in equation (3.34b).

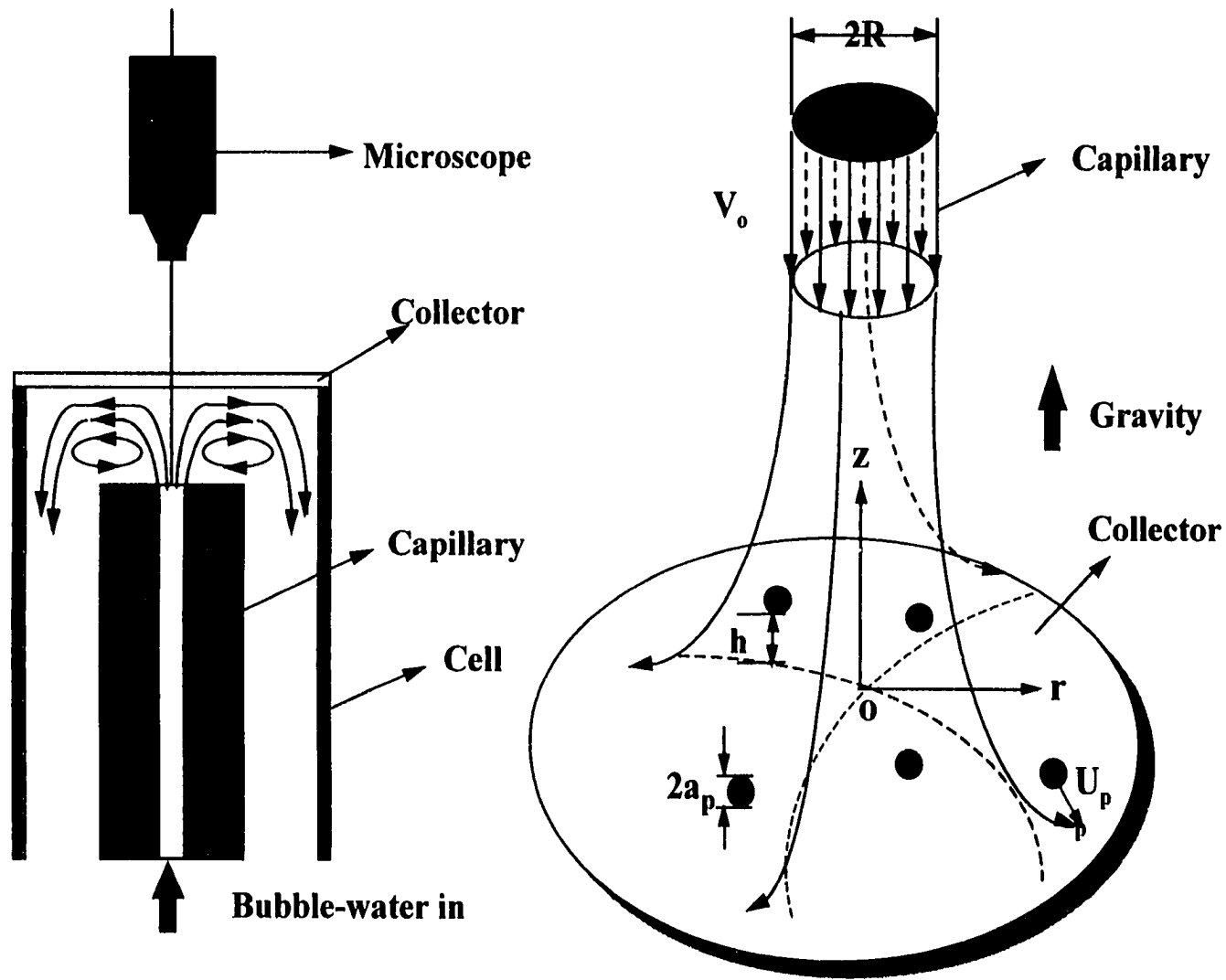


**Figure 3.1** Diagram illustrating the basic features of the impinging jet system



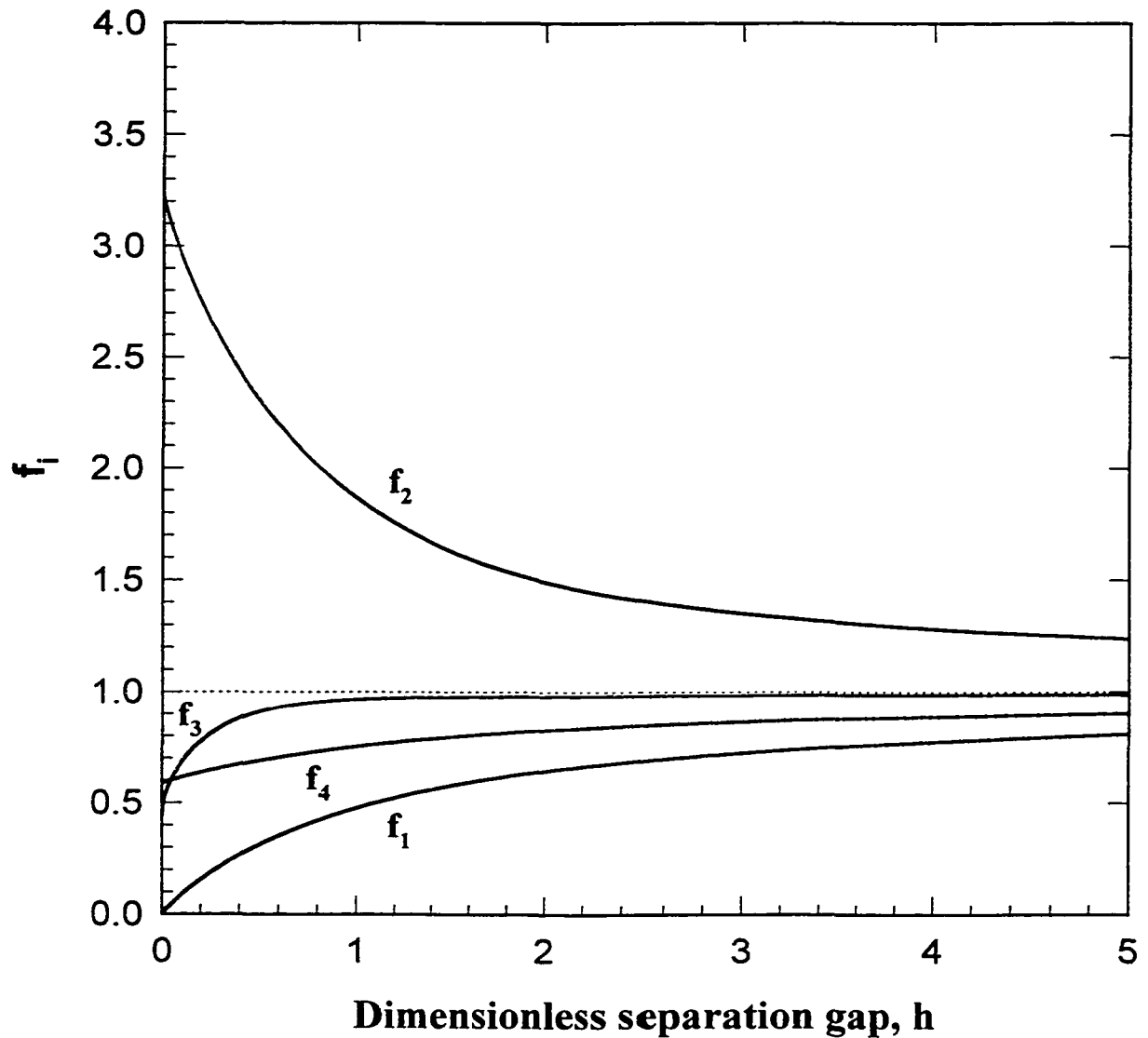


**Figure 3.2** Universal hydrodynamic correction coefficients for a spherical particle diffusion and motion near a plane

# CHAPTER 4

## THEORETICAL RESULTS FOR BUBBLE ATTACHMENT

### 4.1 Introduction

In Chapter 3, the transport of fine bubbles from the flowing jet onto a solid surface in the impinging jet region was modeled. Examination of the bubble transport equation reveals that the bubble concentration distribution or the bubble mass transfer is dependent upon hydrodynamic convection measured by  $Pe$ , gravity force represented by  $Gr$ , and colloidal interaction forces characterized by  $Ad$ ,  $\bar{\lambda}$ ,  $DI$ ,  $Da$ , and  $\tau$ . In this chapter, analytical solutions of the bubble transport equation under limiting conditions will first be presented. A numerical method for solving the bubble transport equation is then described. To validate the numerical model, a comparison is made between the theoretical predictions obtained using the numerical model and experimental results reported in the literature. A parametric study is then conducted to examine the effect of dimensionless groups, including  $Pe$ ,  $Gr$ ,  $Ad$ ,  $DI$ ,  $Da$ , and  $\tau$ , on the bubble attachment rate,  $Sh$ , and the results are presented. In addition, it is shown that the models derived for the impinging jet system can be used to evaluate transport of fine bubbles onto a large particle surface (Yang et al., 1999a).

### 4.2 Limiting Analytical Solutions to Mass Transfer Equation

Under circumstances where certain assumptions are made, limiting analytical solutions of the bubble transport equation, equation (3.33), can be found. Such solutions can provide valuable insights into the bubble attachment process and may be used as a criterion for examining the numerical solution as well.

It was shown in Chapter 3 that the transport of fine bubbles from the impinging jet flow onto a solid surface can be described by

$$(1 + \bar{h}) Pe f_3(\bar{h}) \bar{n} = \frac{d}{d\bar{h}} \left\{ f_1(\bar{h}) \left[ \frac{d\bar{n}}{d\bar{h}} + \frac{1}{2} (1 + \bar{h})^2 Pe f_2(\bar{h}) \bar{n} - \bar{F}_z(\bar{h}) \bar{n} \right] \right\} \quad (4.1)$$

where  $\bar{h} = \frac{z - a_p}{a_p}$  is the dimensionless separation between the bubble and the collector surface. Equation (4.1) is subject to the following boundary conditions

$$\bar{n} = 1 \quad \text{as } \bar{h} \rightarrow \infty \quad (4.2a)$$

$$\bar{n} = 0 \quad \text{at } \bar{h}_o = \bar{\delta} = \frac{\delta}{a_p} \quad (4.2b)$$

**Case I: Fine bubbles rising in a quiescent fluid**

Since there is no flow, the Peclet number is zero, i.e.,  $Pe = 0$ . Equation (4.1) can therefore be simplified to

$$\frac{d}{d\bar{h}} \left\{ f_1(\bar{h}) \left[ \frac{d\bar{n}}{d\bar{h}} - \bar{F}_z(\bar{h})\bar{n} \right] \right\} = 0 \quad (4.3)$$

where  $\bar{F}_z$ , the net axial forces acting on a bubble, is defined in equation (3.32).

Integrating equation (4.3) once gives

$$f_1(\bar{h}) \left[ \frac{d\bar{n}}{d\bar{h}} - \bar{F}_z(\bar{h})\bar{n} \right] = C_1 \quad (4.4)$$

The integration constant  $C_1$  is easily determined from the condition that when  $\bar{h} \rightarrow \infty$ ,  $\bar{n} = 1$ ,  $\frac{d\bar{n}}{d\bar{h}} = 0$ ,  $f_1(\bar{h}) = 1$ , and  $\bar{F}_z = -Gr$ . Thus, it can be seen that  $C_1 = Gr$ .

Realizing that the Sherwood number  $Sh$  (characterizing nondimensional mass transfer flux) is defined as

$$Sh = f_1(\bar{\delta}) \frac{d\bar{n}}{d\bar{h}} \Big|_{\bar{h}_o = \bar{\delta}} \quad (4.5)$$

substitution of equations (4.2b) and (4.5) into equation (4.4) yields

$$Sh = Gr \quad (4.6)$$

This equation is referred to as the Stokes law. It suggests that in this case, the bubble flux is independent of the colloidal surface forces, and is determined only by gravity.

**Case II:** In the absence of energy barrier (defined as the maximum of the bubble - collector interaction energy), transport of fine bubbles in the diffusion controlled regime

In this case, it can be assumed that neither hydrodynamic interactions nor colloidal surface interactions are involved, i.e.,  $f_1(\bar{h}) = f_2(\bar{h}) = f_3(\bar{h}) = 1$  and  $\bar{F}_{VDW} = \bar{F}_{EDL} = 0$ . In practice, this corresponds to the situation where the hydrodynamic resistant interactions are counterbalanced by attractive colloidal interactions. With this assumption, equation (4.1) becomes

$$\frac{d^2 \bar{n}}{d\bar{h}^2} + \left[ \frac{1}{2}(1 + \bar{h})^2 Pe + Gr \right] \frac{d\bar{n}}{d\bar{h}} = 0 \quad (4.7)$$

Integrating equation (4.7) once gives

$$\frac{d\bar{n}}{d\bar{h}} = C_2 \exp \left[ -\frac{1}{6}(1 + \bar{h})^3 Pe - Gr \bar{h} \right] \quad (4.8)$$

Integrating equation (4.8) again and making use of the boundary conditions, equations (4.2a) and (4.2b), one obtains

$$\bar{n} = \frac{\int_{\bar{\delta}}^{\bar{h}} \left\{ \exp \left[ -\frac{1}{6}(1 + \bar{h})^3 Pe - Gr \bar{h} \right] \right\} d\bar{h}}{\int_{\bar{\delta}}^{\infty} \left\{ \exp \left[ -\frac{1}{6}(1 + \bar{h})^3 Pe - Gr \bar{h} \right] \right\} d\bar{h}} \quad (4.9)$$

From this, the Sherwood number,  $Sh$ , can be calculated as

$$Sh = \frac{d\bar{n}}{d\bar{h}} \Big|_{\bar{h}=\bar{\delta}} = \frac{\exp \left[ -\frac{1}{6}(1 + \bar{\delta})^3 Pe - Gr \bar{\delta} \right]}{\int_{\bar{\delta}}^{\infty} \left\{ \exp \left[ -\frac{1}{6}(1 + \bar{h})^3 Pe - Gr \bar{h} \right] \right\} d\bar{h}} \quad (4.10)$$

Introducing a new variable,  $u$ , defined as

$$u = (1 + \bar{h}) \left( \frac{Pe}{6} \right)^{1/3} \quad (4.11)$$

and assuming that  $Gr = 0$ , equation (4.10) is rewritten as

$$Sh = \frac{\left(\frac{Pe}{6}\right)^{1/3} \exp\left[-\frac{1}{6}(1+\bar{\delta})^3 Pe\right]}{\int_{(1+\bar{\delta})(Pe/6)^{1/3}}^{\infty} \exp(-u^3) du} \quad (4.12)$$

Noting that  $\bar{\delta} \ll 1$  and, for diffusion-controlled regime,  $Pe \ll 1$ , the above equation can be further simplified to

$$Sh = \frac{\left(\frac{Pe}{6}\right)^{1/3}}{\Gamma\left(\frac{4}{3}\right)} \approx 0.616 Pe^{1/3} \quad (4.13)$$

where  $\Gamma$  is the gamma function. It follows that under the condition of diffusion-dominated regime, in the absence of energy barriers and force fields, the bubble transport is governed by the well-known Levich formula, expressed by equation (4.13) (Levich, 1962).

### Case III: Geometric interception limit in external force dominated regime

In this situation, since both the Peclet number  $Pe$  and the gravity number  $Gr$  are very large for gas bubbles, bubble attachment rate (flux) is essentially determined by the bubble trajectories, which are deterministic. Using the Lagrangian approach, Spielman and Fitzpatrick (1973) developed a model to analyze the trajectories of non-Brownian particles near a rotating disc. They derived the following approximate formula from assuming large Peclet number, i.e.,  $Pe \gg 1$  and neglecting the diffusion term

( $f_1 \frac{d\bar{n}}{dH} \approx 0$ ) in the mass transfer equation (4.1):

$$\eta = \exp\left\{2 \int_{\bar{\delta}}^{\infty} \left[ \frac{1}{1+\bar{h}} - \frac{(1+\bar{h}) f_3(\bar{h})}{(1+\bar{h})^2 f_1(\bar{h}) f_2(\bar{h}) - \frac{2 f_1(\bar{h}) \bar{F}_z(\bar{h})}{Pe}} \right] d\bar{h} \right\} \quad (4.14)$$

where  $\eta$  is the particle capture efficiency. In this case, the capture efficiency in the Lagrangian approach can be related to the Sherwood number based on the Eulerian approach through the following relationship (Masliyah, 1994)

$$Sh = \frac{1}{2} Pe \eta \quad (4.15)$$

It has been demonstrated that mathematically, the mass transfer equation for colloidal particles in rotating disc has exactly the same form as that for bubbles in the impinging jet system (Dabros and Adamczyk, 1979; Yang, et al., 1998c; 1999a). Therefore, under the same conditions specified by Spielman and Fitzpatrick (1973), the mass transfer of fine bubbles in the impinging jet region can be expressed as

$$Sh = \frac{1}{2} Pe \exp \left\{ 2 \int_{\bar{\delta}}^{\infty} \left[ \frac{1}{1+\bar{h}} \frac{(1+\bar{h}) f_3(\bar{h})}{(1+\bar{h})^2 f_1(\bar{h}) f_2(\bar{h}) - \frac{2 f_1(\bar{h}) \bar{F}_z(\bar{h})}{Pe}} \right] d\bar{h} \right\} \quad (4.16)$$

By further assuming that there are no hydrodynamic and colloidal surface interactions, that is,  $f_1(\bar{h}) = f_2(\bar{h}) = f_3(\bar{h}) = 1$ ,  $\bar{F}_{VDW} = \bar{F}_{EDL} = 0$ , and  $\bar{F}_z = -Gr$ , one can show that equation (4.16) can be simplified to

$$Sh = \frac{1}{2} Pe \frac{(1+\bar{\delta})^2 + \frac{2Gr}{Pe}}{(1+\bar{\delta})^2} \quad (4.17)$$

Noting that  $\bar{\delta}$  is very small, i.e.,  $\bar{\delta} \ll 1$ , equation (4.17) becomes

$$Sh = \frac{1}{2} Pe + Gr \quad (4.18)$$

This equation is called the geometric interception, which indicates that if the Peclet number,  $Pe$ , is large and the colloidal interactions are weak or negligible, the bubble mass transfer is completely controlled by hydrodynamic convection and gravitational forces.

### 4.3 Numerical Method for Solving Bubble Transport Equation

The bubble mass transfer equation (4.1), with boundary conditions (4.2a) and (4.2b), form a two-point boundary value problem. Introducing the variable  $\bar{j}$  as the local dimensionless particle flux toward the collector surface, equation (4.1) can be decomposed into two first-order equations:

$$\frac{d\bar{n}}{d\bar{h}} = \frac{\bar{j}(\bar{h})}{f_1(\bar{h})} - \frac{1}{2} (1+\bar{h})^2 Pe f_2(\bar{h}) \bar{n} + \bar{F}_z(\bar{h}) \bar{n} \quad (4.19a)$$

$$\frac{d\bar{j}(\bar{h})}{d\bar{h}} = (1 + \bar{h}) Pe f_3(\bar{h}) \bar{n} \quad (4.19b)$$

For simplicity, the original problem is converted into an initial value problem by choosing a guess value for  $\bar{j}$  at  $\bar{h} = \bar{\delta}$  together with  $\bar{n} = 0$ . Noting that equations (4.19a) and (4.19b) are linear, one can relate a guess value for  $\bar{j}_o$  to the corresponding actual value of the bulk concentration by

$$\frac{(\bar{j}_o)_{act}}{(\bar{j}_o)_{guess}} = \frac{(\bar{n}_\infty)_{act}}{(\bar{n}_\infty)_{cal}} \quad (4.20)$$

In this method, the second boundary condition, where  $\bar{n}(\bar{\delta}) = 0$  and  $\bar{j}_o(\bar{\delta}) = f_1(\bar{\delta}) \frac{d\bar{n}}{dH} \Big|_{\bar{\delta}}$ , is satisfied by assigning a value  $(\bar{j}_o)_{guess}$  to  $\bar{j}_o$ , since its actual value  $(\bar{j}_o)_{act}$  is unknown. The numerical integration from the initial condition, where  $\bar{n}(\bar{\delta}) = 0$ , to an “infinite” distance  $\bar{h} = \bar{h}_\infty$  subsequently provides a calculated value for the particle bulk concentration at  $\bar{h} = \bar{h}_\infty$ , which is expressed as  $(\bar{n}_\infty)_{cal}$  in equation (4.19). This value may not be unity as required by the first boundary condition, equation (4.2a), where  $(\bar{n}_\infty)_{act} = 1$ . Hence, the only remaining unknown in equation (4.19) is  $(\bar{j}_o)_{act}$ , the actual value of the dimensionless mass flux at the collector surface.

Mathematically, the ordinary differential equations (4.18a) and (4.18b) are ‘stiff’ due to rapid changes of coefficients over small separation distances resulting from the presence of the colloidal interaction terms. Accordingly, conventional methods of numerical integration, such as Runge-Kutta, do not work well. To circumvent this difficulty, a numerical routine (competitive with the best Gear-type method) called Semi-Implicit Extrapolation method specifically developed for handling stiff problems (Numerical Recipe, 1986), is implemented to perform the numerical calculations. In addition, a specific transforming function is introduced in the numerical scheme to

transform the coordinate, the dimensionless separation distance  $\bar{h}$ , into a new variable  $\bar{\beta}$  through the following relationship

$$\bar{\beta} = \frac{\bar{h} - \bar{h}_o}{\bar{h} - \bar{h}_o + 1} \quad (4.21)$$

With this transformation, the computational domain reduces from  $[\bar{\delta}, \infty)$  to  $[0, 1]$ .

Dividing the new computational domain,  $[0, 1]$ , into  $N$  equal portions, one can obtain a fine uniform mesh size

$$\Delta \bar{\beta} = \frac{1}{N} \quad (4.22)$$

Accordingly, the corresponding nonuniform mesh size in the old physical domain,  $[\bar{\delta}, \infty)$ , is

$$\Delta \bar{h}_i = \frac{\Delta \bar{\beta}}{(1 - \bar{\beta}_i)(1 - \bar{\beta}_i - \Delta \bar{\beta})} = \frac{1}{(N - i)(N - i - 1)} = \frac{1}{N - i - 1} - \frac{1}{N - i} \quad (4.23)$$

where  $i = 1, 2, \dots, N$ . Clearly, equation (4.23) shows that  $\Delta \bar{h}_i$  starts at small steps, and gradually increases as  $i$  goes up. Hence, without need of any more computations, the transformation enables one to enhance calculation accuracy at the small separation distance and to slow down the change of the coefficients in the mass transport equation (i.e., to make the equation less stiff). Mathematically, the bubble transport equation (4.19) and its boundary conditions (3.34) can be transformed as follows:

$$\frac{d \bar{n}}{d \bar{\beta}} = \frac{1}{(1 - \bar{\beta})^2} \left[ \frac{\bar{j}(\bar{\beta})}{f_1(\bar{\beta})} - \frac{1}{2} (1 + \eta)^2 Pe f_2(\bar{\beta}) \bar{n} + \bar{F}_z(\bar{\beta}) \bar{n} \right] \quad (4.24a)$$

$$\frac{d \bar{j}(\bar{\beta})}{d \bar{h}} = \frac{1}{(1 - \bar{\beta})^2} (1 + \eta) Pe f_3(\bar{\beta}) \bar{n} \quad (4.24b)$$

$$n(\bar{\beta}) \Big|_{\bar{\beta}=0} = 0 \quad n(\bar{\beta}) \Big|_{\bar{\beta}=1} = 1 \quad (4.24c)$$

where  $\eta(\bar{\beta}) = \frac{\bar{\beta}}{1 - \bar{\beta}} + \bar{h}_o$ .

Computational tests are performed to estimate the influence of the lower and upper integration limits on the results. It is found that the results are insensitive to the



choice of the integration limits as long as  $\bar{h}_o \leq 5 \times 10^{-3}$  (for fine bubbles,  $\bar{h}_o \leq 10^{-3}$ ) and  $\bar{h}_\infty \geq 30$ . Here, “insensitivity” means that a doubling of the lower or upper integration limit causes a change in the calculated result of no more than 1%. In the numerical calculations, the lower and upper integration limits are normally taken to be  $\bar{h}_o = 10^{-3}$  (for fine bubbles  $\bar{h}_o = 5 \times 10^{-4}$ ) and  $\bar{h}_\infty = 50$ . It should be emphasized that since the Sherwood number,  $Sh$ , is defined at the separation distance  $\bar{h}_o = \bar{\delta}$ , it is expected that the upper integration limit,  $\bar{h}_\infty$ , will have little influence on  $Sh$ . Specifically, this is the case for fine bubble attachment where  $Pe$  is high.

Once knowing the bubble concentrations  $\bar{n}(\bar{h})$ , the bubble attachment flux is given by

$$j_o = -D(\delta) \left( \frac{d\bar{n}}{d\bar{z}} \right)_\delta = -\frac{f_1(\bar{\delta}) D_\infty n_\infty}{a_p} \left( \frac{d\bar{n}}{d\bar{h}} \right)_{\bar{\delta}} \quad (4.25)$$

Here, the negative sign means that the bubble mass flux is towards the collector surface.

The non-dimensional bubble flux, as quantified by the Sherwood number, can be expressed by the reduced non-dimensional particle concentration gradient at  $\bar{\delta}$

$$Sh = \frac{a_p |j_o|}{D_\infty n_\infty} = f_1(\bar{\delta}) \left( \frac{d\bar{n}}{d\bar{h}} \right)_{\bar{\delta}} \quad (4.26)$$

Recognizing that neither the mass flux  $j_o$  nor the Sherwood number  $Sh$  depends on the radial coordinate  $\bar{r}$ , this shows that the mass transfer is uniform over the stagnation region. This is one of the basic features of the impinging jet system.

#### 4.4 Numerical Model Validation

This study reports original research on fine bubble attachment using the impinging jet technique. Since the developed numerical model will be used to predict bubble attachment under the influences of  $Pe$ ,  $Gr$ ,  $Ad$ ,  $DI$ ,  $Da$ , and  $\tau$  later in this section,

and its results will be directly compared with experimental observations in Chapter 7, it is necessary to test the numerical model. The first test is to compare numerical results with analytical solutions under limiting cases. In the second test, through using the same parameters, a comparison is made between the results obtained from the numerical model and the experimental results for latex particles and oil droplets reported in the literature. The theoretical support for making this comparison is based on the fact that regardless of the type of colloidal particles, transport of colloidal particles in the impinging jet region is governed by the same mass transport equation.

The numerical model was first tested by using it to calculate the mass transfer rate (in terms of the Sherwood number,  $Sh$ ) in the absence of energy barriers (e.g., high electrolyte concentration), i.e.,  $DI = Da = 0$ . The dependence of the Sherwood number,  $Sh$ , on the Peclet number,  $Pe$ , for different gravity numbers,  $Gr$ , is depicted in Figure 4.1. The adhesion number,  $Ad$ , is chosen as 0.4, which corresponds to a typical Hamaker constant of  $A_{132} = 1.2 \times 10^{-20} J$ . For most colloidal particles, typical values of  $Gr$  and  $Pe$  are usually in the range of  $-10^2$  to  $10^2$  and  $10^{-3}$  to  $10^3$ , respectively. Large particles such as micrometer-sized fine bubbles normally have  $Gr \geq 10^4$  and  $Pe \geq 10^4$ . It is noted that the shape of each curve, representing the change of  $Sh$  as a function of  $Pe$  at a fixed  $Gr$ , bears strong resemblance to that for colloidal particle deposition onto a spherical collector under similar conditions as reported by Prieve and Ruckenstein (1974). Quantitatively, it can be seen that for positive values of  $Gr$ ,  $Sh$  approaches a constant value in the limiting case of  $Pe \rightarrow 0$ , which in fact can be estimated from the Stokes law, equation (4.6). In particular, as clearly shown in Figure 4.1, within the diffusion-controlled regime ( $Pe \leq 1$ ), there is an excellent agreement between the calculated  $Sh$  for  $Gr = 0$  and that predicted from the Levich formula, equation (4.13) (shown in dotted line). Physically, a negative value of  $Gr$  means that the combined effect of gravity and buoyancy is directed outward from the collector surface. Thus, as expected, for large negative values for  $Gr$ , stronger hydrodynamic flow intensities (i.e., larger  $Pe$ ) are required for particle deposition. In addition, it is observed that the geometric interception always overestimates the value of  $Sh$  when  $Pe$  is high. The discrepancy is due to the

neglect of the hydrodynamic interactions (i.e.,  $f_1(\bar{h}) = f_2(\bar{h}) = f_3(\bar{h}) = 1$  are assumed) in the derivation of the geometric interception equation (4.18). Recently, it has been shown by Yang et al. (1998c) that, with consideration of the hydrodynamic interactions, the effect of radial flow causes the unusual dependence of  $Sh$  on  $Pe$ , i.e., in a certain range,  $Sh$  decreases as  $Pe$  increases. The general discussion of the dependence of  $Sh$  upon  $Pe$  in the impinging jet system is given in Appendix A.3. It is also important to note from the definition of the Sherwood number (i.e., equation (4.5)) that  $Sh$ , indeed, is the reduced dimensionless concentration gradient at  $\bar{\delta}$  because the hydrodynamic interaction effect is taken into account. Overall, it can be concluded that the numerical model is in accordance with the analytical solutions in limiting situations.

It should be reiterated that Dabros and van de Ven (1983) were pioneers to develop the impinging jet technique for studying colloidal particle deposition. Using such a technique, numerous experiments were conducted on the deposition of latex particles and oil droplets onto solid surfaces, and the results are well documented in the literature. In the second test, numerical calculations are performed to reproduce the same theoretical analyses as reported by Dabros and van de Ven (1987) and Sanders et al. (1995). Then the numerical predictions are directly compared with the experimental results by Dabros and van de Ven (1987) and Sanders et al. (1995) for latex particles and oil droplets, respectively. The results of such comparison are summarized in Figure 4.2 and Figure 4.3, for latex particles and oil droplets, respectively. In all cases, good agreement is found, suggesting the validity of the present numerical model.

#### **4.5 Numerical Analyses of Bubble Attachment**

Numerical calculations for the bubble transfer equation (4.1), together with boundary conditions (i.e., equations (4.2a) and (4.2b)), were performed to examine the effects of the physicochemical parameters (characterized by dimensionless groups  $Pe$ ,  $Gr$ ,  $Ad$ ,  $DI$ ,  $Da$ , and  $\tau$ ) on bubble attachment. The values of these dimensionless groups chosen for the numerical calculation essentially cover a wide range of practical situations of interest. Detailed numerical results of the influence of these dimensionless parameters

on the dimensionless mass transfer rate,  $Sh$ , will be presented and analyzed in the following sections.

#### 4.5.1 Effect of van der Waals Interaction

As a unique feature of gas bubble attachment, the adhesion number  $Ad$  (or the dimensionless Hamaker constant) is assumed negative, reflecting the fact that the van der Waals ( $VDW$ ) interaction is repulsive. In the literature, it is well established that repulsive  $VDW$  interaction exists between gas bubbles and solid surfaces through aqueous medium (Somasundaran, 1983). The mechanisms of negative Hamaker constant and the conditions for repulsive  $VDW$  interaction were discussed extensively by Visser (1981) and van Oss (1990). In Figure 4.4, the calculated Sherwood number,  $Sh$ , is plotted as a function of the Peclet number,  $Pe$ , for adhesion numbers  $Ad$  ranging from  $-0.001$  to  $-1.0$ , representing weak and strong van der Waals interaction, respectively. Here the dashed line arising from equation (4.18), the limiting solution of geometric interception, was drawn as a reference. In the calculation, the electrostatic double layer ( $EDL$ ) interaction parameters and the gravity number were chosen as  $DI = 1000$ ,  $Da = 2$ ,  $\tau = 1000$  and  $Gr = 10^5$ . These typical values correspond to the bubble (being  $10\mu\text{m}$  in radius) and the collector surface with zeta potentials of about  $10\text{ mV}$  and  $60\text{ mV}$  in a 1:1 ion-type electrolyte having ionic concentration of  $10^{-3}\text{ M}$ . It should be noted that, for small Peclet numbers ( $Pe < 10^2$ ), the Sherwood number,  $Sh$ , approaches the value of the gravity number,  $Gr$ , as indicated by equation (4.6). This reveals that for  $Pe < 10^2$ , bubble transport is dominated by buoyancy. Furthermore, it can be observed that the Sherwood number,  $Sh$ , for different adhesion numbers,  $Ad$ , falls in a narrow range (the maximum change of  $Sh$  is only 5 %) irrespective of the three-order-of-magnitude variation in the adhesion number ( $Ad$  changes from  $-0.001$  to  $-1.0$ ). This suggests that the magnitude of the adhesion number does not significantly affect the bubble attachment rate. In other words, the numerical results clearly show that the Sherwood number  $Sh$  is insensitive to the value of  $Ad$ . This is desirable as an accurate determination of the adhesion number (or the Hamaker constant) is always difficult in the modeling of bubble attachment.

#### 4.5.2 Effect of Hydrodynamic Conditions and Bubble Size

Figure 4.5 illustrates the dependence of the normalized bubble flux  $j_o/n_\infty$  on the bubble radius  $a_p$  for different hydrodynamic conditions (characterized by the Reynolds number  $Re$ ). Again, the repulsive *VDW* interaction was assumed by choosing a negative value for the adhesion number ( $Ad = -0.1$ ) or the Hamaker constant ( $A = -2.5 \times 10^{-21} J$ ) in the calculation. The *EDL* interaction parameters are exactly the same as those used in Figure 4.4. By definition, both the Peclet number,  $Pe$ , and the gravity number,  $Gr$  (representing hydrodynamic convection and buoyancy forces respectively) are proportional to  $a_p^4$ . As Figure 4.5 shows, when the bubble size becomes large, higher bubble attachment flux is observed. This suggests (i) strong impact of the bubble size on the bubble attachment rate; (ii) significant positive contributions of hydrodynamic convection and buoyancy forces to the bubble attachment in impinging jet flow. In essence, the bubble size effect on the attachment rate presented here exhibits a very similar trend to the particle size effect on the deposition of colloidal particles onto a rotating disc (Dabros et al., 1977). It can also be seen that for low Reynolds numbers, because of the presence of an energy barrier (defined as the maximum of the bubble - collector interaction energy), there exists a minimum critical bubble size for attachment. Above this size, the hydrodynamic convection and buoyancy forces are strong enough to overcome the energy barrier and cause bubble attachment. However, such a minimum critical bubble size does not exist for high Reynolds numbers, for instance  $Re = 1000$ , indicating that under such circumstances the attachment process is overwhelmingly dominated by hydrodynamic convection (at least for bubble sizes larger than  $5 \mu m$ ). By closer examination of Figure 4.5, it is also interesting to note that the dependence of  $j_o/n_\infty$  on  $Re$  for bubbles is completely different from that for colloidal particles reported in the literature (Dabros et al., 1977; Yang et al., 1998c). For instance, the value of  $j_o/n_\infty$  corresponding to  $Re = 10$  is even higher than that of  $Re = 100$ . Such unusual phenomena are attributed to the coupling effects of high buoyancy force and the radial component of the stagnation flow (see Appendix A.3 for detailed discussion).

### 4.5.3 Effect of Gravitational Forces

Figure 4.6a shows the dependence of the Sherwood number,  $Sh$ , as a function of the Peclet number,  $Pe$ , for various gravity numbers,  $Gr$ , at fixed *EDL* parameters,  $DI = 1000$ ,  $Da = 2$ ,  $\tau = 1000$ . A strong impact of  $Gr$  on bubble attachment flux is observed. However, a comparison of Figure 4.6a with Figure 4.3 indicates that the influence of  $Gr$  on  $Sh$  in the presence of energy barriers is significantly different from that in the absence of energy barriers. For small values of  $Gr$  (e.g.,  $Gr = 10^4$ ), attachment rate is reduced until hydrodynamic convection (characterized by  $Pe$ ) becomes strong enough to push bubbles into overcoming the energy barriers. While in the case of large  $Gr$  (e.g.,  $Gr = 10^6$ ), the Sherwood number  $Sh$  is almost independent of the Peclet number  $Pe$ , indicating that the bubble attachment process under such conditions is dominated by gravity. The results shown in Figure 4.6a can be better illustrated by presenting the corresponding bubble-collector interaction force profile as shown in Figure 4.6b. It should be mentioned that, in addition to *VDW* and *EDL* interaction forces, the total interaction force constructed here also includes the gravitational force. This is because, based on the bubble transport equation, equation (4.1), the gravitational force interaction plays exactly the same role as both *VDW* and *EDL* interactions. In fact, according to Figure 4.6b, it is clear that  $Gr$  has considerable effects on the shape of the interaction force profile, and hence the bubble attachment rates. For instance, under strong gravitational forces (e.g.,  $Gr = 10^6$ ), the interaction force is always negative (i.e., attractive). As a result, no energy barrier is present so that significant bubble attachment can be observed. Therefore, it can be concluded that both gravitational buoyancy and hydrodynamic flow are capable of pushing the bubbles to overcome energy barriers, and hence resulting in attachment, even if the *VDW* and *EDL* interactions are repulsive.

### 4.5.4 Effect of Electrostatic Double Layer (EDL) Interaction

When formulating *EDL* interaction parameters, special attention was given to the so-called asymmetric *EDL* interaction, described by  $Da$  in equation (3.29c). Such asymmetric *EDL* interaction was mostly ignored in previous theoretical treatments of particle deposition studies. Physically, the asymmetric *EDL* interaction implies the

existence of a short-range attractive interaction between two charged interfaces with different surface potentials, even though they carry the same sign of electrostatic potentials. This short-range attractive interaction can be predicted either from the *HHF* formula, equation (3.26), or the more “rigorous” solution to the Poisson - Boltzmann equation (Carnie et al., 1994; McCormack et al., 1995).

The effects of *EDL* interaction on bubble attachment are shown in Figures 4.7a and 4.8a. Their corresponding interaction force profiles are displayed in Figures 4.7b and 4.8b, respectively. Basically, the impact of the *EDL* parameter, *DI*, and the dimensionless ionic strength,  $\tau$ , on bubble attachment follows the same trend as those reported for particle deposition (Dabros and Adamczyk, 1977; Faibish et al., 1998; Yang et al., 1998c).

By definition (i.e., equation (3.29a)), the *EDL* parameter, *DI*, is related to the bubble and collector zeta potentials which are, in turn, dependent upon the solution concentration and pH. Hence, *DI* is a parameter that directly measures the strength of the *EDL* interaction between a bubble and the collector. It is worthwhile reiterating that *DI* = 1000 represents fine bubbles (being  $10\mu m$  in radius) and the collector surface with zeta potentials of about  $10 mV$  and  $60 mV$  in a 1:1 ion-type electrolyte having ionic concentration of  $10^{-3} M$ . In Figure 4.7a, the influence of the *EDL* parameter, *DI*, on *Sh* is presented as a function of *Pe* for  $Gr = 10^5$ . It is noted that a larger *DI* usually yields lower attachment rate. This is due to the presence of a higher energy barrier (shown in Figure 4.7b), whereby revealing that in such circumstances, the resistance arising from the energy barrier dominates the bubble attachment process. For instance, the energy barrier for the curve of *DI* = 3000 is much higher than that for *DI* = 1000. Accordingly, there is very low bubble attachment for *DI* = 3000 except in the case of strong hydrodynamic convection.

Figure 4.8a displays the influence of the *EDL* dimensionless ionic strength,  $\tau$ , on the Sherwood number, *Sh*, as the latter is plotted against the Peclet number, *Pe*. In the

calculations, the values chosen for  $\tau$  are 1000, 3500, and 10000, corresponding to fine bubbles of  $a_p = 10 \mu m$  dispersed in a 1:1 electrolyte of concentrations  $10^{-3}$ ,  $10^{-2}$ , and  $10^{-1}$  M, respectively. It is interesting to note that in Figure 4.8a, the shape of  $Sh$  dependence on the *EDL* ionic strength,  $\tau$ , is very similar to that on the *EDL* parameter,  $DI$ , (shown in Figure 4.7a), suggesting that the influence of *EDL* interaction is significant to bubble attachment. According to equations (3.20) and (3.29b), for a fixed bubble size, a larger value of  $\tau$  usually implies a higher electrolyte concentration or thinner *EDL* thickness, and hence resulting in a weaker *EDL* repulsive interaction between a fine bubble and the collector surface. Therefore, a higher bubble attachment rate can be achieved.

In addition, it should be pointed out that in Figures 4.6b, 4.7b, and 4.8b, the interaction force profile, without the presence of the asymmetric *EDL* interaction (i.e.,  $Da = 0$ ), is shown as the dotted line. Clearly, it is seen that in the absence of the asymmetric *EDL* interaction, the interaction force profile forms so high an energy barrier that it is difficult for bubbles to overcome it to achieve attachment. This inference is further supported by performing numerical calculations for the case of  $Da = 0$  while keeping other parameters  $Ad$ ,  $Gr$ ,  $DI$ , and  $\tau$  unchanged, and  $Sh = 0$  is found. This strongly demonstrates that, with repulsive *VDW* interaction, it is the asymmetric *EDL* interaction that yields short-range attraction and makes it possible for bubbles to achieve attachment. It should be noted that when two charged surfaces have the same sign but different strength in zeta-potentials, the prediction of the short-range *EDL* attraction is within the framework of Poisson-Boltzmann (P-B) equation subject to constant potential boundary conditions. Mathematically, the presence of the short-range *EDL* attractive interaction can be interpreted as a change of the slope of the electrostatic potential curve at one of two closely-separated boundaries so that the electrostatic potential profiles between these two constant potential boundaries always follow the P-B equation. From a physical point of view, it results from a change in the sign of electrostatic charge on one of the two charged surfaces (with constant potentials) due to the overlapping of the two *EDL*s. Therefore, it can be stated that, despite the repulsive van der Waals interaction



and both the bubble and the collector have the same sign of electrostatic potentials, there exists a realistic window within which bubble attachment can occur without the need of invoking additional non-*DLVO* attractive forces, such as the so-called hydrophobic interaction.

#### 4.5.5 Application of Bubble Transport Equation to Fine Gas Bubbles Attachment onto a Large Solid Particle

So far, general analyses have been performed to account for the effects of van der Waals interaction, hydrodynamic condition, gravity force, and electrostatic double layer interaction on bubble attachment. In the following, it can be shown that these results can be applicable to practical situations.

Consider in an aqueous solution, a falling particle of radius  $a_o = 1 \text{ mm}$  and fine gas bubbles rising from below. From a hydrodynamic point of view, the flow pattern (created by the falling particle) near the foremost part of the sphere is equivalent to that existing in the impinging jet region. Therefore, the bubble transport equation (4.1) can be used to estimate whether the fine bubbles would attach onto the falling particle or not.

When the particle reaches its terminal velocity,  $U_o$ , the gravitational force is precisely balanced by the viscous drag on the particle. Then the friction factor  $f$  is expressed as (Bird et al., 1960):

$$f = \frac{8}{3} \frac{g a_o \rho_o - \rho_f}{U_o^2 \rho_f} \quad (4.27)$$

where  $\rho_o$  is the density of the particle and is chosen here to be  $\rho_o = 2200 \text{ Kg m}^{-3}$ . For the considered particle size, the drag does not follow the Stokes law. Alternatively, as suggested by Bird et al. (1960), the friction factor  $f$  is approximated by

$$f \cong \frac{12.2}{\text{Re}_o^{3/5}} \quad (4.28)$$

Combining equations (4.27) and (4.28), one can estimate the particle terminal velocity as  $U_o \approx 0.27 \text{ m s}^{-1}$ , leading to the particle Reynolds number of  $\text{Re}_o = 270$ . In such a case,

an analytical solution to the disturbance flow induced by the falling particle does not exist, since neither the creeping flow nor the potential flow conditions are applicable. However, as mentioned earlier, special attention is paid only to the region near the stagnation point where the flow pattern is very similar to that created by the impinging jet flow. Following Levich (1962), at small distance  $z$  from the surface of the particle, the stream function  $\psi$  is simplified to

$$\psi \approx \frac{3}{4} U_o z^2 \sin^2 \theta \quad (4.29)$$

The velocity components along the tangential,  $t$ , and normal,  $n$ , directions are defined as

$$u_n = -\frac{1}{R^2 \sin \theta} \frac{\partial \psi}{\partial \theta} \quad (4.30a)$$

$$u_t = \frac{1}{R \sin \theta} \frac{\partial \psi}{\partial R} \quad (4.30b)$$

where  $R = a_o + z$ . Noting that  $z \ll a_o$ , it can be further assumed that  $R \approx a_o$ ,  $\sin \theta \approx r/a_o$ , and  $\cos \theta \approx 1$  (here, the cylindrical coordinates defined earlier are used).

Substituting equation (4.29) into equations (4.30a) and (4.30b) yields the velocity distributions in the stagnation region:

$$u_n = -\frac{3}{2} U_o \frac{z^2}{a_o^2} \quad (4.31a)$$

$$u_t = \frac{3}{2} U_o \frac{z r}{a_o^2} \quad (4.31b)$$

By comparing the velocity distributions given by equations (4.31a) and (4.31b) with the stagnation point flow patterns defined for the impinging jet flow, equation (2.33), one is able to obtain the intensity of the stagnation point flow to be:

$$\alpha = \frac{3}{2} \frac{U_o}{a_o^2} \quad (4.32)$$

and for the given conditions  $\alpha$  is about  $4.0 \times 10^5 \text{ m}^{-1} \text{ s}^{-1}$ .

Once the stagnation flow intensity  $\alpha$  is known, both the bubble Peclet number,  $Pe$ , and the gravity number,  $Gr$ , can be calculated. Two bubble sizes ( $a_p = 10 \mu\text{m}$  and

$a_p = 20 \mu m$ ) are chosen in the calculations. For the sake of consistency, the same parameters for van der Waals and electrostatic double layer interactions are chosen; they are  $Ad = -0.1$ ,  $Dl = 1000$ ,  $Da = 2$ , and  $\tau = 1000$ . Putting these parameters back into the bubble transport equation (4.1), one can estimate the rate of fine bubble attachment onto the falling particle. The results are listed in Table 4.1. From the values given in the table, it can be seen that the bubble of  $a_p = 10 \mu m$  will attach onto the particle if the asymmetric double layer interaction is included ( $Da = 2$ ). Otherwise, bubble attachment will not happen, i.e.,  $Sh \approx 0$  when  $Da = 0$ . This indicates that there is a significant impact of short-range attraction due to the asymmetric double layer interaction on bubble attachment. It should also be noted that, as the bubble radius increases to  $20 \mu m$ , both  $Pe$  and  $Gr$  are increased by one order of magnitude. The driving forces generated by the large  $Pe$  and  $Gr$  are sufficiently strong to overcome the energy barrier formed by repulsive van der Waals and electrostatic double layer interactions. Accordingly, the numerical model predicts that bubbles of  $a_p = 20 \mu m$  can always attach onto the particle surface. These results clearly demonstrate that, under certain circumstances, it is not necessary to include additional attractive forces, e.g., hydrophobic interaction force, to explain bubble-solid attachment.

#### 4.6 Summary

Analyses were made on the influences of the dimensionless groups ( $Pe$ ,  $Gr$ ,  $Ad$ ,  $Dl$ ,  $Da$ , and  $\tau$ ) on bubble attachment. The results showed that due to the large values of  $Pe$  and  $Gr$  for gas bubbles, the behavior of bubble attachment in many aspects is significantly different from that of colloidal particle deposition. It was evident that bubble attachment is extremely insensitive to the adhesion number,  $Ad$ . However, hydrodynamic convection,  $Pe$ , the gravity number,  $Gr$ , and the EDL interactions ( $Dl$ ,  $Da$ , and  $\tau$ ) all have strong impact on the bubble attachment rate,  $Sh$ . More importantly, it was demonstrated that, without hydrophobic interaction bubble attachment is feasible even though there exists a repulsive  $VDW$  interaction force and both bubble and solid surfaces carry the same sign of electrostatic potentials. In addition, a practical case of fine bubble transport onto a falling particle was chosen as an illustration. It was shown

that due to similarity in hydrodynamic conditions, the models derived for the impinging jet flow could be used to calculate the mass transfer rate of fine bubble attachment onto a falling particle. This suggests that the information derived from the impinging jet region can be used to understand flotation processes.

**Table 4.1** Results of mass transfer rate of fine gas bubbles attachment onto a large solid particle by using the bubble transport equation (4.1)

<b>R<sub>o</sub></b> <b>(mm)</b>	<b>a<sub>p</sub></b> <b>(μm)</b>	<b>Ad</b>	<b>DI</b>	<b>τ</b>	<b>Da</b>	<b>Pe</b>	<b>Gr</b>	<b>Sh</b>
1.0	10	-0.1	1000	1000	0	3.7x10 <sup>4</sup>	1.0x10 <sup>5</sup>	0
1.0	10	-0.1	1000	1000	2	3.7x10 <sup>4</sup>	1.0x10 <sup>5</sup>	3.5x10 <sup>4</sup>
1.0	20	-0.1	1000	1000	0	6.0x10 <sup>5</sup>	1.6x10 <sup>6</sup>	5.7x10 <sup>5</sup>
1.0	20	-0.1	1000	1000	2	6.0x10 <sup>5</sup>	1.6x10 <sup>6</sup>	5.9x10 <sup>5</sup>

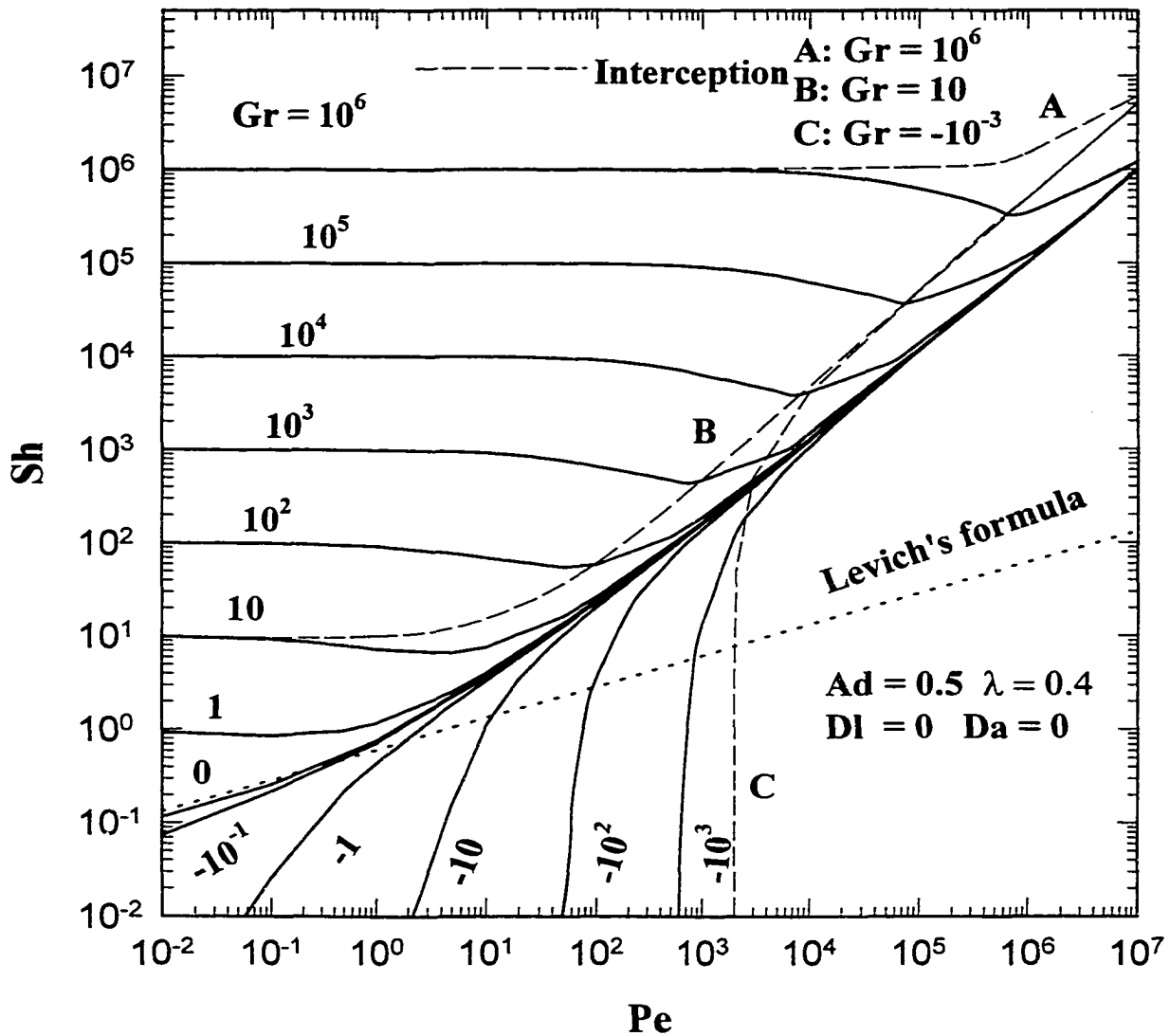


**Figure 4.1** Calculated Sherwood number,  $Sh$ , versus Peclet number,  $Pe$  for different Gravity numbers,  $Gr$ . Solid lines, a fixed  $Gr$ ; dashed lines, the geometric interception solution; dotted line, Levich's formula

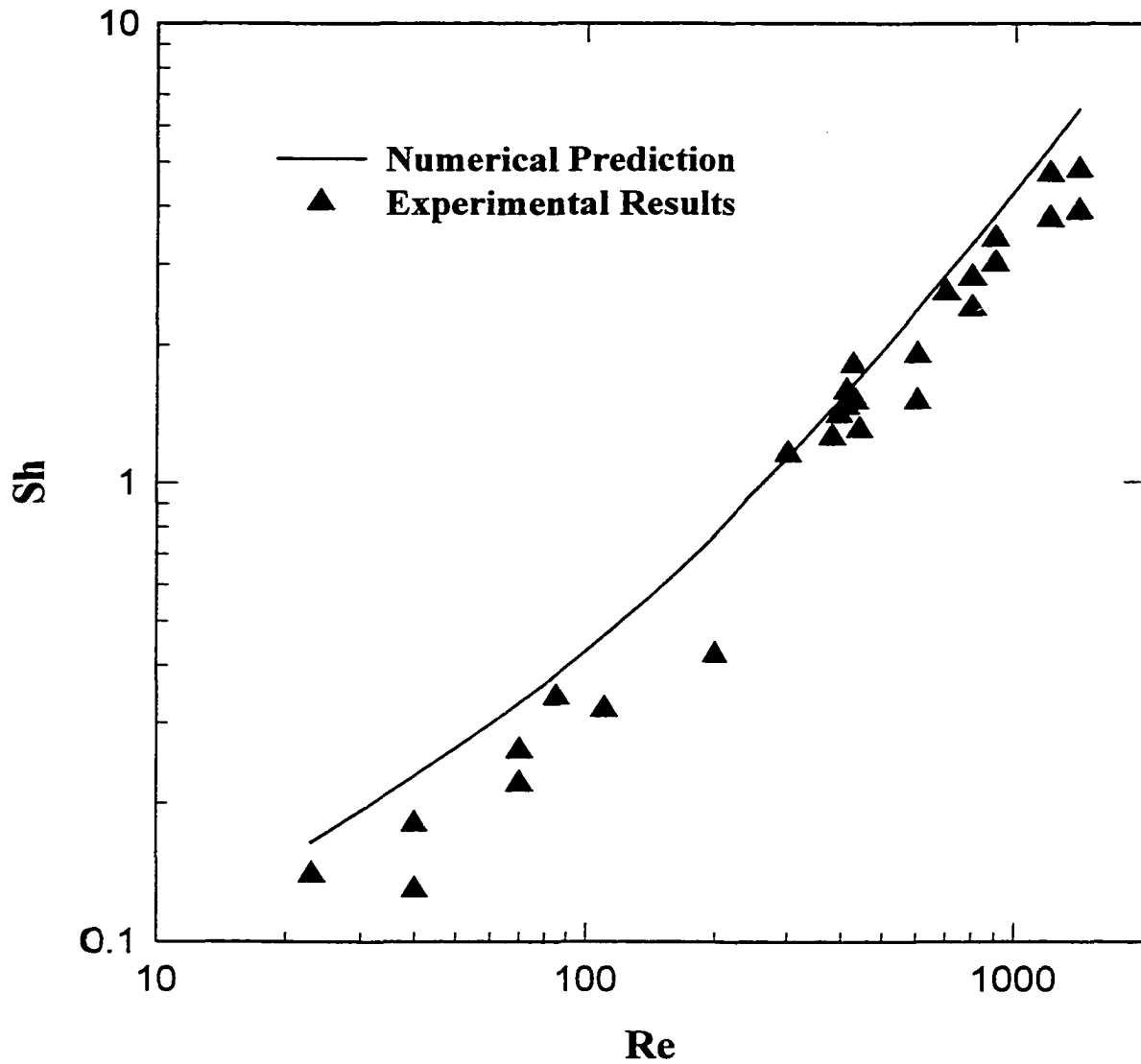


**Figure 4.2** Comparison of numerical prediction of Sherwood number for latex particle deposition with experimental results obtained by Dabros and van de Ven. Parameters used in numerical model:  $a_p=0.502 \mu\text{m}$ ;  $Ad=0.2$ ;  $Dl=0$ ;  $\bar{\lambda}=0.4$ ;  $\bar{\alpha}=0.87 \text{Re}^{0.5}$

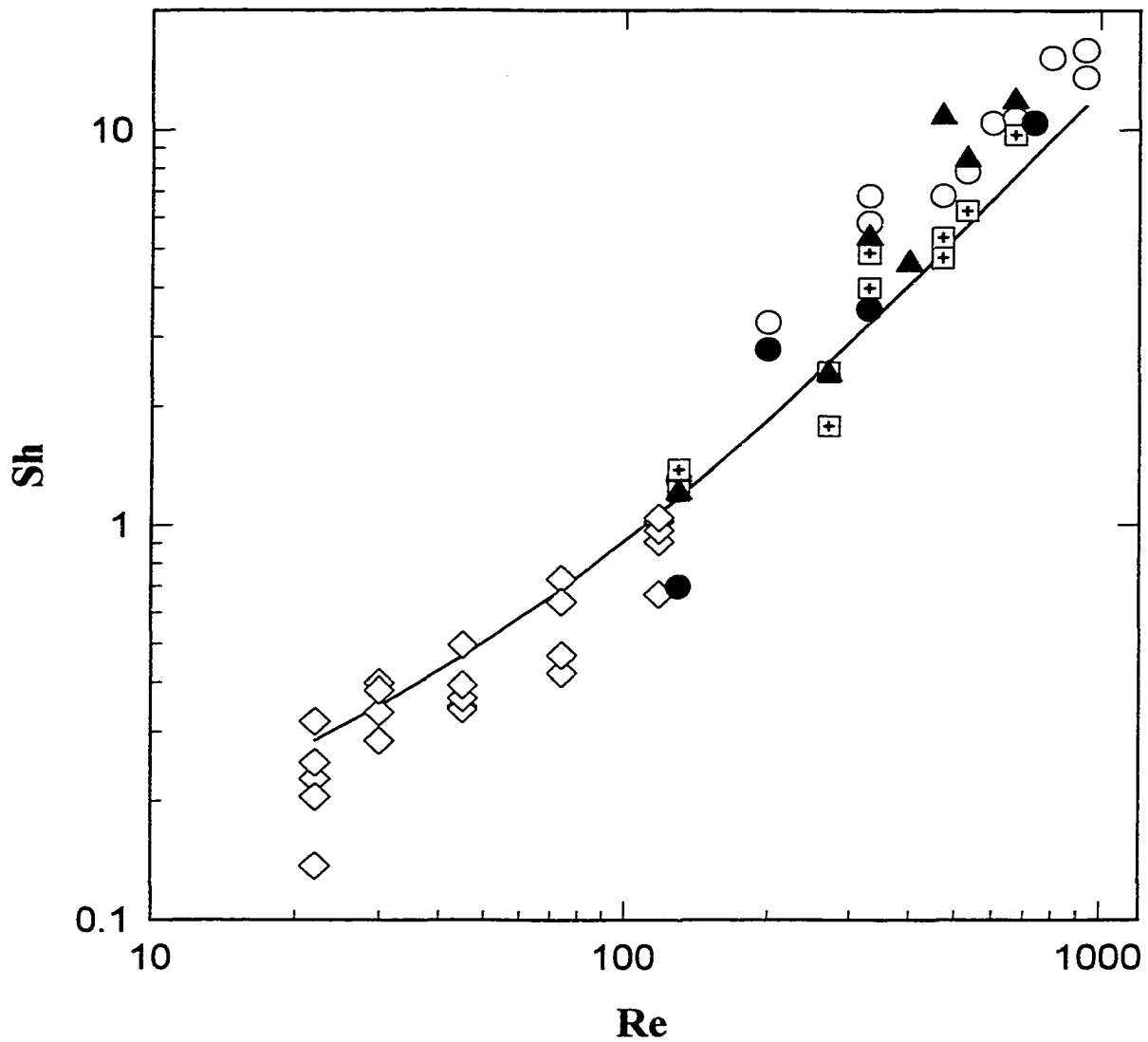


**Figure 4.3** Comparison of numerical prediction of Sherwood number for oil droplets deposition with experimental results obtained by Sanders et al. Solid line represents model prediction and parameters used are:  $a_p=0.59 \mu\text{m}$ ;  $Ad=0.45$ ;  $Dl=0$ ;  $\bar{\lambda}=0.2$ ;  $\bar{\alpha}=0.52 \text{Re}^{0.5}$ . Symbols represent different group of oil droplets.



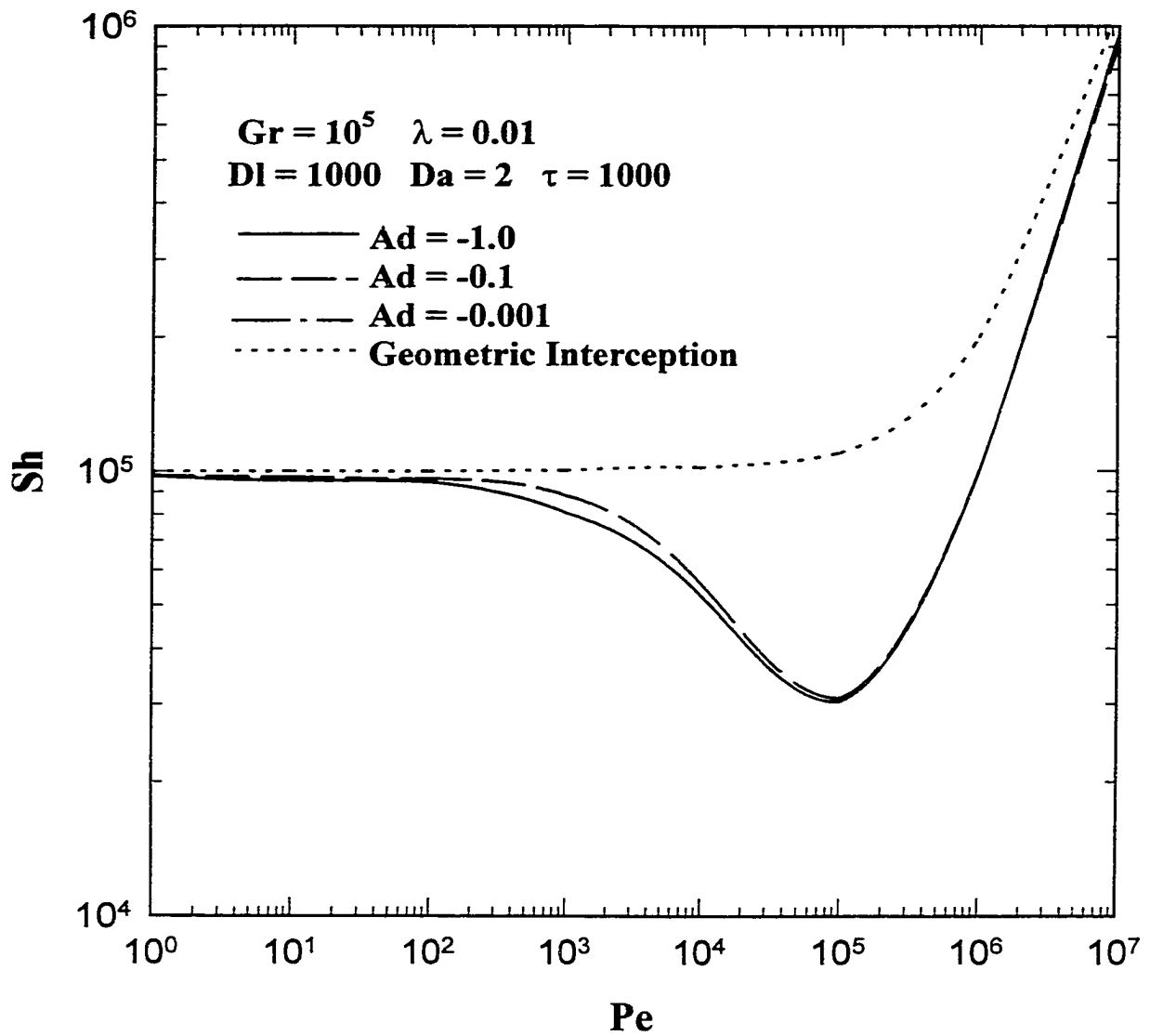


**Figure 4.4** Calculated Sherwood number,  $Sh$ , versus Peclet number,  $Pe$  for different adhesion numbers,  $Ad$  with a fixed gravity number  $Gr = 10^5$

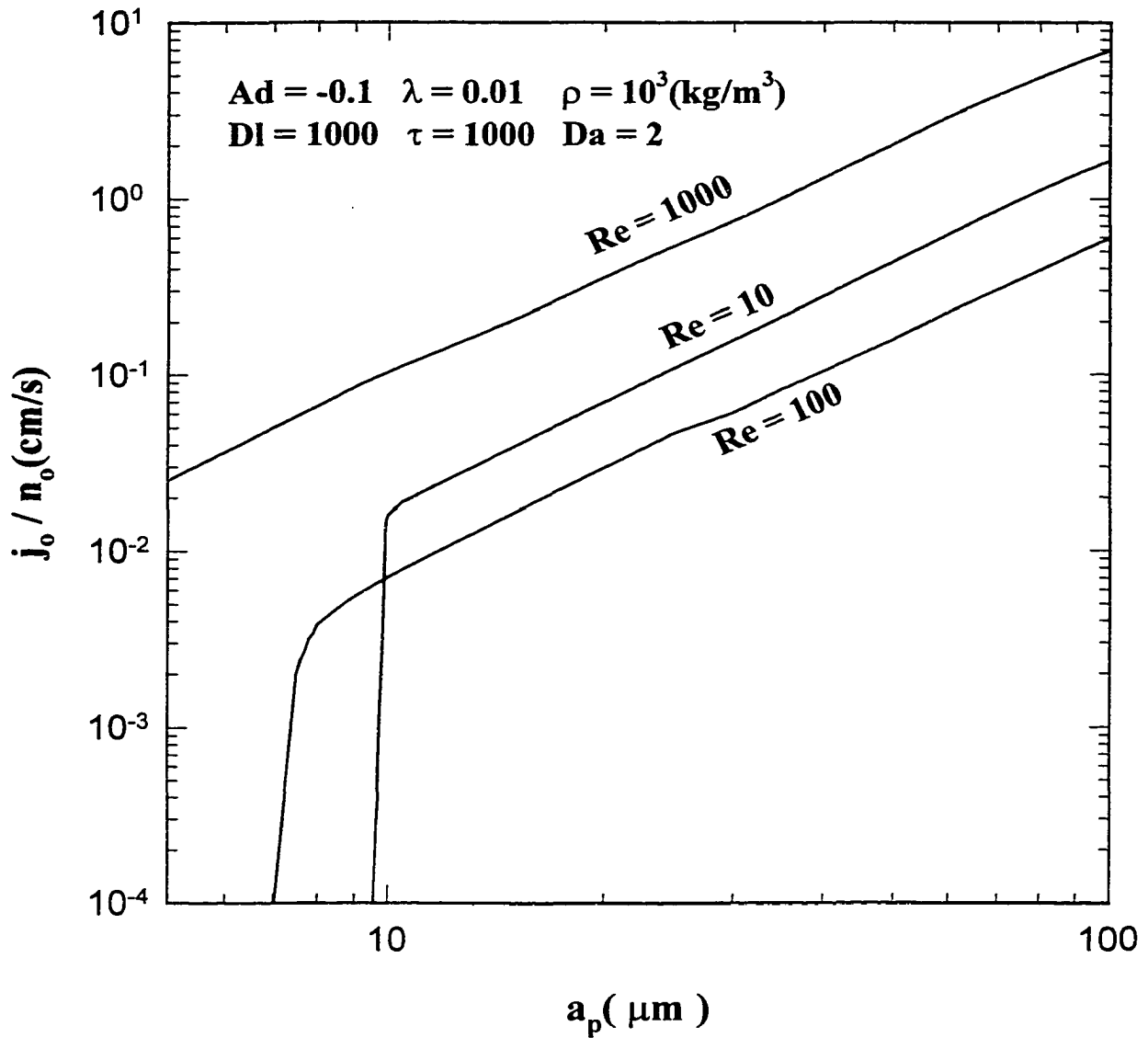


**Figure 4.5** Normalized bubble attachment flux versus bubble radius,  $a_p$ , for different Reynolds numbers with the *EDL* interaction. All curves are plotted for the repulsive van der Waals interaction with  $Ad = -0.1$

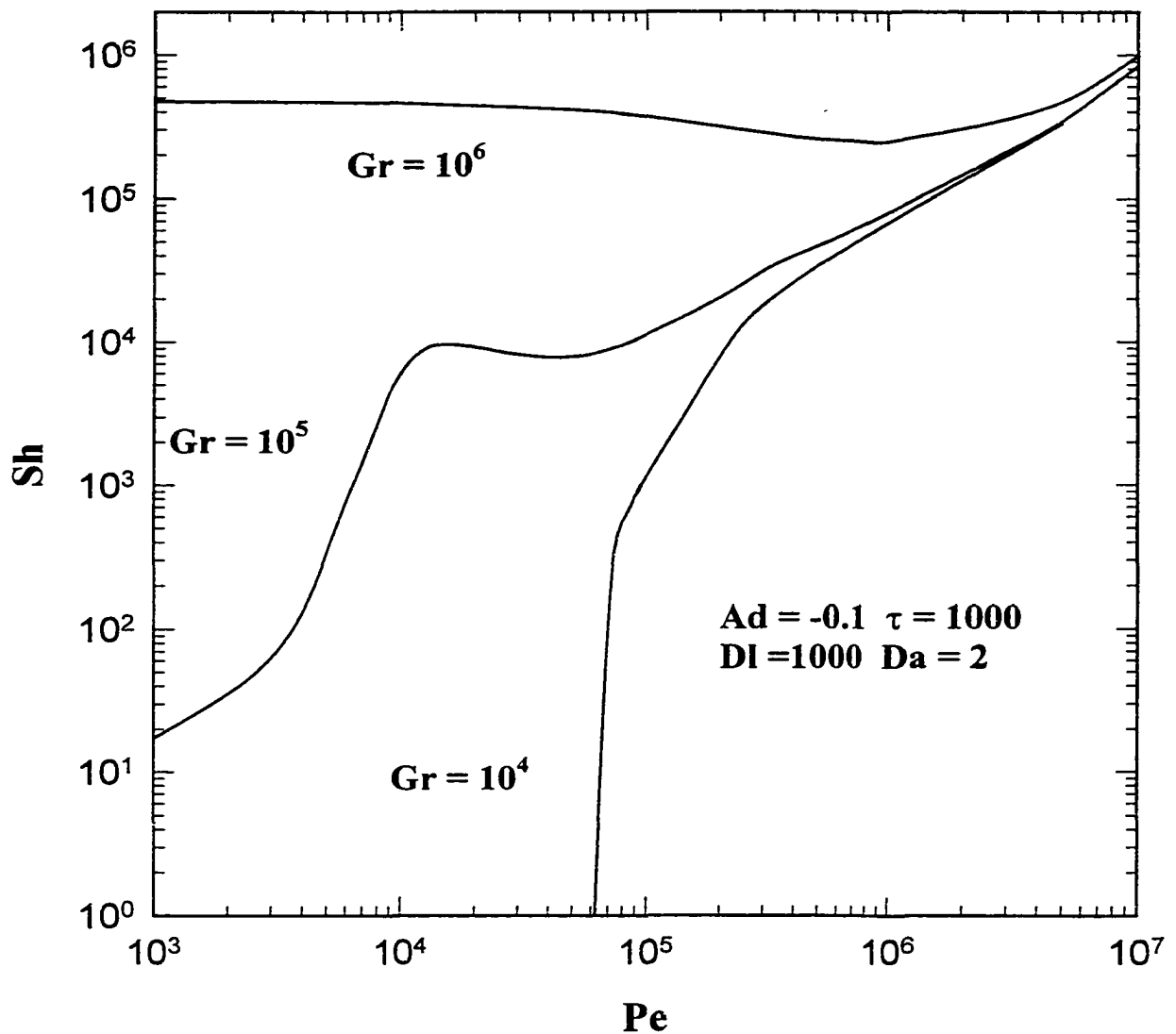


**Figure 4.6a** Calculated Sherwood number,  $Sh$ , versus Peclet number,  $Pe$ , for different gravity numbers,  $Gr$ , under combined effects of the repulsive van der Waals interaction ( $Ad=-0.1$ ) and the EDL interaction ( $DI=1000$ ,  $\tau=1000$ , and  $Da=2$ )

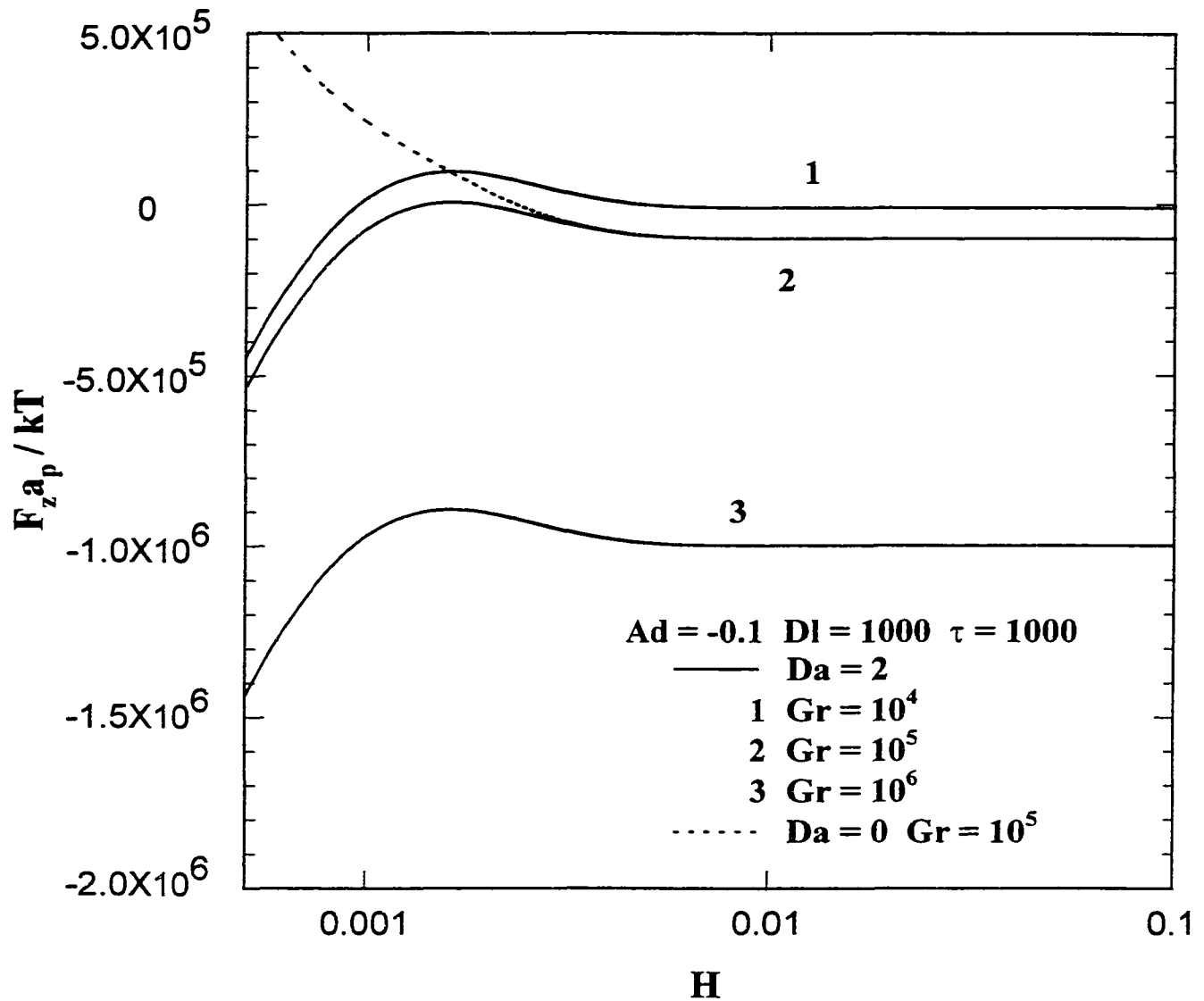


**Figure 4.6b** Dimensionless bubble-collector interaction force profiles corresponding to Figure 4.6a. Dotted line shows the interaction force without the asymmetric EDL interaction ( $Da=0$ )

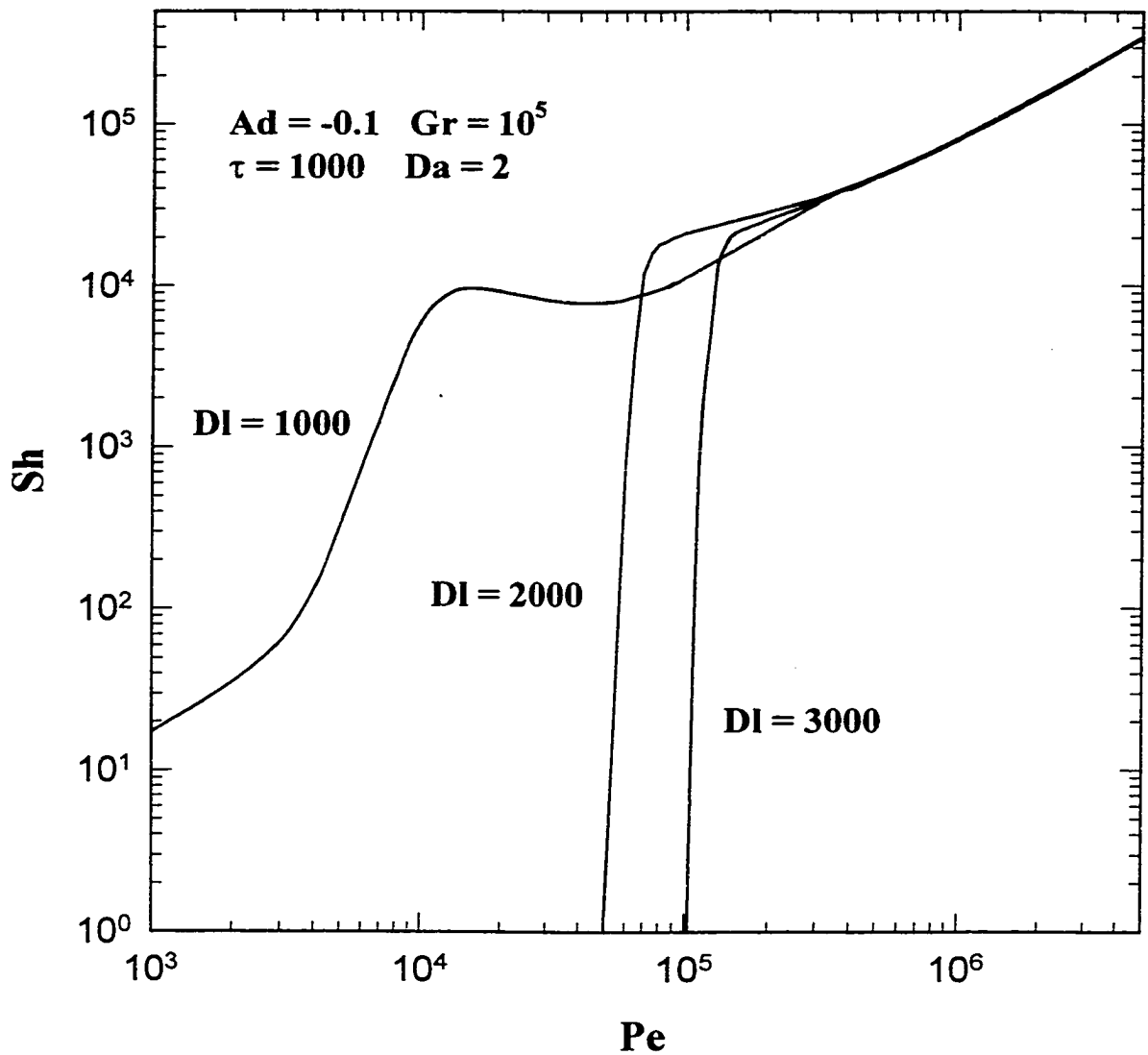


**Figure 4.7a** Calculated Sherwood number,  $Sh$ , versus Peclet number,  $Pe$ , for different EDL parameters,  $DI$ , under combined effects of the repulsive van der Waals interaction ( $Ad=-0.1$ ) and the EDL interaction ( $\tau=1000$  and  $Da=2$ )

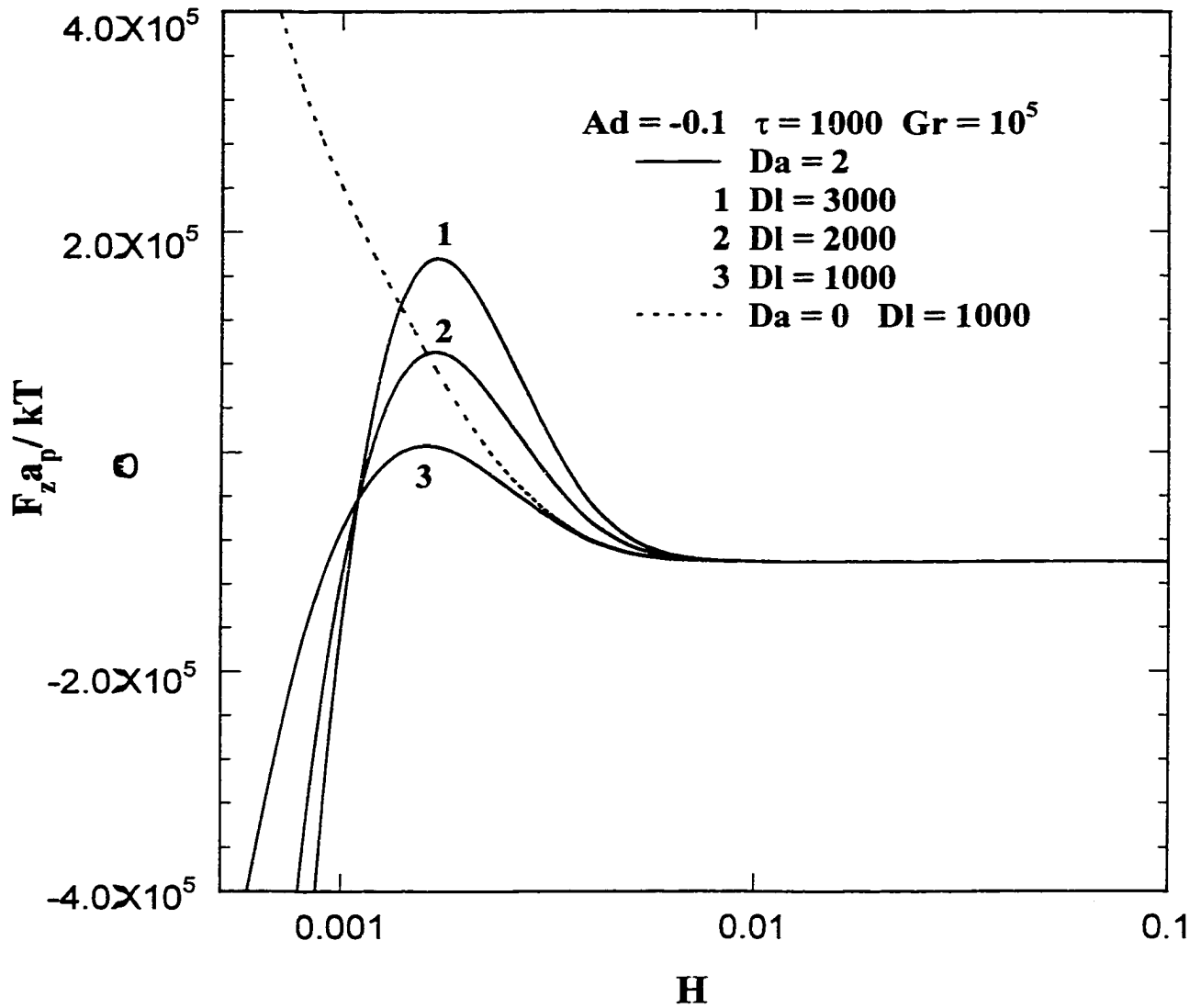


**Figure 4.7b** Dimensionless bubble-collector interaction force profiles corresponding to Figure 4.7a. Dotted line shows the interaction force without the asymmetric EDL interaction ( $Da=0$ )

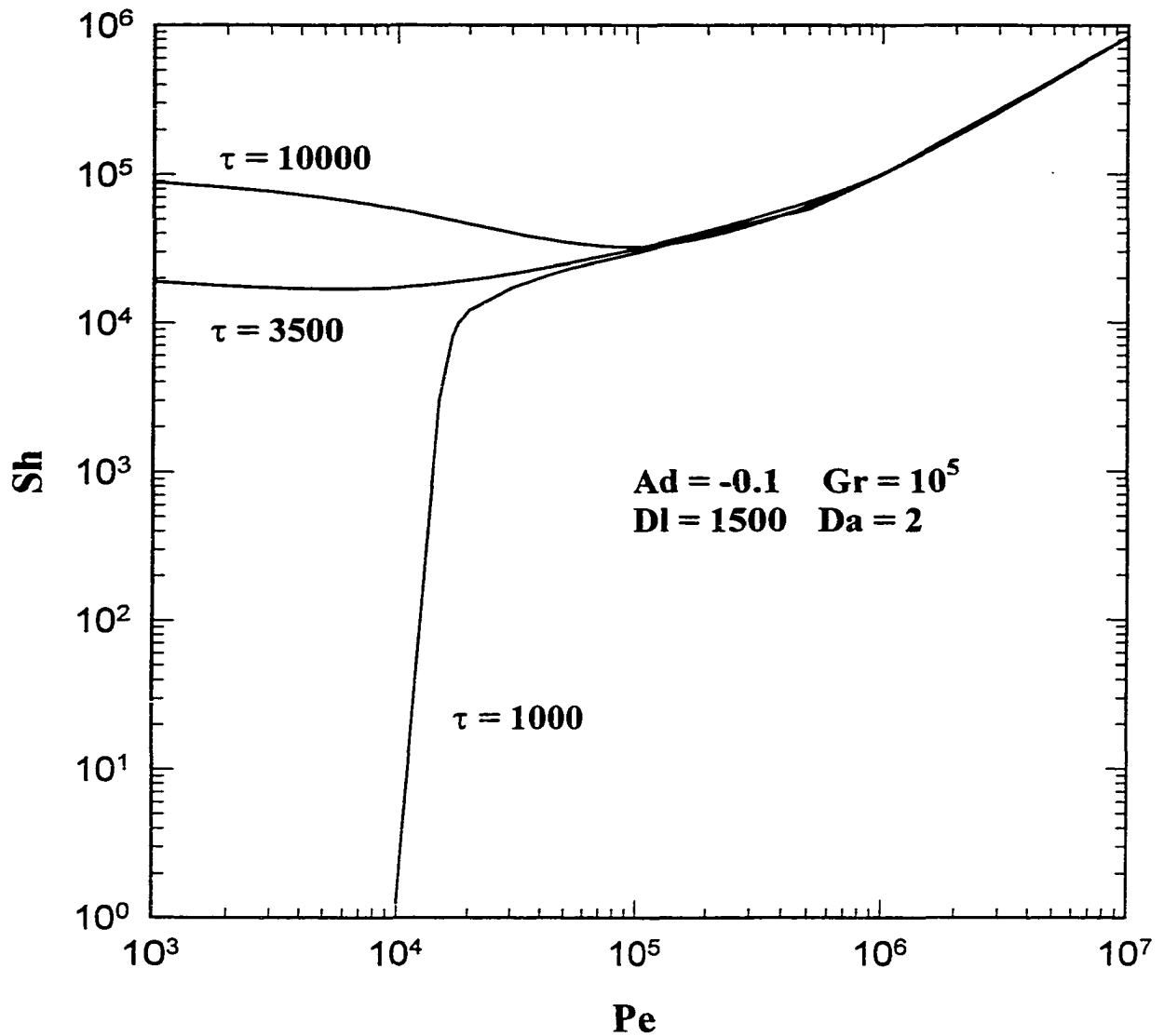


**Figure 4.8a** Calculated Sherwood number,  $Sh$ , versus Peclet number,  $Pe$ , for different EDL ionic strength,  $\tau$ , under combined effects of the repulsive van der Waals interaction ( $Ad=-0.1$ ) and the EDL interaction ( $DI=1500$  and  $Da=2$ )

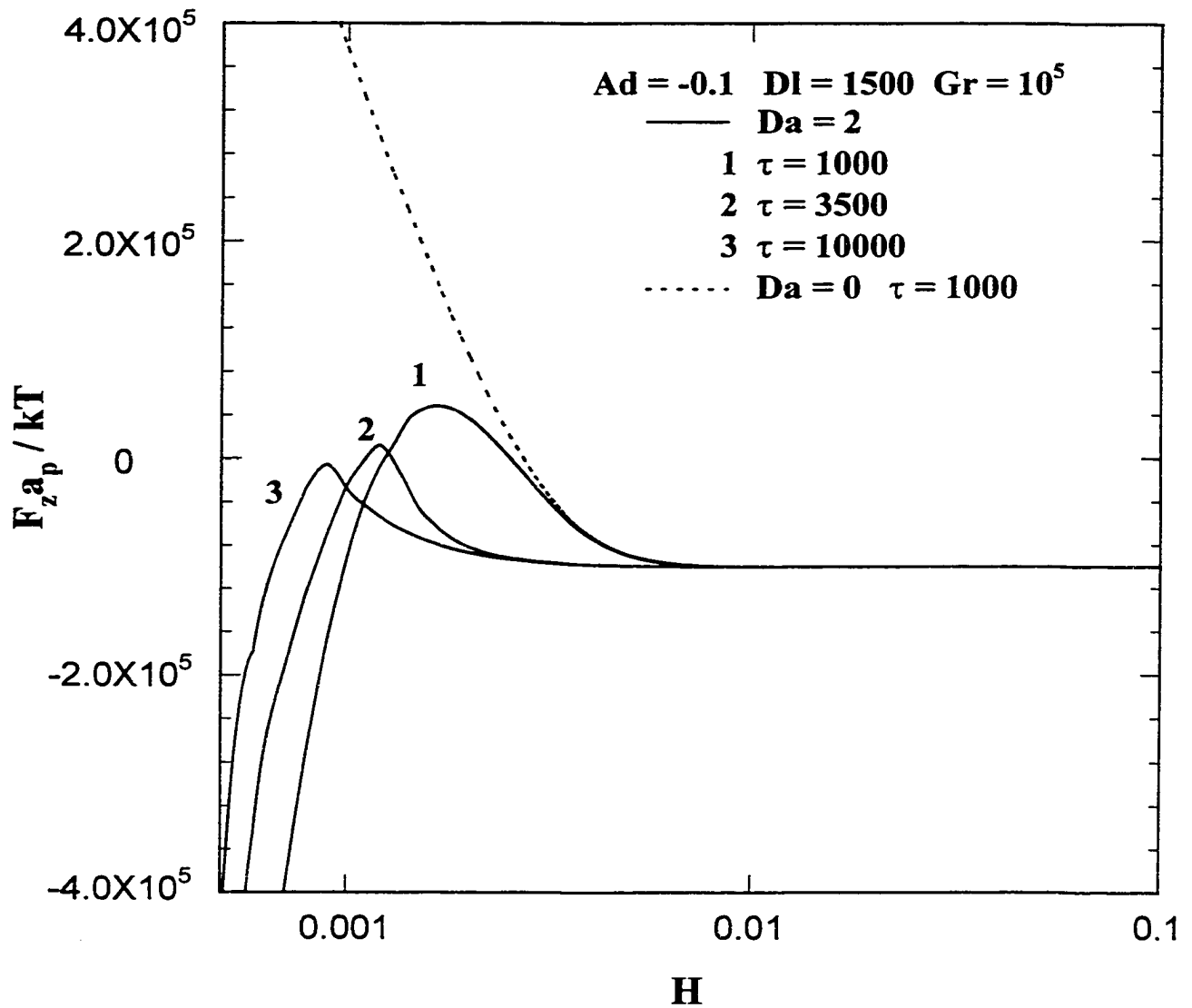


**Figure 4.8b** Dimensionless bubble-collector interaction force profiles corresponding to Figure 4.8a. Dotted line shows the interaction force without the asymmetric EDL interaction ( $Da=0$ )



## CHAPTER 5

# EXPERIMENTAL METHOD FOR BUBBLE ATTACHMENT STUDIES

### 5.1 Overview

The objective of this chapter is to describe experimental methods used for studying bubble attachment onto a solid surface from impinging jet flow. The impinging jet system is presented first; a detailed description of the configuration of the system is then provided. Even though the impinging jet experiments were conducted under a wide variety of hydrodynamic and physicochemical conditions, a general set of step-by-step procedures was followed all the time. The general procedures for performing bubble attachment test include preparation and characterization of the collector surfaces, determination of bubble attachment density, measurement of bubble sizes, and determination of bubble bulk number concentration.

### 5.2 The Impinging Jet System

A conventional impinging jet system is modified to specifically study bubble attachment. A schematic diagram of the experimental setup for performing laboratory-scale bubble attachment tests is shown in Figure 5.1. The emphasis in designing such a system is total flexibility in controlling hydrodynamic flow and changing physicochemical conditions as well as the ability to visually observe the bubble attachment process in real time. The impinging jet system can essentially be decomposed into three portions: the impinging jet cell, the optical video-image system, and the flow controlling system. A brief introduction of each portion is given as follows.

In the test section, the major component is a specifically designed impinging jet cell placed under an Olympic microscope. The cell itself consists of two parts, the upper and the lower, connected by a glass capillary tube with an inner diameter ( $ID$ ) of

2.65 mm . The upper part is used as an impinging chamber with a glass slide placed on the top to collect gas bubbles. The lower part serves as an electrolysis chamber. By applying an electrical potential (E3611A, Hewlett-Packard, USA) to the two platinum electrodes, fine bubbles can be generated at a platinum wire of 25  $\mu\text{m}$  in diameter. Typical diameter of the bubbles produced by such a method usually falls within a wide range - from 5 to 100  $\mu\text{m}$  , with a mean size around 20  $\mu\text{m}$  . The inner glass capillary tube has a length of  $L = 50\text{ mm}$  , so that the ratio of  $L$  to  $ID$  is large enough to ensure a steady, fully-developed flow at the exit of the tube. The distance between the tube exit and the glass slide (i.e., collector) is adjustable but was fixed at 2.65 mm during all experiments.

The flow part includes two reservoirs, a peristaltic pump (E302, Watson-Marlow Ltd., UK), and a rotameter that are connected to the impinging jet cell through Tygon tubings. The main function of the flow system is to monitor and control flow rates and to keep flow in circulation. Solution flow is introduced into the lower chamber from the bottom and carries gas bubbles generated by an electrode to go through the inner glass capillary tube. When the flowing jet exits at the tube outlet in the upper cell, it impinges on the glass slide (collector). Some bubbles attach on the collector surface as shown in Figure 5.2, which is a typical snapshot of attachment configuration. Other bubbles that are not captured by the collector are swept away by the flow. The flow exits from the bottom corner of the upper cell, and returns to the lower reservoir for circulation. The fluid is then driven by a peristaltic pump to an upper reservoir to maintain a constant hydrostatic head so that a steady flow rate can be maintained. The flow rate (with capacity of 200 g/min) can be adjusted, and it is measured by a rotameter (Matheson, USA). The rotameter has two working scaled tubes, suitable for measuring lower and higher flow rates. It is calibrated at room temperature (22 °C ), using the weighing method, in which the flow rate is determined by measuring an amount of water collected for a known time. The calibration data are summarized in Figures 5.3a and 5.3b, and they show that readings on the rotameter are accurate to within  $\pm 3\%$  .

As stated earlier, one of the important features of the impinging jet technique is that the entire process of bubble attachment can be visualized in real time. This is realized by means of a video-image system that consists of an Olympic microscope, a Sony CCD color camera, a Panasonic color monitor, a time generator, and a Panasonic S-VHS VCR. The microscope is positioned to focus on the bubble attachment cell, and it is connected to the CCD camera through an adapter. The image captured by the CCD camera and the time sequences produced by the timer are displayed on the monitor for observation and are recorded by the VCR for subsequent analysis. Such a video-image system provides a means to observe the behaviors of bubbles in the vicinity of the collector surface and to record the bubble attachment process for subsequent playback and analyses.

### 5.3 Experimental Procedure

Experiments were conducted for various Reynolds numbers (defined here as  $Re = \rho_f V_o R / \mu_f$ , where  $V_o$  is the mean velocity at the exit of the capillary of radius  $R$ ,  $\rho_f$  is the density of the aqueous solution, and  $\mu_f$  is the dynamic viscosity of the aqueous solution), ionic concentrations, pH values, and types of electrolytes. Irrespective of the system and conditions chosen in each experimental run, a general step-by-step procedure was followed all the time. The experimental procedure essentially consists of preparation and characterization of the collector surfaces, determination of zeta-potentials of the bubbles and the collector surface, and performing impinging jet test including bubble attachment test and determination of bubble bulk number concentration.

#### 5.3.1 Preparation and Characterization of Glass Collector Surfaces

As mentioned earlier, the experimental apparatus is designed in such a way that the flow jet carrying dispersed fine bubbles impinges onto a microscope glass slide (i.e., collector surface). Two different types of collector surfaces were used in experiments to examine the effect of surface characteristics on bubble attachment. These two types of collectors are: untreated and methylated glass surfaces. Precleaned microscope slides

( $50 \times 75 \times 1 \text{ mm}$ , Fisher Scientific) were chosen as the collector surfaces in these experiments. All slides were used only once.

A procedure for cleaning glassware was used to prepare untreated glass collector. It consisted of the following steps: The slides were first put in an ultrasonic bath (Bransonic, USA) filled with *DIUF* water and 5% Ducan (a detergent for cleaning glassware) for 20 minutes, rinsed thoroughly with *DIUF* water, and immersed in a mixing acid solution of the ratio 3 : 1 concentrated nitric acid to hydrochloric acid at 2 hours successively. After the slides were removed from the mixing acid solution, they were washed extensively with *DIUF* water and finally stored in *DIUF* water to protect the surface from accumulation of dust particles and adsorption of contaminants from air.

In order to prepare methylated slides, the slides need to be cleaned first. A cleaning procedure, similar to that of Drelich and Miller (1994), was followed. The slides were initially placed in an ultrasonic bath filled with *DIUF* water and 5% Ducan for 20 minutes. They were then rinsed thoroughly with *DIUF* water. Subsequently the slides were soaked in a chromic-sulfuric acid solution at  $60 \text{ }^\circ\text{C}$  for about 2 hours. Once the slides were removed from the chromic-sulfuric acid solution, they were washed intensively and stored in *DIUF* water. The methylated glass slides were prepared by immersing cleaned slides into a 20 % v/v dimethyldichlorosilane (Aldrich) in toluene solution (Fisher Scientific) and soaking for about 4 hours at room temperature. The slides were then rinsed with methanol (Fisher Scientific), dried in air, and stored in a closed glass jar. After treatment, a thin molecular hydrophobic film is uniformly formed on the glass surface due to chemical reaction. It should be pointed out that the procedure used here to alter the surface wetting characteristics is well documented in the literature (Laskowski and Kitchener, 1969; Araujo et al., 1995). Research has shown that the thin molecular hydrophobic film is very stable, even in extremely aggressive chemical environments such as common organic solvents. Recently, Araujo et al. (1995) used X-ray photoelectron spectroscopy to determine a change in surface composition of the slides before and after treatment and found the surfaces of the methylated slides to be modified through chemical adsorption of carbon groups. As shown in Figure 5.4, a mechanism

was proposed by Araujo et al. (1995) to illustrate the chemical carbon group adsorbed on a glass slide.

It is widely accepted that the characteristics of the glass surfaces (i.e., the untreated and methylated) can be evaluated by contact angle measurements. The measurements were made using the so-called captive-bubble method by a goniometer (Rame-Hart Inc.). A schematic of the experimental setup used for contact angle measurements is shown in Figure 5.5, and a more detailed description was provided by Zhou et al. (1998). A set of experiments was conducted to examine the effect of bubble aging time on contact angle. Virtually no change was observed for aging time from 10 – 15 min. Therefore, a 20-min equilibrium period was chosen in all contact angle measurements. To minimize variations of contact angle with bubble size, a relatively large bubble, of volume larger than a few microliters, was generated. For each solution condition, five measurements were carried out by varying bubble volumes and changing the test locations on the slides. Only receding contact angles, corresponding to the situations when bubbles are created by injecting air, were measured. Measurements were taken on both sides of each bubble and the readings were averaged. According to Zhou et al. (1998), the captive bubble method gives contact angle measurements with errors of  $\pm 5^\circ$ . It has been recognized that an accurate measurement of contact angle depends on many factors such as line tension (Li, 1996), surface roughness (Lin and Li, 1995), and mechanical instabilities (Li and Neumann, 1992b). A more comprehensive review on contact angle measurements was provided by Li and Neumann (1992a).

From the perspective of colloidal surface interactions, the transport of fine bubbles from the impinging jet flow onto a solid surface is analyzed entirely within the framework of the *DLVO* theory. One of the important assumptions in *DLVO* theory is ideal, smooth, and homogenous interacting surfaces. In reality, however, no such perfect surface exists. Any real surface may be approximated as ‘smooth’ only with respect to a certain level (or reference), such as optically smooth or molecularly smooth. Therefore, the collector surface roughness needs to be characterized in order to explore the applicability of the *DLVO* theory to the impinging jet experiments, and to account for a

possible non-*DLVO* contribution due to surface heterogeneity effects. The roughness of collector surfaces was characterized using the atomic force microscope (*AFM*) technique. The *AFM* scanned image can provide direct information on the surface roughness patterns of the collector surfaces.

### **5.3.2 Determination of Zeta-Potentials of Fine Bubbles and Collector Surfaces**

One of the major objectives of this study was to evaluate how and why the water chemistry of the testing solution affects bubble attachment. Within the theoretical scope of this study, a change in chemistry of the aqueous solution means alteration of the *EDL* interaction between a bubble and the collector surface. Therefore, the zeta – potentials of fine bubbles and collector surface are another essential parameter, which needs to be quantified for the study of bubble attachment. They are required in the theoretical calculation for a comparison of theory with experiments to verify and/or improve the theory. Also, zeta-potentials of bubbles and the collector surface can be used to theoretically predict the range of conditions that would be favorable for bubble attachment. This information was used as a guideline for the design of impinging jet experiments, such as the choice of solution pH and concentration. The zeta-potential of the collector surface can be fortunately taken from the literature directly. The zeta-potential of fine bubbles, however, was not available. A specific experimental apparatus was therefore developed for measuring the bubble zeta-potentials; that will be presented in next chapter (Chapter 6).

### **5.3.3 Impinging Jet Experimental Test**

As the stagnation point region is found to be susceptible to impurities, cleanliness is absolutely required to avoid any potential contamination. First, all experiments were run in a closed system. Furthermore, whenever the solution changes, a rigorous cleaning procedure, similar to that described for preparing untreated glass slides, was used to clean glassware including the two reservoir containers, the upper and lower parts of the impinging jet cell, and the inner capillary tube. The tubing and the flowmeter were also intensively washed using *DIUF* water several times, and finally rinsed with the to-be-tested solution.

Before each experiment, a fresh solution, with the desired water chemistry, was prepared and filled into the two reservoir containers (flasks). Then, the peristaltic pump was turned on to drive the solution through the cell and the entire tubing system. The flow rate indicated by the flowmeter was adjusted to a desired level. After the fluid flow reached a steady state, electric current across two platinum electrodes was switched on to generate gas bubbles. The microscope was first adjusted such that the stagnation point appeared at the center of the field of view and the focus was on the bubbles attached on the glass slide (collector). The bubble attachment process was usually videotaped for 10 – 12 min. A typical bubble attachment configuration is displayed in Figure 5.2. Through careful control of the voltage or current across the electrodes, the number of attached bubbles ranged from 10 to over 100 within the recording period, depending on experimental conditions. The attachment experiment was repeated at two different locations of each glass slide, and two slides were used for each experimental condition; the final result was taken as the average of these four measurements. This recording will be used later for analysis of bubble attachment density and determination of bubble size distributions.

Unlike deposition experiments for latex particles and oil droplets, where the bulk number concentration of the colloidal particles are usually known, the bulk number concentration of gas bubbles must be determined experimentally. This, as it turns out, is not a trivial task. An approach developed for determination of the bubble bulk number concentration is described below. After completing bubble attachment recording, the microscope focus was shifted to the outlet of the inner capillary tube to record the number of bubbles passing through the centre of the tube exit ( $100 \mu\text{m}$  in radius) over a given time interval. Figure 5.6 shows how the bubbles usually appear as they pass through the exit of the capillary tube. For each experimental condition, the normal period of recording was 3 min. The total number of bubbles appearing in the field of view was in the range of 300 – 800 per minute, and it was directly related to the bubble bulk number concentration for a given flow rate through the following analysis.

Replaying the recorded video frame by frame (30 frames per second), the number of bubbles,  $N(t)$ , passing through a central section of the tube exit (with radius

$r_c = 100 \mu m$ ) over a given time interval,  $\Delta t$  (s), can be counted. Mathematically, the number of bubbles,  $N$ , is related to the bubble bulk number concentration,  $c_o$  ( $m^{-3}$ ), by the following expression

$$N(t) = 2\pi \Delta t \int_{r=0}^{r=r_c} u_b(r) c_o r dr \quad (5.1)$$

where  $u_b(r)$  is the bubble velocity, relative to a stationary observer, at a distance  $r$  from the symmetry axis.  $u_b(r)$  consists of contributions of the fluid flow  $v(r)$  (relative to a stagnant liquid) and the buoyancy effect  $u_g$  (relative to the fluid flow) due to gravity acting on the bubbles, i.e.,

$$u_b(r) = v(r) + u_g \quad (5.2)$$

For a contaminated bubble whose surface gives rise to the no-slip hydrodynamic boundary condition,  $u_g$  can be approximately treated as a terminal velocity given by Stokes law,

$$u_g = \frac{2 \Delta \rho g a_p^2}{9 \mu_f} \quad (5.3)$$

where  $a_p$  is the radius of the bubble and  $\Delta \rho_f = \rho_f - \rho_p$  is the density difference between the liquid phase ( $\rho_f$ ) and the gas phase ( $\rho_p$ ).

Assuming a uniform bubble distribution (i.e.,  $c_o$  is constant) and a parabolic velocity profile for the fluid exiting the inner capillary tube, integration of equation (5.1) can be carried out analytically and one can show that

$$c_o = \frac{N(t) / \Delta t}{2Q \left( \frac{r_c}{R} \right)^2 \left[ 1 - \frac{1}{2} \left( \frac{r_c}{R} \right)^2 \right] + \pi r_c^2 u_g} \quad (5.4)$$

where  $Q$  is the volumetric flow rate of the fluid measured during the experimental run. Equation (5.4) shows that the bubble concentration can be determined by dividing the number of bubbles counted in a given time interval,  $\Delta t$ , by the volume of the liquid



flowing through the same area (an outlet section at the tube exit with radius of  $r_c = 100 \mu m$ ) over the same time period with a correction for buoyancy effects. Depending upon the range of bubble size and the Reynolds number, effect of bubble buoyancy on the bubble bulk number concentration varies from 0.5 to 5 %. In all impinging jet experiments, the bubble bulk number concentration,  $c_o$ , ranged from  $10^9$  to  $10^{12} m^{-3}$ . Taking a bubble average radius of  $a_p = 10 \mu m$ , it can be readily shown that the volumetric ratio of gas bubbles to liquid is less than 0.5 %, indicating a negligible impact on the fluid flow due to the presence of fine bubbles.

#### 5.4 Bubble Attachment Data Analyses

Once the attachment experiments were completed, each experimental run was analyzed by replaying the video at a slow speed to count the number of attached bubbles,  $N_t$ , over the stagnation region as a function of time. The stagnation region was chosen as a circular area of radius  $R_s = 300 \mu m$  from the stagnation point on the collector surface. The bubble attachment density  $n_t$  is then defined as the ratio of attached bubbles to the area of the stagnation region, and is expressed as

$$n_t = \frac{N_t}{\pi R_s^2} \quad (5.5)$$

Obviously, given all the hydrodynamic and physicochemical conditions, the value of  $n_t$  is strongly affected by the bubble bulk concentration,  $c_o$ . A more rational parameter is therefore introduced, and is called the normalized bubble attachment density,  $\bar{n}_t$ , given by

$$\bar{n}_t = \frac{n_t}{c_o} (m) = \frac{100 n_t}{c_o} (cm) \quad (5.6)$$

With the normalized bubble attachment density  $\bar{n}_t$  plotted against time  $t$ , the experimentally determined normalized bubble attachment flux,  $\bar{j}_o$ , is obtained from the initial slope of the curve:

$$\bar{j}_{\text{exp}} = \left. \frac{d\bar{n}_t}{dt} \right|_{t=0} (m s^{-1}) = 100 \left. \frac{d\bar{n}_t}{dt} \right|_{t=0} (cm s^{-1}) \quad (5.7)$$

At the same time, the bubble size distribution, based on a few hundred randomly selected bubbles rolling on or approaching the glass slide, was estimated from the same recording. Since the total magnification of the optical system was fixed during all experiments, the scale was calibrated using a standard optical grid before experiment. It can be estimated that the accuracy in determining bubble sizes is roughly around several microns.

On the other hand, the theoretical results for the normalized bubble attachment flux,  $\bar{j}_o$ , is also calculated by numerically solving the bubble transport equation (4.1); it is expressed as

$$\bar{j}_o = \frac{j_o}{n_\infty} = -\frac{f_1(\bar{\delta}) D_\infty}{a_p} \left( \frac{d\bar{n}}{d\bar{h}} \right)_{\bar{\delta}} \quad (5.8)$$

Note that the theoretical  $\bar{j}_o$  is calculated on the basis of a specified bubble size. In reality, fine bubbles generated in the impinging jet experiments exhibit a wide range of sizes. To account for bubble size distributions, a theoretical mean bubble attachment flux  $\bar{J}_o$  can be calculated using the following formula

$$\bar{J}_o = \sum \bar{j}_o(a_{pi}) p(a_{pi}) \quad (5.9)$$

where  $\bar{j}_o(a_{pi})$  is the normalized bubble attachment flux calculated on the basis of a uniform bubble size,  $a_{pi}$ , and  $p(a_{pi})$  is the bubble size distribution intensity function with respect to  $a_{pi}$ , determined from the bubble size distributions. The theoretical mean flux  $\bar{J}_o$  will then be compared to the experimentally-determined, normalized bubble attachment flux  $\bar{j}_{\text{exp}}$ , defined in equation (5.7).

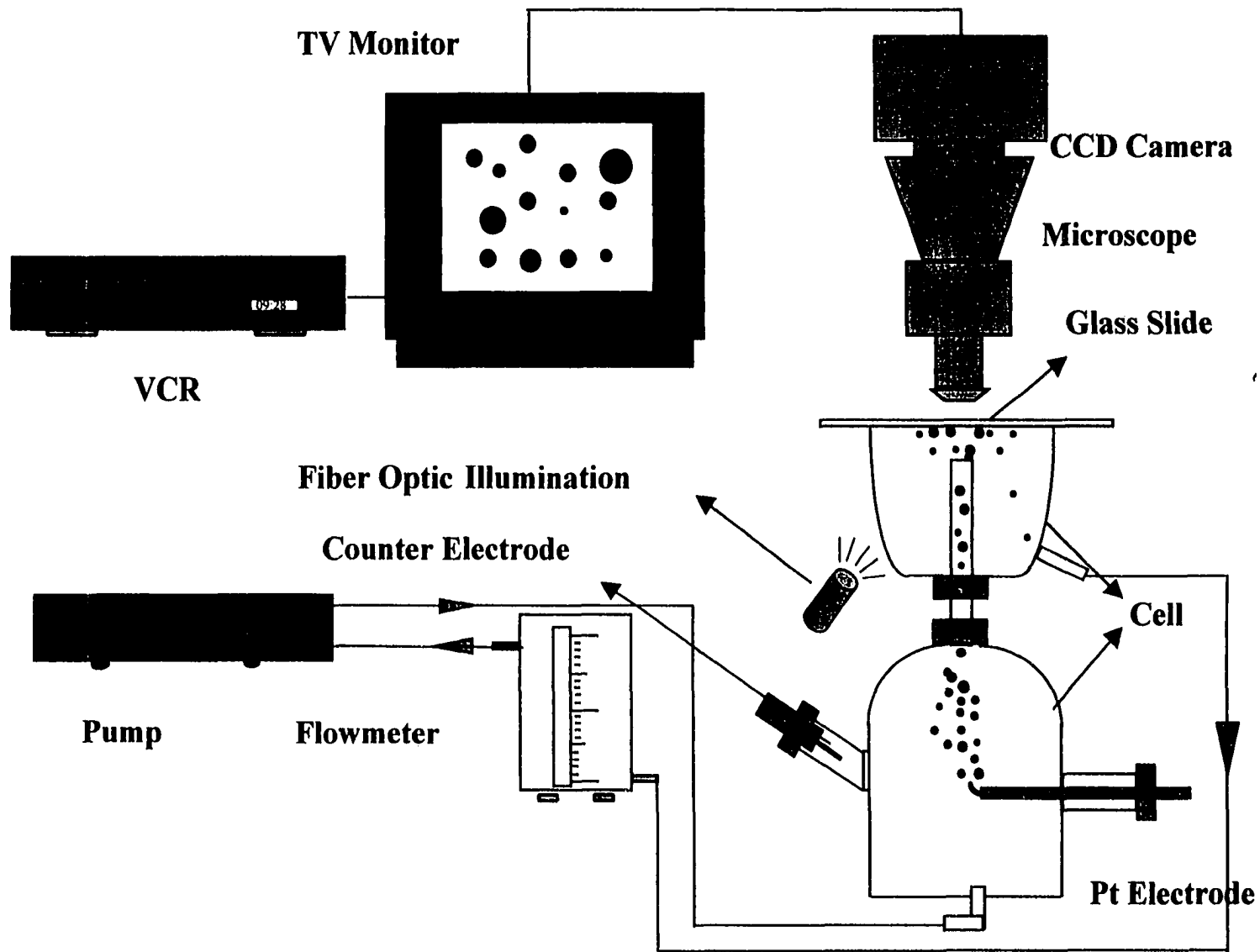


**Figure 5.1** Schematic of experimental setup for the performing laboratory-scale bubble attachment measurements

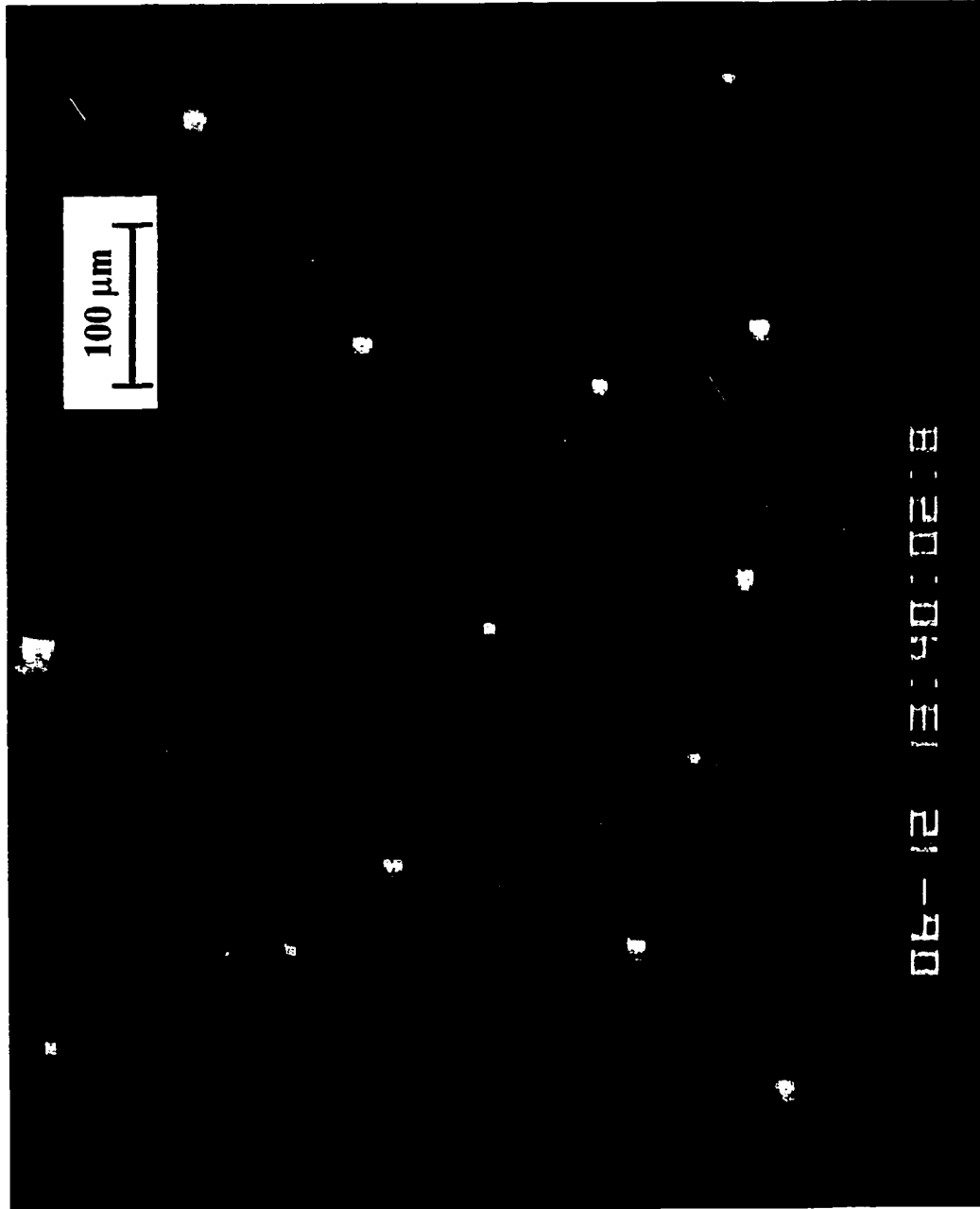


**Figure 5.2** A typical bubble attachment pattern on a glass surface

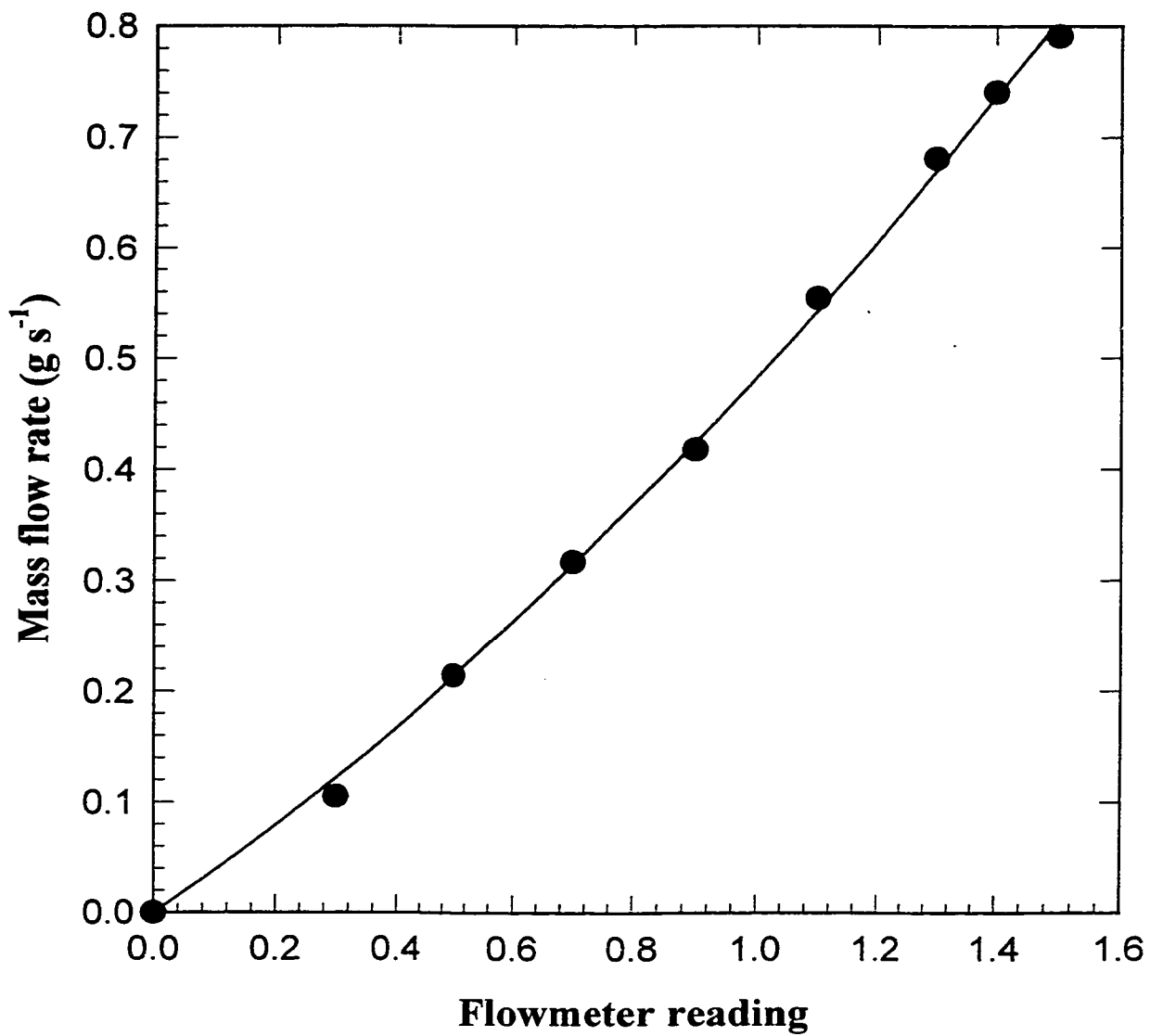


**Figure 5.3a** Calibration of the flowmeter for the low flow rate region

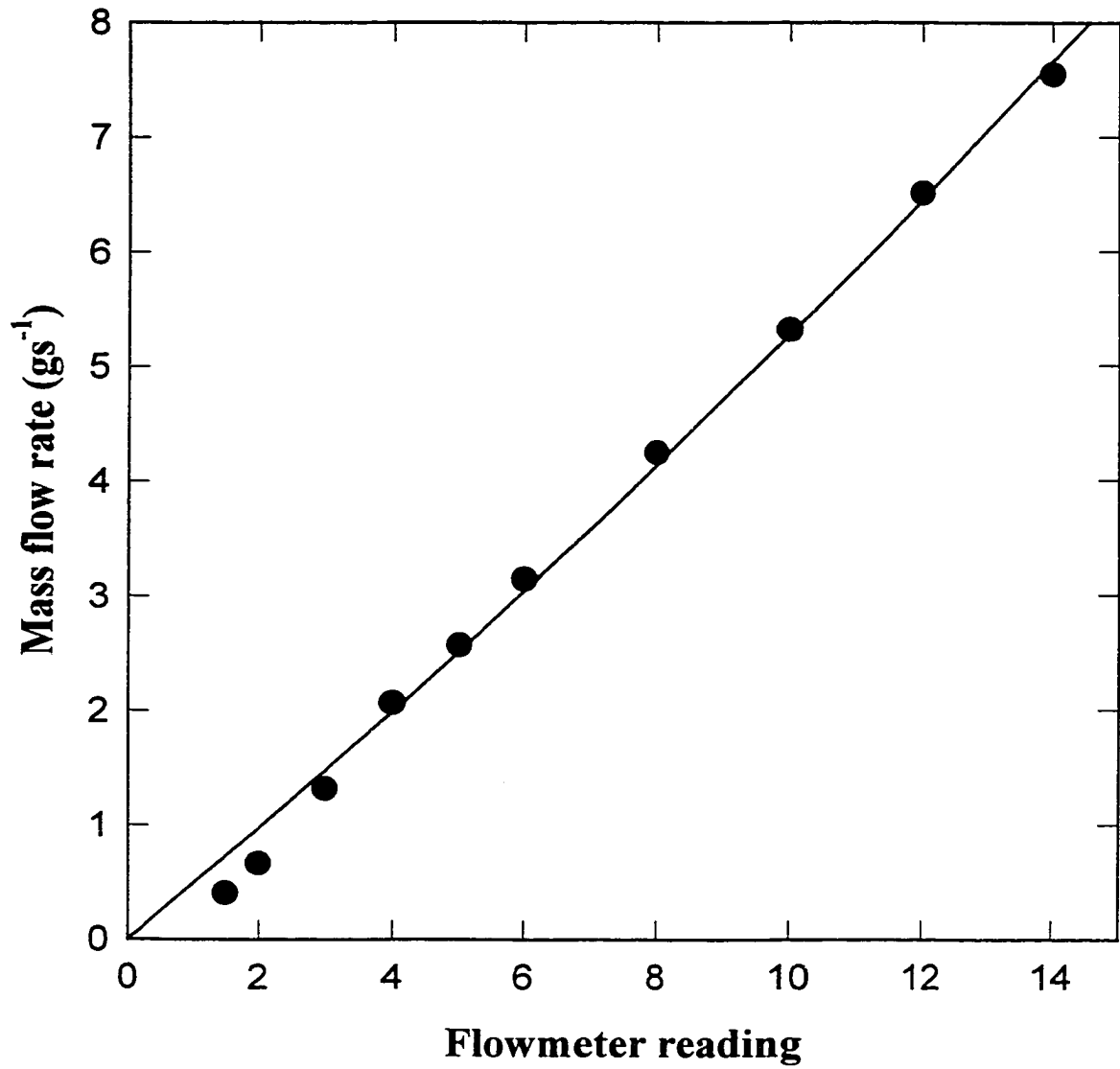


**Figure 5.3b** Calibration of the flowmeter for the high flow rate region

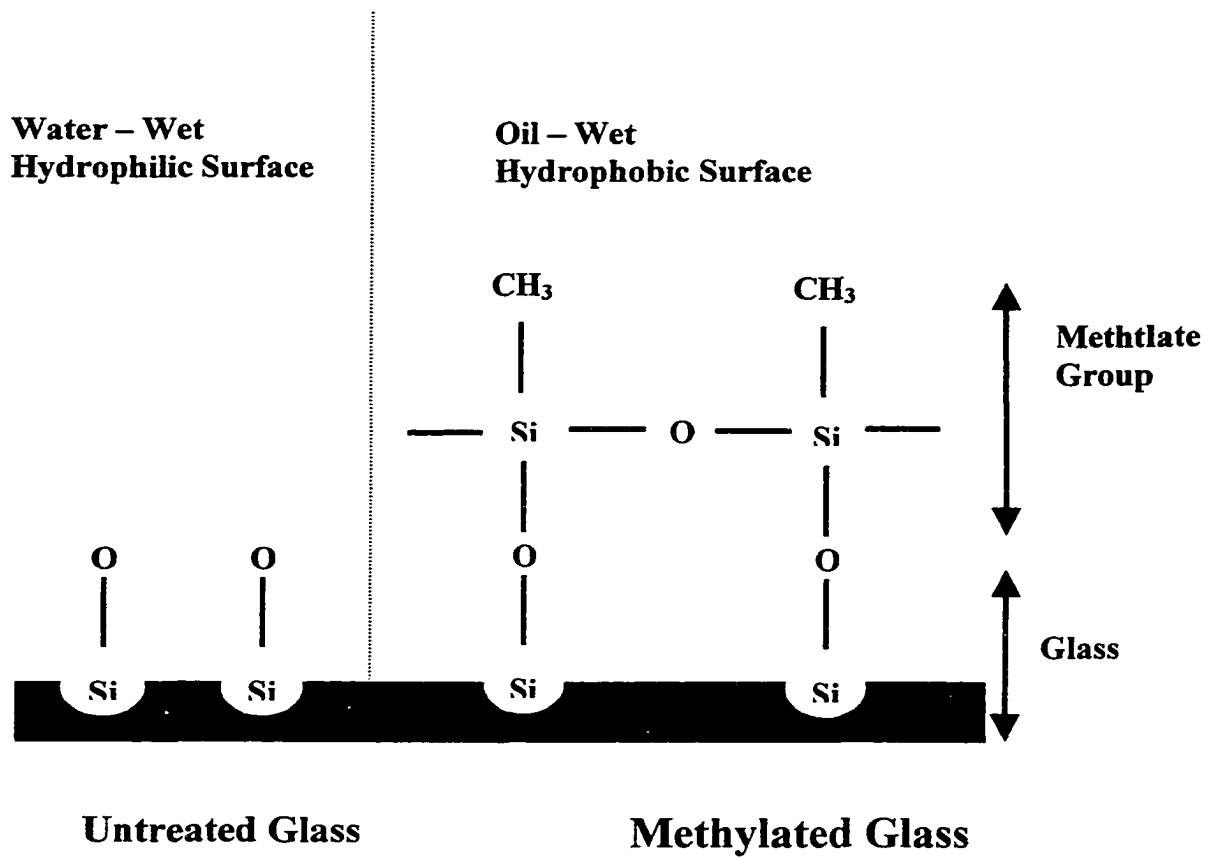


**Figure 5.4** Schematic diagram of chemical structures for untreated and methylated glass surfaces, proposed by Araujo et al. (JCIS, 1995)

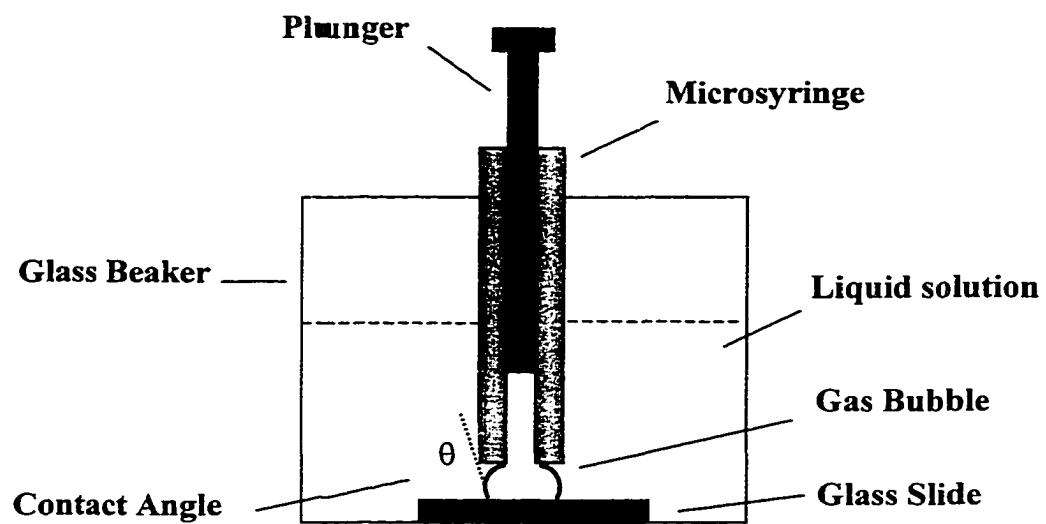


**Figure 5.5** Schematic of experimental setup for contact angle measurement





**Figure 5.6** An image used for determination of bulk bubble number concentration

## CHAPTER 6

# MEASUREMENT OF THE ZETA – POTENTIAL OF FINE BUBBLES

### 6.1 Introduction

#### 6.1.1 Background and Objectives

It is well known that gas bubbles suspended in most aqueous solutions acquire a surface charge. The most likely charging mechanism is due to asymmetric dipole water molecules staying at the gas-liquid interface. Other mechanisms responsible for the bubble surface charge include adsorption of ions, dissociation of ionic groups, and charge separation (Hunter, 1981; Schechter, 1998). The presence of such electrostatic charge on the gas bubble surface causes the arrangement of balancing charge in the solution, leading to redistribution of free ions. Such free ions are governed by a balance of thermal and electrical forces in the aqueous solution, which is referred to as the electrostatic double layer (Hunter, 1981).

The electrostatic double layer (*EDL*) of the gas bubble plays an important role in bubble-solid particle/oil droplet interactions and attachment (Fukui and Yuu, 1980; Okada et al., 1990; Yoon and Mao, 1996; Celik et al., 1998) and bubble coalescence, which are commonly encountered in many practical processes including froth flotation, slurry transport, and wetting phenomena (Bucklet et al., 1989). For instance, Derjaguin and Dukhin (1981) stated that when bubbles and particles have opposite charges, flotation is almost instantaneous. Despite the importance of the surface charge at the gas-liquid interfaces, compared to the surface charge or zeta-potential of solid particles or oil droplets which have been extensively studied and well-documented in the literature, relatively little information about the zeta-potential of gas bubbles is known. To date, a few methods have been developed in an attempt to measure the zeta-potential of gas bubbles but, no commercial instrument is available to furnish such information because

of difficulties in introducing gas bubbles into the measurement cell and controlling bubble buoyancy forces. Further, a survey of published data for the zeta-potential of gas bubbles indicates a considerable discrepancy. Indeed, the surface charge or the zeta-potential of gas bubbles has never been satisfactorily determined. Therefore, the objective of this study was to develop a reliable technique to measure the zeta-potential of gas bubbles and to obtain more information about the zeta-potential of gas bubbles in various solution conditions. Another major objective was to obtain the zeta-potential of gas bubbles under conditions that are identical to the bubble attachment experiment performed using the impinging jet cell technique (see Chapter 7). Once the measured data of bubble zeta-potential have been obtained, the *EDL* interaction defined in equations (3.28) and (3.29) can be quantified and the bubble attachment experimental results, which will be presented in Chapter 7, can be directly compared with theoretical models presented in Chapter 3 of this thesis.

This chapter is divided into five sections. First, a critical review is provided on previously developed techniques for bubble zeta-potential measurements. An experimental approach is then proposed to acquire the data of the bubble zeta-potential. The second part of the chapter (i.e., section 6.2) illustrates the theoretical background of bubble electrophoresis measurements. A widely used electrokinetic equation (i.e., Smoluchowski equation) is presented to relate measured electrophoretic mobility to the bubble zeta-potential. Several phenomena involved in bubble electrophoresis measurements are discussed in details. These phenomena include electroosmotic flow, temperature rise during measurement, and “relaxation time” needed for exchange of ions between a bubble and the solution. A simple analysis is also provided to estimate experimental errors of bubble zeta-potential measurements. Section 6.3 describes the experimental configuration used in bubble zeta-potential measurements and outlines the experimental procedure. In the section 6.4, experimental results of the bubble zeta-potentials are presented and discussed. Finally, a summary is provided in the last section 6.5. In addition, other relevant sections to Chapter 6 include Appendices 4 and 5. Appendix 4 describes a rigorous theoretical approach to quantify the electroosmotic flow in an electrophoretic cell of rectangular geometry. In Appendix 5 (Yang and Li, 1998b),

a theoretical proof is provided to illustrate the validity of application of the Poisson-Boltzmann equation to an electroosmotic flow inside a microelectrophoretic cell.

### **6.1.2 Review of Bubble Zeta-Potential Measurements**

The surface charge residing at the liquid – gas interface has been a subject of intermittent study for over the last one hundred years. According to McTaggart (1922), Quincke was probably the first to carry out studies on this subject. Quincke's major findings were that air bubbles acquire different charges depending on the solution composition. Quincke also investigated the movement of an air bubble in a glass capillary and found that the bubble in pure water moved to the anode when direct voltage was applied to the capillary tube, indicating that air bubbles in pure water are negatively charged. Since the turn of this century, there have been numerous attempts to measure the surface charge of gas bubbles. These previous studies may be divided into three groups based on the method of measurement.

The pioneers of the first group were McMaggart (1922) and Alty (1926). They captured a bubble at the center of a horizontal glass tube filled with water. The ends of the tube were sealed with metal discs acting as electrodes. By rotating the tube, the bubble could be held on the center axis. The speed of the bubble movement along the axis was measured as a function of the applied direct voltage. The measurements revealed that the surface charge does not depend on the type of gas. However, their method was justifiably criticized because they did not take account of the electroosmotic flow that originated from applying an electric field along a charged wall in the closed tube. As pointed out by Bach and Gilman (1938) and Samygin et al. (1964), failure to consider the electroosmotic flow could affect not only the magnitude but also the polarity of bubble charge inferred from the measurements. It is very clear that the electrophoretic mobility measurement conducted at the center axis was a combination of electrophoresis and electroosmosis effects, which definitely cannot be directly used to calculate the zeta-potential of gas bubbles. In fact, a solid sphere moving along the axis of a spinning tube, as a fluid mechanics problem itself, is extremely complicated (Moore and Saffman 1969). This problem was solved by Sherwood (1986) who examined the electrophoresis

of a spherical rigid bubble in a rotating fluid. Recently, the spinning tube electrophorometer method has been re-examined by Garaciaa and co-workers (1995a, 1995b, 1996, and 1998). They improved this classic apparatus by coating a layer of polymer called diethylaminothyl dextran (*DEAED*) onto the inner surface of the tube so that the surface charge can be neutralized and therefore, the electroosmotic flow may be eliminated or reduced. Using the modified technique, they measured the zeta-potential of air bubbles in pure water and various kinds of surfactant solutions. Although it was a great improvement, two questions arise regarding their experiments. First, relatively large bubbles (approximately from 0.6 to 2.0 mm in diameter) were introduced in their experiments. Undoubtedly, such large bubbles inside a high speed spinning tube are subject to a shape change. They did not account for this possible error since the electrokinetic model they used was developed only for a spherical, rigid particle (Sherwood, 1986). Theoretically, Jun and Kim (1989), who calculated electrophoresis of spheroidal particles, demonstrated that the effect of orientation and shape on the electrophoretic mobility is significant due to a local change of both hydrodynamic and electrostatic forces acting the particle. Second, their experimental results showed that the electroosmotic flow only could be eliminated within a very narrow range of pH and at a certain level of solution ionic concentration. Similar results were also obtained by Herren et al. (1987). Therefore, as suggested by Hunter (1981), the general applicability of this surface treatment method is not recommended. In fact, as shown by Brooks (1973) and Hsu and Kuo (1995), coating neutral polymers on the tube inner surface causes alteration of the *EDL* structure inside the tube and thus, makes it even more difficult to quantify electroosmotic flow under such situations.

In the second group, Sirois and Millar (1973) initiated a method where the motion of a single rising bubble, generated from electrodes, is observed in aqueous solutions. If a uniform electric field horizontally is imposed, the charged bubble will deviate from its original rising trajectory. The measured electrophoretic transverse deviation of the rising bubble then can be related to the bubble's surface charge. Sirois and Millar, however, realized that the cell used in their experiment was so big that the applied electric field generated convection currents inside the cell, forcing them to carry out their

measurements within 0.3 to 0.4 sec of applying the electric field. Based on the same principle, Collins et al. (1978) developed a so-called microelectrophoretic technique by reducing the size of cell to the millimeter order of magnitude. As expected, the convection current was greatly reduced. Measurements were supposed to be taken at the so-called stationary level where the electroosmotic flow was eliminated. However, this was difficult to do practically since it was impossible to always produce oxygen bubbles, generated from the tiny tip of platinum wire inserted at the bottom of the flat cell, coincidentally at the same position as the stationary level. Moreover, the bubble size in their experiments was still too large, resulting in bubbles that rose too fast to follow. In fact, all their measurements were conducted within 1 sec only, and hence it is difficult to obtain consistent results. Kubota et al. (1983) used the same microelectrophoretic technique with smaller bubbles generated using the dissolved air technique, which made the whole experimental system very complicated. Later, Yoon and Yordan (1986) modified the flat cell by introducing a microbubble suspension from the side of the cell. The electrophoretic mobility was measured in the same direction as the flow of microbubble suspension, which may have caused a significant error in determining electrophoretic mobility. Furthermore, since the size of microbubble was also in the range of 40–80  $\mu\text{m}$  in diameter, they were also subject to the same gravitational buoyancy force difficulty as Collins et al. (1978). More recently, Li and Somasundaran (1991, 1992), using the same approach as Yoon and Yordan's, collected more data of the zeta-potential of gas bubbles in various of aqueous solutions, but did not yield any technical improvement.

In the third group, Usui and Sasaki (1978) tried a different approach that utilized the Dorn effect, that is the potential created by a cloud of rising bubbles. They reported that the zeta-potential of gas bubbles strongly depended upon the bubble size, which is not supported by Smoluchowski theory. Dibbs et al. (1974) employed a method based on the streaming current technique, which was essentially the same as the Dorn potential technique. Neither experimental details nor theory were reported to show how to relate the measured streaming potential to the bubble's zeta-potential.

### **6.1.3 Proposed Approach for the Present Study**

Among the above addressed three different techniques, it appears that each method developed so far has its own advantages and drawbacks. In view of simplicity and reliability, it seems that the microelectrophoretic method is the most promising technique for the current bubble zeta-potential measurement. More importantly, the electroosmotic flow created in the microelectrophoretic cell is well characterized so that the true electrophoretic mobility can be readily obtained. In fact, most currently available commercial electrophoresis instruments used for measuring the zeta-potential of solid particles or liquid droplets, such as Malvern Zeta Meter, Rank Brothers MK, and Pen-Kem Laser Zeta Meter, are designed on the basis of this method. Therefore, the microelectrophoretic technique was utilized in the present study. The technique is based on the apparatus developed by Collins et al. (1978) with some technical modifications. First, the electrodes for generating microbubbles were designed in such way that bubbles can be produced across the whole cell. Thus, one can readily pick a bubble at the stationary level to conduct measurement. Secondly, an advanced experimental system was built which utilizes a computer-controlled vertical translator stage. By introducing such motorized translator stage, the movement of gas bubbles with diameter up to 80  $\mu\text{m}$  is easily followed and bubble trajectory can be traced for 4 to 8 seconds depending on bubble size. In other words, the electrophoretic measurement can be taken much longer and hence, more reliable data can be obtained. The gravitational buoyancy problem is essentially solved.

## **6.2 Electrophoresis Method**

### **6.2.1 Electrophoresis, Electrophoretic Mobility, and Zeta-Potential**

Electrophoresis is the movement of charged particles suspended in a liquid under the influence of an applied electric field. Electrophoresis measurements are carried out to determine electrophoretic velocity first, and then convert it into electrophoretic mobility, defined as the ratio of the electrophoretic velocity to the strength of the applied electric field. The electrophoretic mobility is directly related to the zeta-potential of the particle, and hence is an intrinsic characteristic property of particle-liquid interfaces.

To define and better interpret the concept of zeta-potential, it is instructive to illustrate the structure of electric double layer (*EDL*) around a charged particle in an aqueous medium. A widely accepted model of the *EDL* structure is largely due to Stern (Hunter, 1981), who embodies the principles put forward by Helmholtz and Gouy and Chapman. Helmholtz predicted that the *EDL* constituted a parallel plate condenser; this was criticized by Gouy and Chapman on the basis that thermal energy would prevent the formation of such a compact double layer and would tend to distribute the ions throughout the liquid medium. In place, they postulated a diffuse ionic region in which the potential falls almost to zero over the distance  $\frac{3}{\kappa}$ , the statistical thickness of the double layer. According to this theory, excess counter ions near the charged surface screen the electrostatic attraction for the counter ions lying further away from the particle surface. This results in the concentration of excess counter ions and hence the electrical potential falling off rapidly near the charged surface and then slowly with increasing distance until the region of uniform charge distribution is reached. This simple picture predicts a capacity of the electric double layer that is higher than that measured experimentally, leading to absurdly high ionic concentration near the surface. Attributing this discrepancy to the treatment of the ions as point charges, Stern showed that neither the sharp nor the diffuse double layer was adequate. He then developed a theory embodying the general characteristics of both. Stern considered the possibility of specific ion adsorption, which produced a layer of counter ions attached to the surface, by electrostatic and by van der Waals forces, strong enough to overcome thermal forces. The first layer, approximately a single ion thickness (the Stern layer), remains almost in contact with the surface. In this layer there is a sharp fall in potential from  $\psi_o$  to  $\psi_\zeta$  (see Figure 6.1). The second layer, which extends into the liquid phase, is diffuse, and here the potential exponentially falls from  $\psi_\zeta$  to zero. In this diffuse region, to which the Guoy-Chapman theories are applicable, thermal agitation permits free movement of the ions. The distribution of the positive and negative ions is not uniform, however, since the electrostatic field at the surface results in attraction of ions of the opposite sign. The potential change in the Stern layer increases with the concentration and valence type of the electrolyte. With polyvalent counter ions it is possible for reversal of charge to occur



within the Stern layer, i.e., for  $\psi_o$  and  $\psi_\zeta$  to have opposite signs. Figure 6.2 summarizes the asymmetrical distribution of ions around a negatively charged particle in suspension.

The charge on the surface is equal in magnitude but opposite in sign to the sum of the charges in the Stern and diffuse parts of the electrical double layer. When an external electric field is applied to a particle suspended in an electrolyte solution, the migration velocity is related to that part of the potential gradient across the shearing plane where the potential is defined as  $\zeta$  (i.e., the zeta-potential). Thus, the numerical value of the  $\zeta$ -potential is dependent on the position of the shearing plane with respect to the demarcation plane between the Stern and diffuse layers. A layer of water about one molecule thick is probably bound to the surface by charge-dipole interaction. This means that the shearing plane is outside the Stern layer, and thus  $\zeta$  is smaller than  $\psi_\zeta$ . An increase in electrolyte concentration produces a lowering of the  $\zeta$ -potential, since more of the potential drop occurs in the immobile part of the electrical double layer.

The ratio of  $\zeta/\psi_o$  found experimentally in several systems of low electrolyte concentrations is about 0.5, suggesting that specific adsorption effects are low at concentrations less than 0.1 M. Above this concentration, for these particular systems, specific adsorption effects become important and reversal of charge may occur.

### 6.2.2 Electrokinetic Equations

Finding an exact relation (or electrophoretic equation) to relate the electrophoretic mobility to the properties of the electric double layer (i.e., the zeta-potential) has been a continuous effort in colloidal science. (Wiersema and Overbeek 1966; Dukhin and Derjaguin 1974; Hunter, 1981; Hidalgo-Alvarez, 1991). The electrophoretic equation, in certain special cases, has been analytically formulated based on the magnitude of a quantity " $\kappa a$ " which physically characterizes the ratio of the particle size,  $a$ , to the electric double layer thickness,  $1/\kappa$ . For the case of large  $\kappa a$  (e.g.,  $\kappa a > 100$ ), the electric double layer is thin and hence, it can approximately be treated as being flat. This

treatment was first examined by Smoluchowski. Thus, the electrokinetic equation derived on the basis of this assumption is referred to as the Smoluchowski equation. On the other hand, when  $\kappa a$  is small (e.g.,  $\kappa a < 1$ ), the electric double layer is thick, and therefore the particles can be considered as point charges. This assumption leads to the Hückel equation. Since only the Smoluchowski equation is applicable to the present study, it will be discussed in detail below.

### 6.2.2.1 Smoluchowski Equation

Physically, electrophoresis is regarded as the reverse of electroosmosis, that is the movement of an electrolyte solution relative to stationary charged surface. (Hunter 1981; Masliyah, 1994). In light of this point, the electroosmosis analyzed by Smoluchowski in a situation where  $\kappa a$  is large can be equally applied to the electrophoretic motion of a large particle with a thin electrostatic double layer simply by regarding the liquid as fixed with the particle moving in the opposite direction. Consider the motion of liquid in the diffuse part of the electric double layer relative to that of a non-conducting flat surface when an external electric field is applied parallel to the surface. Each layer of liquid will rapidly attain a uniform velocity parallel to the surface with electrical and viscous forces balanced. By equating the electrical force to the viscous force on a thin liquid layer of unit area, thickness  $dy$ , a distance  $y$  from the surface, and having a bulk charge density  $\rho_e$ , the following relation is found:

$$E \rho_e dy = (\mu_f \frac{dv_e}{dy})_y - (\mu_f \frac{dv_e}{dy})_{y+dy} = - \frac{d}{dy} (\mu_f \frac{dv_e}{dy}) dy \quad (6.1)$$

where  $E$  is the electrostatic field strength,  $\mu_f$  is the dynamic viscosity of the aqueous solution, and  $v_e$  is the local electroosmotic velocity of the fluid. The local volumetric density of charge near the liquid-solid interface,  $\rho_e$ , is related to the Poisson equation which, in the present case, is expressed as follows:

$$\frac{d}{dy} (\epsilon_r \epsilon_o \frac{d\psi}{dy}) = -\rho_e \quad (6.2)$$

where  $\epsilon_r$  is the relative dielectric permittivity of the solution,  $\epsilon_o$  is the dielectric permittivity of vacuum, and  $\psi$  is the local electrostatic potential.

Inserting the Poisson equation into equation (6.1) leads to the expression:

$$E \frac{d}{dy} (\varepsilon_r \varepsilon_o \frac{d\psi}{dy}) = \frac{d}{dy} (\mu_f \frac{dv_e}{dy}) \quad (6.3)$$

Integration yields the following:

$$E \varepsilon_r \varepsilon_o \frac{d\psi}{dy} = \mu_f \frac{dv_e}{dy} + \text{constant} \quad (6.4)$$

The integration constant is zero, since as  $y \rightarrow \infty$ ,  $\frac{d\psi}{dy} = 0$  and  $\frac{dv_e}{dy} = 0$ .

Further integrating equation (6.4), with an assumption that both the dielectric permittivity and the viscosity of the solution are constant throughout the whole electrostatic double layer region, produces another expression:

$$E \varepsilon_r \varepsilon_o \psi = \mu_f v_e + \text{constant} \quad (6.5)$$

This equation is subjected to the boundary conditions:  $y \rightarrow \infty$ ,  $\psi = 0$  and  $v_e = 0$ , so that the above integration constant is equal to zero. By introducing the electrophoretic parameters at  $y =$  surface plane of shear,  $\psi = \zeta$  and  $v_e = v_E$  (here  $\zeta$  and  $v_E$  are the zeta-potential of the solid-liquid interface and the electrophoretic velocity, respectively), one finally may obtain the Smoluchowski equation:

$$V_E = \frac{v_E}{E} = \frac{\varepsilon_r \varepsilon_o \zeta}{\mu_f} \quad (6.6)$$

where  $V_E$ , by definition, is the electrophoretic mobility.

It follows from equation (6.6) that the electrophoretic mobility of a non-conducting particle for large  $\kappa a$  should be independent of particle size and shape provided that the dielectric permittivity and dynamic viscosity of liquid solution have the same values within the *EDL* as in the bulk liquid. In this study, the typical bubble size is on the order of 10  $\mu\text{m}$  in radius. The Debye – Hückel length  $\kappa^{-1}$  varies from 0.001 to 0.03  $\mu\text{m}$  depending on the solution concentration. Therefore, the value of  $\kappa a$  falls within the range of 330 to 10000, suggesting that Smoluchowski equation is applicable in most of situations. It also should be pointed out that in deriving the Smoluchowski equation, two implicit assumptions were made. First, the Debye - Hückel approximation (i.e., the

linearized version of the Poisson – Boltzmann equation) was used. Obviously, such assumption will be invalid when the zeta-potential of the particle is high. Secondly, the applied external field and the local *EDL* field were simply superimposed. This means that the applied field is unaffected by the presence of the migrating particle and conversely, the local field of the *EDL* does account for the effect of the applied field. This is strictly valid when the conductivity of the particle is identical to that of the solution medium or when the particle is so small that no appreciable distortion of the field occurs within the *EDL* of the particle.

#### **6.2.2.2 Improved Theories of Electrophoresis**

Henry compromised the discrepancy between the Smoluchowski equation and the Hückel equation by accounting for the effect of the relative values of the particle size and the thickness of the *EDL*. Henry derived a more general electrophoretic equation, for which both the Smoluchowski equation and the Hückel equation are two special limiting cases. However, Henry's theory is still based on the same two assumptions that the Smoluchowski theory used.

A great deal of work has been done on the theory of electrophoresis since Henry. Elaborate treatments were provided by Wiersema and Overbeek (1966) and O'Brien and White (1978) with consideration of the so-called relaxation effect. The relaxation effect implies the distortion of the *EDL* field induced by the movement of the particle. As the particle moves, the ions of the *EDL* around the particle must be re-adjusted in accordance with particle's motion. It has been shown that the relaxation effect gives a significant contribution when the thickness of the *EDL* is comparable to the particle radius and when the zeta-potential is high. Parallel work has been done by Dukhin and Deryaguin (1974), who sought to develop an alternative analytical approach for particles undergoing electrophoresis. Their method is referred to as polarized *EDL* treatment since the *EDL* around the particle is regarded as being distorted from its equilibrium shape by the motion of the particle. It is essentially similar to the incorporation of the relaxation effect into the Smoluchowski equation. Nevertheless, these formulations, although being of fundamental significance, involve a significant amount of mathematical complexity.

Specifically, a comparison made by Hidalgo-Alvarez (1991) clearly demonstrated that as the *EDL* becomes thinner (i.e., the value of  $\kappa a$  is larger), the differences among the Smoluchowski equation, the Wiersema approach, and the Dukhin and Deryaguin treatment are gradually smoothed out. To this end, it indicates that the Smoluchowski equation can be safely used to determine the zeta-potential of gas bubbles in this study, as the value of  $\kappa a$  for the bubble electrophoresis is, at least, larger than a few hundreds.

### 6.2.3 Coupled Phenomena Involved in Electrophoresis Measurement

Electrophoretic velocity is determined using a microelectrophoresis flat cell. As the cell used in this work is rectangular, several known effects, which may be involved in this experimental study, need to be addressed. Precautions have to be taken so that their potential influence on the measured results of the zeta - potential of gas bubbles can be minimized or ideally be eliminated.

#### 6.2.3.1 Electroosmotic Flow and Stationary Level

As mentioned in the introduction of this chapter, electroosmotic flow is known to occur in any type of electrophoretic cell. It is potentially a major source of error in electrophoretic mobility measurement. Extensive discussion regarding the electroosmotic flow is provided by Hunter (1981). The origin of the electroosmotic flow is due to the presence of a surface charge at the cell wall that results in formation of an *EDL* in the aqueous phase near the solid-liquid interface. Under an applied electric field, there is a relative movement of the liquid within the *EDL* (called the electroosmotic flow) and, in a closed cell, a compensation return flow through the center of the cell. The observed particle velocity,  $v_{OB}(y)$ , in fact is the algebraic sum of two superimposed velocities, namely the absolute electrophoretic velocity of the particle relative to a stationary liquid,  $v_E$ , and the velocity of the liquid relative to the stationary wall surface,  $v_{OM}(y)$ :

$$v_{OB}(y) = v_E + v_{OM}(y) \quad (6.7)$$

As shown in Figure 6.3a,  $v_{OM}$  varies throughout the depth of the cell, while  $v_E$  is constant at all depths. Thus, it is impossible to measure the true electrophoretic velocity

by observation at any random depth of the cell. However, there will be a certain location between the wall and the cell centerline where no net flow of liquid occurs. Such a null position is denoted the “stationary level”, and it is the only level in the cell where true electrophoretic velocity can be measured.

To determine electroosmotic flow inside the cell, a hydrodynamic description of fluid flow in the cell is required. Following Komagata’s treatment, consider a closed rectangular cell filled with electrolyte where electroosmotic flow is induced by a uniform electric field of strength  $E$  applied along the length of the cell (the  $z$  direction according to the scheme of Figure 6.3b). With establishment of steady-state, fully-developed, laminar flow in the cell, a hydrodynamic description of the flow is afforded by the Navier–Stokes equation:

$$\frac{\partial^2 u}{\partial x^2} + \frac{\partial^2 u}{\partial y^2} = \frac{-\Delta p}{\mu_f l} \quad (6.8)$$

where  $u(x,y)$  is fluid velocity in the  $z$  direction,  $\mu_f$  is the dynamic viscosity of the aqueous solution,  $l$  is the cell length, and  $\Delta p = p_2 - p_1$  is the pressure difference along the  $z$  direction.

In a rectangular cell of height  $2b$  and depth  $2a$  (as shown in Figure 6.3b), one seeks a solution to equation (6.8) that is subject to the following boundary conditions at the cell wall:

$$u(\pm b, y) = u_{os} \quad (6.9a)$$

$$u(x, \pm a) = u_{os} \quad (6.9b)$$

where  $u_{os}$  is the electroosmotic flow velocity induced at the cell wall.

By using the separation of variable method, the following solution is obtained:

$$u(x,y) = u_{os} + \frac{\Delta p}{2\mu_f l}(a^2 - y^2) + \frac{\Delta p}{\mu_f l} \sum_{n=0}^{\infty} (-1)^{n+1} \frac{16a^2}{\pi^3(2n+1)^3} \frac{\cosh\left[\frac{(2n+1)\pi x}{2b}\right]}{\cosh\left[\frac{(2n+1)\pi b}{2a}\right]} \cos\left[\frac{(2n+1)\pi y}{2b}\right] \quad (6.10)$$

For a closed system,

$$\int_b^b \int_a^a u(x,y) dy dx = 0 \quad (6.11)$$

or

$$4bau_{os} + \frac{4ba^3 \Delta p}{3\mu_f l} - \frac{\Delta p}{\mu_f l} \sum_{n=0}^{\infty} \frac{256a^4}{\pi^5(2n+1)^5} \tanh\left[\frac{(2n+1)\pi b}{2a}\right] = 0 \quad (6.12)$$

For large values of  $b/a$ , the velocity equation (6.10) for  $x=0$  reduces to the approximate form:

$$\frac{u(0,y)}{u_{os}} = 1 - \frac{3(1 - \frac{y^2}{a^2})}{2 - \frac{384a}{\pi^5 b}} \quad (6.13)$$

and so the depth,  $y_o$ , at which the velocity is zero in the median plane of the cell is given by

$$y_o = \pm \sqrt{\frac{1}{3} + \frac{128a}{\pi^5 b}} \quad (6.14)$$

This expression is referred to as the Komagata correction, and it shows that the position of the stationary level is a function of the geometric parameters of the cell only. If the cell is narrow, for example, the ratio of  $b/a \geq 20$ , the second term in equation (6.14) is small enough to be negligible, and hence it leads to the stationary level occurring at

$$y_o = \pm \sqrt{\frac{1}{3}} \quad (6.15)$$

which indicates for a channel of  $b/a \geq 20$ , the hydrodynamic flow inside the cell can be approximately treated as a parallel-plate flow (i. e., a parabolic flow (Hunter, 1981)) and the relative error induced by this approximation is less than 3 %. It should be noted that in the Komagata's treatment, the electroosmotic flow was considered to occur at the cell

wall with a constant velocity  $u_{or}$  (see the boundary conditions expressed by equations (6.9a, b)). This was based on an assumption that neither the hydrodynamic velocity profile nor the net electrostatic charge was present inside the *EDL* near the wall. This obviously goes against the fact that the electroosmotic flow is induced from the presence of the net electrostatic charge inside the *EDL*. As a matter of fact, the physical process occurring within the cell is very complicated. There exists a strong coupling among velocity, pressure, electric, and ion concentration fields, so that the real electroosmotic flow distributions should resemble the curves shown in Figure 6.3a. Recently, electrokinetic phenomena inside a rectangular geometry were investigated by Yang and Li (1997, 1998a, 1998b). Following the approach proposed by Yang and Li, a more rigorous model for describing the electroosmotic flow inside a rectangular geometry with taking into account all aforementioned effects has been developed and the detail is given in Appendix 4. While, this new model adds to the theory of electrokinetics, compared to the Komagata correction (i.e., equation (6.14)), the newly derived mathematical expression for the electroosmotic flow (see Appendix 4) is so complex that it is not trivial issue to obtain the “real” value for  $y_o$ .

### 6.2.3.2 Temperature Rise during Measurement

Liquid temperature rise during measurement is another potential problem existing at the electrophoresis cell. It has been recognized that the presence of temperature change will introduce thermal convection, and hence cause a measurement error in the electrophoretic mobility (Sirois and Millar, 1973; Collins et al. 1978). Two possible sources are responsible for causing an increase in liquid temperature. One is absorption of thermal radiation emitted from an optical source; the other is Ohmic heating (Hunter, 1981) created from the applied electric field. In the present apparatus, only a weak illumination was used. By using an infrared filter, most of thermal radiation was eliminated before the light entered the cell. Major attention should be focused on effectively control or minimize the so-called Ohmic heating effect. In the following, a quantitative relation will be established in order to evaluate the liquid temperature increase due to the Ohmic heating.



Similar to the problem addressed for hydrodynamic flow inside the cell, it is also difficult to precisely formulate heat transfer inside the cell. Strictly speaking, the heat transfer process itself should be classified as a thermal convection with non-uniform heat generation, and coupled with hydrodynamic flow, electrostatic potential, and ionic concentration fields. In this situation, even seeking a numerical solution is very cumbersome. Since the cell depth is only 1 mm, for simplicity, the heat transfer is approximately treated as lumped system of rectangular geometry. Accordingly, the total power of Ohmic heating,  $W$ , generated from the applied uniform electric field of strength  $E$  across the electrolyte is calculated as follows:

$$W = i^2 R \quad (6.16)$$

where  $i$  is the electric current through the cross-section of the cell and  $R$  is the electric resistance of the aqueous phase inside the cell.

From the definition, the electric resistance is given by

$$R = \frac{l}{K A} \quad (6.17)$$

where  $l$  is the cell length,  $A$  is the cross-section area of the cell, and  $K$  is the electric conductivity of the aqueous solution. The electric conductivity  $K$ , in turn, can be related to the ionic mole concentration,  $c$ , and the mole conductivity,  $\lambda$ , of the same type of the electrolyte by the following

$$K = 1000 \lambda c \quad (6.18)$$

Meanwhile, the electric current  $i$  is determined by

$$i = E K A \quad (6.19)$$

On the other hand, the heat gain of the system,  $Q$ , due to an increase of liquid temperature,  $\Delta T$ , is expressed as

$$Q = c_{v,f} \rho_f l A \Delta T \quad (6.20)$$

where  $c_{v,f}$  and  $\rho_f$  are the specific constant volume heat capacity and the density of the liquid solution, respectively. If the heat loss through the cell wall is neglected, the heat gain should balance the heat generated, which takes the form

$$c_{vf} \rho_f l A \Delta T = i^2 R \Delta t \quad (6.21)$$

where  $\Delta t$  is the time interval during which the electric field is imposed. Substituting equations (6.17 – 6.19) into the above equation and rearranging leads to an expression for  $\Delta T$ :

$$\Delta T = \frac{K E^2 \Delta t}{c_{vf} \rho_f} = \frac{1000 \lambda c E^2 \Delta t}{c_{vf} \rho_f} \quad (6.22)$$

This equation clearly shows the liquid temperature increase inside the cell is proportional to the solution mole conductivity  $\lambda$ , solution concentration  $c$ , time of imposing electric field  $\Delta t$ , and the square of the field strength  $E$ , but is independent of the cell geometric parameters. Typical calculations of liquid temperature increase under different solution conditions are listed in Figure 6.4.

### 6.2.3.3 Mass Transfer and Hydrodynamic Behavior of a Microbubble

Electrophoresis is classified as a dynamic method to characterize a surface charge. In the present method, microbubbles were generated from electrodes, and then measurements were carried out right away. As mentioned earlier, several mechanisms, such as asymmetric water dipole molecules and adsorption of ions from solution, may be responsible for the charge of bubbles. Schechter (1998) has proven that bearing charge of the interface is thermodynamically energy favorable. When any new interface is created, the charge due to asymmetric water dipole molecules occurs instantly. However, the adsorption of ions from solution usually takes time. Therefore, questions arise as to when the measurement is taken, and whether the process of bubble charging has reached equilibrium or not. In the following, an approach is developed to approximately model the bubble charging process due to adsorption of ions from solution. The surface adsorption concentration is assumed as the Gibbs surface excess (Collins et al., 1978; Perea-Carpio et al., 1986). A correlation for low Reynolds number mass convection is used to estimate mass transfer coefficient. Then based on mass transfer rate, the time for bubbles to achieve equilibrium is calculated.

By definition, the mole number of ions,  $N_A$ , transferred from the bulk solution to the surface of the bubble in time  $\Delta t$  is

$$N_A = \alpha_A A \Delta c \Delta t \quad (6.23)$$

where  $A$  is the area of the bubble surface,  $\Delta c$  is the ion concentration difference between the bubble interface and the bulk phase, and  $\alpha_A$  is the mass transfer coefficient. The mass transfer process occurring in this experiment is approximated as low Reynolds number convection diffusion around spheres. The corresponding models of mass transfer in creeping flow were formulated by Happel (1958) for spheres and by Epstein and Masliyah (1972) and Coutelieis et al. (1993) for non-spheres. For simplicity, if a dilute bubble number concentration is assumed, then the problem can be formulated as mass transfer from a quiescent unbounded fluid to an adsorbing sphere moving through it. An analytical expression was obtained by Levich (1962)

$$Sh = 0.997 Pe^{1/3} \quad (6.24)$$

where  $Sh$  is Sherwood number ( $Sh = \frac{\alpha_A a_p}{D}$ ) and  $Pe$  is Peclet number ( $Pe = \frac{U_b a_p}{D}$ ). The mass diffusivity coefficient,  $D$ , is determined from the Einstein – Stokes equation

$$D = \frac{kT}{f} \quad (6.25)$$

where  $k$  is the Boltzmann constant,  $T$  is the absolute temperature of the solution, and  $f$  is ion or large molecule friction coefficient, which is obtained from the literature (van de Ven, 1989).

It should be pointed out that equation (6.24) holds when the Stokes law is applicable to the rising bubble having a constant velocity. According to Collins et al. (1978), a gas bubble with a radius of  $a_p = 40 \mu m$  reaches its terminal velocity within 0.05 seconds, suggesting that microbubbles can attain their terminal velocity almost instantly. Furthermore, the implementation of Stokes law to the bubble suggests that the microbubble can be treated as a rigid sphere. To explore this treatment, first consider the Reynolds number of a microbubble, that is defined as

$$\text{Re}_b = \frac{\rho_f U_b a_p}{\mu_f} \quad (6.26)$$

where  $U_b$  is the bubble's terminal rising velocity, which is estimated on the basis of a force balance between buoyancy and Stokes drag acting on the bubble:

$$\frac{4}{3}\pi a_p^3 \Delta\rho g = 6\pi\mu_f a_p U_b \quad (6.27)$$

where  $\Delta\rho = \rho_f - \rho_p$  is the density difference between the liquid phase,  $\rho_f$ , and the gas phase,  $\rho_p$ .

Rewriting equation (6.27) gives

$$U_b = \frac{2\rho_f a_p^2 \Delta\rho g}{9\mu_f} \quad (6.28)$$

Submitting  $U_b$  into equation (6.25), the Reynolds number for a microbubble of radius  $a_p = 50 \mu\text{m}$ , under room temperature of  $20^\circ\text{C}$  is estimated to be on the order of  $\text{Re}_b = 0.1$ . As discussed earlier, the deformation of gas bubble is characterized by both the Capillary number,  $Ca$ , and Weber number,  $Wb$ , which were defined in Chapter 3. For the same bubble size ( $a_p = 50 \mu\text{m}$ ), both  $Ca$  and  $Wb$  are estimated to be in the order of magnitude of  $10^{-5}$  to  $10^{-4}$ , leading to a conclusion that microbubbles retain spherical shape during the whole measurement process. Another related condition is the no-slip boundary condition must be fulfilled at the bubble surface. This issue has already been addressed in the section 3.10 of Chapter 3.

At the equilibrium, the number of moles  $N_A$  on the surface of the bubble is also equal to

$$N_A = \Gamma_A A \quad (6.29)$$

where  $\Gamma_A$  is the surface excess, which is related to the change of interfacial tension through the following Gibbs thermodynamics equation (Gibbs, 1961):

$$\Gamma_A = -\frac{c}{2RT} \frac{d\gamma_{lv}}{dc} \quad (6.30)$$

where  $R$  is the universal gas constant,  $T$  is the absolute temperature,  $c$  is the ionic concentration of the solution, and  $\gamma_{lv}$  is the interfacial tension of between the solution and gas bubble.

Substitution of equations (6.29) and (6.30) back into equation (6.23) yields the time required for equilibrium

$$\Delta t = - \frac{c}{2RT\alpha_A \Delta c} \frac{d\gamma_{lv}}{dc} \quad (6.31)$$

Even though that the exact value of  $\frac{d\gamma_{lv}}{dc}$  is dependent on the type of solution and the solution concentration, it can be approximated as  $\left| \frac{d\gamma_{lv}}{dc} \right| \approx \frac{\gamma_o}{c}$  ( $\gamma_o$  is the gas-water interfacial tension and is taken as  $72.6 \text{ mJ/m}^2$ ). Obviously, the concentration difference,  $\Delta c$ , shown in equation (6.31) decreases with time, but as a guide it may be chosen as the bulk concentration in the calculation, since at the initiating moment,  $t=0$ , the freshly generated bubble surface contains no solution.

For a  $40 \mu\text{m}$  diameter microbubble in an aqueous solution with ionic concentration of  $10^{-3} \text{ M}$ , the Stokes rising velocity is approximately equal to  $0.87 \text{ mm s}^{-1}$ . Assuming the ion size is of the order  $10^{-9} \text{ m}$ , the mass diffusivity coefficient,  $D$ , is estimated as  $2.2 \times 10^{-10} \text{ m}^2 \text{ s}^{-1}$ . From the mass transfer correlation given in equation (6.24), the Sherwood number  $Sh$  is 2.0, leading to the mass transfer coefficient  $\alpha_A = 4.2 \times 10^{-5} \text{ m s}^{-1}$ . Hence, equation (6.31) gives  $\Delta t \cong 0.33 \text{ s}$ . This “time to equilibrium” is only a rough guide but it suggests that the microbubbles reach equilibrium after moving only a few bubble diameters from the place of formation.

#### 6.2.4 Error Estimate for Electrophoresis Measurement

Based on Smoluchowski equation (6.6), the zeta – potential of gas bubbles can be rewritten as

$$\zeta = \frac{\mu_f v_E}{\varepsilon_r \varepsilon_o E} \quad (6.32)$$

Replacing the electric field strength  $E$  by equation (6.19) yields

$$\zeta = \frac{\mu_f v_E K A}{\varepsilon_r \varepsilon_o i} \quad (6.33)$$

Equation (6.33) is used to calculate the bubble zeta-potential from experimentally measured parameters,  $v_E$ ,  $K$ ,  $A$ , and  $i$ . Since  $\frac{\mu_f}{\varepsilon_r \varepsilon_o}$  is only dependent upon physical properties of the solution, it can be considered as constant throughout the experiments. Taking the logarithmic operation on the equation (6.33) and then differentiating the resultant equation gives the error transfer equation for the zeta – potential measurement of fine bubbles

$$|\Delta\zeta| = \sqrt{|\Delta v_E|^2 + |\Delta K|^2 + |\Delta A|^2 + |\Delta i|^2} \quad (6.34)$$

As will be described in the following experimental part, the electrophoretic velocity of gas bubbles is determined from transverse distance of the bubble divided by the time during which the electric field is applied. For the present system, the accuracy of measuring the transverse distance and the time are around 1  $\mu\text{m}$  and 0.05 s, respectively, giving  $|\Delta v_E|$  of about 1.5 %. It should be noted that this error estimate is based on an assumption that the electrophoretic velocity is measured at the stationary level. Because of the presence of the electroosmotic flow, the deviation of the stationary level will also induce measurement error in  $|\Delta v_E|$ , which unfortunately is difficult to quantify from theory but is approximated from the experiments as 8 % here (details to follow in the following experimental section). According to the manual of the electric conductance meter (for the electric conductivity) and the multiple-meter (for the electric current), it suggests that the measurement errors of  $\Delta K$  and  $\Delta i$  are within 3 % and 0.5 %, respectively. In addition, the cross-section area  $A$  of the cell is the product of the cell depth by the cell height. The cell height is taken from manufacturer value as 10 mm. The cell depth, needs calibration with a micrometer (see section 6.3.2), which gives an uncertainty of 2.5 %. Overall, the relative measurement error for the zeta – potential of gas bubbles using the present apparatus is approximately 10%.

## 6.3 Experimental

### 6.3.1 Equipment Configuration

An experimental setup was built for measuring the zeta-potential of gas bubbles. A schematic diagram of such experimental apparatus is shown in Figure 6.5. The entire system of the apparatus can be decomposed of three parts: the electrophoresis system, the positioning and motion control system, and the optical video-image system. A brief description of each part is given below.

#### 6.3.1.1 Electrophoresis System

The electrophoretic system consists of a microelectrophoretic cell, a pair of electrodes for generating an electric field, and a unit for producing microbubbles across the cell. A commercial microelectrophoretic cell (Rank Brothers Co., Cambridge, England), originally designed for particle electrophoresis measurement, is used in this experiment. The quartz cell has a rectangular cross section and internal dimensions of  $l$  (depth,  $2a$ ) $\times$ 10 (height,  $2b$ ) $\times$ 40 (length,  $l$ ) mm as shown in Figure 6.3b. Two original platinum electrodes (Rank Brothers Co., Cambridge, England) are inserted into two wings extending from each side of the cell. The electrodes are connected to a circuit that consists of a DC constant voltage power supply (Xantrex Technology Inc., Burnaby, B. C., Canada) for generating a uniform electric field along the cell length, a specially-designed switch box for change of polarity of the electrodes, and a digital meter for recording electric current (needed to determine the strength of the electric field). Near the bottom of the cell, two fine holes are drilled into the front and back of the cell wall. These two holes are aligned in such a way that a line going through them forms a certain angle, for example  $45^\circ$ , with the cell wall. A tiny platinum wire with a diameter of  $25\ \mu\text{m}$  is slotted in these two holes and sealed with silicon sealant to prevent liquid leakage. By imposing the electric voltage to the platinum wire, microbubbles in essence can be evenly generated across the whole cell (along the cell depth). The platinum wire is grounded so that the bubbles are not charged from the circuit.

### **6.3.1.2 Positioning and Motion Control System**

The positioning and motion control system includes a tilt table, a vertical translation stage and its controlling system, and a manually controlled X-Y translation stage. A specially constructed cell holder is mounted on the tilt table (ORIEL Instruments, Straford, CT, U.S.A.) that allows for the adjustment of the working plate of the tilt table around two horizontal axes to within a resolution of  $0.25^\circ$ . This ensures that the cell wall remains vertical. The tilt table is placed on a vertical translation stage driven by DC motor (Newport Co., Irvine, CA, U.S.A.) which is connected up to a computer through a motion controller (Newport Co., Irvine, CA, U.S.A.) using a standard RS 232 interface. By manipulating a joystick, the vertical translation stage can move up-and-down instantly at a variable speed up to 2.5 mm/s. The base of the vertical translation stage is attached to a manually operated X-Y (i.e., horizontal) translation stage with a LCD indicator (ORIEL Instruments, Straford, CT, U.S.A.) with a resolution of  $1\ \mu\text{m}$ . This allows the cell to be positioned in alignment with the microscope. Since the zeta-bubble potential measurement is very sensitive to vibration, all systems are set on a vibration isolation table (TMG, CT, U.S.A.).

### **6.3.1.3 Optical Video-Image System**

Illumination produced by a fiber optical light is incident on the cell. On the other side of the cell, a microscope is placed to focus on the cell. The microscope is attached with an adapter connected to a CCD camera, a timer, a TV monitor, and a S-VHS VCR. Such an optical video-image system provides the means to view the bubble's motion and to record the whole process for subsequent determination of the electrophoretic velocity.

### **6.3.2 Calibration of the Cell Depth**

Since the depth of the cell is directly related to the location of the stationary level that is where the bubble's electrophoretic mobility was observed, a method used for determination of such cell depth in this study is described below. When the microscope (using  $40\times$  objective lens) was focused on the inner front wall of the cell, the reading on the LCD of the X-Y horizontal translation stage was set to zero. Then the fine adjust was turned until the inner back wall of the cell was in focus and the reading was taken as the



depth of the cell. The cell walls were easily identified due to flecks of dirt or small imperfections on the glass. Calibrations were carried out for the cell under both dry and wet (filled with *DIUF* water) conditions with the results being summarized in Table 6.1. Generally speaking, as shown in Table 6.1, there was no significant difference in the cell depth between dry and wet measurements. In addition, measurements taken at different positions within the cell indicate that the cell is quite uniform in depth (see Table 6.1). The uniformity of cell depth is important, since variability in cell depth would cause more complicated hydrodynamic flow patterns inside the cell. Furthermore, non-uniformity in cell depth would mean that the location of stationary levels would vary locally rather than being fixed at the two requisite planes as indicated by equation (6.14).

### 6.3.3 Determination of the Stationary Level

The electrophoresis is essentially simple observation of electrophoretic velocity in response to an applied external electric field. In reality, determination of the electrophoretic velocity is not as simple as dividing the measured travel distance by a randomly chosen bubble over a recorded time interval. The measurements are complicated by the simultaneous occurrence of electroosmotic flow due to the presence of surface charge of the cell wall. As was mentioned earlier, upon application of an electric field, not only does electrophoretic migration occur, but also an electroosmotic flow of liquid is present near the cell wall. For a closed system, this is coupled with a compensation return flow of liquid with the maximum velocity occurring at the cell center. The result is a parabolic distribution of particle velocity varying with cell depth. As such, true electrophoretic velocity can only be observed at the so-called stationary level, where the electroosmotic flow and the return flow of liquid exactly balance each other as shown in Figure 6.3a.

Komagata (1937) developed a theoretical approach to evaluate the electroosmotic flow inside a rectangular cell, from which an equation (i.e., equation (6.14)) was derived to determine the stationary level within microelectrophoretic cell of rectangular geometry. Realizing some unrealistic assumptions made by Komagata (1937), a more rigorous model of describing the electroosmotic flow inside rectangular cell has been

developed in this work (see Appendix 4). However, the rigorous model leads to cumbersome mathematics. Instead, an experimental approach is introduced here to find out the location of the stationary level (Hunter, 1981).

Equation (6.7) indicates that in electrophoretic measurements, the observed velocity,  $v_{OB}$ , usually is the summation of the true electrophoretic velocity,  $v_E$ , and the liquid velocity,  $v_{OM}(y)$ , resulted from electroosmosis. As shown in Figure 6.3a,  $v_{OM}(y)$  varies throughout the depth of the cell, while  $v_E$  is constant at all depths. Integrating equation (6.7) over the cell depth leads to

$$\int_{-a}^a v_{OB}(y) dy = 2 a v_E + \int_{-a}^a v_{OM}(y) dy \quad (6.35)$$

According to electrokinetics theory (Hunter, 1981; Masliyah, 1994), for a closed cell system the volume flow due to electroosmosis at the median plane of the cell (i.e.  $z = \frac{1}{2}$ ) should be zero,

$$\int_{-a}^a v_{OM}(y) dy = 0 \quad (6.36)$$

Then the second term on the right hand of equation (6.35) drops off and the electrophoretic velocity,  $v_E$ , can be expressed as

$$v_E = \frac{1}{2a} \int_{-a}^a v_{OB}(y) dy = \frac{1}{2} \int_{-1}^1 v_{OB}\left(\frac{y}{a}\right) d\left(\frac{y}{a}\right) = \frac{1}{2} \int_{-1}^1 v_{OB}(Y) dY \quad (6.37)$$

where  $Y = \frac{y}{a}$  is the non-dimensional coordinator along the cell depth. Equation (6.37) shows that the electrophoretic velocity is the integral area under the observed velocity ( $v_{OB}$ ) curve divided by the cell depth  $2a$ .

Submitting equation (6.37) back into equation (6.7) gives an expression for the liquid electroosmotic velocity

$$v_{OM} = v_{OB} - \frac{1}{2} \int_{-1}^1 v_{OB}(Y) dY \quad (6.38)$$

As indicated in equation (6.38), the electroosmotic velocity can be obtained by conducting measurements at varying positions within the cell, or more directly, from the observed velocity distributions across the cell.

Electrophoretic experiments were carried out for spherical silicon particles (Geltech, Inc., U.S.A.) having a mean size of  $2.5 \pm 0.5 \mu\text{m}$  dispersed in a  $10^{-4} \text{ M NaCl}$  solution (prepared in an ultrasonic bath). The results are shown in Figure 6.6, in which the solid circle represents the observed velocity,  $v_{OB}$ , and the solid line was fitted by using the statistical least square method from these data. The dotted line in Figure 6.6 is the distribution of the electroosmotic velocity,  $v_{OM}(y)$ , determined from equation (6.38). By setting  $v_{OM} = 0$ , the stationary level of the cell can be found from the values of  $y$ , giving almost symmetric values from the center of the cell, 0.286 and  $-0.299$ . Taking an average of these two values, one obtains 0.293 as the stationary level of the cell where the influence of the electroosmotic flow can be neglected. This is the position where the bubble zeta-potential measurements will be carried out. This value agrees quite well with the theoretical value of the stationary level, 0.306, predicted by the Komagata correction equation (6.14). Furthermore, the zeta-potential of the silicon powder was calculated to be  $-43.1 \pm 4.5 \text{ mV}$  based on the measured electrophoretic velocity distributions. As a comparison, an electrophoretic measurement for the silicon powders was carried out under the same solution condition using Lazer Zee Meter (Pen Ken, U.S.A.) and an average zeta-potential value of  $-47.6 \text{ mV}$  was obtained.

It should be mentioned that the theoretical prediction of the stationary level inside the cell assumes that the point of observation is at the center of the cell. In the experiments, the bubble trajectory was actually observed in the range of about 3.0 mm vertically above and below the center. To check the validity of this range, the electrophoresis experiment for silicon powders in  $10^{-4} \text{ NaCl}$  was also performed at these two extreme points, i.e. 3.0 mm vertically above and below the center. As shown in Figure 6.6 (open triangles represent experiments conducted at +3mm, while open squares represent experiments conducted at -3mm), it was found the difference of the

electrophoretic velocity between these two points is only about 8%. It is expected the average error in the electrophoretic velocity of a bubble would be less since the bubble traverses the whole region, and in the middle of its path the error should be zero.

#### **6.3.4 Experimental Procedure**

Cleanliness of the cell is extremely important for electrophoretic measurements. Each newly-purchased cell was cleaned by using the following rigorous procedure: First, the cell was submerged in an ultrasonic bath filled with detergent diluted in *DIUF* water for 15 minutes, and followed by intensively washing with Acetone and then *DIUF* water. Following the wash, the cell was soaked in a mixture of Chromic-Sulfuric Acid solution for 2 hours, subsequently thoroughly rinsed with *DIUF* water. Then a platinum wire was inserted through the two holes near the bottom of the cell and sealed with silicon. Once the silicon was complete dried, the cell was cleaned again using a mixture of Nitric acid and Hydrochloric acid. Finally the cell was rinsed and stored in the *DIUF* water.

Before each experiment, the cleaned cell was installed and aligned. The alignment procedures were as follows. At first, the pre-cleaned cell filled with the prepared testing solution was assembled on the cell holder. Next a pair of pre-cleaned electrodes were inserted into the cell wings and then gently twisted to make the two roughed glass parts, between the cell and the electrodes, firmly connected. This ensures that when an external electric field is imposed, the electroosmotic flow occurred inside in a closed system. As mentioned earlier, one of the important features of the current experimental setup is that the electrophoretic measurements were carried out at the stationary level where the trajectory of bubbles was followed by utilizing a computer-controlled vertical translation stage. In order to ensure that the measurements were always conducted at the stationary level when the cell moves down, it is required that the cell wall should be perpendicular to the microscope objective. Hence, the cell wall should be vertical. This requirement was achieved using the following steps: 1) Move the translation stage up to the top of the cell and adjust the focus of the microscope on the one side of the cell wall and record the value of X-Y translation stage; 2) Pull the vertical translation stage down to the bottom of the cell, adjust the focus of the microscope on the

same side of the cell wall, and take down another value of X-Y translation stage; 3) Set the X-Y translation stage to the average value of these two and simultaneously adjust the tilt table to make the microscope focus on the cell wall; 4) Repeat the above steps until the cell is aligned in such a position that the cell wall is always on focus when the vertical translation stage is moved up or down.

Once the adjustment was complete, the focus of the microscope was switched from the cell wall to the stationary level inside the cell and the video-image system was now ready to display and capture the bubble's trajectory during the electrophoretic measurement. When a short controlled burst of current, supplied by a power supply, was passed through the solution, fine gas bubbles were liberated (by gravity) via the platinum wire from the bottom of the cell. For an arbitrarily chosen bubble that was clearly in focus and moved at its terminal velocity, its trajectory (shown on the screen) is followed by moving the cell down via the motorized vertical translation stage that was controlled by the joystick. The diameter of examined bubbles fell within 10 to 70  $\mu\text{m}$ , because larger bubbles rose too fast to follow and smaller bubbles were readily dissolved due to effect of Laplace pressure on the solubility. At the same time, the digital multimeter read the electric current going through the cross section of the cell. Each measurement usually took only about a few seconds and the power was turned off immediately so that the effect of the aforementioned Ohmic heating could be minimized. The whole process was recorded on a S-VHS video cassette for later analysis. Following the same procedure, another fourteen measurements were repeated under the same solution conditions. In order to minimize the electrode polarization effect, the polarity of the electrodes was alternatively changed between two consecutive measurements. All tests were performed at the constant room temperature 22°C.

## **6.4 Results and Discussion**

Experiments of bubble electrophoretic mobility were carried out for various solution conditions including concentration, pH, and metal ion, which are essentially the same as those run for impinging jet experiments that will be described in Chapter 7. Aqueous solutions were prepared from *DIUF* water (purchased from Fisher Scientific,

Canada) with addition of American Chemistry Society (ACS) certified reagent grade chemicals such as  $NaCl$ ,  $CaCl_2$ , and  $AlCl_3$  supplied by Fisher Scientific and used without further purification. In addition, the bubble electrophoretic mobility in the so-called synthetic water and process water was also examined. The electrokinetic information of fine bubbles in these two solutions is of great interest to the flotation process used by Syncrude Canada Ltd. for bitumen recovery. The process water was taken directly from an operation plant of Syncrude. The synthetic water is a simulation of the process water on the basis of the same inorganic components, but free of surfactants and impurities.

As defined earlier, the electrophoretic mobility,  $V_E$ , is the ratio of the electrophoretic velocity,  $v_E$ , to the electric field strength,  $E$ . Recorded video was replayed to determine the electrophoretic velocity by dividing the transverse travel distance of a bubble under the influence of an applied external electric field by the time interval (also shown on the tape). The real transverse travel distance of the bubble was calibrated (under the same optical magnification) using a standard optic grid with a resolution of 1  $\mu m$ . Due to the complex charging mechanisms of fine bubbles dispersed in an aqueous solution, it was expected that randomly picked bubbles may not always acquire the same charge, even under the same solution conditions. In the literature, this scenario is referred to as a non-uniform distribution of bubble charge. Statistically, however, the mean value of the zeta-potentials measured over multiple bubbles dispersed in the same aqueous solution should strongly correlate to the aqueous solution property. Therefore, for the remainder of the chapter the final electrophoretic velocity refers to a mean value of electrophoretic velocity calculated by taking an average of fifteen to twenty measurements under the same solution conditions. According to equation (6.19), the electric field strength for each individual measurement was calculated on the basis of the recorded electric current,  $i$ , and the measured solution conductivity,  $K$ . Once the electrophoretic mobility was obtained, the zeta-potential of bubbles was calculated using Smoluchowski equation (6.33). In the subsequent sections, the results of bubble zeta-potentials under various solution pH values, solution concentrations, type of metal ions will be presented.

### 6.4.1 pH Effect

During the bubble zeta-potential measurements, the range of the solution pH varied approximately from 2.0 to 12.0. The solution pH was adjusted by adding reagent grade solution, either *NaOH* or *HCl*, into the prepared electrolyte solution. In Figure 6.7, the measured zeta-potential of fine bubbles dispersed in  $10^{-4}$  M *NaCl* solution is plotted as a function of the solution pH. It is well-known that for a non-ionogenic surface like the bubble-liquid interface, its electrokinetic property can be modified with alteration of solution pH values through the adsorption of anions (e.g.,  $OH^-$ ) and/or desorption of cations (e.g.,  $H^+$ ). Since decreasing the solution pH results in an exponential increase in the concentration of  $H^+$ , the adsorption of  $H^+$  ions onto the bubble-liquid interface neutralizes and hence reduces the negative zeta-potential as shown in Figure 6.7. Further lowering the pH values even reverses the charge sign, giving a positive zeta-potential. The change in charge sign at low pHs was also observed for the zeta-potential of oil droplets by Sanders et al. (1995) and even for coal particles by Hamieh and Stiffert (1994). On the other hand, when the solution pH increases, the adsorption of  $OH^-$  onto the bubble-liquid interface leads to development of strong negative zeta-potential of the bubble-liquid interface. Clearly, it can be seen from Figure 6.7 that the bubble zeta-potential monotonously declines from +21.7 to  $-64.6$  mV as the solution pH value changes from 2.4 to 11.8. This general trend was found in all zeta-potential measurements, irrespective of the type of particles (Hunter, 1981). Nevertheless, in comparison with  $Cl^-$  ions at low pHs or  $Na^+$  ions at high pHs,  $H^+$  or  $OH^-$  ions seem to have much stronger adsorption at the bubble-liquid interface and thus are responsible for positive or negative zeta-potential at low or high pH cases.

In addition, it is important to note from this plot that the measurement errors around the point of zero zeta-potential ( $pH \cong 3.5$ ) are larger than those at other pHs. This could be attributed to a deficiency in selecting bubbles exactly at the stationary level due to effect of the focus depth of microscope. Since bubbles are weakly charged at pH around the point of zero zeta-potential, a slight deviation of the stationary level may give rise to a relatively large measurement error.

Figure 6.8 shows a comparison of the bubble zeta-potentials in a  $10^{-2} M NaCl$  solution measured from this study and the data reported by Li and Somasundaran (1991). A common point is readily to identify that both studies show a similar dependence of the bubble zeta-potential upon the solution pH. However, it is notable that there is a systematical difference between the results obtained by Li and Somasundaran (1991) and those reported in this study. It turns out that the measured results by Li and Somasundaran (1991) may exaggerate the absolute values of the bubble zeta-potential. For instance, a bubble zeta-potential in a  $10^{-5} M NaCl$  solution at  $pH = 6.0$  was recorded to be  $-80 mV$  in their experiments. In contrast, Garaciaa and co-workers (1995a) reported that bubbles in deionized water ( $pH \cong 6.0$ ) only acquire a zeta-potential of  $-63 mV$ . Another supporting point is that in present study the bubble zeta-potential in  $10^{-2} M NaCl$  solution at  $pH = 7.0$  was found to be  $-34 mV$ , which is very close to the value of  $-32.78 mV$ , observed by Yoon and Mao (1996) for the bubble zeta-potential in  $10^{-2} M KCl$  solution under the same pH condition. From a chemistry point of view, the bubble zeta-potential in a  $NaCl$  solution should be comparable with that in a  $KCl$  solution under the same ionic strength and pH conditions.

#### 6.4.2 Electrolyte Concentration Effect

Experiments were run for  $NaCl$  solutions of concentration,  $10^{-4}$ ,  $10^{-3}$ ,  $10^{-2}$ , and  $10^{-1} M$  under a wide range of pH conditions. The effect of  $NaCl$  concentrations on the bubble zeta-potential is shown in Figure 6.9. It can be seen that the fine bubbles are negatively charged over a large portion of the pH range and the point of zero zeta-potential (pzz) occurs between  $pH = 2.5$  and  $pH = 3.5$  depending upon  $NaCl$  solution concentration. Furthermore, Figure 6.9 also shows that within the range of  $NaCl$  solution concentration studied, the bubble zeta-potential was found to decrease with an increase in  $NaCl$  concentration. It turns out that all colloidal particles give a very similar pattern of variation of the zeta-potential with concentration of electrolyte. This scenario can be understood as follows; Since bubbles usually bear a negative charge, an increase of  $NaCl$  solution concentration will cause more  $Na^+$  ions to absorb onto the bubble-liquid



interface due to mass convection – diffusion and electrostatic interactions. Accordingly, this results in neutralizing the bubble charge and hence decreasing the magnitude of bubble zeta-potentials.

### 6.4.3 Metal Ions Effect

Electrolyte effect, or more specifically multivalent metal ion effect, on the electrokinetic behavior of bubbles was examined in the same background solution of  $10^{-2} M NaCl$ . The bubble zeta-potential versus solution pH for various  $CaCl_2$  and  $AlCl_3$  concentrations are given in Figure 6.10 and 6.11, respectively. Two important features are readily identified from Figure 6.10. First, in the presence of  $Ca^{2+}$  ions, the absolute value of the bubble zeta-potential becomes less negative as the concentration of  $CaCl_2$  increases. Second, the location of the P.Z.Z. shifts to a larger pH with an addition of the ionic concentration level of  $CaCl_2$ . Presumably, these two features exhibited herein can be attributed to specific adsorption of divalent cations  $Ca^{2+}$  at the bubble-liquid interface.

It is worth mentioning that in principle, the electrokinetic behavior of particles in  $CaCl_2$  solution should be similar to that in  $MgCl_2$  due to a similarity in their chemical structure. This argument is experimentally supported by Rios et al. (1998) who performed experimental measurements of the zeta-potential of oil droplets in various aqueous solutions using the electrophoretic lighting scattering technique. However, the results of  $CaCl_2$  effect on the bubble zeta-potential given in Figure 6.10 do not exactly follow those of  $MgCl_2$  effect on the bubble zeta-potential observed by Li and Somasundaran (1991), but are consistent with those of  $CaCl_2$  effect on the coal particle and oil droplet zeta-potential, obtained by Hamieh and Stiffert (1994) and Rios et al. (1998), respectively.

In contrast to  $CaCl_2$ ,  $AlCl_3$  produced some unexpected effects. As shown in Figure 6.11, when the concentration of  $AlCl_3$  is  $10^{-5} M$ , the measured bubble zeta-

potential is very close to that without presence of  $AlCl_3$ , indicating that such a low concentration of  $AlCl_3$  does not have significant effect on the bubble zeta-potential. As the ionic strength of  $AlCl_3$  increases, for instance  $10^{-4}$  or  $10^{-3}$  M  $AlCl_3$ , it is noted that the bubble zeta-potential starts to change dramatically due to the presence of  $AlCl_3$ . Bubbles even become positively charged in the neutral pH range between 4.0 and 8.0, reaching a maximum of  $+33.5$  mV. Interestingly, above  $pH = 10.5$ , all curves merge together regardless of different concentrations of  $AlCl_3$ . These results clearly show that the addition of  $AlCl_3$  has a pronounced influence on the electrokinetic behavior of bubbles. In the literature, a strikingly similar trend of the trivalent cation  $Al^{3+}$  effect on the bubble zeta-potential was experimentally observed by Li and Somasundaran (1992). Based on a knowledge of the thermodynamic free energy of all possibly formed species, they constructed the species distribution diagrams and showed that within different pH zones, the bubble zeta-potential could exhibit positive or negative depending upon the selective adsorption of the potential dominating species such as  $Al^{3+}$  or  $Al(OH)_n$ . Obviously, the results presented in this study also can be rationalized using the same species distribution diagrams. Additional supporting examples are that bubbles were reported to carry positive charges in  $AlCl_3$  (Fukui and Yuu, 1980) and  $Al_2(SO_4)_3$  (Okada and Akagi, 1987) solutions. Nevertheless, it follows that in the presence of  $CaCl_2$  and  $AlCl_3$ , the bubble zeta-potential is completely determined by multivalent cations, while the anions have an insignificant effect on the bubble electrokinetic behavior.

#### 6.4.4 Zeta – Potential of Bubbles in Synthetic Process Water

As mentioned earlier, the bubble electrokinetic information is of great importance to the flotation process used by Syncrude Canada Ltd. for extracting bitumen from oil sands. Therefore, the bubble zeta-potential in the process water was studied, and the results are given in Figure 6.12. In all experiments, the solution  $pH$  varied from 7.7 to 8.6 due to the addition of different concentrations of  $CaSO_4$ . Before electrophoretic measurements were performed, the process water that was directly taken from an

operation plant at Syncrude was centrifuged (around 1000g) to remove fine solids. As shown in Figure 6.12, bubbles are strongly negatively charged in the process water. It is also noticed that the bubble zeta-potential becomes slightly less negative with the addition of  $CaSO_4$  because of the adsorption of  $Ca^{2+}$ .

Undoubtedly, the process water contains complex chemical components such as organic and surfactant species, and it is naturally “dirty” because of impurities. In laboratory tests, it is always advantageous to make synthetic water that is basically free of surfactants and impurities and chemically simple. Such synthetic water is simulating the process water on the basis of inorganic chemical components, which include 0.0587 M  $NaCl$ , 0.0023 M  $KCl$ , 0.0023 M  $Na_2SO_4$ , and 0.0246 M  $NaHCO_3$ . The bubble zeta-potential in the synthetic water was examined under influences of solution pH and calcium ions (through  $CaSO_4$ ). The corresponding results are presented in Figure 6.13 and Figure 6.14, respectively. A comparison made between Figure 6.12 and Figure 6.14 would show that the magnitude of the bubble zeta-potential in the synthetic water is approximately half of that in the process water. This could be largely attributed to the presence of anionic surfactants in the process water. In addition, Figure 6.13 indicates that an increase in pH value of the synthetic water tends to lower the absolute bubble zeta-potentials.

## 6.5 Summary

An experimental system was built to successfully implement the microelectrophoretic technique to measure the zeta potential of fine bubbles in various aqueous solutions. Micron-sized bubbles of diameters between 10 and 70  $\mu m$  were generated using the electrolysis method. The bubble trajectory could be followed and observed over 4 – 8 seconds by using computer-controlled motorized translation stage. The distribution of electroosmotic velocity was examined, and it was shown that the bubble electrophoretic velocity can be accurately measured provided the electrophoretic measurements were conducted at the stationary level. An experimental approach was developed to determine the stationary level in the cell. In addition, several other

phenomena involved in bubble electrophoresis measurements were discussed. These phenomena include temperature rise due to the Ohmic heating, hydrodynamic behaviors of fine bubbles in liquid, and “relaxation time” needed for exchange of ions between a bubble and the solution. Overall, the measured results presented herein are in a good agreement with those available in the literature.

The aqueous solution conditions were altered by varying pH values, concentrations, and electrolyte cations. In the cases of univalent *NaCl* solutions, it was found that bubbles are negatively charged in a large portion of pH range, and the point of zero zeta-potential is located approximately around  $pH \approx 3.0$ . The measured results indicate that neither  $Na^+$  nor  $Cl^-$  ions strongly adsorb at the bubble-liquid interface, and  $H^+$  or  $OH^-$  ions are essentially the potential-dominating ions in the present situation. Moreover, in the presence of multivalent metal ions such as  $Ca^{2+}$  and  $Al^{3+}$ , it was shown that the multivalent metal ions can change the magnitude of the bubble zeta-potential to a great extent and reverse bubble's charge polarity as well. The point of zero zeta-potential was found to shift to a larger pH value. Bubbles in  $AlCl_3$  solutions with concentration over  $10^{-4} M$  are positively charged even in the neutral pH range between 4.0 and 8.0. Nevertheless, all measured results have shown that the variation of the bubble zeta-potential with solution pH depends not only on the electrolyte concentration but also on the type of metal ions that may undergo specific interaction or adsorption with the bubble-liquid interface.

In addition, the zeta-potential of bubbles in Syncrude process water and synthetic water were presented, which is of significance to Clark Hot Water Process incorporated by Syncrude.

**Table 6.1** Calibration results for the cell depth

<b>Calibration of the cell depth 2a (<math>\mu\text{m}</math>)</b>	<b>Empty Cell</b>			<b>Filled with Water</b>
	<b>Point A</b>	<b>Point B</b>	<b>Point C</b>	<b>Point D</b>
<b>1</b>	1055	1079	1056	781
<b>2</b>	1095	1104	1043	827
<b>3</b>	1101	1082	1045	794
<b>4</b>	1065	1069	1078	770
<b>5</b>	1119	1092	1053	805
<b>6</b>	1089	1054	1072	824
<b>Average depth (<math>\mu\text{m}</math>)</b>	1072	1080	1058	800
<b>Converted depth (<math>\mu\text{m}</math>)</b>				1066

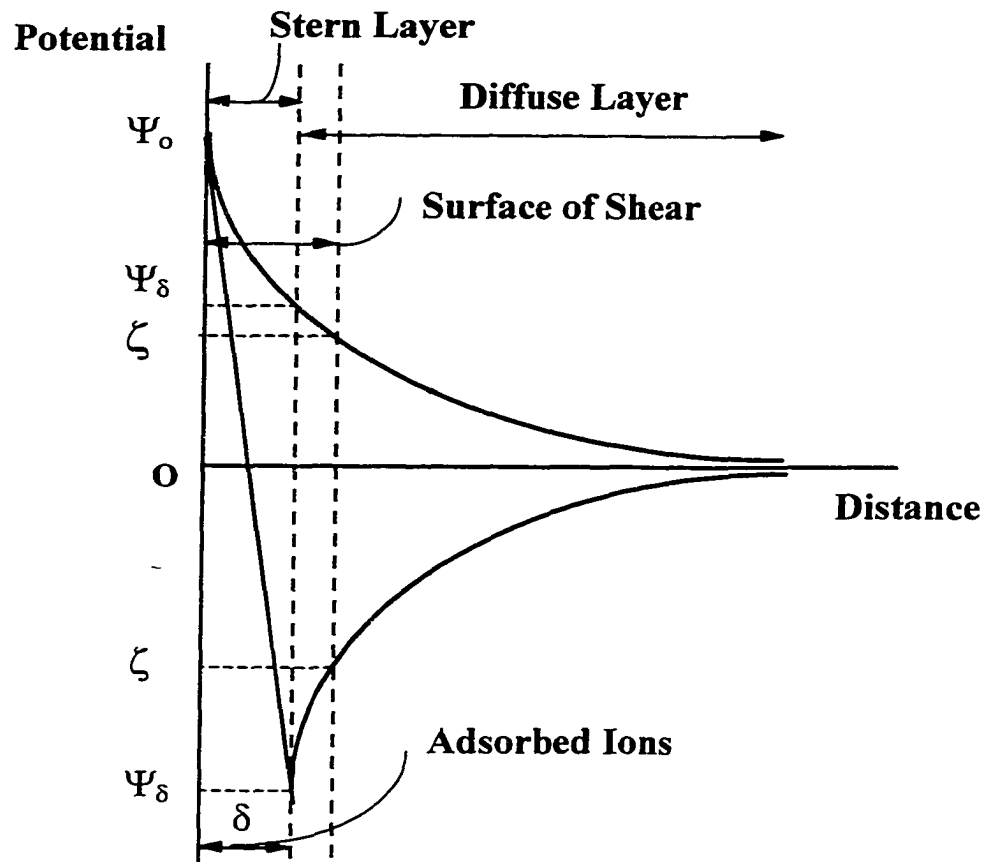


**Figure 6.1** The structure of the *EDL* formed at a surface of potential  $\Psi_0$ ; The lower curve representing strong adsorption within the Stern layer

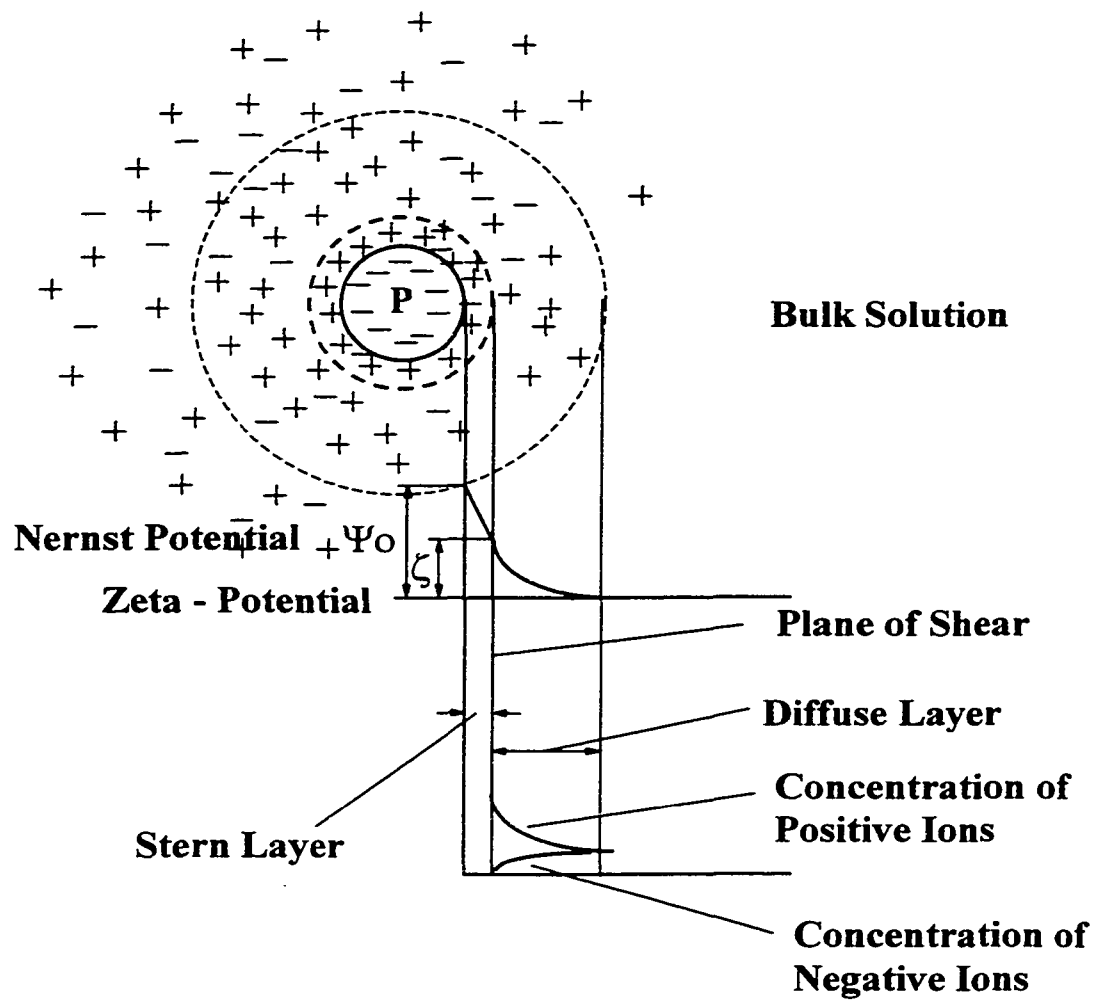


**Figure 6.2** Schematic diagram representing charge distributions around a negatively charged particle

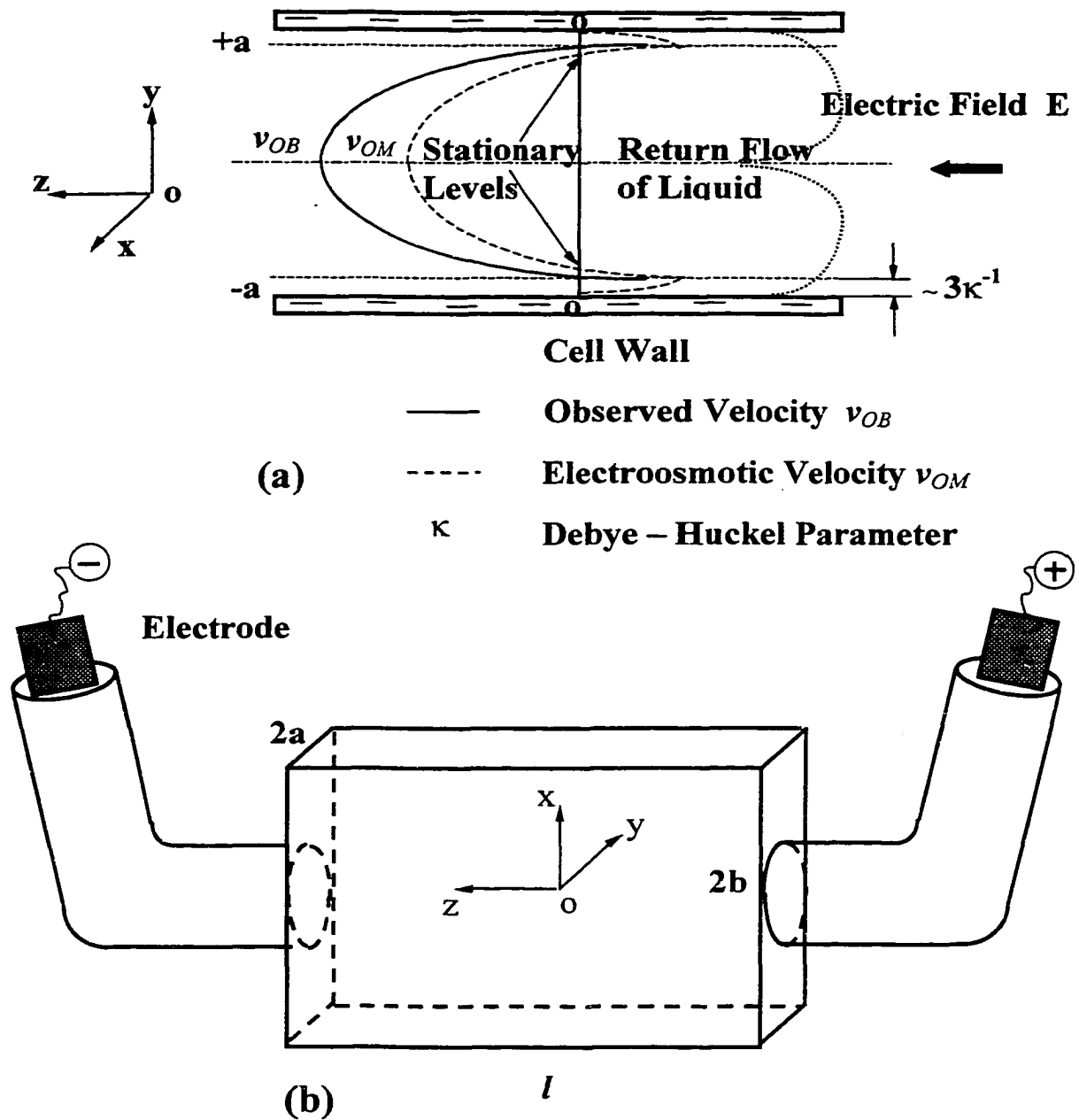


**Figure 6.3 (a)** Velocity distributions in X-Y cross section of the rectangular electrophoretic cell (the thickness of EDL layer of varying velocity close the cell wall has been greatly exaggerated.)

**(b)** Geometric configuration of the electrophoresis cell and Cartesian coordinate system for evaluation of electroosmotic flow in the rectangular cell



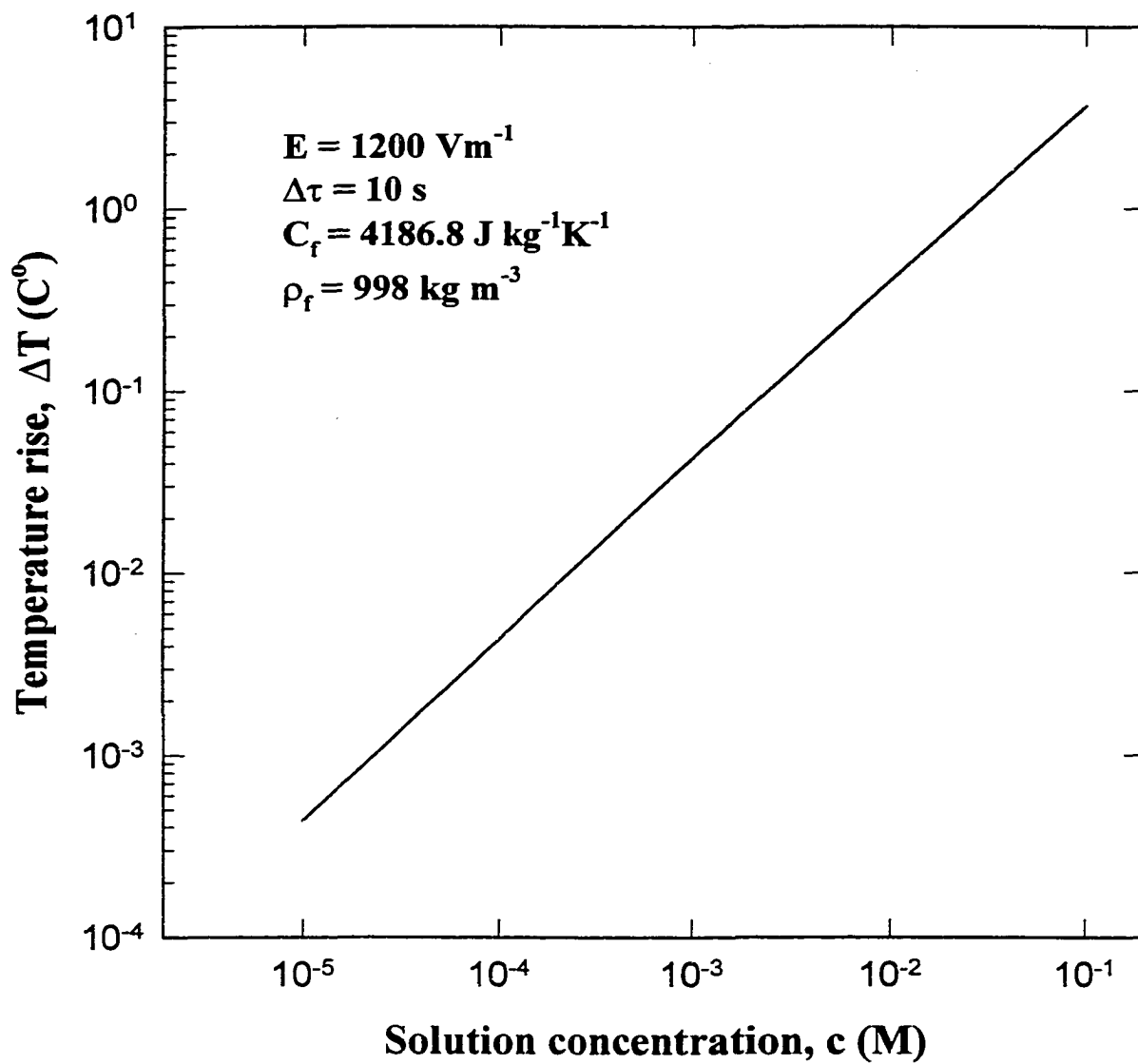


**Fig 6.4** Temperature rise of solution during electrophoresis measurements due to Ohmic heating

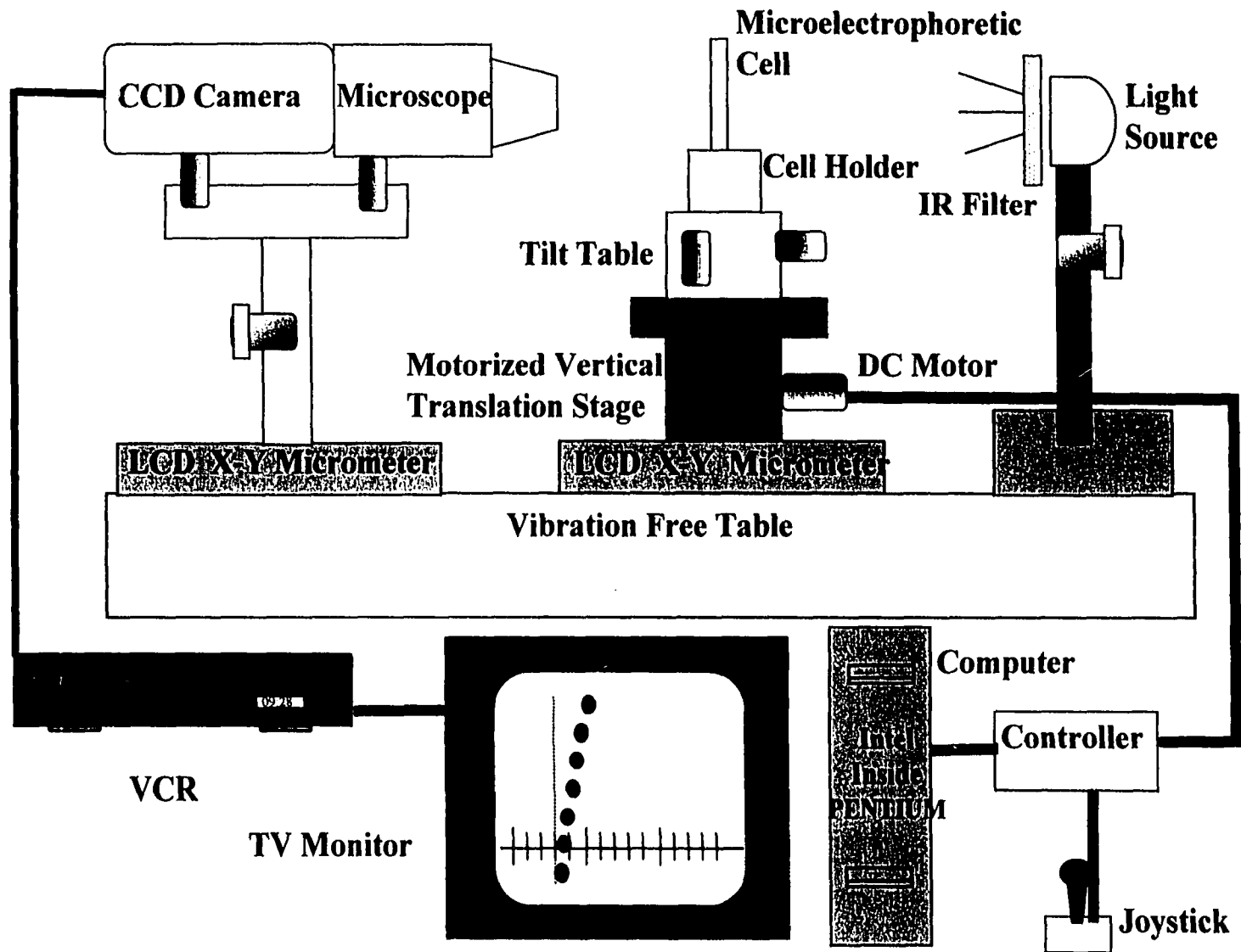


**Figure 6.5** Schematic of experimental setup for measurement of the zeta-potential of fine bubbles using microelectrophoresis technique

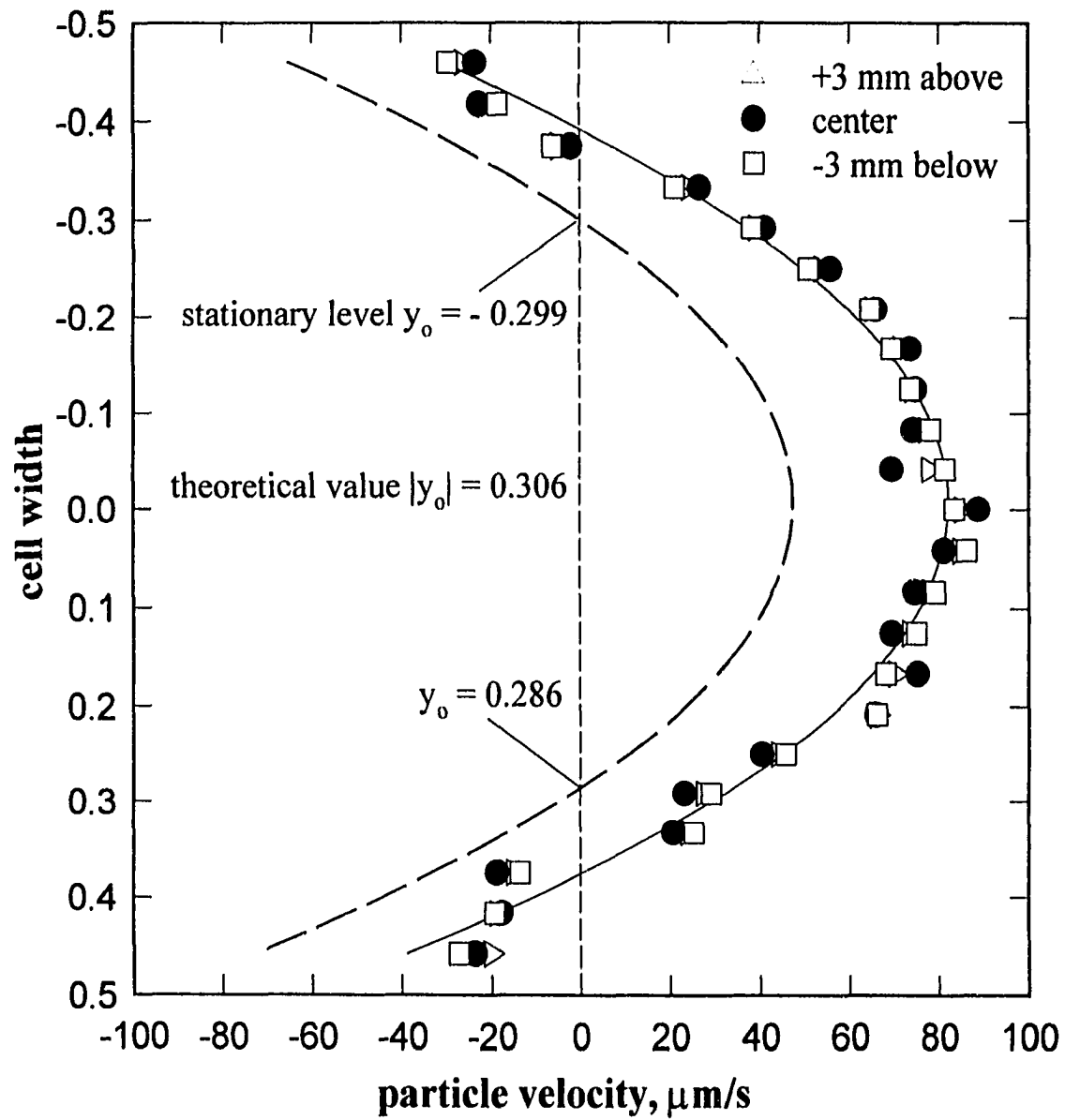


**Figure 6.6** Measured particle velocity distributions

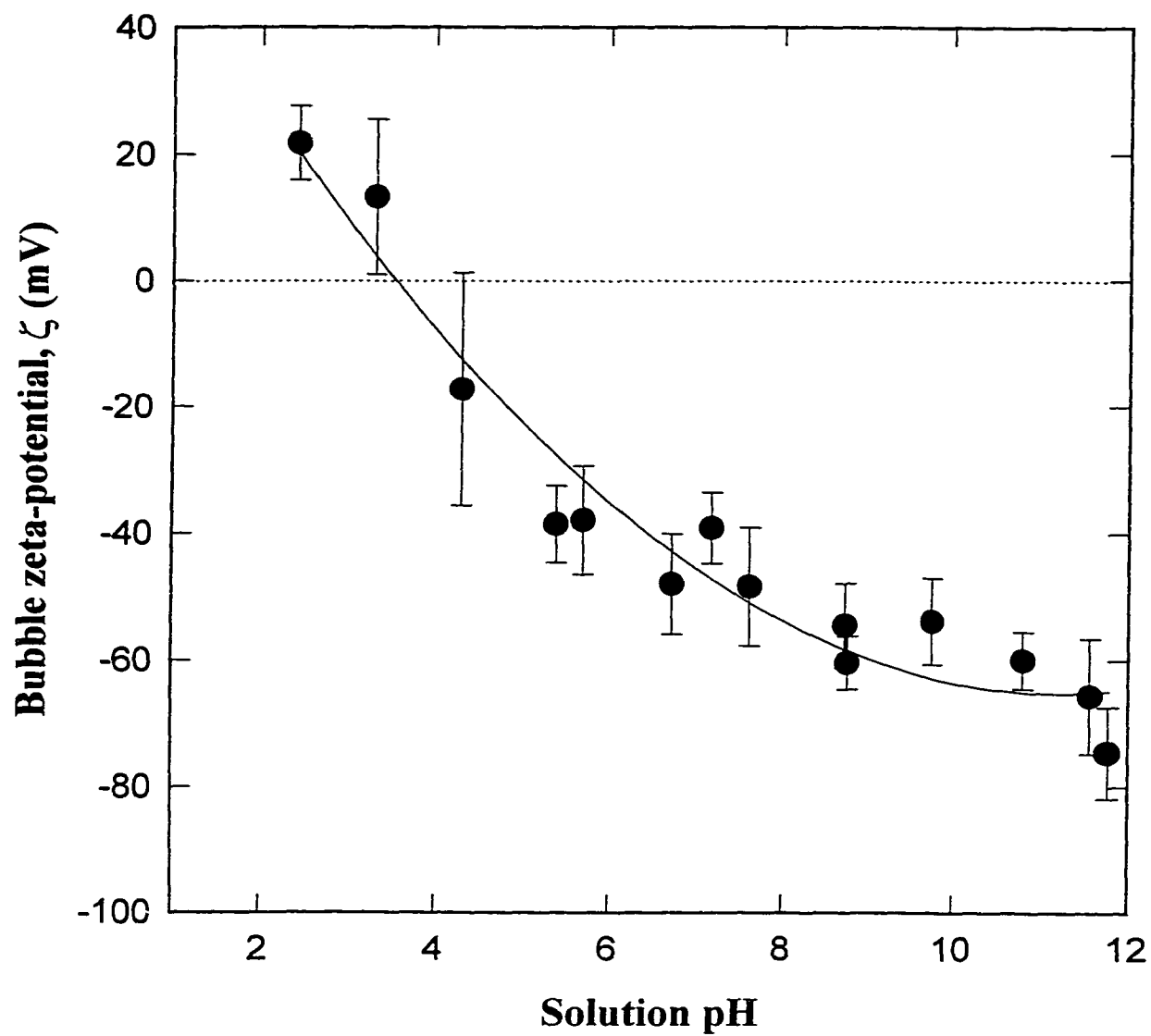


**Figure 6.7** Measured zeta-potential of fine bubbles dispersed in a  $10^{-4}$  M NaCl solution

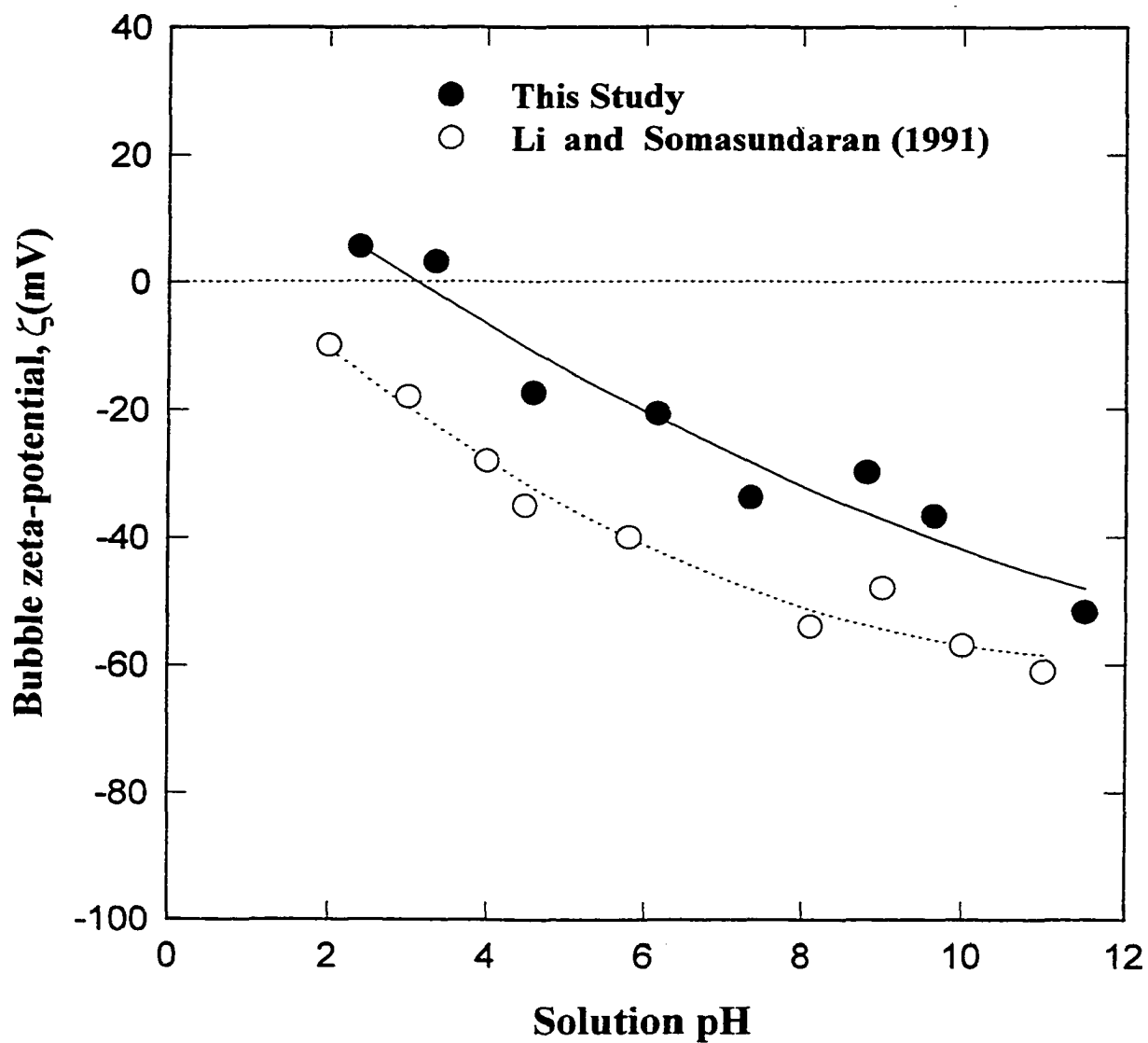


**Figure 6.8** Comparison of the bubble zeta-potentials in a  $10^{-2}$  M NaCl solution measured from this study with the data reported by Li and Somasundaran (1991)

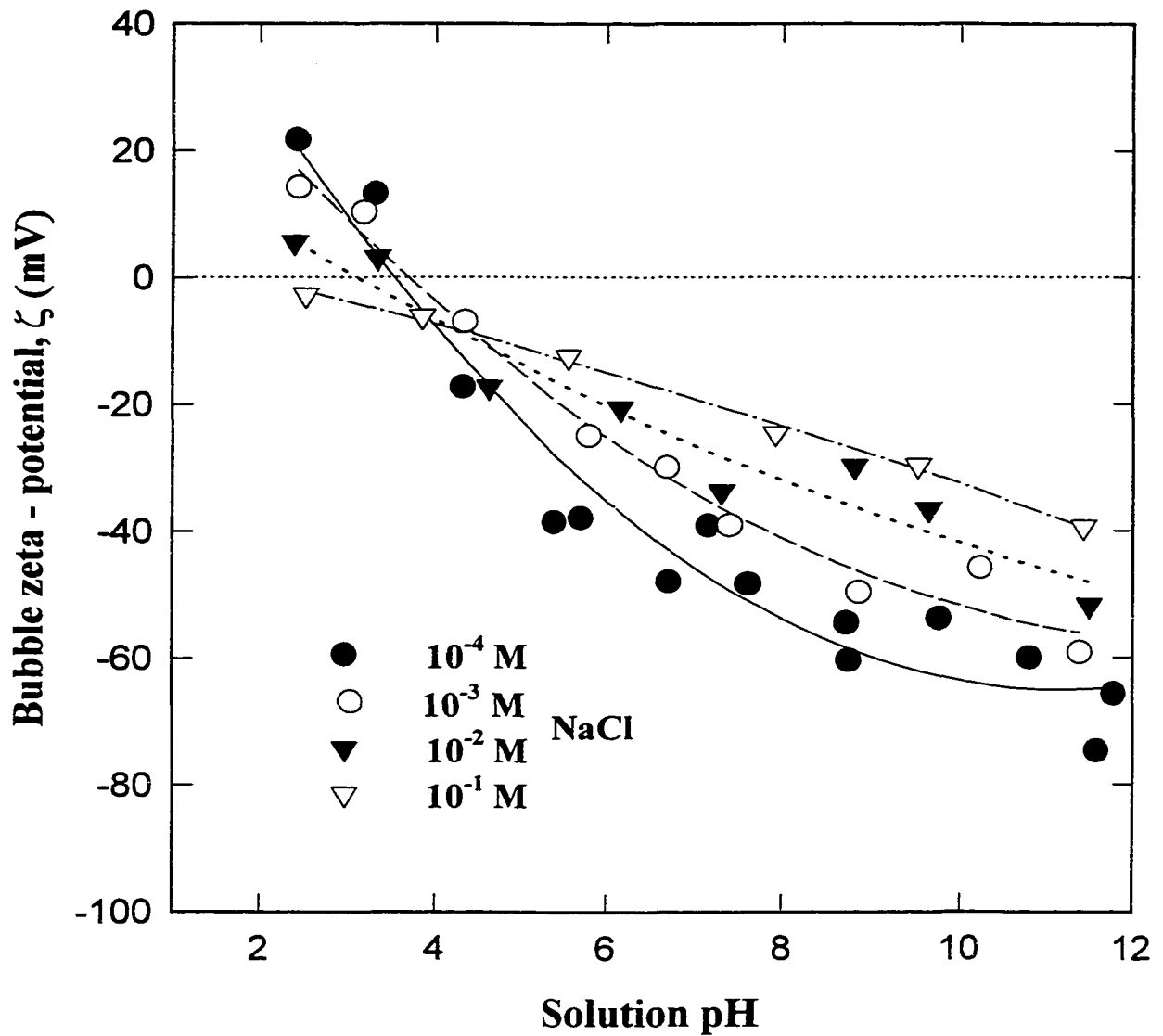


**Figure 6.9** Measured zeta-potential of fine bubbles versus solution pH for different concentrations of the *NaCl* solution

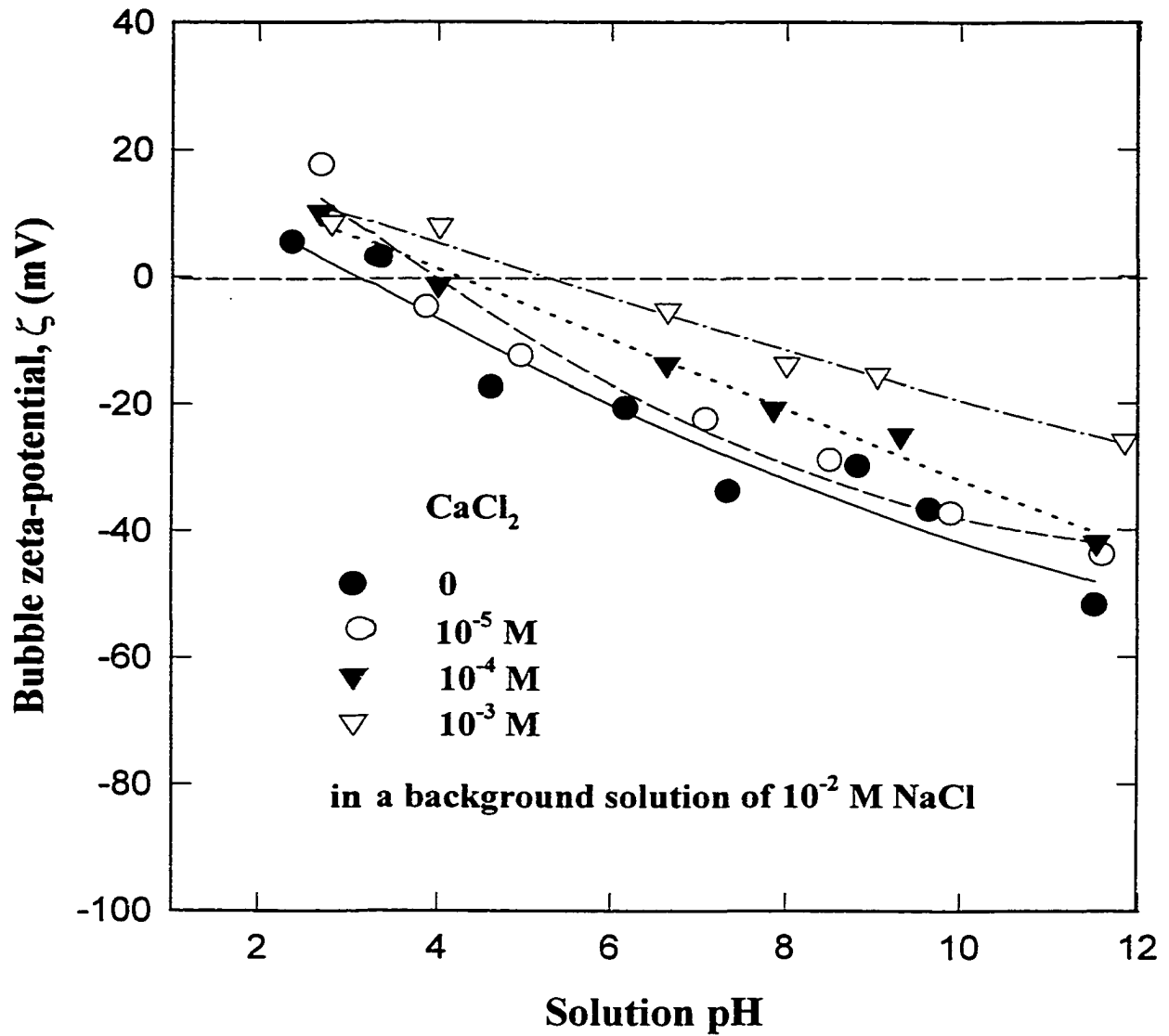


**Figure 6.10** Measured zeta-potential of fine bubble versus solution pH in a  $10^{-2}$  M  $\text{NaCl}$  solution with addition of  $\text{CaCl}_2$

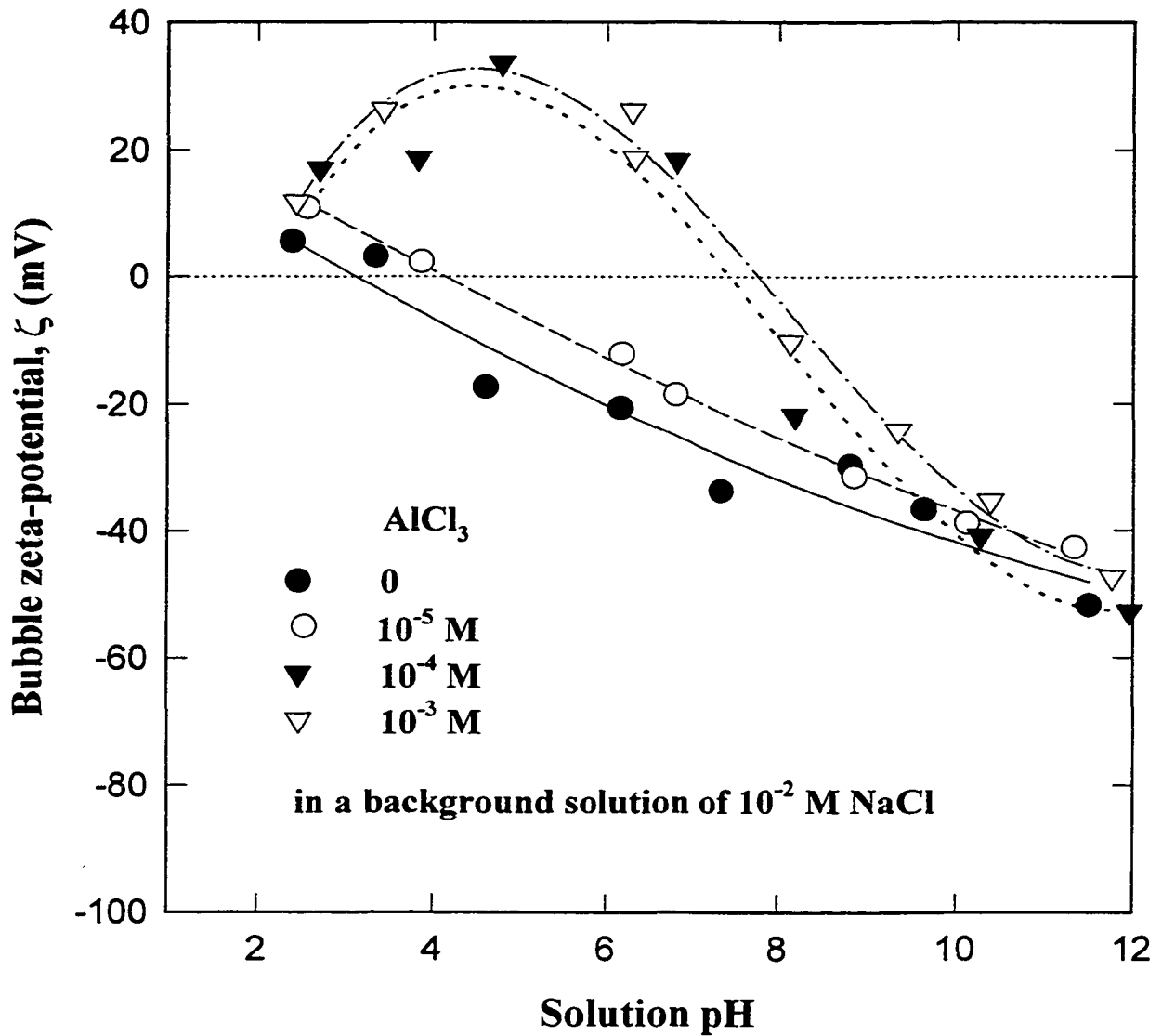


**Figure 6.11** Measured zeta-potential of fine bubbles versus solution pH in a  $10^{-2}$  M  $\text{NaCl}$  solution with addition of  $\text{AlCl}_3$



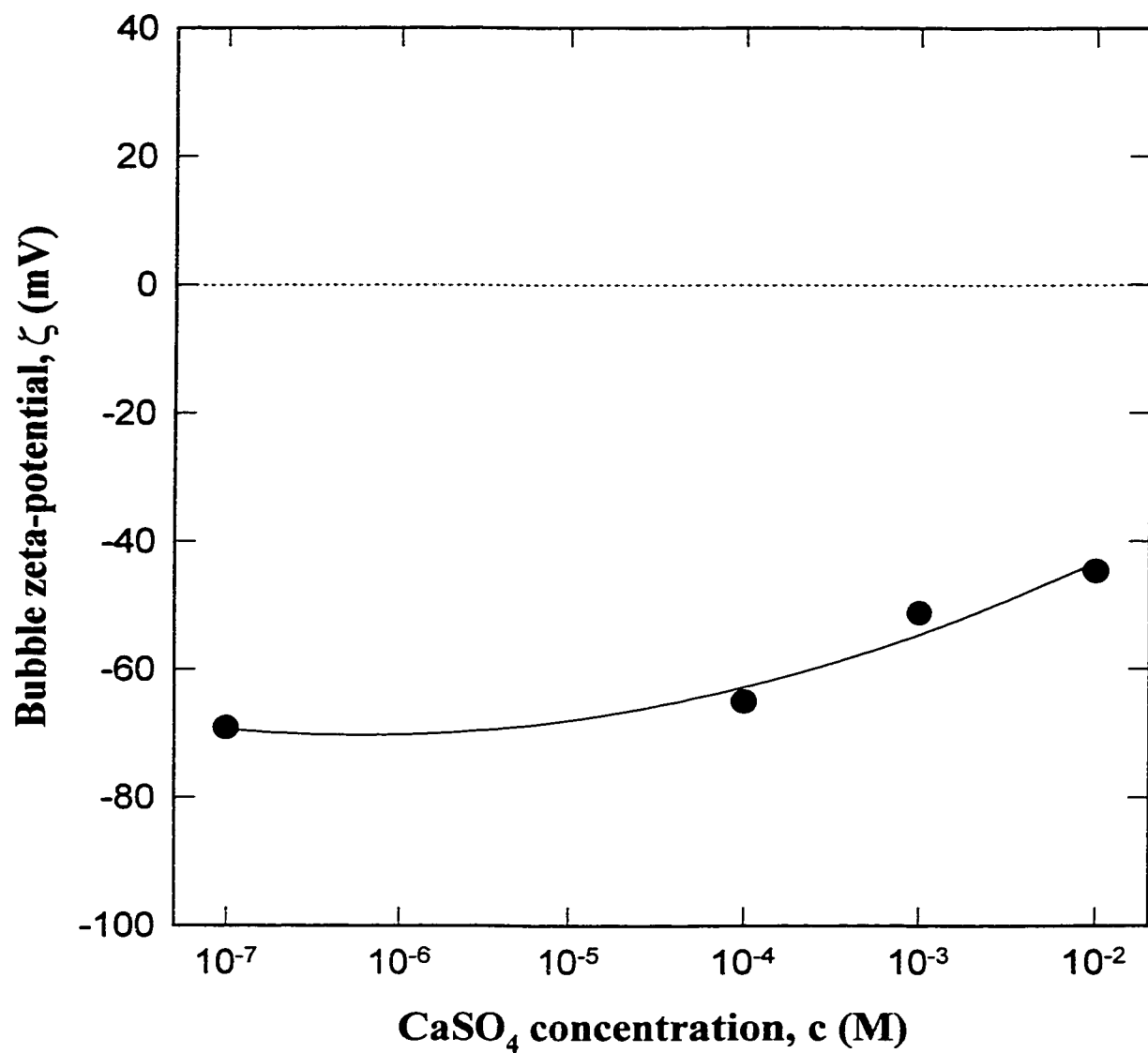


**Figure 6.12** Bubble zeta-potential in Syncrude process water with addition of  $\text{CaSO}_4$

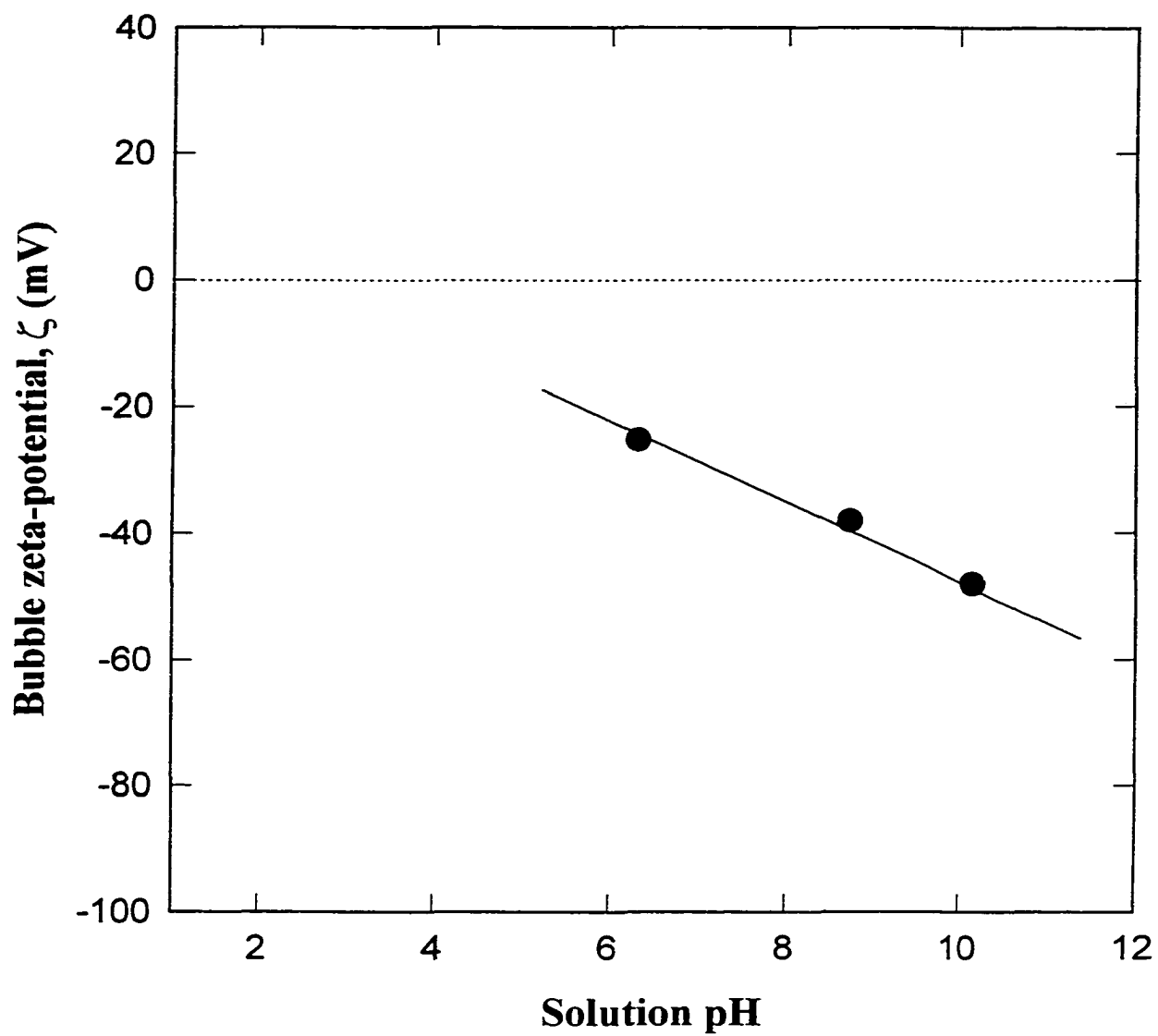


**Figure 6.13** Bubble zeta-potential in synthetic water for different pH values

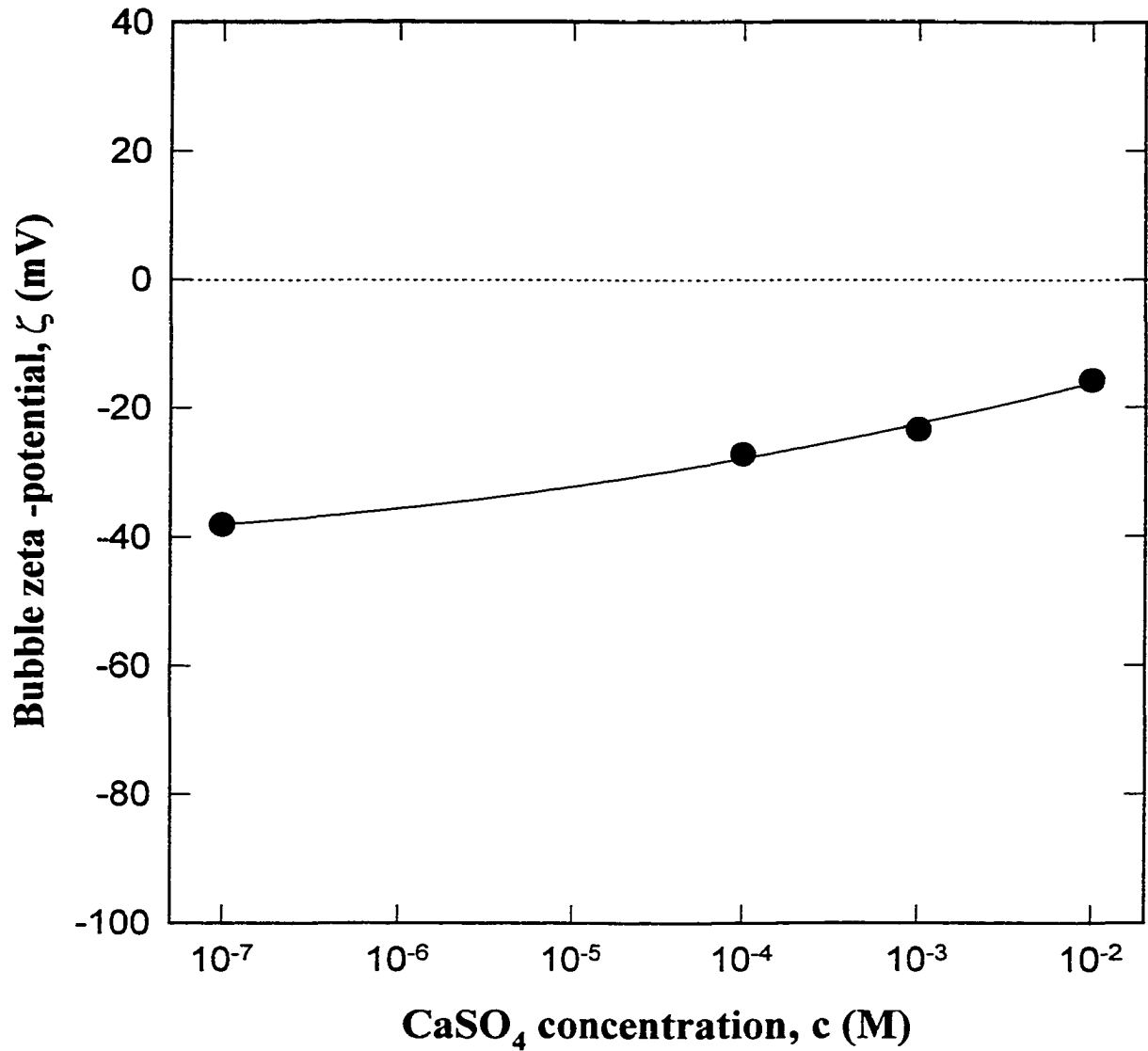


**Figure 6.14** Bubble zeta-potential in synthetic water with addition of  $\text{CaSO}_4$

## CHAPTER 7

# BUBBLE ATTACHMENT RESULTS FOR MODEL COLLECTOR SURFACES

### 7.1 Introduction

In Chapter 3, a model was developed to describe bubble attachment onto a solid surface in the impinging jet region. The model shows that the bubble attachment process (characterized by the Sherwood number,  $Sh$ ) is governed by buoyancy force, hydrodynamic convection, and colloidal surface forces. These effects are expressed in terms of the dimensionless parameters  $Gr$ ,  $Pe$ ,  $Ad$ ,  $Dl$ ,  $Da$  and  $\tau$ . In Chapter 4, thorough parametric tests were performed to evaluate the effects of these dimensionless parameters on the bubble attachment rates by numerically solving the bubble transport equation. Numerical predictions presented in Chapter 4 not only revealed the role of each dimensionless parameter in bubble transport processes, but also provided a guideline for designing the corresponding experimental investigations. From an experimental point of view, the impinging jet technique is fairly straightforward to implement. Through manipulation of experimental conditions, the Reynolds number ( $Re$ ) and  $EDL$  parameters ( $Dl$ ,  $\tau$ , and  $Da$ ) are readily controlled and quantified. However, this is not the case for gravity force,  $Gr$ , and van der Waals interactions, which are characterized by the bubble size,  $a_p$ , and Hamaker constant,  $A$ , respectively. Both  $a_p$  and  $A$  are usually not controllable during the experiments. Fortunately, numerical analysis presented in Figure 4.4 amply demonstrates that bubble attachment in the impinging jet region is insensitive to the choice of the adhesion number,  $Ad$ , or Hamaker constant,  $A$ . In other words, this suggests that it is relatively meaningless to create experimental conditions to change the Hamaker constant within a range of one or two orders of magnitude only. Thus, no attempt was pursued to experimentally examine the effect of van der Waals interaction on bubble attachment. The gravity number,  $Gr$ , on the other hand, can always be determined through experimentally measured bubble size distributions. Therefore, experimental

emphasis in this work was placed on the influence of the hydrodynamic ( $Re$ ) and  $EDL$  parameters ( $DI$ ,  $\tau$ , and  $Da$ ) on bubble attachment; such an approach has never been satisfactorily pursued in the literature before.

The main purpose of this chapter is to conduct a systematic experimental investigation of fine bubble attachments onto two model collector surfaces (i.e., hydrophobic methylated and hydrophilic untreated glass slides) under varying Reynolds number,  $Re$ , electrolyte concentration (i.e., ionic strength), solution pH, and types of metal ions. Another important goal is to provide thorough experimental data which can be directly compared with the numerical predictions to ensure validation and improvement, if possible, of fundamental bubble attachment models. Furthermore, it is also worth mentioning that experiments carried out for two model collector surfaces having significantly different surface characteristics enable one to directly observe the different dynamic behaviors of bubbles as they approach or attach on the collector surfaces. Accordingly, the role of collector surface characteristics in bubble attachment can be further elucidated.

In the following sections, the model surfaces will first be characterized in terms of contact angle and surface roughness using the captive bubble method (described in Chapter 5) and the Atomic Force Microscope (AFM) technique respectively. Then, the bubble size distribution and the bubble zeta-potential under each experimental condition will be determined. After that, the impinging jet experimental results of bubble attachment will be presented, and these experimental data will subsequently be compared with numerical predictions based on the bubble transport equation. Finally, detailed discussions are provided to rationalize the bubble attachment results.

## **7.2 Collector Surface Preparation and Characterization**

Both untreated and methylated collector surfaces were made from glass microscopic slides ( $50 \times 75 \times 1$  mm, Fisher Scientific). They were prepared according to the approach outlined in Chapter 5. First, a rigorous cleaning procedure was followed to prepare the untreated glass. Then the methylated glass was obtained by coating the

cleaned glass surface with “organofunctional silanes” (Araujo et al., 1995). The characteristics of these glass surfaces can be evaluated using contact angle measurement, which was described in Chapter 5. The results of contact angle measurements for both untreated and methylated glass surfaces under corresponding experimental conditions are summarized in Table 7.1. It should be pointed out that for untreated glass slides, contact angle measurements could only be accomplished for those bubbles that were immobilized at the slide surface. However, most of the freshly created bubbles very slowly slipped away, indicating a very small - perhaps zero contact angle. Indeed, it was always difficult to accurately measure such small contact angles. As expected, relatively large measurement errors were associated with these contact angle measurements. Furthermore, it was observed that water droplets placed on the untreated glass slide spontaneously spread over the surface, clearly demonstrating a high-energy, hydrophilic surface for such collectors. Nonetheless, average contact angles of the untreated glass were less than  $10^\circ$ . On the other hand, contact angles for methylated glass slides were found to be always larger than  $90^\circ$ , indicating that the surface is very hydrophobic in nature. Moreover, measurements showed no apparent dependence of contact angle on solution concentration, pH, and type of metal ions. This observation is in accordance with the results reported for contact angles of paraffin surfaces (Zhou et al., 1998). In addition, it is also noted that the measured contact angles obtained here are higher than those reported by Yoon and Mao (1996). The discrepancy may be attributed to the different procedures used for treatment of the methylated surface. In the literature, it has been demonstrated that the contact angle of methylated surfaces is strongly dependent on treatment conditions such as temperature, concentration, chemical ingredients, and procedures, under which the methylated surfaces are prepared.

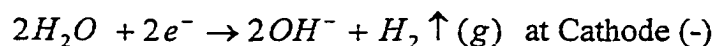
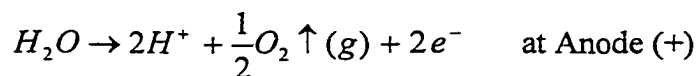
The roughness of the collector surface is another important characteristic which can be quantified using atomic force microscope (*AFM*) techniques. The *AFM* scan images for both untreated and methylated glass slides are shown in Figures 7.1a and 7.1b, respectively. The surface roughness for these two surfaces falls in the range of 10 – 30 nanometers. It can be seen that the surface roughness of methylated glass falls in the lower bound of this range, while the surface roughness of untreated glass is in the higher

bound of this range, indicating that the methylated glass is slightly smoother than the untreated glass due to formation of a thin film on the methylated surface during treatment of the glass surface. Thus, with the use of “organofunctional silanes”, not only does it modify the hydrophobicity of the surface, but it also smoothens the roughness.

Generally, there exists two widely-accepted methods of measuring zeta-potentials of solid-liquid interfaces (Hunter, 1981; Lyklema, 1993). The first method is based on electrophoresis, in which the glass slide is first ground into fine powders, and which are then dispersed into an aqueous solution for measurements. Following the procedure discussed in Chapter 6, the glass zeta-potential can be obtained through measurement of its electrophoretic mobility. In the second method, the so-called streaming potential technique is implemented to measure the streaming potential of a liquid flowing through a channel whose wall is made from the glass material. Both of these two methods are well-established and commercial apparatus is available. Since a large amount of work on measurement of glass zeta-potentials has been published, all such zeta-potential used in the present study were directly taken from the literature and they are listed in Table 7.2.

### 7.3 Bubble Generation and Characterization

There are several ways such as electrolysis, dissolved gas and dispersed gas, by which fine bubbles can be generated. Of these, the electrolysis method is the most promising for the present study as it could produce small bubbles with a relatively narrow distribution of bubble sizes (Burns et al., 1997). In this method, water is split into its molecular constituents by applying a voltage over two electrodes across the solution. Fine bubbles formed during electrolysis are generated due to the following reactions occurring at these two electrodes:



Bubble sizes can be analyzed from the same recording as for the bubble attachment experiments. By playing back the recorded videotape at a slow speed, bubble

sizes were estimated by randomly selecting a few hundred bubbles rolling on or approaching the glass slide. An optical grid was videotaped for reference calibration. Figures 7.2 shows the bubble size distributions measured in a  $10^{-2} M NaCl$  solution for various Reynolds numbers. It can be seen that the diameter of most bubbles falls in the range from 10  $\mu m$  to 80  $\mu m$  with average size of 20 – 30  $\mu m$ , consistent with the results reported by Burn et al. (1997). Furthermore, the bubble sizes were found to be strongly dependent on the Reynolds number. In addition, experiments showed that the number of bubbles produced per unit time was related to the applied voltage or current. However, it appears that the bubble size distribution was not strongly correlated with the solution concentration, pH, and type of electrolytes. No appreciable difference in the bubble size was observed for different types of collector surfaces.

Under certain circumstances in which the colloidal repulsive forces are weak or negligible and the bubble Peclet number is large, the following approximate formula for bubble attachment rate (in terms of the Sherwood number  $Sh$ ) in the impinging jet flow can be readily developed

$$Sh = \frac{1}{2} Pe + Gr \quad (7.1)$$

The above relation is identical to equation (4.18) (for a detailed derivation of this equation, refer to Chapter 4). This equation indicates that with the above assumptions, the bubble attachment rate  $Sh$  is essentially controlled by the Peclet number,  $Pe$ , and the gravity number,  $Gr$ . By definition, both  $Pe$  and  $Gr$ , in turn, are proportional to  $a_b^4$  ( $a_b$  being the radius of bubble). This suggests that the bubble size plays a crucial role in bubble attachment.

The zeta-potentials of fine bubbles under various experimental conditions were determined using the method described in Chapter 6, and the results are shown in Table 7.2



## 7.4 Bubble Attachment onto Methylated Glass Collectors

Attachment of a bubble was considered to take place when a bubble adheres on the glass slide. This criterion includes those bubbles that temporarily landed on the glass slide for a short duration and then were swept away by the flow. A typical computer-scanned image of gas bubbles attaching on glass collector surfaces is displayed in Figures 5.2, from which the number of bubble attachment was determined. Through close observations of the bubbles captured by the collector (shown in Figure 5.2), one can find that the attached bubbles were nearly evenly distributed in the field of view, suggesting that bubbles have the same probability of accessing to the homogenous collector surface. In other words, this observation shows that the bubble attachment flux is uniform over the view region near the stagnation point. Indeed, this is one of the most important features of the impinging jet cell, and can be predicted from theory (Yang et al., 1998c).

As outlined in Chapter 5, the impinging jet experimental results can be characterized by the normalized bubble attachment density,  $\bar{n}_t$ , and the normalized bubble attachment flux,  $\bar{j}_o$ . The former was defined in equations (5.5) and (5.6); the latter was given in equation (5.7). In the subsequent sections, the effects of hydrodynamic and physicochemical parameters on bubble attachment rate onto methylated glass surfaces, in terms of the normalized bubble attachment density, will be presented and discussed. All data presented represent the average of four different measurements under the same experimental conditions.

### 7.4.1 Effect of Hydrodynamic Conditions (i.e., Reynolds number)

Figure 7.3 shows the normalized bubble attachment density, which is the number of bubbles attached on per unit area normalized by the bulk bubble number concentration, as a function of time under various hydrodynamic conditions (in terms of the Reynolds number  $Re=100 - 700$ ). The presented results were obtained from experiments carried out in a  $10^{-2} M NaCl$  solution. The solid lines are fitted by a least-squares linear regression to the experimental values which are shown as symbols. As can be observed in Figure 7.3, the variation of the normalized bubble attachment density with time is

described very well by the linear function, thereby revealing the absence of the so-called blocking effect. The blocking effect on particle deposition, giving rise to a *relative decrease* in deposition flux due to masking effects by the already deposited particles, was discussed in length by Dabros and van de Ven (1982, 1983a, 1983b). They demonstrated that the blocking effect is dependent not only on change of the shape of the collector surface and modification of local hydrodynamic conditions near the collector surface due to the deposited particle but also on alteration of the intrinsic colloidal interactions between particles. Such blocking effect is the major factor that accounts for the non-linearity of deposition rate changing with time during particle deposition processes. The absence of the blocking effect observed in the experiments could be attributed to a sufficiently low bulk bubble concentration used in the present experiments as well as the fact that small bubbles (less than 30  $\mu\text{m}$ ) were usually dissolved within a minute after attachment onto the glass slide. Furthermore, the observed linear relationship of the normalized bubble attachment density shown in Figure 7.3 also suggests a constant attachment rate of bubbles onto the collector surface. This fact therefore ensures that the obtained normalized bubble attachment flux,  $\bar{j}_o$ , which will be presented in Section 7.5, no longer represents the initial attachment flux, as originally defined in equation (5.7).  $\bar{j}_o$ , in fact, is a mean attachment flux over the entire experimental duration, and hence denotes a more reasonable measure for evaluation of the bubble attachment intensity in the stagnation region.

#### 7.4.2 Effect of Electrolyte Concentration (or Ionic Strength)

The effect of electrolyte concentration on bubble attachment was investigated for *NaCl* solutions having different molar concentrations from  $10^{-4}$  to  $10^{-1}$  M. Experiments were conducted at a fixed  $Re=200$ , and the results are given in Figure 7.4. This figure clearly shows more bubbles (in terms of an increase of normalized bubble attachment density) attached on the methylated collector when the *NaCl* concentration increased. For instance, the normalized bubble attachment density for the  $10^{-4}$  M *NaCl* solution is considerably lower than that for the  $10^{-1}$  M solution. These results were qualitatively described by Fukui and Yuu (1980), Okada et al. (1990), Yoon and Mao (1996), and Dai

et al. (1998) in their column flotation experiments. This scenario in fact can be understood as follows. In this study, it has been shown that both gas bubbles and glass collector surfaces carry negative charges, indicating the electrostatic double layer (*EDL*) interactions between these two charged interfaces are essentially repulsive. According to the *EDL* theory, the extent of the electrostatic double layer interaction (i.e., the *EDL* thickness) is of the same order as the Debye length  $\kappa^{-1}$  (in SI units) defined as

$$\kappa^{-1} = \left( \frac{1000 e^2 N_A c \sum z_i^2}{\varepsilon_r \varepsilon_0 kT} \right)^{-1/2} \quad (7.2)$$

where  $z_i$  is the valence of type- $i$  ion in the electrolyte,  $e$  is the elementary charge,  $N_A$  is Avogadro's number,  $c$  is the solution molar concentration (M or mol/l),  $\varepsilon_r$  is the dielectric permittivity of the solution,  $\varepsilon_0$  is the permittivity in the vacuum,  $k$  is the Boltzmann constant, and  $T$  is the absolute temperature. This equation shows that when the solution concentration increases, the range of the *EDL* interaction is decreased. In other words, the *EDL* thickness is compressed, resulting in a weaker *EDL* repulsion. Furthermore, as shown in Table 7.2, when the solution concentration increases, the values of  $\zeta$ -potential of both the bubbles and the glass collector surface decline (i.e., become less negative), leading to a reduction in repulsive *EDL* interaction forces.

### 7.4.3 Effect of Solution pH

Bubble attachment experiments were carried out for the same solution concentration ( $10^{-2}$  M NaCl) with four different pH levels, namely  $pH = 2.5, 4.0, 6.5,$  and  $9.0$ , while keeping the Reynolds number constant ( $Re=200$ ). The effect of solution pH on the normalized bubble attachment density is presented in Figure 7.5. The general trend is: the higher the solution pH value, the lower the normalized bubble attachment density. From a theoretical point of view, this observed trend can be interpreted by a strong dependence of the  $\zeta$ -potentials of both gas bubbles and the glass collector on the solution pH. At low pH values, the  $H^+$  ions are essentially the potential-determining ions. A decrease in the solution pH exponentially increases the  $H^+$  ions in the solution. Thus, the adsorption of  $H^+$  ions onto the bubble-liquid and the glass-liquid interfaces neutralizes and hence reduces the  $\zeta$ -potentials of both gas bubbles and the glass collector (i.e., the

zeta-potentials become less negative). On the other hand, when the solution pH is high, the adsorption of  $OH^-$  ions (at high pH, the  $OH^-$  ions are responsible for the negative charge of the interface) onto the bubble-liquid and the glass-liquid interfaces leads to development of strong negative  $\zeta$ -potentials for both the gas bubbles and the glass collector. Based on electrophoretic mobility measurements, the trend of the above-described variations of the  $\zeta$ -potentials with the solution pH was confirmed, and the results are shown in Table 7.2. In summary, it can be stated that as the solution pH varies, the change in  $\zeta$ -potentials of both gas bubbles and the glass collector alters the *EDL* interaction forces and hence modifies the bubble attachment rate.

#### 7.4.4 Effect of Metal Ions

Multivalent metal ions such as  $Ca^{2+}$  and  $Al^{3+}$  are present in many flotation systems. In this study, the effects of  $CaCl_2$  and  $AlCl_3$  on bubble attachment onto methylated collectors were examined. The normalized bubble attachment density versus time, obtained for solution having three different  $CaCl_2$  concentrations ( $10^{-5}$ ,  $10^{-4}$ , and  $10^{-3}$  M) but at fixed  $NaCl$  ionic strength of  $10^{-2}$  M and pH of 4.0, is shown in Figure 7.6. The dotted line in Figure 7.6 represents bubble attachment for a solution of  $10^{-2}$  M  $NaCl$  and  $pH = 4.0$  in the absence of  $Ca^{2+}$  ions. All experiments were performed under the same hydrodynamic condition ( $Re=200$ ). The results given in Figure 7.6 show that the normalized bubble attachment density monotonically increased as the level of  $CaCl_2$  increases from 0 to  $10^{-3}$  M. At an elapsed time of 10 min, the normalized bubble attachment density for  $10^{-3}$  M  $CaCl_2$  is significantly higher than that in the absence of  $Ca^{2+}$  ions, implying a considerable influence of such ions on the bubble attachment. The increased bubble attachment due to the presence of  $Ca^{2+}$  ions is in agreement with experiments conducted for static adhesion between air bubbles and oil droplets (Okada et al., 1987) and solid particle flotation (Celik et al., 1998) as well. The mechanism of  $Ca^{2+}$  ion effect was explained in terms of preferential adsorption of multivalent metal ions (Celik et al., 1998; Okada et al., 1987) or formation of insoluble surface reaction products (i.e., the hydroxylated precipitates) (Celik et al., 1998),

depending on the pH range and the level of  $Ca^{2+}$  concentration. It turns out that the presence of  $Ca^{2+}$  ions could significantly lower the negative  $\zeta$ -potential of the bubble, namely making the bubble zeta-potential less negative. Interestingly, experimental results show that most mineral particles, oil droplets and gas bubbles exhibit a similar dependence of  $\zeta$ -potential on the solution pH in the presence of multivalent metal ions (Celik et al., 1998; Li and Somasundaran, 1991; Okada et al., 1987; and Li and Somasundaran, 1992). This, in turn, reveals that these particulates acquire a surface charge through similar mechanisms and, to a large extent, in accordance with dominant multivalent metal ions ( $M^{n+}$ ) or hydroxylated ( $M(OH)_n$ ) species. Therefore, as the  $Ca^{2+}$  concentration increases, the enhanced bubble attachment flux occurs as a result of a decrease in the *EDL* interaction due to lower absolute values of the  $\zeta$ -potentials for both the bubble and the glass collector.

Figure 7.7 shows the effects of metal ions ( $Na^+$ ,  $Ca^{2+}$  and  $Al^{3+}$ ) on the normalized bubble attachment density for solutions having fixed  $pH = 4.0$ . In view of results illustrated in Figure 7.7, a difference in the bubble attachment rate is noted and the corresponding bubble attachment densities for different electrolytes take (decreasing) order of  $AlCl_3 > CaCl_2 > NaCl$ . Again, these results can be interpreted in terms of the *EDL* interaction argument. The supporting evidence comes from experimental data on the bubble  $\zeta$ -potential under the same solution conditions as shown in Table 7.2; in accordance with the cation valence, the measured data indeed show

$\xi_{bub}|Al^{3+} > \xi_{bub}|Ca^{2+} > \xi_{bub}|Na^+$ . Coincidentally,  $\zeta$ -potential measurements for oil droplets (Rios et al., 1998) and solid particles (Hamieh and Stiffert, 1994) reveal a striking similarity with these cation valence effects. Nevertheless, this finding is another example that demonstrates at such pH levels, electrostatic charges accumulating at the gas-liquid and solid-liquid interfaces are completely controlled by specific adsorption of multivalent metal ions.

## 7.5 Bubble Attachment: Comparison between Experiments and Theoretical Predictions

Instead of using the normalized bubble attachment density, experimental results of bubble attachment are expressed in terms of the normalized bubble attachment flux, calculated from the slope of the normalized bubble attachment density versus time curves according to equation (5.7). The values of the normalized bubble attachment flux to the collector surface are then compared with numerical predictions to validate the proposed theoretical model for bubble attachment and to explore the applicability of the *DLVO* theory to the bubble attachment. It should be noted herein that in reality, fine bubbles generated in the impinging jet experiments exhibited a wide range of sizes. To account for bubble size distributions, the experimentally obtained bubble attachment flux was actually compared with the theoretical mean bubble attachment flux,  $\bar{J}_o$ , which was defined in equation (5.9) before. For simplicity, the theoretical mean bubble attachment flux will be referred to as theoretical bubble attachment flux hereafter in the subsequent sections.

For the numerical calculations, the *EDL* interaction parameters ( $DI$ ,  $Da$ , and  $\tau$ ), by themselves, are fairly straightforward to quantify according to their definitions given by equations (3.29a, b and c), as long as the solution conditions and the zeta-potentials of both bubble and glass collector are specified before. The van der Waals interaction is characterized by the adhesion number  $Ad$  or the Hamaker constant  $A$ . The Hamaker constant of the untreated glass /water/ air system simply can be calculated on the basis of combining rules given by equation (3.19). Quoted published values of the Hamaker constant in vacuum for water, glass, and air are  $A_w = 4.38 \times 10^{-20} J$ ,  $A_G = 14.7 \times 10^{-20} J$ , and  $A_A = 4.1 \times 10^{-26} J$ , respectively (Vincent, 1973). According to equations (3.16) and (3.19), the Hamaker constant and the adhesion number for the untreated glass /water/ air system are respectively calculated as  $A_{untreated} = -3.64 \times 10^{-20} J$  and  $Ad = -1.2$ . The Hamaker constant of the methylated glass /water/ air system, however, requires additional attention because a thin film was formed during the surface treatment process. The presence of such a thin film not only modified the hydrophobicity of the glass

surface as demonstrated in the contact angle measurements, but also could affect the van der Waals interaction between the methylated glass and a bubble through an aqueous solution. In the literature, the effect of a thin layer on the van der Waals interaction was well-documented (Israelachvili, 1985). Consider a spherical bubble with a separation distance  $h$  from a flat glass plate; between them lies a hydrophobic methylated thin film of thickness  $\delta$  as shown in Figure 7.8. In the literature, an expression for van der Waals interaction between a sphere and a flat plate was derived by Usui and Barouch (1990), which takes the form:

$$V_{vdW} = -\frac{a_p}{6h} \left( \frac{a_p + \delta}{a_p} A_a + \frac{h}{h + \delta} A_b + \frac{a_p + \delta}{a_p} A_c + \frac{h}{h + \delta} A_d \right) \quad (7.3)$$

where

$$A_a = (\sqrt{A_M} - \sqrt{A_W})(-\sqrt{A_W}) \quad (7.4a)$$

$$A_b = (\sqrt{A_G} - \sqrt{A_M})(-\sqrt{A_W}) \quad (7.4b)$$

$$A_c = (\sqrt{A_M} - \sqrt{A_W})(\sqrt{A_A}) \quad (7.4c)$$

$$A_d = (\sqrt{A_G} - \sqrt{A_M})(\sqrt{A_A}) \quad (7.4d)$$

Comparing equation (7.3) with equation (3.14) gives the effective Hamaker constant for the methylated glass /water/ air system

$$A_{132} = \left( \frac{a_p + \delta}{a_p} A_a + \frac{h}{h + \delta} A_b + \frac{a_p + \delta}{a_p} A_c + \frac{h}{h + \delta} A_d \right) \quad (7.5)$$

Note that the order of magnitude of the methylated layer thickness,  $\delta$ , is of order  $O(10^{-9})$  m, while the bubble radius,  $a_p$ , is of order  $O(10^{-6})$  m. Thus, it can be

approximated that  $\frac{a_p + \delta}{a_p} \approx 1$ . It should be pointed out that the Hamaker constant for

dimethyldichlorosilane is not available in the literature. However, the Hamaker constant for polymethylchlorine can be a good substitute; it is  $A_M \approx 6.1 \times 10^{-20}$  J. With these quoted values of the Hamaker constant for different materials, the effective Hamaker constant of the methylated glass /water/ air system  $A_{methylated}$  can be readily calculated from equation (7.5). Figure 7.9 gives the effective Hamaker constant of the methylated

glass /water/ air system for various thicknesses of the methylated layer. In this figure, the dotted line represents the Hamaker constant of the untreated glass /water/ air system, and it was drawn as a reference. As shown in Figure 7.9, compared with the Hamaker constant of the untreated glass /water/ air system, the negative Hamaker constant of the methylated glass /water/ air system is greatly reduced due to the effect of the methylated layer. Such an effect was included in the numerical calculations, in which the thickness of the methylated layer was chosen as  $0.5 \text{ nm}$ .

Experimental values of the normalized bubble attachment flux onto methylated glass surfaces are presented in Figure 7.10, where the normalized bubble attachment flux was plotted as a function of the Reynolds number for three different levels of  $\text{NaCl}$  ionic strength:  $10^{-3} \text{ M}$ ,  $10^{-2} \text{ M}$ , and  $10^{-1} \text{ M}$ . Two important features are readily identified from the experimental results presented here. The first is that larger values of the bubble attachment flux were observed in a higher concentration of electrolyte. For instance, the values of the normalized bubble attachment flux for the  $10^{-1} \text{ M}$   $\text{NaCl}$  solution are systematically higher than those for the  $10^{-3} \text{ M}$   $\text{NaCl}$  solution over the entire range of Reynolds numbers. Such an increase in bubble attachment flux with electrolyte concentration, consistent with results shown in Figure 7.3, is largely due to the reduced extent (characterized by the Debye-Huckel length defined in Chapter 3) of the repulsive  $\text{EDL}$  interaction and the neutralization effect of the electrolyte concentration on the zeta-potentials of both bubbles and glass surface. The second noticeable feature in Figure 7.10 is that the normalized bubble flux onto the methylated glass surface is strongly dependent on the Reynolds number. When the Reynolds number varies from 100 to 700, the corresponding bubble attachment flux increases by an order of magnitude. This indicates that the hydrodynamic condition (i.e., the Reynolds number) has a significant impact on the bubble attachment process.

A comparison between experimentally measured and numerically predicted normalized bubble attachment flux onto methylated glass surfaces for  $10^{-2} \text{ M}$   $\text{NaCl}$  electrolyte is presented in Figures 7.11a and 7.11b. The filled symbols in this figure



show the measured values of the experimental bubble attachment flux, while the open symbols represent the theoretical attachment flux calculated from the bubble transport equation (4.1) with correction for experimentally determined bubble size distributions. The solid lines obtained from the numerical solution of equation (4.1), representing the bubble attachment flux of a uniform bubble size, are also superimposed on Figure 7.11b. Overall, as Figure 7.11 illustrates, the theoretical bubble attachment flux to the methylated glass is in a reasonable agreement with the experimental results. This suggests that the process of fine bubbles attaching onto the methylated glass can be satisfactorily described by the bubble transport equation developed on the basis of the *DLVO* theory. In particular, it may seem surprising that there is an excellent agreement between theory and experiment when the Reynolds number is high, for example  $Re \geq 400$ , even though the stagnation point flow patterns were utilized to approximate the hydrodynamic conditions in the bubble attachment region. However, the experiments at intermediate Reynolds numbers ( $100 \leq Re \leq 300$ ) yielded bubble attachment fluxes that were higher than the theoretical predictions. The increased attachment flux at such a low Reynolds number range is likely caused by the so-called non-*DLVO* and stochastic contributions, such as surface roughness (Czarnecki, 1986; Walz, 1998), non-uniform distributions of the (bubble) zeta-potential (Prieve and Lin, 1982; Warszynski and Czarnecki, 1989) and discrete surface charge (Kostoglou and Karabelas, 1992), as well as electroviscous effect (Warszynski and van de Ven, 1990; 1991), which were not included in the present model. Although, in the past, a large amount of information has been accumulated on the importance of these non-*DLVO* and stochastic factors to colloidal interactions, rigorous theoretical analyses, which illustrate the non-*DLVO* and stochastic effects, have only recently begun to appear in the literature. Specifically, there is a lack of well-controlled experiments which can provide strong experimental evidence to confirm the proposed theory. A brief introduction of these non-*DLVO* and stochastic factors and, particularly, their possible influences on the present bubble attachment flux will be presented later in Section 7.7.

Furthermore, it is of interest to note that theoretical calculations represented by the solid lines in Figure 7.11b predict an unusual dependence of the normalized bubble

attachment flux on the Reynolds number. Figure 7.11b shows that as the Reynolds number increases, the bubble attachment flux is found to first decrease (when  $Re \leq 100$ ), then reaches a minimum at around  $Re = 100$ , finally increases (when  $Re \geq 100$ ). Such a prediction was evidently supported by experimental results that were obtained within the intermediate Reynolds number range, i.e.,  $100 \leq Re \leq 700$ . Unfortunately, experiments were not extended to the low Reynolds number range to make further verification due to a limitation of the experimental setup. Based on the theoretical analysis, there always exists a competition among the tangential and normal hydrodynamic forces and the buoyancy force on the bubble in the impinging jet region. As discussed in Chapter 4 and Appendix 3, previous theoretical studies indicated that the dependence of the bubble attachment flux upon the Reynolds number may exhibit a quite different trend, depending on whether the process is dominated by diffusion or convection. Nevertheless, the experimental results displayed in this figure amply demonstrate that the bubble attachment process is overwhelmingly controlled by hydrodynamic convection under experimental conditions studied here. An increase in hydrodynamic intensity (i.e., the Reynolds number) is always favorable to bubble attachment.

In the literature, Elimelech (1994) examined the effect of particle size on the kinetics of particle deposition, and revealed the importance of particle size to the colloidal interactions. As shown in Chapter 4 and Section 7.3, the bubble size also plays a significant role in the bubble attachment process. The strong impact of bubble size on the attachment flux is evidenced in Figure 7.11b. In particular, such an impact becomes more pronounced when the Reynolds number is large, e.g.,  $Re \geq 100$ . Unfortunately, the sizes of fine bubbles generated in experiments were not controllable and were difficult to accurately determine. Therefore, it can be stated that any error generated in the determination of bubble size distributions could be another cause for the difference between theory and experiment.

The effect of electrolyte concentration on the normalized bubble attachment flux is presented in Figure 7.12. This figure clearly shows that the measured attachment flux

monotonically increases as the concentration of  $NaCl$  increases from  $10^{-4} M$  to  $10^{-1} M$ , while keeping the same conditions of  $Re = 200$  and  $pH = 6.5$ . Furthermore, the theoretical attachment flux is also seen to follow the same trend as the experimental results over these electrolyte concentrations, indicating the proposed model basically can describe the bubble attachment, although the difference between theory and experiment exists under current conditions. Theoretically, such an increase of the bubble attachment flux with the electrolyte concentration can be understood as follows: As the electrolyte concentration increases from  $10^{-4} M$  to  $10^{-1} M$ , on the one hand, the reciprocal of the Debye-Huckel parameter,  $\kappa^{-1}$ , shrinks from  $32 nm$  to  $1 nm$ , representing a greatly reduced extent of the *EDL* interaction. On the other hand, as shown in Table 7.2, the corresponding zeta-potentials of bubbles and the methylated glass decrease from  $-50 mv$  and  $-46 mv$  to  $-18 mv$  and  $-11 mv$ , respectively. As a result, the repulsive *EDL* interaction is considerably reduced, leading to higher bubble attachment rates. Furthermore, a comparison made between Figure 7.12 and Figure 7.11 reveals that the impact of the *EDL* interaction, although important to bubble attachment, is not as strong as that of the Reynolds number and the bubble size.

Figure 7.13 shows the influence of the electrolyte pH on the normalized bubble attachment flux under conditions of  $Re = 200$  and  $10^{-2} M NaCl$ . It is seen that more bubbles attached onto the methylated glass when the electrolyte pH is low, and both theory and experiment follow this pattern. As Table 7.2 indicates, this can be interpreted as a decrease in the zeta-potentials of bubble and glass surface with an increase in solution pH. However, compared with electrolyte concentration, the pH seems to have a smaller influence on bubble attachment. Furthermore, it is also noted that the experimental results shown in Figures 7.12 and 7.13 do not closely match the theoretical predictions. As pointed out earlier, the discrepancy between theory and experiment can be largely attributed to non-*DLVO* and stochastic effects mentioned before.

Figure 7.14 summarizes experiments carried out in  $10^{-2} M NaCl$  for bubble attachment onto the untreated glass surface. The corresponding calculated attachment

flux is included in this figure for comparison. It is seen that when the Reynolds number is high, e.g.,  $Re \geq 400$ , the proposed model provides a fairly good prediction of bubble attachment onto the untreated glass. A striking similarity was also observed for bubble attachment onto the methylated glass shown in Figure 7.11. A good agreement between numerically calculated and experimentally measured attachment fluxes at high Reynolds numbers indicates that the bubble attachment process is completely dominated by hydrodynamic conditions (in terms of the Reynolds number). In other words, this means that under such circumstances, colloidal forces such as the *EDL* interaction become less important. On the contrary, the theoretical model based on the classical *DLVO* theory failed to predict bubble attachment onto the untreated glass at low-ranged Reynolds numbers (i.e.,  $100 \leq Re \leq 300$ ). It is clear that the theoretical calculations do not predict that bubbles would attach to the untreated glass until the Reynolds number reaches 300, above which an abrupt increase in bubble attachment flux is expected. The experimental results, however, show a systematic and gradual increase as the hydrodynamic conditions become increasingly favorable to the attachment processes. A significant difference between theory and experiment is found under such situations. This result is consistent with other studies of physicochemical parameter effects on particle deposition (Gregory and Wishart, 1980; Adamczyk, 1989; Tobiason, 1989; Elimelech and O'Melia, 1990). According to the literature, the use of alternative *EDL* interaction models (e.g., constant charge, linear superposition, etc.) may alter, to a limited extent, the conditions for transition where the abrupt change occurs, but does not change the nature of the attachment prediction. Nevertheless, the deviation of theory from experiment observed here is also ascribed to those non-*DLVO* and stochastic effects that have been addressed earlier. A concise discussion of such deviation will be provided in Section 7.7.

## **7.6 Remarks on Bubble Attachment onto Untreated / Methylated Glass Collectors**

Figures 7.11 and 7.14 gave the bubble attachment fluxes to the methylated and untreated glass surfaces, respectively. Two distinct features can be observed from the results presented in these figures. First, a quantitative comparison indicates that, as expected, bubble attachment onto the methylated glass is considerably higher than that to

the untreated glass. Obviously, the difference in the bubble attachment flux to these two different collector surfaces arises from the influence of a higher energy barrier, formed by stronger repulsive van der Waals and *EDL* interactions between the bubble and the untreated glass. A second notable feature is that, the difference between attachment fluxes to the untreated and methylated glass surfaces becomes larger for higher Reynolds numbers. This particular phenomenon may be qualitatively explained as follows: In the impinging jet region, both hydrodynamic and buoyancy forces push bubbles toward the collector. The presence of a higher interaction energy barrier, between the bubble and the untreated collector, may cause a bubble accumulation close to the untreated collector. When  $Re$  increases, on the one hand, more bubbles will attach onto the collector due to an increase in normal hydrodynamic forces. On the other hand, however, some bubbles are likely to be swept away by increasing tangential flow, resulting in a relatively lower attachment.

Taking advantage of the impinging jet system, the videotaped recording of the attachment processes for untreated and methylated glass surfaces was reviewed to visualize the bubbles' behavior at low Reynolds numbers when they were in the proximity of the collector. Close examination of the attachment process revealed that the attachment characteristics for untreated glass are considerably different from those for methylated glass. It was noted that when gas bubbles approached the untreated glass collector, the bubbles did not appear to instantaneously stick to the untreated glass surface. Many bubbles rolled or slipped over a short distance along the collector surface before they became attached, and most of the sliding bubbles were never immobilized. Even if some bubbles temporarily adhered to the collector, due to weak adhesive forces formed between the attached bubble and the collector, they were frequently removed by the tangential flow if a small disturbance in the flow was present. For attached bubbles on the untreated glass, the bubbles looked to stick to the collector surface by a very small contact area, indicating small contact angle of bubbles on the untreated glass (as shown in Figure 7.15a). Two types of attachment configurations are hypothesized here: one is that, similar to the methylated glass, bubble attachment is the result of formation of a three-phase contact line; the other is that attachment is due to the local deformation of the

bubble that essentially experiences the same mechanism as solid particle deposition. Therefore, for the latter situation, the formation of a three-phase contact line may not be necessary for bubble attachment.

In contrast, the behavior described above is significantly different from that of the bubble attachment onto the methylated glass. For methylated glass experiments, there were almost no instances of bubble detachment. Once a bubble hit the collector surface, it appeared to adhere strongly to the methylated glass, even at fairly high Reynolds numbers. In other words, this implies that much more work is needed to detach attached bubbles from the methylated glass than from the untreated glass. According to the literature, bubble attachment onto a hydrophobic surface is related to drainage of the thin liquid film between the bubble and the collector surface. If such a thin film becomes unstable or is broken, a three-phase contact line is created and a contact angle is formed. It was observed that most of the bubbles quickly landed on the methylated glass, and then the thin liquid film between the bubble and the methylated glass was ruptured instantly, suggesting that the so-called "induction time" was very short under such conditions. As shown in Figure 7.15b, the diameter of contact area between the attached bubble and the methylated glass surface is almost the same as the bubble size, indicating a relatively large contact angle (approximately  $90^\circ$ ) of attached gas bubble on the methylated glass. For attached bubbles, both contact angle hysteresis and surface force at the three-phase contact line can immobilize the bubble. Therefore, it can be stated that even if the difference in attachment flux between the untreated glass and the methylated glass is within one order of magnitude only, a significantly distinctive attachment behavior was identified for the bubbles in the state of immobilization.

## **7.7 Deviation of Theory from Experiment at Low Reynolds Numbers**

Although it has been shown that the theoretical predictions agree well with the experimental results at high Reynolds numbers ( $400 \leq Re \leq 700$ ), it is noted that the proposed theory deviated from experiment for both untreated and methylated glass surfaces when the Reynolds number is low ( $100 \leq Re \leq 300$ ). In particular, for the untreated glass, the theoretical predictions that the bubbles would not attach to the

untreated glass until the Reynolds number reach at 300, above which a drastic increase in bubble attachment flux will occur did not observed by experiment. The experimentally measured data, however, showed a systematic and gradual increase in attachment as the Reynolds number increases from 100 to 700. It should also be pointed out that, despite experimental evidence, the scenario of gas bubble attachment onto untreated glass is difficult to explain by the existing classical thin film theory. According to the literature, the prerequisite condition for bubble attachment onto a solid surface is that thin film rupture must occur. The film rupture is associated with the instability of the thin film which, in turn, is determined by the colloidal interactions between the bubble and the collector surface. As the present situation involves the interaction of a hydrophobic gas bubble and a hydrophilic untreated glass in the  $10^{-2} M NaCl$  solution, definitely no short-ranged attractive forces, such as hydrophobic or hydration forces, are present. As addressed earlier, the van der Waals interaction is repulsive for the considered bubble/water/glass system (Visser, 1981; Usui and Barouch, 1990; and van Oss, 1990), and so is the *EDL* interaction between the bubble and the untreated glass. Overall, bubble attachment onto an untreated glass can be considered to occur under unfavorable conditions. Then two questions arise: what is the driving force for fine bubbles to attach onto the untreated glass surface? Why did the discrepancy between theory and experiment exist? In the literature, it has been frequently reported that when the deposition conditions are unfavorable, the measured rate of particle deposition has been found to be orders of magnitude greater than predicted (Czarnecki, 1986; Tobiason, 1989; Elimelech and O'Melia, 1990; and Walz, 1998). As yet, it is not clear what are the real sources for such discrepancy. It has been recognized that rigorous application of the *DLVO* theory is restricted to a model system under thermodynamic equilibrium. Assumptions made in the theory are the two interacting surfaces, a bubble and the collector, are ideally smooth and homogenous and have the deterministic values of surface properties (e.g., the zeta-potential) for bubbles and the collector surface. In reality, any test surface is, to some extent, relatively rough and heterogeneous. As such, several possible effects were speculated to be responsible for bubble attachment onto untreated glass surfaces. Hypotheses proposed herein include the effects of asymmetric *EDL* interaction, surface heterogeneity (e.g., surface roughness of the glass collector, the

discrete surface charge of the glass, and non-uniform distributions of the bubble zeta-potential), and dynamic nature of *EDL* interactions (e.g., electroviscous effect). A brief introduction to these non-*DLVO* and stochastic factors and a discussion of their possible influences on bubble attachment are provided below.

As discussed in Chapters 3 and 4, the asymmetric double layer interaction implies the existence of a short-range (approximately the same order of magnitude as the Debye length) attractive interaction between two charged interfaces having different surface potentials but of the same sign. This short-range attractive interaction can always be predicted within the framework of the constant potential mode of the Poisson-Boltzmann equation, regardless of the *HHF* approximate formula (Hogg et al., 1966) or the “rigorous” complete solution of the nonlinear Poisson - Boltzmann equation (McCormack et al., 1995). Based on more sophisticated models, Chu and Wasan (1996) even predicted attractive interactions between similarly charged concentrated colloidal particles. More recently, a long-range attraction was experimentally discovered between a pair of similarly charged colloidal spheres near a charged glass wall (Larsen and Grier, 1997). Despite experimental evidence, such observations are difficult to rationalize on the basis of existing theories. Recently, Yang et al. (1998c) examined the role of the asymmetric double layer interaction in bubble attachment and demonstrated that, under certain circumstances, gas bubbles could attach onto a hydrophilic surface. However, under the current experimental conditions, the reported data for the  $\zeta$ -potentials of the bubble and the untreated glass surface, respectively, are  $-27$  mV and  $-23$  mV (see Table 7.2), giving an asymmetric *EDL* interaction parameter of  $Da = 0.013$ . Hence, the influence of asymmetric *EDL* interaction seems insufficient to yield any short-range attraction.

The heterogeneity of surface charge density has twofold implications. One is the non-uniform surface charge density of the collector surface due to discrete ions (of finite sizes) unevenly distributing over the surface. In the literature, such spatially varying surface charge is referred to as the so-called discrete surface charge (Kostoglou and Karabelas, 1992). By assuming a certain type of charge distribution patterns (e.g.,



Fourier cosine series) on the charged collector surface, a newly constructed model for the *EDL* interaction between the particle and the collector can be developed. The other implication is the fluctuation of surface potentials with consideration of the zeta-potential of the particle randomly varying with specified probability density functions (Prieve and Lin, 1982), while the zeta-potential of an individual particle can be uniform. In this case, a usual approximation is to assume the particle zeta-potentials to be a normally distributed variable with mean and standard deviation based on measured or estimated values (Onorato and Tien, 1980; Tobiasson, 1989). Following these approaches, analyses for particle deposition flux showed that the whole interaction energy barrier was greatly reduced and the particle deposition occurred at unfavorable conditions (i.e., strongly repulsive interaction energy) whereas for interactions based on the same mean values, no particle deposition was predicted. Applying the same approach to bubble attachment processes, one may expect that consideration of surface heterogeneity of surface charge effect (if it exists) could also result in reduction in the interaction energy barrier or even lead to bubble attachment onto the untreated glass surface, depending on the  $\zeta$ -potential values of both the bubble and the collector as well as hydrodynamic and other physicochemical conditions.

Surface roughness is another type of surface inhomogeneity. Obviously, most of interacting surfaces (e.g., the collector) cannot be molecularly smooth as required by the theory. Accordingly, surface roughness effect seems unavoidable in practical situations, and is believed to play a crucial role in bubble attachment. In the literature, the effect of surface roughness on particle deposition is well recognized and comprehensive reviews on this subject can be found from excellent papers furnished by Czarnecki (1986) and Walz (1998). According to Walz (1998), such an effect is most likely to depend on the ratio of the mean roughness to some characteristic scale, such as particle size or the extent of surface interaction forces. To examine the surface roughness effect on interaction energy, Czarnecki and coworkers (1980; 1984; 1986) developed a model considering a smooth, large sphere moving parallel to a smooth plate surface on which a number of small spheres of randomly varying sizes and a Gaussian distribution of surface potentials were placed. The analysis indicated that possible local net attractive energy

minima could occur for a case where a net repulsion was predicted for smooth surfaces. Hence, particle deposition could occur at these local attractive minima. Using the optical technique of total internal reflection microscopy, the effect of surface roughness on colloidal interactions between a particle and a flat plate was experimentally evidenced by Walz and co-workers (1996; 1997). They found the interaction energy barrier to be greatly lowered due to the presence of the rough surface. In the present experimental system, smooth gas bubbles interact with a relatively rough collector. As shown in Figure 7.1a, which is the surface roughness image of the untreated glass scanned by *AFM*, the surface has roughness in the range of 10 to 30 nanometers. Such a degree of surface roughness is small compared to the bubble size but large compared to the *EDL* interaction thickness (the Debye-Huckel length is about 3nm in 0.01 M NaCl) and the extent of the van der Waals interaction. The bubble is likely to experience fluctuations in local interaction energies as it travels along the collector surface. Accordingly, the effect of such degree of surface roughness could substantially lower the interaction energy barrier and may even lead to locally attractive interaction between the bubble and the untreated glass surface. According to Adamczyk et al. (1985), if the duration of period of attractive energy is long compared to the time required to travel across the energy barrier, then bubble attachment may occur in a system where no attachment occurs for smooth collector surfaces.

The traditional theory does not consider dynamic aspects of the *EDL*. It was demonstrated in Chapter 3 that the effect of hydrodynamic convection on the *EDL* interaction in the impinging jet flow region is negligible. Another recognized phenomenon related to the dynamic *EDL* effect is the so-called electroviscous effect, which is referred to as a change of the hydrodynamic interactions between a bubble and the collector of interactions due to the presence of electrostatic charges on the bubble and the collector surfaces. Such an electroviscous effect was examined by Warszynski and van de Ven (1990; 1991), and they claimed that it could play an important role in particle coagulation and deposition. However, it is difficult to link this effect to the current experiments due to lack of sufficient data. Nevertheless, for gas bubbles where  $\kappa a_p$

(here  $a_p$  is the radius of the bubble) is very large as in the present situation, it is expected that the electroviscous effect is negligible (Warszynski and van de Ven, 1991).

Based on the arguments presented above and the experimental conditions used in this study, the observation that fine bubbles can attach onto hydrophilic untreated glass surfaces can be understood as follows: When bubbles are far away from the collector surface, the transport of bubbles is overwhelmingly controlled by hydrodynamic and gravity forces acting on the bubble. As the separation distance is of the order of the bubble size, the hydrodynamic interactions between the bubble and the collector surface become appreciable. Since the hydrodynamic flow and gravity forces are relatively strong, they can facilitate bubbles to overcome the energy barrier, formed by the repulsive van der Waals and *EDL* interactions between the bubble and the collector surface, and reach a distance of the order of several nanometers. Within this distance, the stability of the thin film, controlled by colloidal interactions between the bubble and the collector surface, plays a crucial role in the bubble attachment process. As addressed above, the possible existence of the aforementioned effects not only could lower the repulsive energy barrier and create local net attractive energy minima, but also may even rupture the thin film. Consequently, bubble attachment is achieved.

Of course, the same arguments can also be applied to the attachment of bubbles to methylated glass and to the explanation of the discrepancy between theory and experiment as well. In conclusion, it should be pointed out that a quantitative analysis of all aforementioned effects at the same time is complex theoretically and difficult experimentally. It seems that more convincing evidence, if available, is required to definitely distinguish each effect.

## **7.8 Summary**

The impinging jet technique provided an effective means of studying gas bubble – solid surface attachment under well-controlled hydrodynamic conditions. The two types of collectors (the methylated and the untreated glass surface) used in such experiments were characterized using contact angle measurements and *AFM* techniques. The results showed contact angles for the methylated and the untreated glass surface are about 90°

and less than  $10^\circ$ , respectively, suggesting the former is hydrophobic and the latter is hydrophilic. Furthermore, the *AFM* scanned images of these two collectors showed that although the surface roughness of both collector surfaces falls in the same range of between 10 and 30 nanometers, it appears that the methylated glass is smoother than the untreated glass. It has been found that the process of bubble attachment onto a solid surface is not only significantly affected by the hydrodynamic conditions and the bubble size, but is also noticeably dependent on the *EDL* parameters. Experimental results showed that with a given set of fixed physicochemical conditions, the normalized bubble attachment density was observed to increase with increasing Reynolds number within the range of *Re* studied. Furthermore, the number of attached bubbles was found to vary linearly with time, indicating negligible blocking effect during the period of an experimental run. By keeping the Reynolds number constant, bubble attachment experiments were conducted for sodium chloride (*NaCl*) solutions of various concentrations and pH values. Results showed that the normalized bubble attachment density was dependent on both the solution pH and the *NaCl* solution concentration, suggesting the importance of *EDL* interactions to the bubble attachment process. Also, in the presence of multivalent metal cations, bubble attachment rate was enhanced. This may be attributed to strong preferential adsorption of multivalent metal cations at the liquid-gas and liquid–solid interfaces. In addition, bubble attachment experiments demonstrated that the bubble flux to the methylated collector is much higher than that to the untreated collector. This indicates that a high energy barrier is present between the bubble and the untreated surface. Taking advantages of the impinging jet technique, direct observations of bubble attachment processes for these two collectors revealed substantially different behaviors when bubbles approach the vicinity of the collector, indicating different attachment mechanisms.

A comparison of experimental results with numerical predictions showed that the theoretical bubble attachment flux to methylated glass was in a reasonable agreement with experimental observations, suggesting the validity of the bubble transport model developed on the basis of the *DLVO* theory. Furthermore, it was found that the theoretically predicted attachment flux to the untreated glass matched well with

experimentally measured when the Reynolds number was high ( $Re \geq 400$ ). However, the proposed model failed to predict bubble attachment at Reynolds numbers in the range of  $100 \leq Re \leq 300$ . This suggests that the bubble attachment process is completely dominated by hydrodynamic conditions at high Reynolds numbers. In other words, colloidal interactions play important roles in the transport of bubbles to a solid surface only when the Reynolds number is low. In addition, it was noted that since both the van der Waals interaction of the bubble/water/glass system and the *EDL* interaction between the bubble and the untreated glass are repulsive, the evidence of gas bubble attachment onto untreated (hydrophilic) glass surfaces could not be explained on the basis of existing thin film theories. The proposed hypotheses for such attachments are asymmetric electrostatic double layer interaction, fluctuation of surface potentials, the discrete surface charge, surface roughness, and the electroviscous effect. It is also believed that these non-*DLVO* and stochastic effects were responsible for the observed discrepancy between theory and experiment of the bubble attachment flux to untreated and methylated glasses when the Reynolds number was low. Finally, a mechanism for fine bubble attachment onto glass surfaces was postulated. However, it seems that further investigation is needed to identify the dominating factor and to draw firm conclusions.

**Table 7.1** Measured contact angles for the untreated and methylated glass collectors using captive bubble method

Aqueous Solution (M)	pH Value	Contact Angle(°) (untreated glass)	Contact Angle(°) (methylated glass)
$10^{-4}$ NaCl	7.0	7	102 ±3
$10^{-3}$ NaCl	7.0	12	104±5
$10^{-2}$ NaCl	7.0	10	99±2
$10^{-1}$ NaCl	7.0	7	100±3
$10^{-2}$ NaCl	9.0	10	106±1
$10^{-2}$ NaCl	4.0	9	101±6
$10^{-2}$ NaCl	2.5	11	97±3
$10^{-2}$ NaCl+ $10^{-5}$ CaCl <sub>2</sub>	4.0	8	102±2
$10^{-2}$ NaCl+ $10^{-4}$ CaCl <sub>2</sub>	4.0	7	101±5
$10^{-2}$ NaCl+ $10^{-3}$ CaCl <sub>2</sub>	4.0	11	107±2
$10^{-2}$ NaCl+ $10^{-4}$ AlCl <sub>3</sub>	4.0	9	106±1
$10^{-2}$ NaCl+ $10^{-5}$ CaCl <sub>2</sub>	9.0	10	98±4
$10^{-2}$ NaCl+ $10^{-4}$ CaCl <sub>2</sub>	9.0	11	106±2
$10^{-2}$ NaCl+ $10^{-3}$ CaCl <sub>2</sub>	9.0	8	102±5
$10^{-2}$ NaCl+ $10^{-4}$ AlCl <sub>3</sub>	9.0	10	103±3

**Table 7.2** Zeta potentials of the bubbles and the collectors

Solution Condition	$\zeta_b$ (mV) <sup>a</sup> bubbles	$\zeta_c$ (mV) <sup>b</sup> methylated glass	$\zeta_c$ (mV) <sup>c</sup> untreated glass	Comments
$10^{-4}$ M NaCl	-50	-48	-82	pH=6.5-7.0
$10^{-3}$ M NaCl	-38	-35	-71	
$10^{-2}$ M NaCl	-27	-23	-63	
$10^{-1}$ M NaCl	-18	-11	-30	
pH = 2.5	+5	-6	-22	In $10^{-2}$ M NaCl
pH = 4.0	-10	-8	-45	
pH = 6.5	-27	-23	-63	
pH = 9.0	-39	-36	-71	
$10^{-5}$ M CaCl <sub>2</sub>	-0	-20	-38	In $10^{-2}$ M NaCl and pH=4.0
$10^{-4}$ M CaCl <sub>2</sub>	+3	-15	-30	
$10^{-3}$ M CaCl <sub>2</sub>	+8	-10	-21	
$10^{-4}$ M AlCl <sub>3</sub>	+28	-7	-14.9	

<sup>a</sup> Bubble zeta-potential data are taken from Chapter 6;

<sup>b</sup> Methylated glass zeta-potential data are quoted from references;

<sup>c</sup> Untreated glass zeta-potential data are quoted from references.

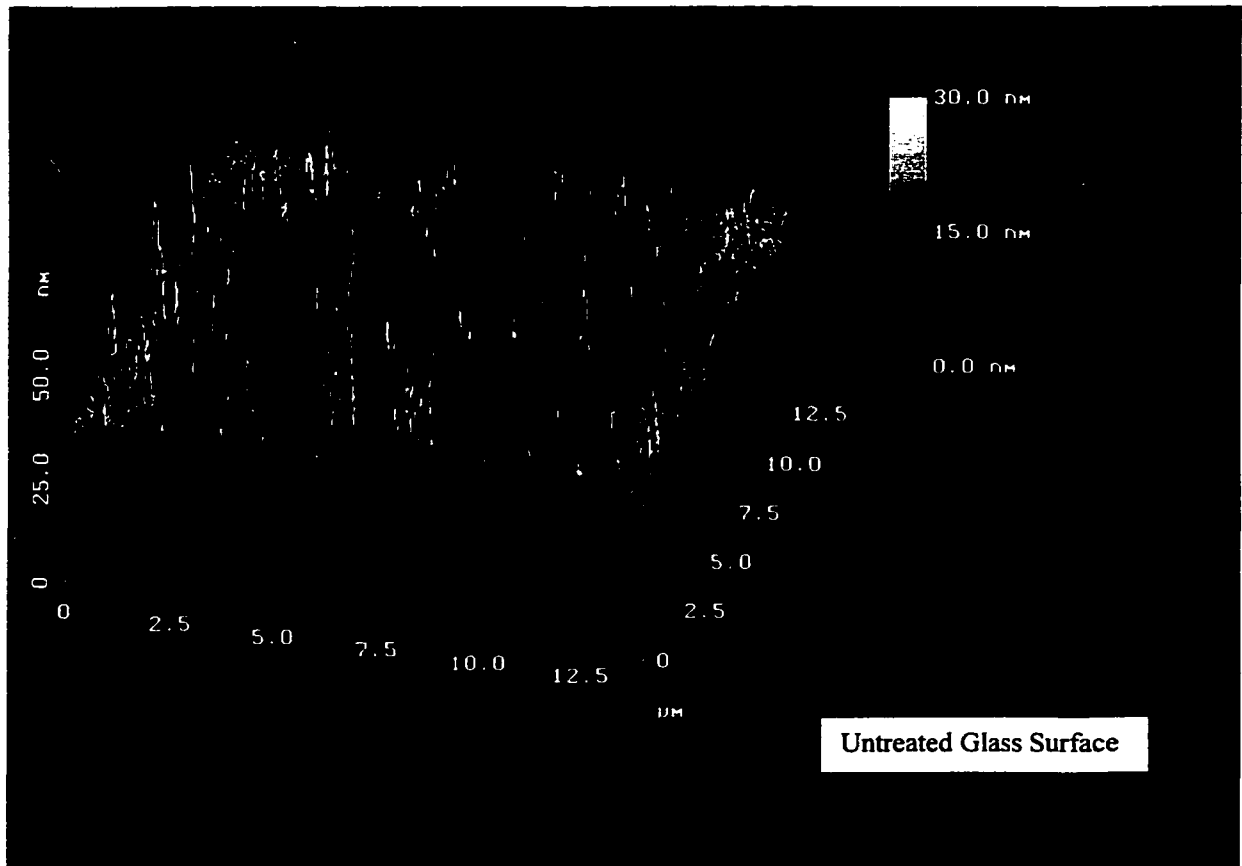


**Figure 7.1a** Surface roughness of the untreated glass scanned by AFM



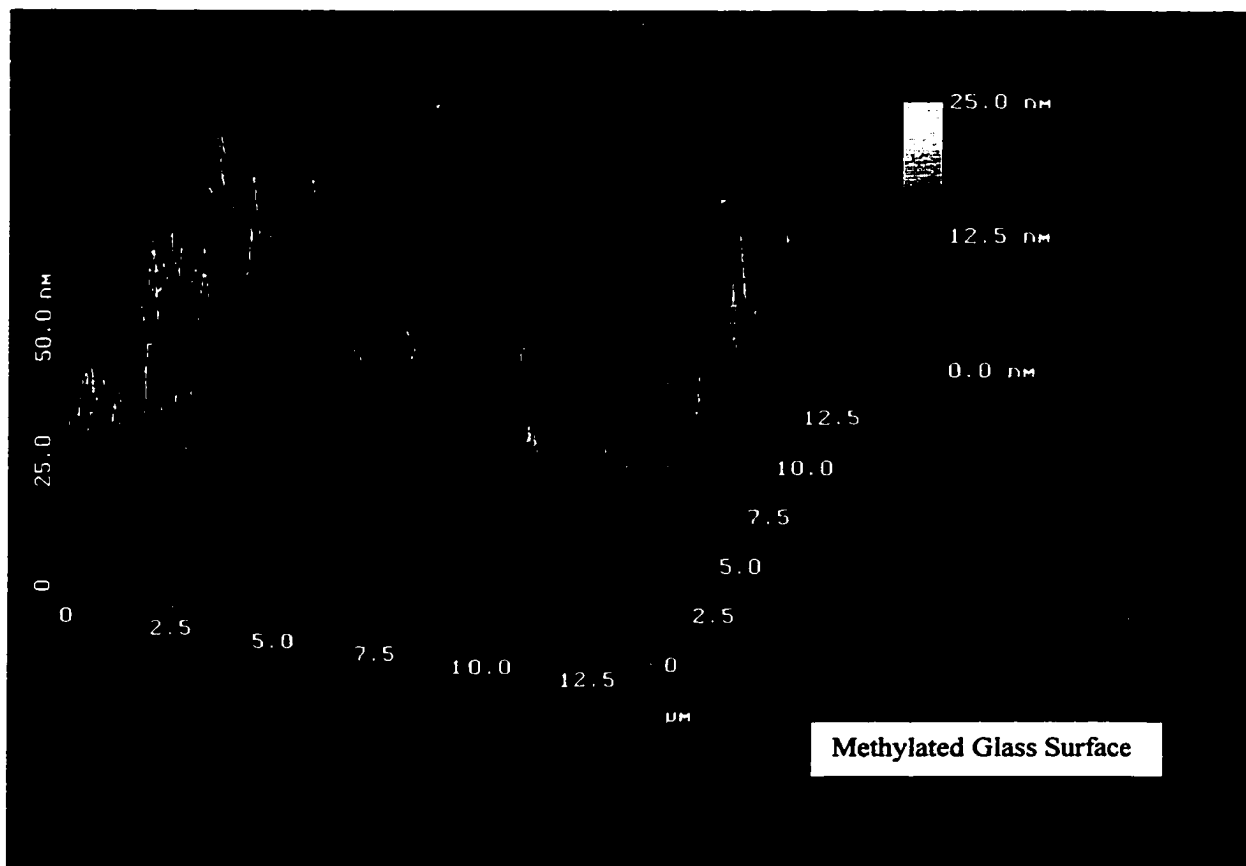


**Figure 7.1b** Surface roughness of the methylated glass scanned by AFM

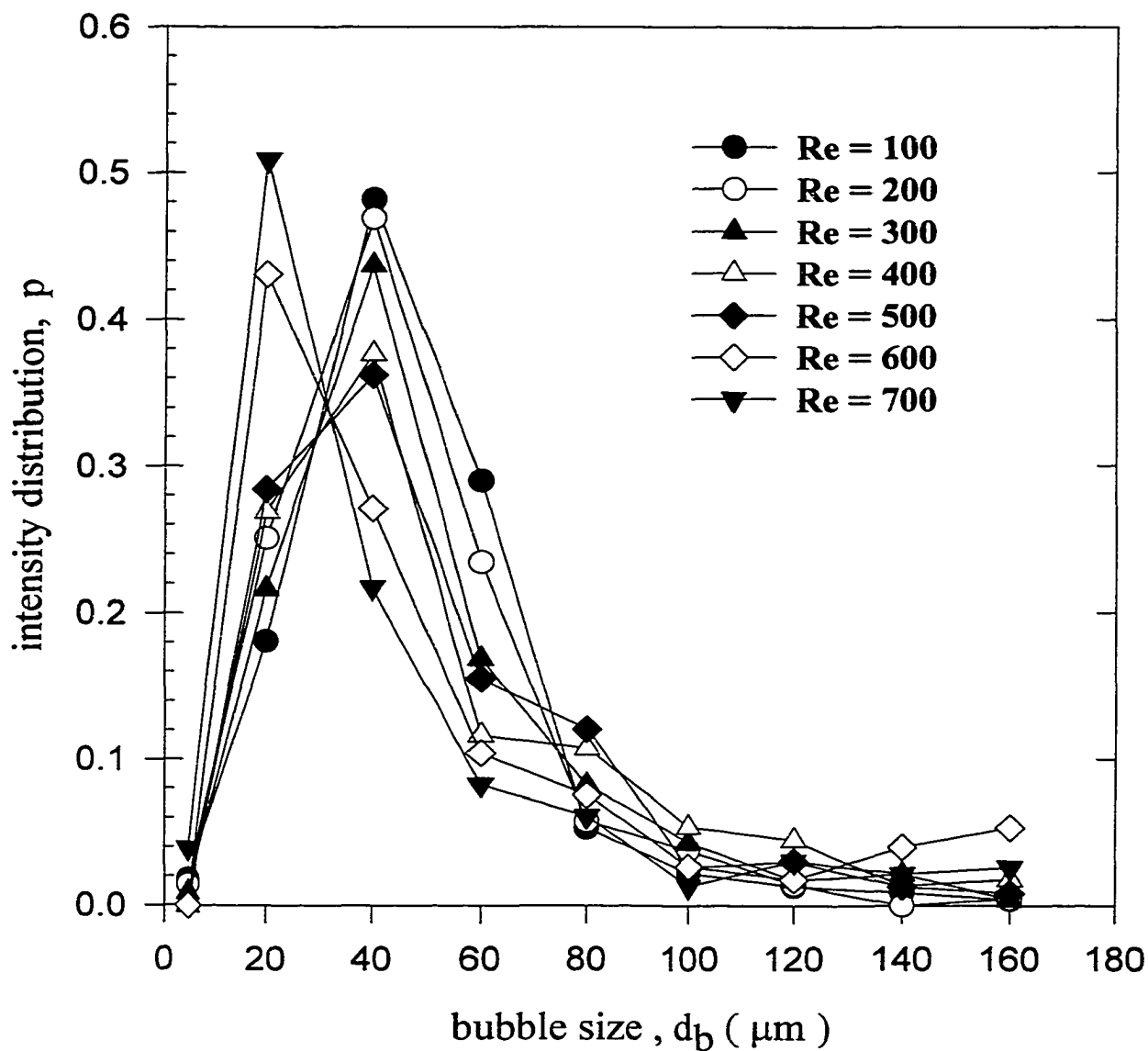


**Figure 7.2 Bubble size distributions for Various Reynolds numbers ( 0.01 M NaCl at PH=6.5 )**

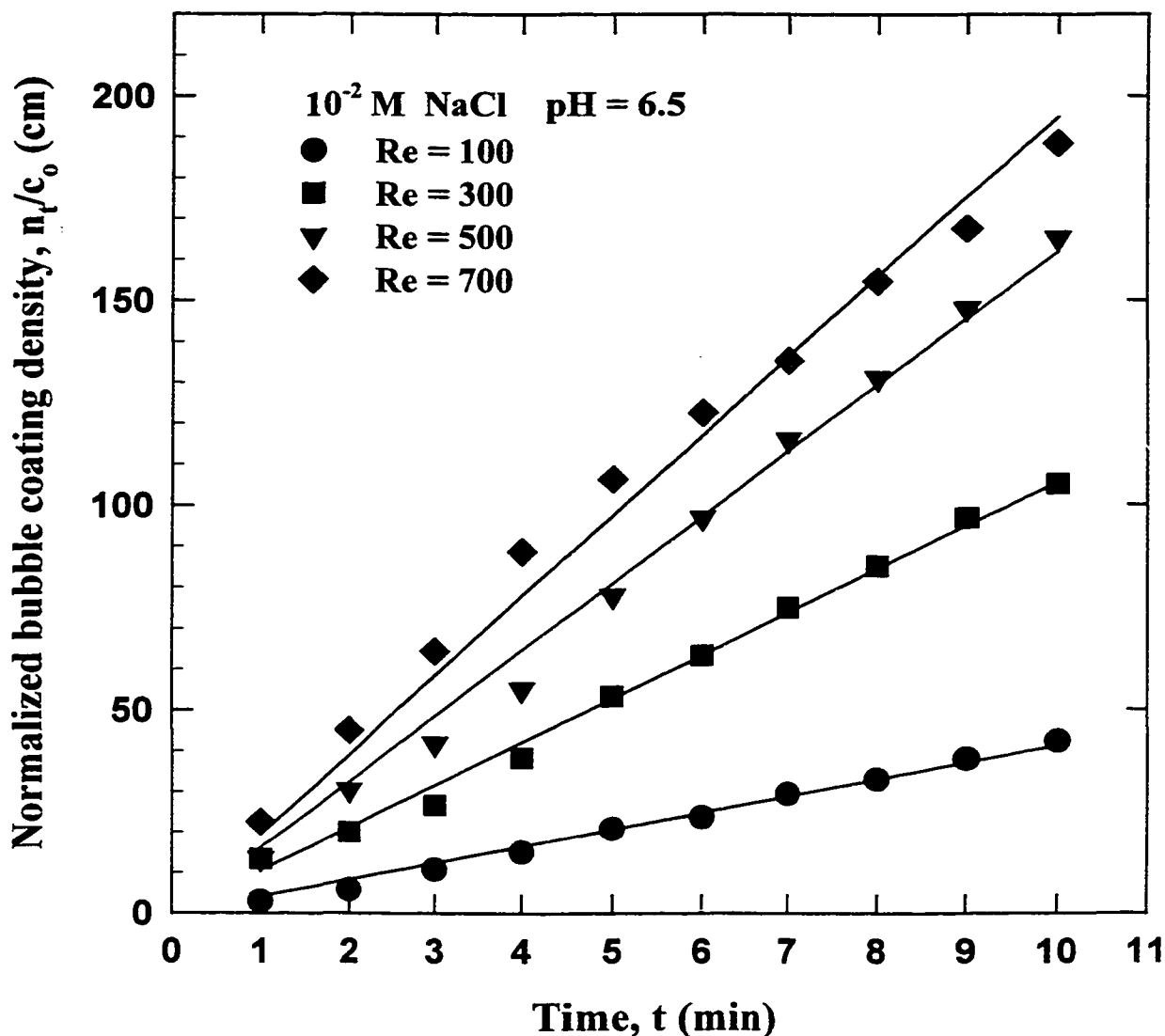


**Figure 7.3** Experimental results of the normalized bubble attachment density on the methylated glass versus time for different Reynolds numbers ( $Re$ ), while keeping both solution concentration and pH constant. The solid lines were obtained from a least-squares linear regression

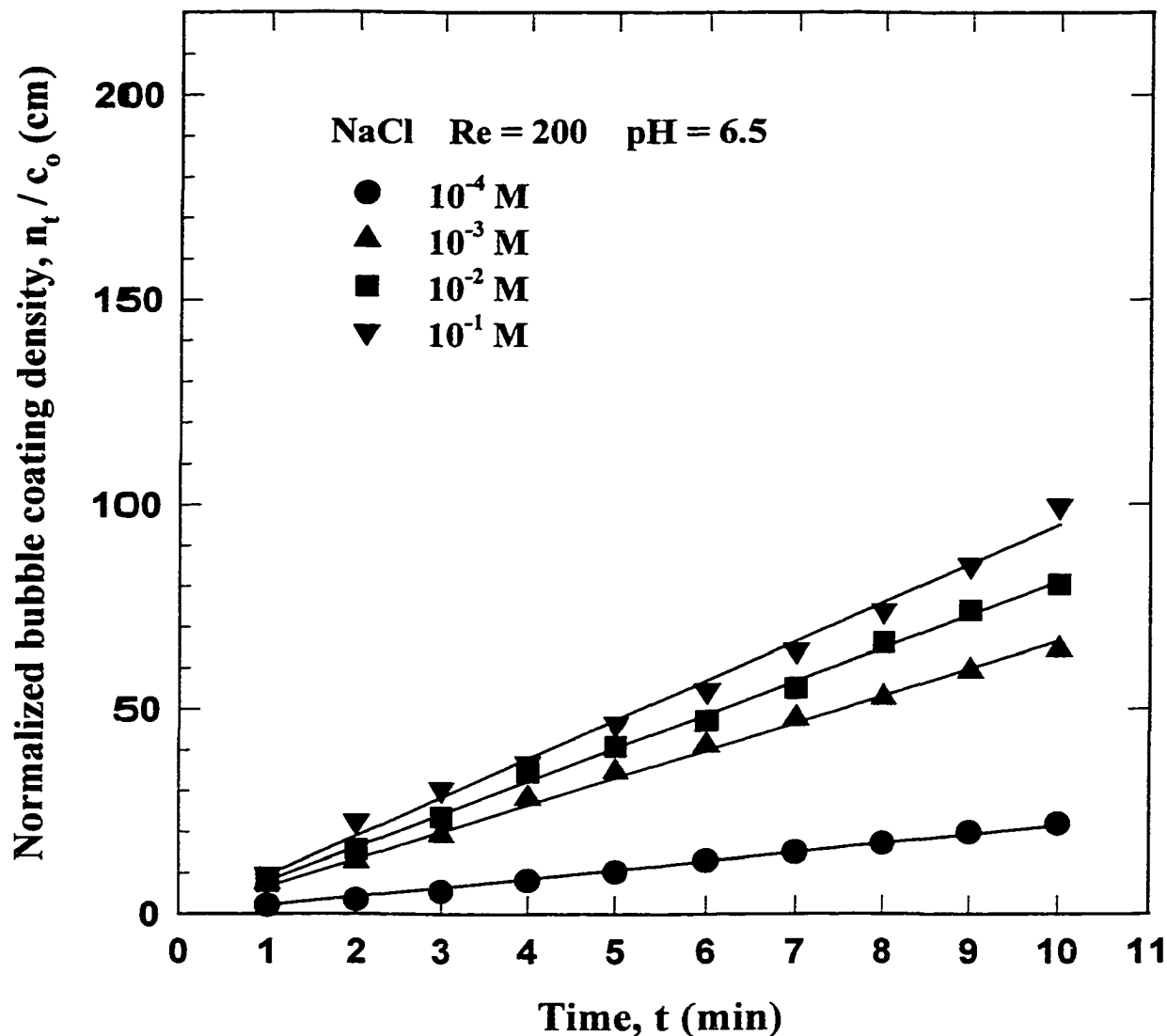


**Figure 7.4** Experimental results of the normalized bubble attachment density on the methylated glass versus time for different solution concentrations with fixed Reynolds number ( $Re$ ) and solution pH. The solid lines were obtained from a least-squares linear regression.

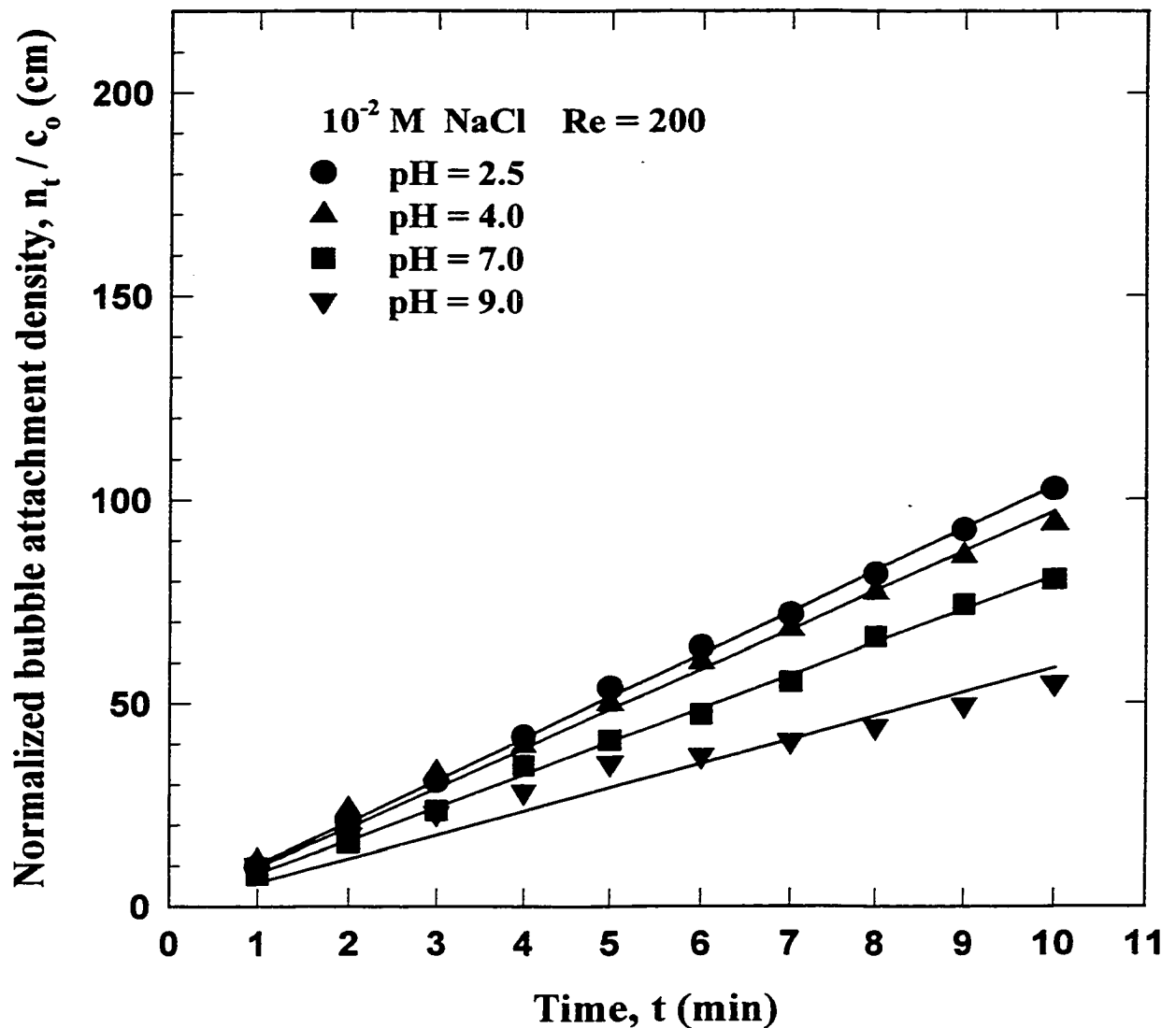


**Figure 7.5** Experimental results of the normalized bubble attachment density on the methylated glass versus time for different solution pH values with a fixed Reynolds number ( $Re$ ). The solid lines were obtained from a least-squares linear regression.

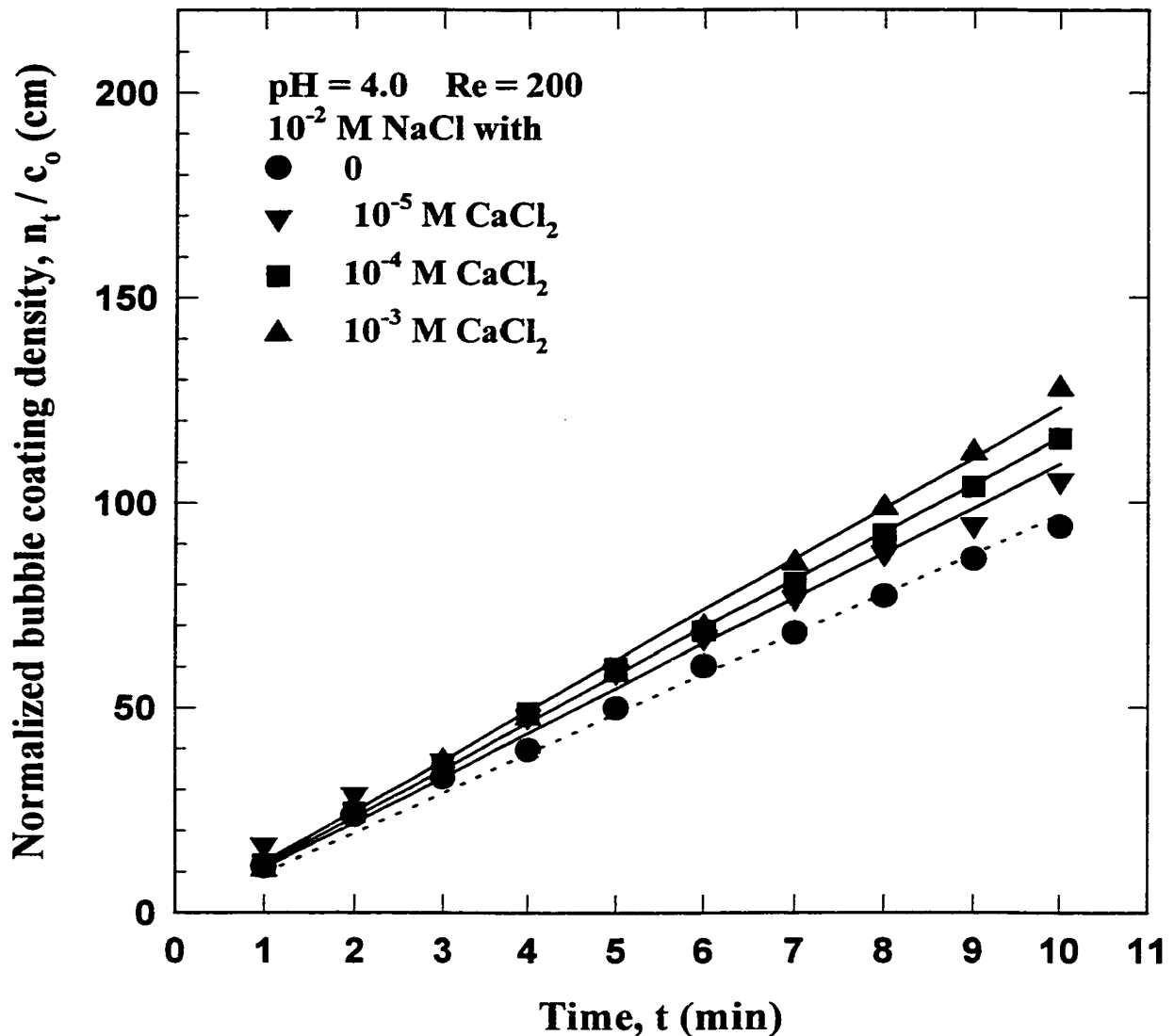


**Figure 7.6** Experimental results of the normalized bubble attachment density on the methylated glass versus time with effect of different levels of CaCl<sub>2</sub> concentration, while keeping Reynolds number (Re) and solution pH constant. The straight line obtained from a least-squares linear regression.

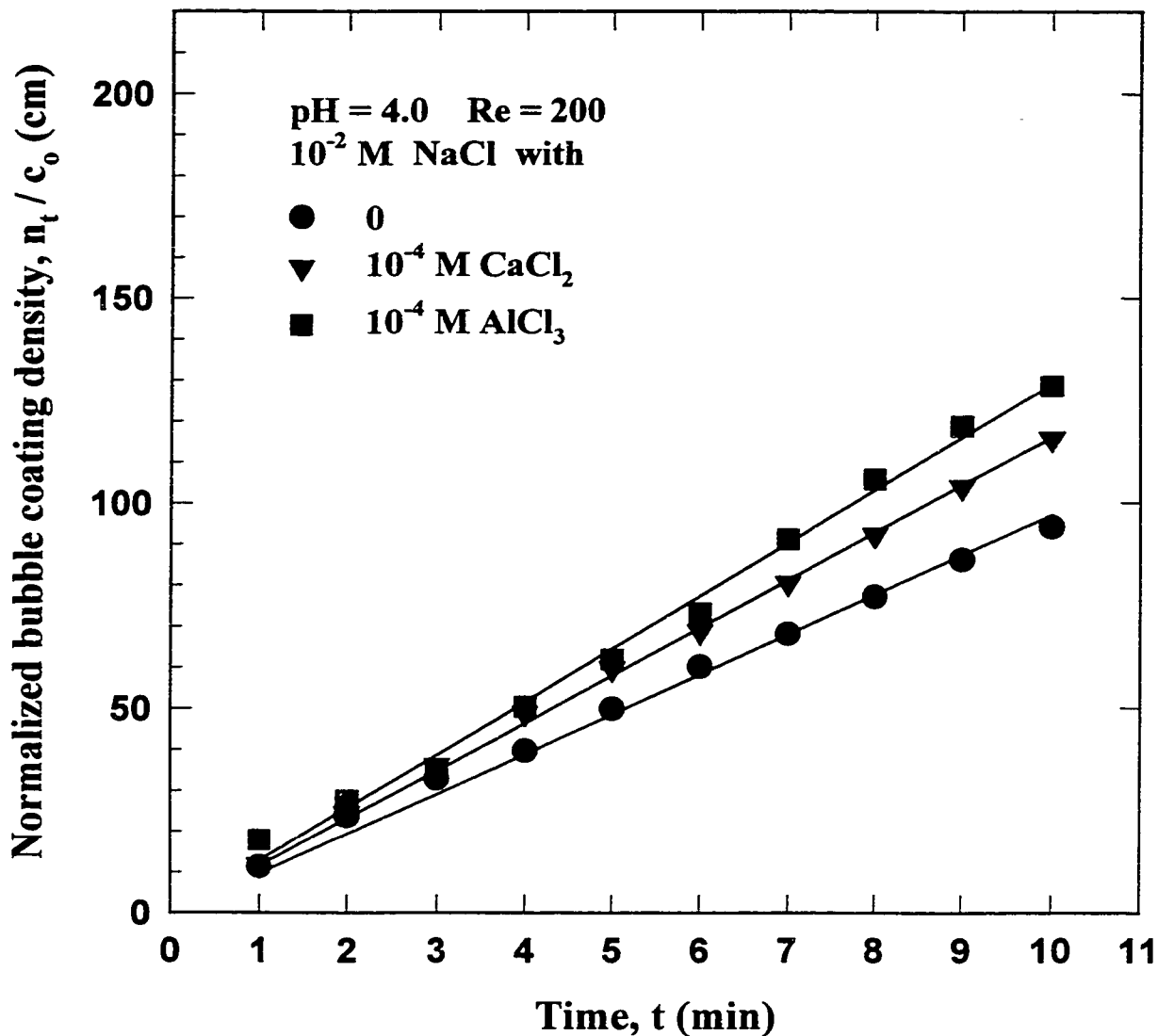


**Figure 7.7** Experimental results of the normalized bubble attachment density on the methylated glass versus time with effect of different metal ions, while keeping Reynolds number ( $Re$ ) and solution pH constant. The straight line obtained from a least-squares linear regression.

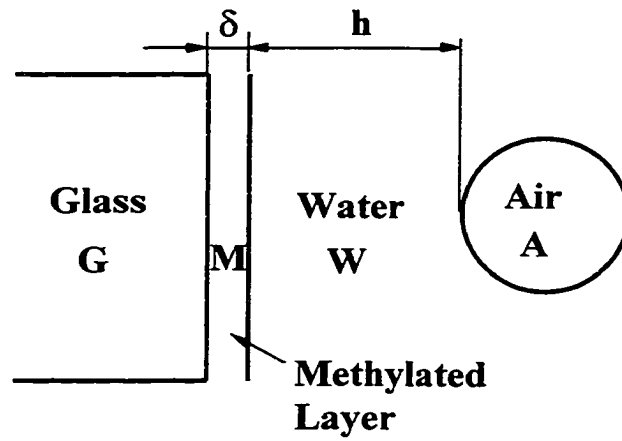


**Figure 7.8** Schematic diagram showing the van der Waals interaction for the methylated glass /water/ air system



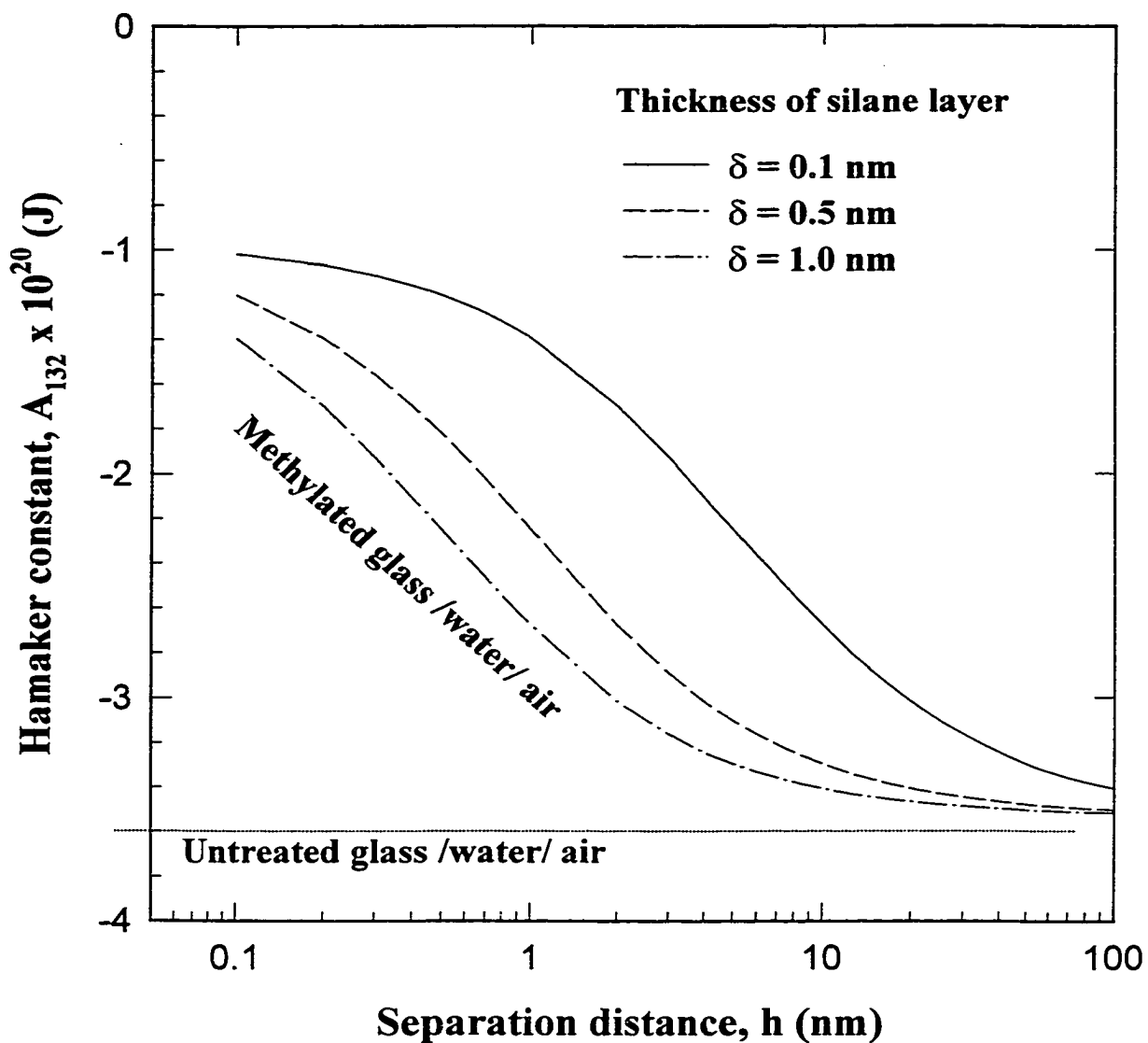


**Figure 7.9** Calculated effective Hamaker constant for the methylated glass /water/ air system

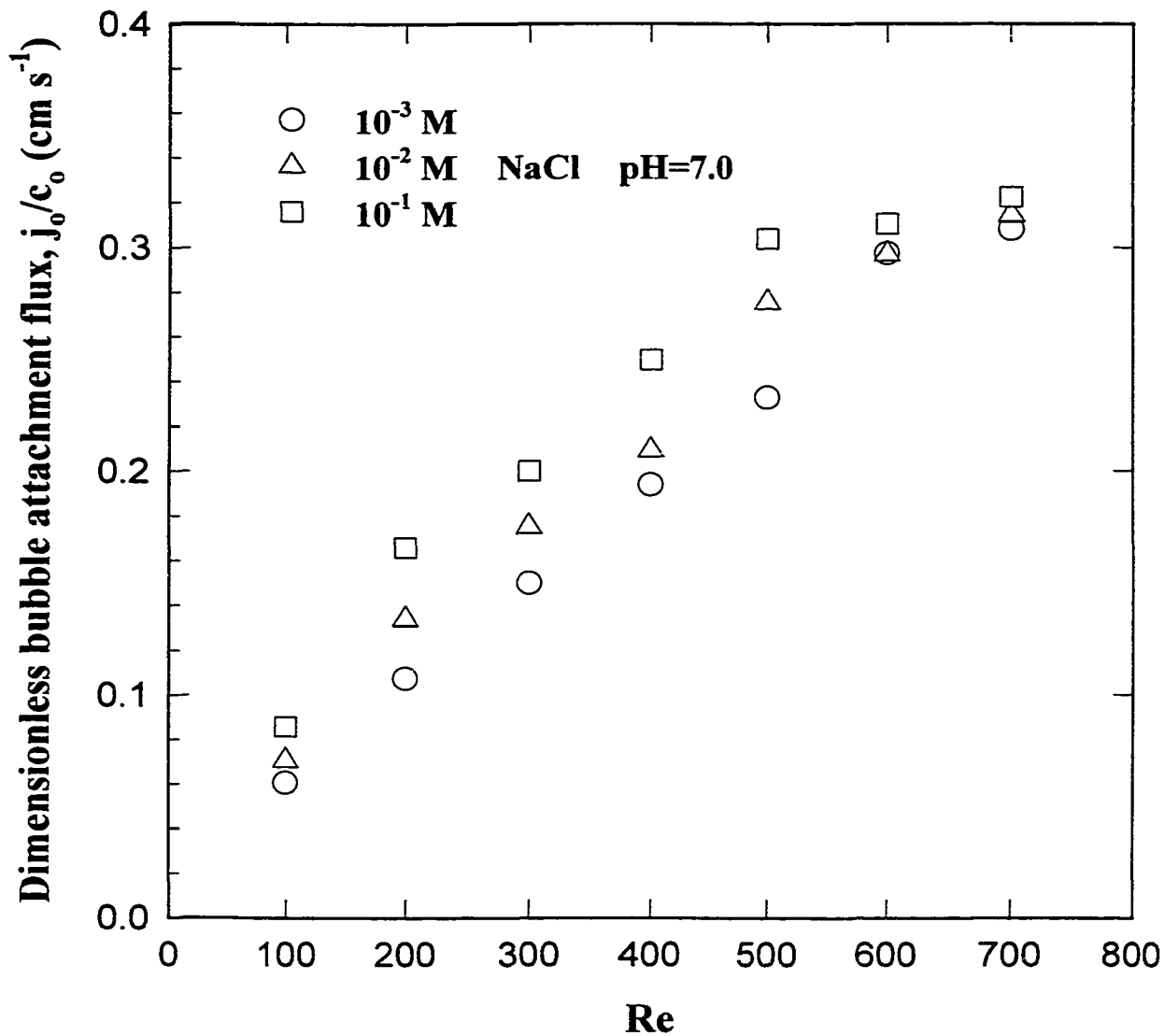


**Figure 7.10** Variation of the normalized bubble attachment flux onto methylated glass surfaces with the Reynolds number for different concentrations of the solution

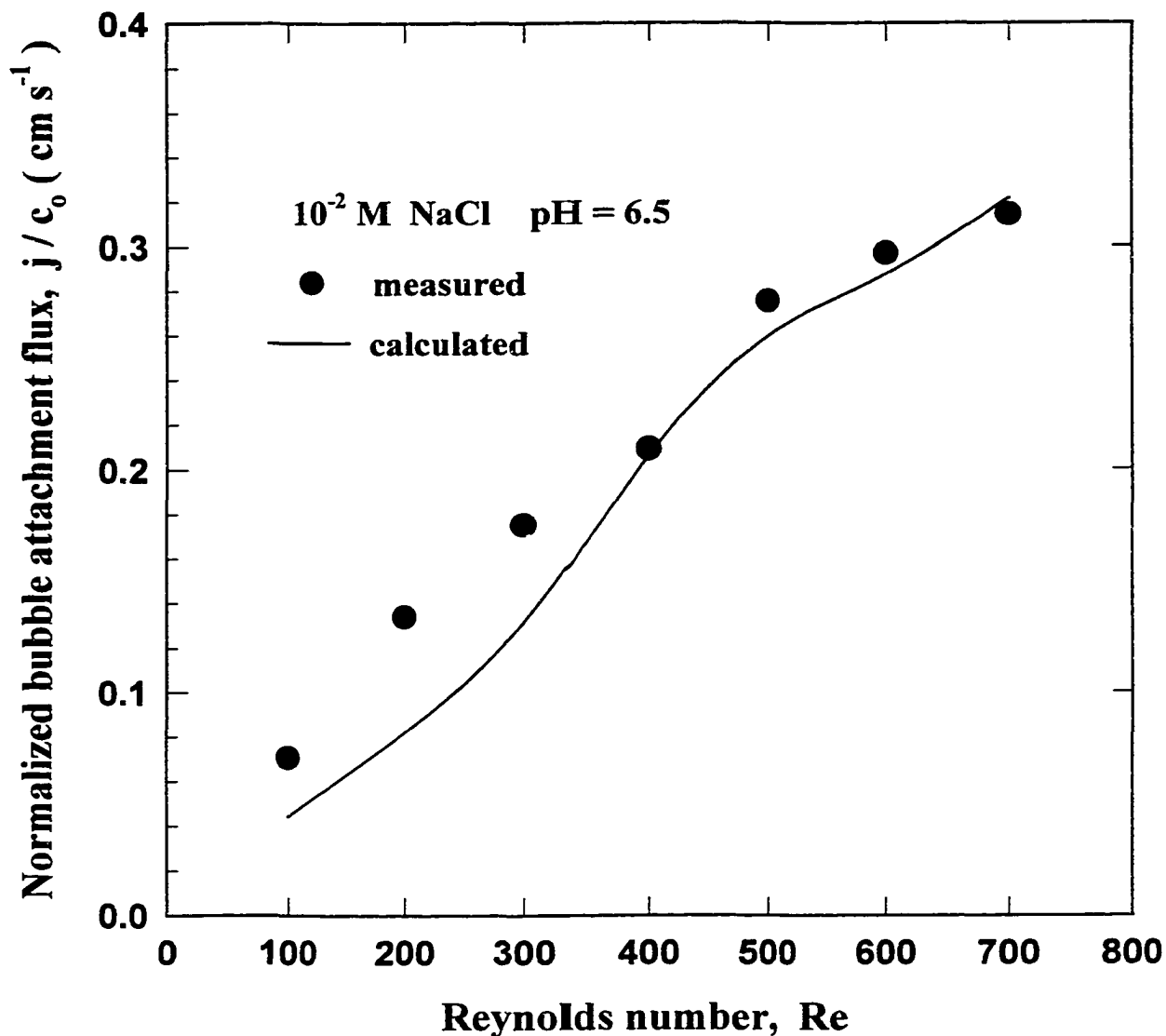


**Figure 7.11a** Variation of the normalized bubble attachment flux onto methylated glass surface with the Reynolds number for fixed solution concentration and pH value. Solid symbols represent experimentally measured flux; Solid line is the calculated bubble mean attachment flux with bubble size distribution corrections.

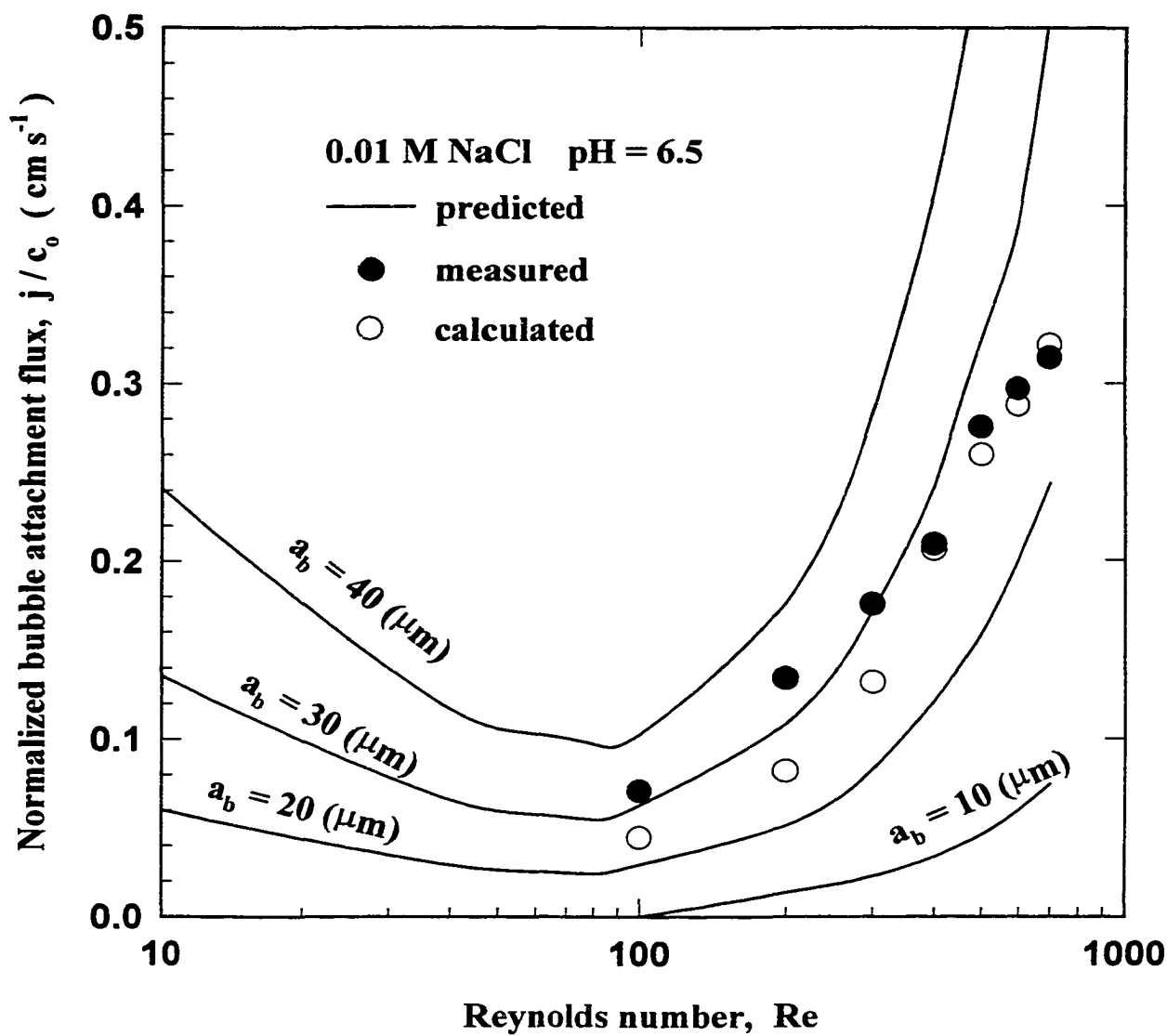


**Figure 7.11b** Variation of the Normalized bubble attachment flux onto methylated glass surface with the Reynolds number. Solid lines represent solutions to bubble transport equation based on a uniform bubble size; Solid symbols are experimentally measured results; Open symbols are calculated bubble attachment flux with bubble size distribution corrections.

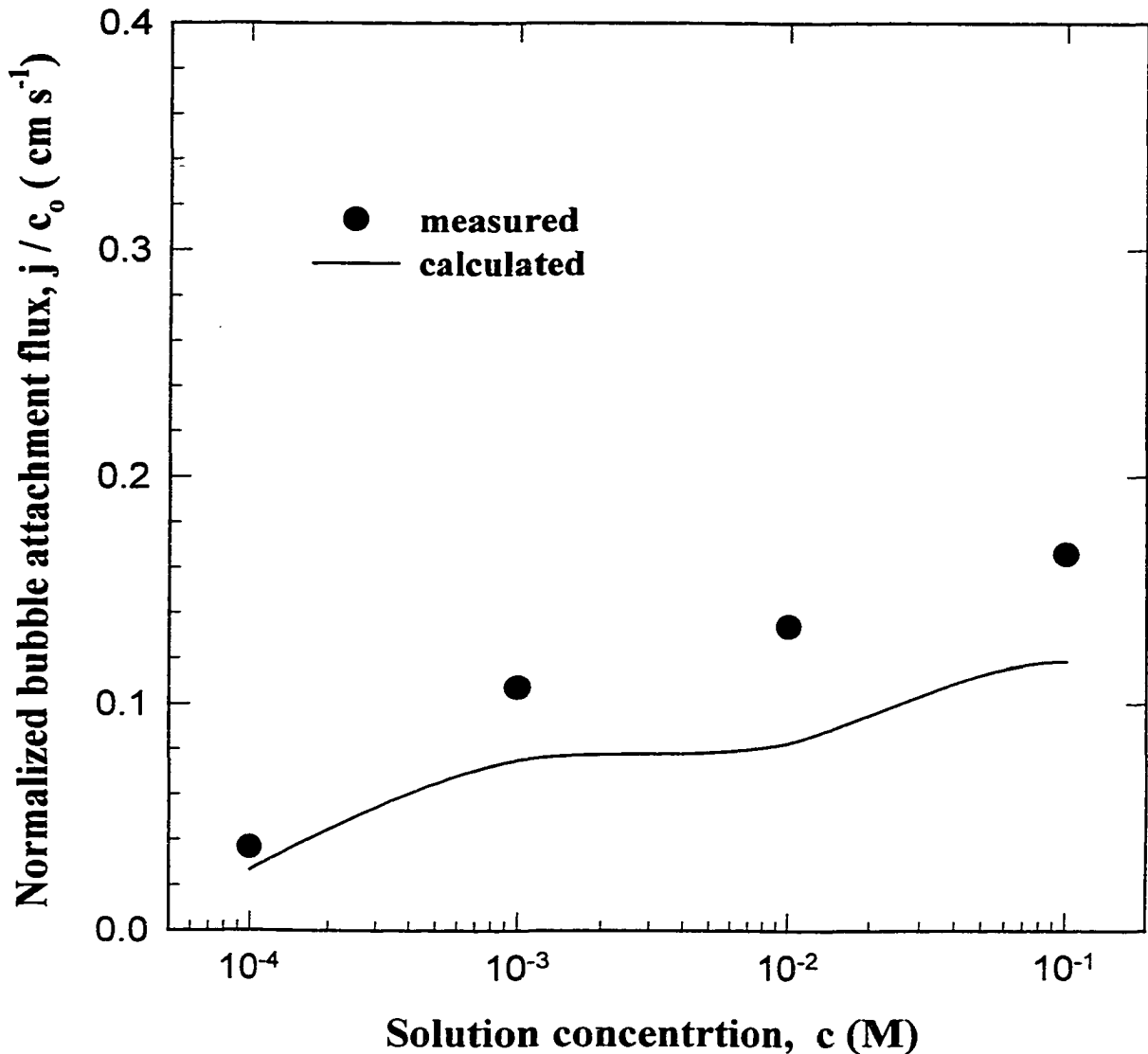


**Figure 7.12** Variation of the normalized bubble attachment flux onto methylated glass surface with NaCl solution concentration under a fixed Reynolds number  $Re=200$ . Solid symbols represent experimental results; Solid line is the calculated mean attachment flux with bubble size distribution correction.

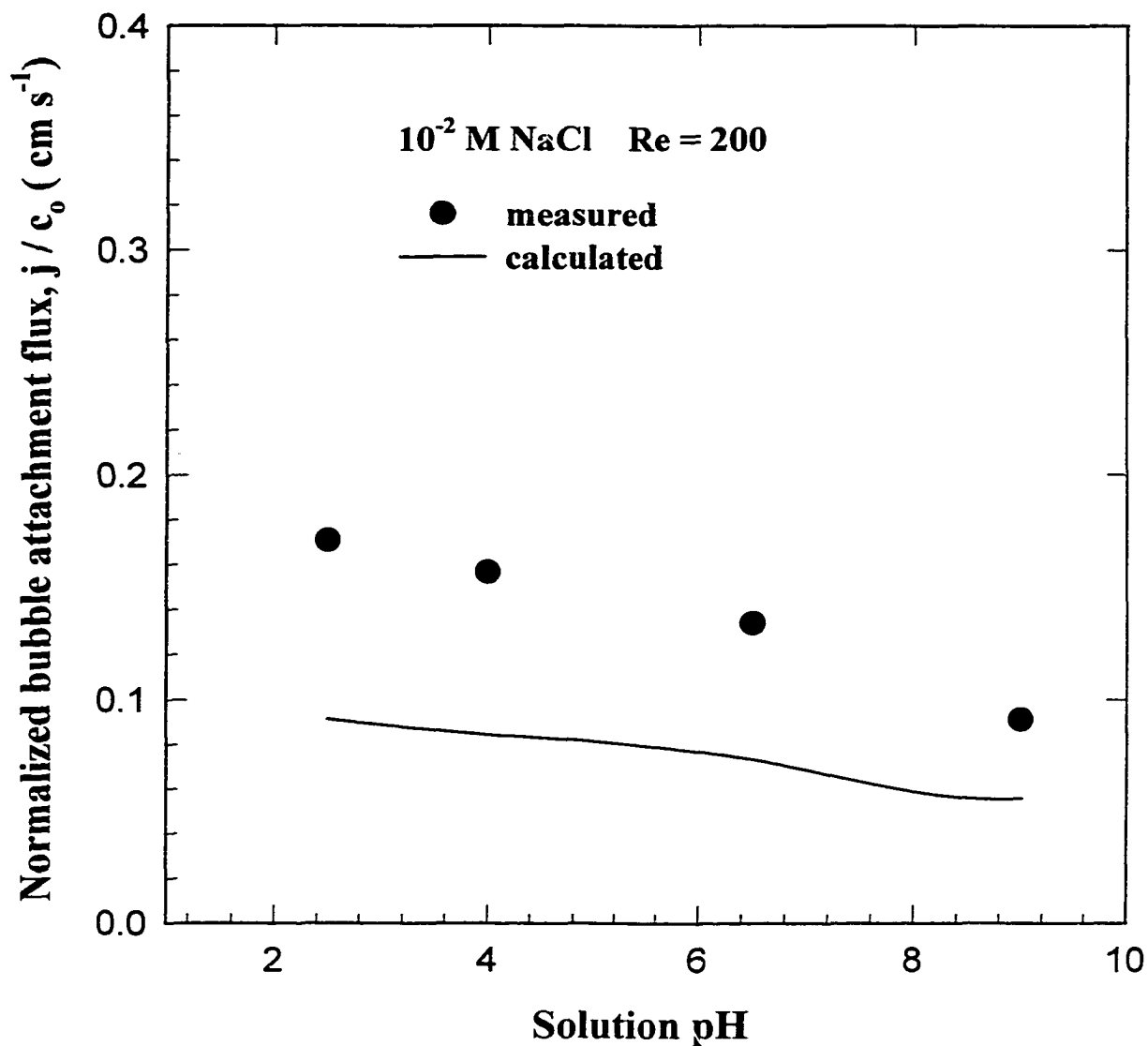


**Figure 7.13** Variation of the normalized bubble attachment flux onto methylated glass surface with NaCl solution pH under a fixed Reynolds number  $Re=200$ . Solid symbols represent experimental results; Solid line is the calculated mean attachment flux with bubble size distribution correction.

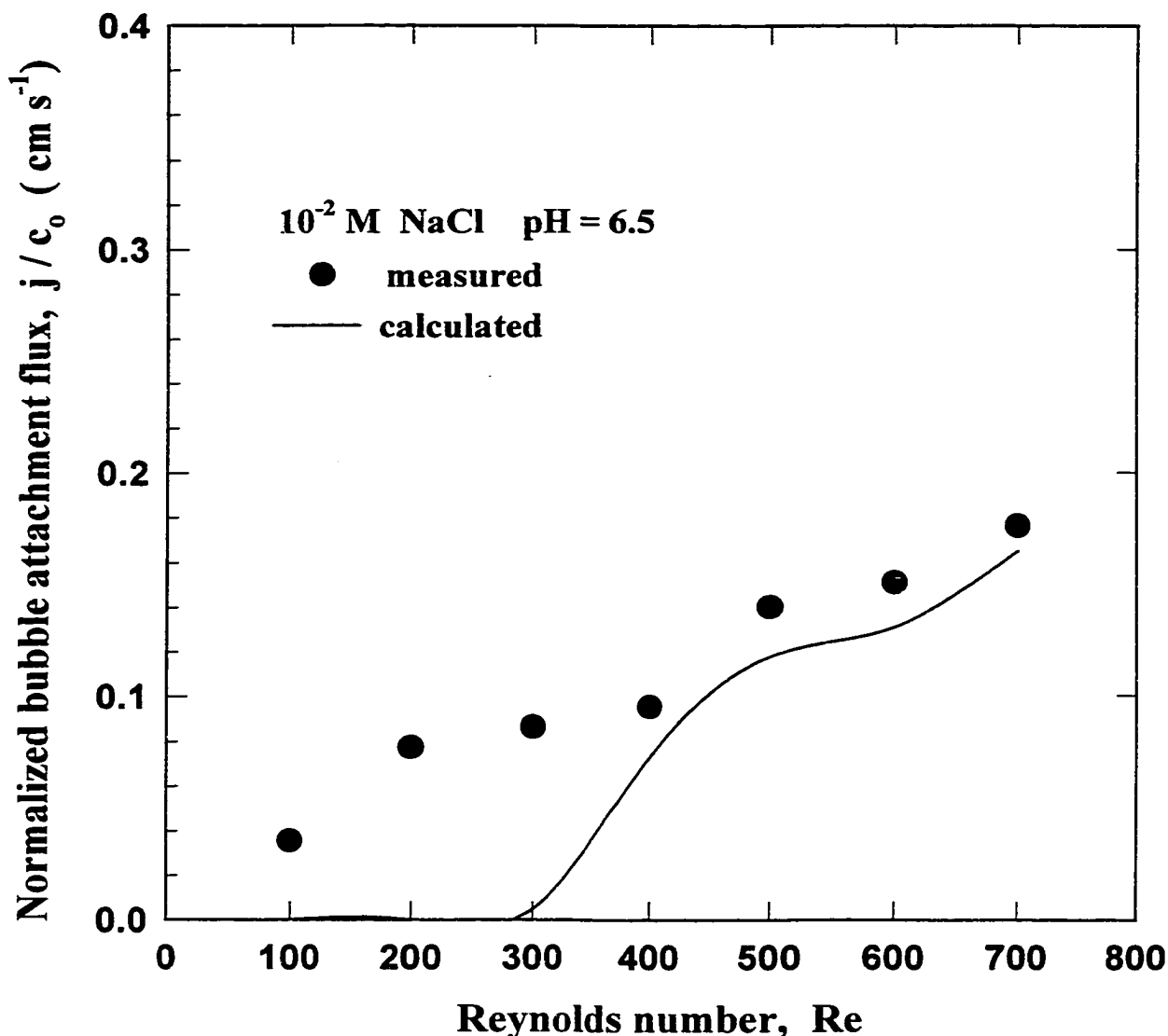
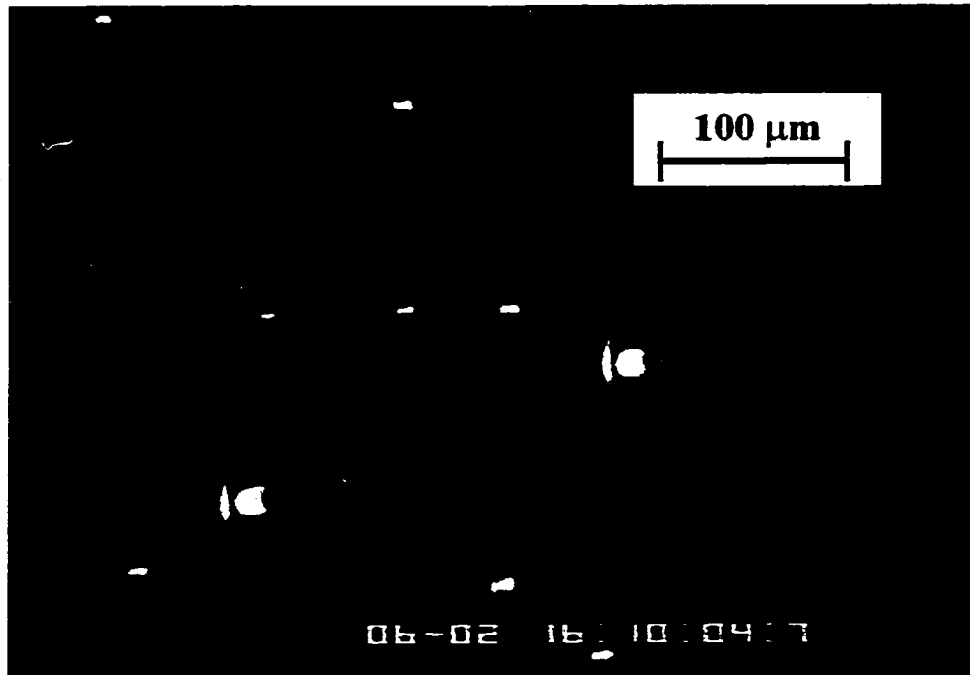


**Figure 7.14** Variation of the normalized bubble attachment flux onto untreated glass surface with the Reynolds number for fixed solution concentration and pH value. Solid symbols represent experimentally measured flux; Solid line is the calculated bubble mean attachment flux with bubble size distribution correction.



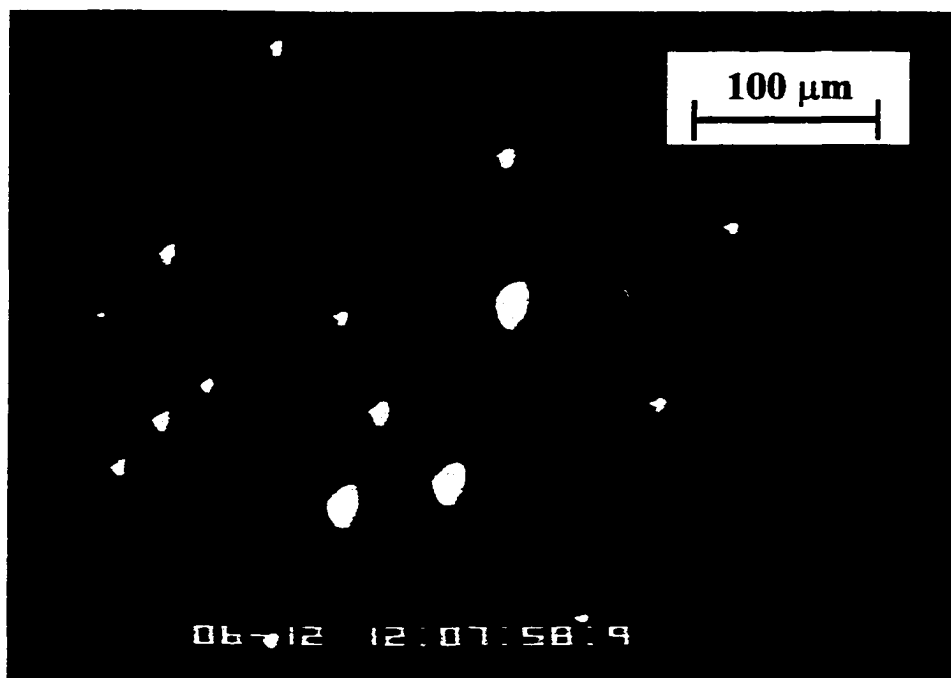
(i) Scanned image for bubble attachment on the untreated glass surface (top view)



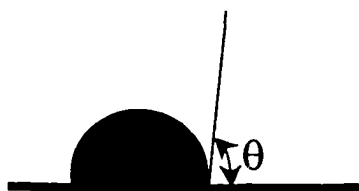
(ii) Configuration of bubble attachment to the untreated glass surface (side view)

**Figure 7.15a**





(i) Scanned image for bubble attachment on the methylated glass surface (top view)



(ii) Configuration of bubble attachment on the methylated glass surface (side view)

**Figure 7.15b**

## CHAPTER 8

### CONCLUSIONS AND RECOMMENDATIONS

#### 8.1 Contributions Made by This Study

Following the research objectives set out in the Introduction, a thorough study of kinetics of the bubble-solid surface attachment was conducted and a more comprehensive understanding of the underlying bubble attachment mechanisms has been achieved. The major contributions made by this dissertation can be summarized as follows:

1 The impinging jet technique has been successfully extended for studying bubble attachment processes. An extensive experimental work has been carried out to reveal the behaviors of bubble attachment onto the untreated and methylated glass collectors over a wide range of hydrodynamic and physicochemical conditions. Contact angle measurements for these two glass collectors indicated that the untreated glass is hydrophilic, while the methylated glass is hydrophobic in nature. The observed experimental results not only showed that the bubble attachment flux to the methylated glass is considerably higher than that to the untreated glass, but also revealed significantly different attachment mechanisms for these two collectors (i.e., the untreated and the methylated glass). The benefits of this study are threefolds: (i) the present study provides insight into the bubble attachment behaviors and mechanisms; (ii) the experiments conducted in this study generate a great deal of first-hand experimental data that would enable validation and improvement of fundamental bubble attachment models; and (iii) since the hydrodynamic conditions created around the stagnation point in the impinging jet region are very similar to those existing at the foremost part of a spherical collector (e.g., a large solid particle) exposed to an induced uniform flow or setting due to gravity, the process of gas bubble attachment onto a solid surface in the impinging jet region can be analogous to bubble-particle interaction and attachment occurring in flotation processes.

2 A theoretical model was developed for quantifying the bubble attachment flux to a solid surface in the impinging jet region. The theoretical work presented in this study represents a synthesis of complex fluid flow, particle mass transfer, and colloidal *DLVO* interaction forces. The important theoretical contributions are highlighted as below. (i) A finite-difference analysis based control volume method was used to numerically solve the axisymmetric two-dimensional Navier-Stokes equations that govern the fluid flow in the impinging jet region. For simplicity, the hydrodynamic conditions around the stagnation point where the colloidal interactions are expected to play important roles in the bubble attachment were approximated by an expression of the stagnation flow patterns. The valid range of such an expression was examined on the basis of a comparison of the stagnation point flow patterns with complete numerical solutions to the Navier-Stokes equations. (ii) Based on the mass conservation equation, transport of fine bubbles from a flowing jet to a solid surface in the impinging jet region was modeled with consideration of hydrodynamic convection, Brownian diffusion, external gravitational force, and colloidal interaction forces with the framework of the *DLVO* theory. The expression for the bubble transport equation was greatly simplified using the proposed stagnation point flow patterns. Furthermore, the validation of such bubble transport equation was examined by considering the bubble shape (or deformation), the hydrodynamic boundary-layer thickness in the impinging jet region, and the perfect sink boundary condition for interception of bubbles. An expression was derived for evaluation of the hydrodynamic boundary-layer thickness in the impinging jet region. (iii) A numerical approach was implemented to solve the stiff ordinary differential equation (i.e., the bubble transport equation) and an extensive parametric study was conducted to examine the influences of dimensionless groups including  $Pe$ ,  $Gr$ ,  $Ad$ ,  $Dl$ ,  $Da$ , and  $\tau$  on the bubble attachment rate,  $Sh$ . An analytical expression of the dependence of  $Sh$  on  $Pe$ , was derived to relate the bubble attachment rate,  $Sh$ , to the contributions due to bubble convection, diffusion, migration as well as the bubble number concentration distributions. (iv) The expressions for the *DLVO* colloidal interaction forces (i.e., the van der Waals and the *EDL* interactions) were constructed. The effect of the methylated layer on the Hamaker constant of the air /water/ methylated glass system was examined. A detailed discussion on the *EDL* interaction mode was provided.

3 A comparison of experimental results with numerical predictions showed that the theoretical bubble attachment flux to the methylated glass was in a reasonable agreement with the experimental observations, and hence it suggested the validation of the bubble transport model developed on the basis of the *DLVO* theory. Furthermore, it was found that the theoretically predicted attachment flux to the untreated glass matched well with the experimentally measured values when the Reynolds number was high ( $Re \geq 400$ ). However, the proposed model failed to predict the bubble attachment at low Reynolds numbers ( $100 \leq Re \leq 300$ ). This fact suggests that the bubble attachment process is completely dominated by hydrodynamic conditions at high Reynolds numbers. In other words, the colloidal interactions play vital roles in the bubble transport to a solid surface only when the Reynolds number is low. In addition, it was noted that since both the van der Waals interaction among the bubble/water/glass system and the *EDL* interaction between the bubble and the untreated glass are repulsive, the evidence of gas bubble attachment onto the untreated (hydrophilic) glass surface could not be explained on the basis of existing thin film theories. The proposed hypotheses for such an attachment are asymmetric electrostatic double layer interaction, fluctuation of surface potentials, the discrete of surface charges, the surface roughness, and the electroviscous effect. It was also believed that these non-*DLVO* effects were responsible for the observed discrepancy between theory and experiment of the bubble attachment flux to the untreated and methylated glass when the Reynolds number is low. Finally, a mechanism for fine bubble attachment onto glass surface was postulated.

4 Since no commercial instrument is available, an apparatus, based on the microelectrophoretic technique, was therefore devised to measure the bubble zeta-potential over a wide range of solution conditions. Such a newly-designed apparatus has the following two unique features: the electrodes were designed in such a way that micro-sized bubbles could be generated across the entire cell. Thus, one could readily locate a bubble to achieve electrophoretic measurements at the stationary level to eliminate the effect of the electroosmotic flow; and the other important feature is the experimental setup utilized a computer-controlled vertical translator stage so that the movement of bubbles with diameter up to  $80 \mu m$  could be easily followed and the bubble's trajectory

could be traced over 4 to 8 seconds (depending on the bubble size). Therefore, the electrophoresis measurement period could be taken much longer, giving more accurate and reliable data for the bubble zeta-potentials. In addition, some relevant phenomena including electroosmotic flow, temperature rise, and “relaxation time” needed for exchange of ions between a bubble and the solution were discussed. A rigorous theoretical approach to quantify the electroosmotic flow in an electrophoretic cell of rectangular shape was developed.

## **8.2 Recommendations for Future Work**

Based on the results presented in this study, the following recommendations can be made to achieve a better and more complete understanding of bubble-solid surface interaction and attachment:

- 1.** Surfactants are often involved in many real flotation systems, where the attachment of bubbles to solids is essential for success of the process. From an interfacial science viewpoint, the presence of surfactants not only can modify the interfacial tension between bubble-aqueous phase that is related to the van der Waals interaction, but also may, to a larger extent, alter the zeta-potential of the bubble-liquid and the solid-liquid interfaces. Therefore, it is expected that the bubble-solid attachment in an aqueous solution having surfactants may behavior quite differently. To this end, the impinging jet technique seems a perfect candidate for such investigation. The experimental results then can be used to compare with numerical predictions to evaluate the applicability of the *DLVO* theory based model to the bubble attachment in a system having surfactants.
- 2.** Experiments carried out in this study were free of fine solids. However, more difficulties arise whenever fine solids are involved into the system, which is frequently encountered in the real world. In this study, several experiments were carried out for bubble attachment onto the bitumen-coated glass using the Syncrude process water with three types of fine clays: Illite, Kaolite, and Montmorillite. It was evidenced that the bubble attachment flux to the bitumen-coated glass slightly decreased due to the effect of clay particles. Furthermore, experiments also showed that no appreciable differences for

the bubble attachment using the Syncrude process water having these three types of clays if no additional  $Ca^{2+}$  ions were added to the testing system. However, an unusually bubble attachment behavior was observed for the system with Montmorillite clays and  $CaSO_4$ . It was found that when a certain amount of  $CaSO_4$ , for example  $10^{-3} M$   $CaSO_4$  was added to the solution, the bubble attachment flux was dramatically declined. So far, it is not quite clear what was the reason for the deterioration of the bubble-bitumen attachment. The results reported on the clay effects should be complemented with more extensive attachment experiments.

In order to provide insight into the mechanism of particle effect on the bubble attachment, it is highly desirable to first study the bubble attachment in a model system, which is a system of bubble attachment experiments conducted for untreated and methylated glass surfaces in the presence of mono-sized particles (e.g. glass beads and silicon powders). Obviously, the presence of fine solids may generate complex interactions between bubble-particle, glass collector -particle, and bubble-glass collector in flowing aqueous media. On the theoretical side, it will be a great challenge to develop a model that is able to quantitatively describe all these interactions and to evaluate how these interactions may affect the bubble-glass collector attachment process. Accordingly, a numerical approach will be developed to solve the proposed model. On the experimental side, experiments will be carried out to study the gas bubble-collector attachment in the presence of fine solid particles. The experimental results then are expected to compare with numerical predictions and to verify and improve the theoretical model.

3. It has been postulated that surface roughness may play a crucial role in bubble-solid attachment. In the literature, several attempts were made to examine the effect of surface roughness on the colloidal interactions. However, as yet, no study has been reported to incorporate such effect in dynamic bubble attachment (or particle deposition) investigation. Therefore, suggestions made here are to derive an expression for colloidal interaction, including the van der Waals and *EDL* interactions, between a smooth bubble and the relatively rough collector surface. Such an expression then will be implemented

to the bubble transport equation to theoretically evaluate the surface roughness effect on the bubble attachment. Meanwhile, the effect of the surface roughness on hydrodynamic conditions should be accounted for in the model. On the other hand, controllable experiments can be performed to study bubble attachment onto glass collector having different quantified surface roughness to compare with and to verify the proposed theory.

4. As pointed out Chapter 7, the discrete surface charge of the glass collector and the non-uniform distributions of the bubble zeta-potential also could be important to bubble attachment. Therefore, a complete theoretical analysis of the discrete glass surface charge and the non-uniform distributions of the bubble zeta-potential, based on an assumption of a certain type of distribution patterns, is absolutely needed to achieve a better understanding of the sensitivity of the bubble attachment to these stochastic effects.

5. The dynamic study of the *EDL* interaction is still in its infancy. Unfortunately, the dynamic *EDL* interaction was not accounted for the present model. It is expected that a rigorous coupling of hydrodynamic and electrochemical aspects of the dynamic *EDL* (e.g, the electroviscous effect) may lead to different results of the bubble attachment.

6. Numerical predictions have reported that an interesting minimum of the bubble attachment flux with respect to the Reynolds number is expected to occur around  $Re = 100$ . Although theoretical explanation was furnished, the corresponding experiments did not extend to Reynolds numbers smaller than 100 due to limited time and a limitation in the experimental setup. It would be highly desirable and interesting that after a sort of modification, experiments could be continued to the entire range of the Reynolds number so that numerical predictions could be confirmed by experiments.

7. It should be pointed out that the presented model describing transport of micro-sized bubbles from the bulk flowing jet onto a solid surface does not take into consideration of the blocking effect. As mentioned in Chapter 7, such a blocking effect was not observed in experiments is attributed to a sufficiently low bubble bulk concentration used in experiments and a fact that small bubble (less than  $30 \mu m$ ) were

usually dissolved within a minute after attachment onto the glass collector. However, it has been evidenced in the literature that the blocking effect has a strong impact on particle deposition, and, in particular, is one of major sources responsible for the nonlinear behavior of deposition. It is expected that the influence of the blocking effect on the bubble attachment becomes significant when the bubble number bulk concentration is high. Accordingly, a more comprehensive description of bubble attachment including the blocking effect needs to be pursued.



## BIBLIOGRAPHY

- Acrivos, A., and Taylor, T. D., *Phys. Fluids* **5**, 387 (1962).
- Adamczyk, Z., and van de Ven, T. G. M., *J. Colloid Interface Sci.* **84**, 497 (1981).
- Adamczyk, Z., Dabros, T., Czarnecki, J., and van de Ven, T. G. M., *Adv. Colloid Interface Sci.* **19**, 183 (1983).
- Adamczyk, Z., Czarnecki, J., and Warszynski, P., *J. Colloid Interface Sci.* **106**, 299 (1985).
- Adamczyk, Z., Zembala, M., Siwek, B., and Czarnecki, J., *J. Colloid Interface Sci.* **110**, 188 (1986).
- Adamczyk, Z., Siwek, B., Zembala, M., and Warszynski, P. *J. Colloid Interface Sci.* **130**, 578 (1989).
- Adamczyk, Z., *Colloids Surf.* **39**, 1 (1989).
- Adamczyk, Z., Siwek, B., Zembala, M., and Warszynski, P. *J. Colloid Interface Sci.* **140**, 123 (1990).
- Adamczyk, Z., Szyk, L., and Warszynski, P. *Colloid Surf.* **75**, 185 (1993).
- Adamczyk, Z., Siwek, B., Zembala, M., and Belouschek, P., *Adv. Colloid Interface Sci.* **48**, 151 (1994).
- Adamczyk, Z., and Warszynski, P., *Adv. Colloid Interface Sci.* **63**, 41 (1996).
- Adamczyk, Z., Szyk, L., and Warszynski, P. *J. Colloid Interface Sci.* **209**, 350 (1999).
- Adamson, A. W., 1982, *Physical Chemistry of Surfaces*, 4<sup>th</sup> ed., Wiley, New York.
- Alargova, R. G., Petkov, J. T., Denkov, N. D., and Ivanov, I. B., *Colloids Surf.* **134**, 331 (1998).
- Alty, T., *Proc. Roy. Soc. A* **112**, 235 (1926).
- Amano, R. S., and Brandt, H., *ASME J. Heat Transfer* **106**, 410 (1984).
- Arujo, Y. C., Toledo, P. G., Leon, V., and Gonzalez, H. Y., *J. Colloid Interface Sci.* **176**, 485 (1995).
- Bach, N., and Gilman, A., *Acta Physicochem.* **9**, 1 (1938).

- Bird, B., Stewart, W., and Lightfoot, E., "Transport Phenomena." John Wiley & Sons, Toronto, 1960.
- Bochkarev, A. A., Pukhovoy, M. V., and Kasyanova, L. N., *J. Colloid Interface Sci.* **175**, 6 (1995).
- Bohmer, M.R., van der Zeeuw, E.A., and Koper, G.J.M., *J. Colloid Interface Sci.* **197**, 242 (1998).
- Boluk, M. Y., and van de Ven, T. G. M., *Colloids Surf.* **36**, 157 (1990).
- Bowen, B. D., Levine, S., and Epstein, N., *J. Colloid Interface Sci.* **54**, 375 (1976).
- Bowen, B. D., and Epstein, N., *J. Colloid Interface Sci.* **72**, 81 (1979).
- Brenner, H., *Chem. Eng. Sci.* **16**, 242 (1961).
- Brook, D. E., *J. Colloid Interface Sci.* **43**, 687 (1973).
- Buckley, J. S., Takamura, K., Morrow, N. R., *SPERE* **4**, (1989).
- Burn, S. E., Yiacoumi, S., and Tsouris, C., *Separation Purification Tech.* **11**, 221 (1997).
- Carnie, S. L., Chan, D. Y. C., and Gunning J. S., *Langmuir* **10**, 2993 (1994).
- Celik, M.S., Yasar, E., and El-Shall, H., *J. Colloid Interface Sci.* **203**, 254 (1998).
- Chan, D. Y. C., and White, L. R., *J. Colloid Interface Sci.* **74**, 303 (1980).
- Chan, S. H., and Moussa, B., *ASME J. Heat Transfer*, **118**, 93 (1996).
- Chen, J., *J. Colloid Interface Sci.* **98**, 329 (1984).
- Chen, Q., and Modi, V., *Int. J. Heat Mass Transfer* **42**, 873 (1999).
- Chu, X., and Wasan, D. T., *J. Colloid Interface Sci.* **184**, 268 (1996).
- Collins, G. L., Motarjemi, M., Jameson, G. J., *J. Colloid Interface Sci.* **63**, 69 (1978)
- Coutelieres, F.A., Burganos, V.N, and Payatakes, A.C., *J. Colloid Interface Sci.* **161**, 43 (1993).
- Czarnecki, J., and Dabros, T., *J. Colloid Interface Sci.* **78**, 25 (1980).
- Czarnecki, J., *J. Colloid Interface Sci.* **98**, 590 (1984).

- Czarnecki, J., *Adv. Colloid Interface Sci.* **24**, 283 (1986).
- Dabros, T., Adamczyk, Z., and Czarnecki, J., *J. Colloid Interface Sci.* **62**, 529 (1977).
- Dabros, T., and Adamczyk, Z., *Chem. Eng. Sci.* **34**, 1041 (1979).
- Dabros, T., and van de Ven, T.G.M., *J. Colloid Interface Sci.* **89**, 232 (1982).
- Dabros, T., and van de Ven, T.G.M., *Colloid Polymer Sci.* **261**, 694 (1983a).
- Dabros, T., and van de Ven, T.G.M., *J. Colloid Interface Sci.* **93**, 576 (1983b).
- Dabros, T., and van de Ven, T. G. M., *Physicochem. Hydrodynamics* **8**, 161 (1987).
- Dai, Z., Dukhin, S., Fornasiero, D., and Ralson, J., *J. Colloid Interface Sci.* **197**, 275 (1998).
- Derjaguin, B. V., and Dukhin, S. S., 1981, in "Proc. 13<sup>th</sup> International Mineral Processing Congress, Warsaw, Poland" (J. Laskowski, Ed.), Elsevier, New York.
- Deshpande, M. D., and Vaishnav, R. N., *J. Fluid Mech.* **114**, 213 (1982).
- Dibbs, H. P., Sirois, L. L., and Bredin, R., *Can. Metallurgical Quart.* **13**, 395 (1974).
- Dijt, J. C., Stuwart, M. A., Hofman, J. E., and Fleer, G. J., *Colloids Surf.* **51**, 141 (1990).
- Drelich, J., and Miller, J. D., *J. Colloid Interface Sci.* **164**, 252 (1994).
- Duhkin, S. S., and Derjaguin, B. V., in "Surface and Colloid Science." Matijevic, E. (ed.), *Electrokinetic Phenomena*, Wiley Interscience, New York, Vol. 7, 1974.
- Dzjalosinskij, I. E., Lifshitz, E. M., and Pitaevskij, L. P., *Adv. Phys.* **10**, 165 (1961).
- Elimelech, M., and O'Melia, C. R., *Langmuir*, **6**, 1153 (1990).
- Elimelech, M., *J. Colloid Interface Sci.* **146**, 337 (1991).
- Elimelech, M., *J. Colloid Interface Sci.* **164**, 190 (1994).
- Epstein, N., and Masliyah, J.H., *Chem. Eng. J.* **3**, 169 (1972).
- Faibish, R. S., Elimelech, M., and Cohen, Y., *J. Colloid Interface Sci.* **204**, 77 (1998).
- Fukui, Y., and Yuu, S., *Chem. Eng. Sci.* **35**, 1097 (1980).
- Gibbs, J. W., *The Scientific Papers*, Vol. 1, Dover, New York, 1961.

- Goldman, A. J., Cox, R. G., and Brenner, H., *Chem. Eng. Sci.* **22**, 621 (1967a); 637 (1967b).
- Goren, S. L., *J. Fluid. Mech.* **41**, 619 (1970).
- Goren, S. L., and O'Neill, M. E., *Chem. Eng. Sci.* **26**, 325 (1971).
- Gosman, A. D., Pun, W. M., Runchal, A. K., Spalding, D. B., Wolfshtein, M., "Heat and Mass Transfer in Recirculating Flows", Academic Press, London, 1969.
- Graciaa, A., Morel, G., Saulner, P., Lachaise, J., and Schechter, R. S., *J. Colloid Interface Sci.* **172**, 131 (1995a).
- Graham, K.M., and Ramadhyani, S., *ASME J. Heat Transfer* **118**, 343 (1996).
- Gregory, J., and Wishart, A. J., *Colloids Surf.* **1**, 313 (1980).
- Gregory, J., *J. Colloid Interface Sci.* **83**, 138 (1981).
- Gregory, J., *Critical Rev. Environ. Control.* **19**, 185 (1989).
- Griffith, R. M., *Chem. Eng. Sci.* **17**, 1057 (1962).
- Hall, D.G., *Adv. Colloid Interface Sci.* **37**, 89-133 (1991).
- Hamieh, T., and Stiffert, B., *Colloids Surf.* **84**, 217 (1994).
- Harwot, P., and van de Ven, T. G. M., *Colloid Surf.* **121**, 229 (1997).
- Happel, J., *AICHE J.* **4**, 197 (1958).
- Heindel, T. J., and Bloom, F., *J. Colloid Interface Sci.* **213**, 101 (1999).
- Herren, B. J., Shafer, S. G., van Alstine, J., Harris, J. M., and Snyder, R. S., *J. Colloid Interface Sci.* **115**, 46 (1987).
- Hidalgo-Alvarez, R., *Adv. Colloid Interface Sci.* **34**, 217 (1991).
- Hogg, R., Healy, T. W., and Fuerstenau, D. W., *Trans. Faraday Soc.* **62**, 1638 (1966).
- Hong, S., Faibish, R. S., and Elimelech, M., *J. Colloid Interface Sci.* **196**, 267 (1997).
- Hsu, J. P., and Kuo, Y. C., *J. Colloid Interface Sci.* **170**, 220 (1995).
- Huisman, I. H., Tragardh, G., and Tragardh, C., *Chem. Eng. Sci.* **54**, 281 (1999).

- Hunter, R. J., "Zeta Potential in Colloid Science: Principles and Applications." Academic Press, London, 1981.
- Israelachvili, J. N., and Tabor, D., *Proc. Roy. Soc. London* **A331**, 19 (1972).
- Israelachvili, J. N., "Intermolecular and Surface Forces." 2<sup>nd</sup> ed., Academic Press, London, 1985.
- Jun, B., and Kim, S., *J. Colloid Interface Sci.* **128**, 275 (1989).
- Kostoglou, M, and Karabelsas, A. J., *J. Colloid Interface Sci.* **151**, 534 (1992).
- Kubota, K., Hayashi, S., and Inaoka, M., *J. Colloid Interface Sci.* **95**, 362 (1983).
- Lakkapragara, S., and Walz, J. Y., *J. Colloid Interface Sci.* **183**, 199 (1996).
- Lakkapragara, S., and Walz, J. Y., *J. Colloid Interface Sci.* **196**, 177 (1997).
- Larsen, A. E., and Grier, D. G., *Nature* **385**, 230 (1997).
- Laskowski, J., and Kitchener, J.A., *J. Colloid Interface Sci.* **29**, 670 (1969).
- Law, H.S., and Masliyah, J.H., *Ind. Eng. Chem. Fundam.* **23**, 446 (1984).
- Leal, L. G., "Laminar Flow and Convective Transport Processes." Butterworth-Heinemann, Boston, 1992.
- Leppinen, D. M., *J. Colloid Interface Sci.* **212**, 431 (1999).
- Levich, V. G., "Physicochemical Hydrodynamics." Prentice-Hall, Englewood Cliffs, New Jersey, 1962.
- Li, D., *Colloids Surf.* **116**, 1-23 (1996).
- Li, D., and Neumann, A. W., *Adv. Colloid Interface Sci.* **36**, 125 (1992a).
- Li, D., and Neumann, A. W., *Colloid Polym. Sci.* **270**, 498 (1992b).
- Li, C., and Somasundaran, P., *J. Colloid Interface Sci.* **146**, 215 (1991).
- Li, C., and Somasundaran, P., *J. Colloid Interface Sci.* **148**, 587 (1992).
- Li, Y., and Park, C. W., *J. Colloid Interface Sci.* **185**, 49 (1997).
- Lin, F. Y. H., and Li, D., *Chem. Eng. Sci.* **50**, 2633 (1995).

- Loewenberg, M., and Davis, R. H., *Chem. Eng. Sci.* **49**, 3923 (1994).
- Luthi, Y., and Ricka, J., *J. Colloid Interface Sci.* **206**, 302 (1998).
- Lyklema, J., "Fundamentals of Interface and Colloid Science." Academic Press, Toronto, 1993.
- Madejski, J., Solidification of Droplets on a Cold Surface, *J. Heat Mass Transfer* **19**, 1009 (1976).
- Mahanty, J., and Ninham, B. W., "Dispersion Forces." Academic Press, London, 1976.
- Mala, Gh. M., Yang. C., and Li., D., *Colloid Surf.* **135**, 109 (1998).
- Masliyah, J. H., "Electrokinetic Transport Phenomena." Alberta Oil Sands Technology and Research Authority (AOSTRA) Technical Publication Series No. 12., AOSTRA, Edmonton, Alberta, 1994.
- McCormack, D., Carnie, S., and Chan, D. Y. C., *J. Colloid Interface Sci.* **169**, 177 (1995).
- McTaggart, H. A., *Philos. Mag.* **44**, 386 (1922).
- Melik, D. H., and Fogler, H. S., *J. Colloid Interface Sci.* **101**, 85 (1984).
- Miklavcic, S. J., Chan, D. Y. C., White, L. R., and Healy, T. W., *J. Phys. Chem.* **98**, 9022 (1997).
- Miklavcic, S. J., Horn, R. G., and Bachmann, D. J., *J. Phys. Chem.* **99**, 16357 (1995).
- Moore, D. W., and Saffman, P. G., *Philos. Trans. Roy. Soc. London A* **264**, 597 (1969).
- Nguyen, A. V., *AIChE J.* **44**, 226 (1998).
- Nguyen-Van, A., *J. Colloid Interface Sci.* **162**, 123 (1994).
- Nishio, S., and Kim, Y.C., *Int. J. Heat Mass Transfer* **41**, 4113 (1998).
- "Numerical Recipes." 2<sup>nd</sup> Ed., Cambridge University Press, 1986.
- O'Brien, R. W., and White, L. R., *Adv. Colloid Interface Sci.* **14**, 1607 (1978).
- Okada, K., and Akagi, Y., *J. Chem. Eng. Jpn.* **20**, 11 (1987).
- Okada, K., and Akagi, Y., Kogure, M., and Yoshioka, N., *Can. J. Chem. Eng.* **68**, 393 (1990).

- Onorato, F. J., and Tien, C., *Ind. Chem. Eng. Symp. Ser.*, **59** 5 (1980).
- Overbeek, J. T., *J. Chem. Soc., Faraday Trans. I* **84**, 3079 (1988).
- Overbeek, J.Th.G., *Colloid Surf.* **51**, 61 (1990).
- Padday, J. F., "Spreading, Wetting and Contact Angles." *J. Adhesion Sci. Technol.* **6**, 1347 (1992).
- Parneix, S., Behnia, M., and Durbin, P.A., *ASME J. Heat Transfer* **121**, 43 (1999).
- Parsegian, V. A., "Physical Chemistry: Enriching Topics from Colloid and Surface Science Theory." (H. V. Olphen and K. J. Mysels, Eds.), Theorex, La Jolla, California, 1975.
- Patankar, S. V., "Numerical Heat Transfer and Fluid Flow." McGraw-Hill, New York, 1980.
- Perea-Carpio, R., Gonzalez-Caballero, F., Bruque, J. M., and Gonzalez-Fernandez, C. F., *J. Colloid Interface Sci.* **110**, 96-101 (1986).
- Polat, S., Huang, B., Mujumdar, A. S., and Douglas, W. J. M., "Numerical Flow and Heat Transfer under Impinging Jets- a Review." *Ann. Rev. Num. Fluid Mech. & Heat Transfer*, Vol. 2, Chapter 4, Hemisphere Publishing Co., New York, 1991.
- Polverari, M., and van de Ven, T. G. M., *J Colloid Interface Sci.* **173**, 343 (1995).
- Prieve, D. C., and Ruckenstein, E., *AIChE J.* **20**, 1178 (1974).
- Prieve, D. C., and Lin, M. M. J., *J Colloid Interface Sci.* **76**, 32 (1980).
- Prieve, D. C., and Lin, M. M. J., *J. Colloid Interface Sci.* **86**, 17 (1982).
- Rajagopalan, R., and Kim, J., *J. Colloid Interface Sci.* **83**, 428 (1981).
- Riley, D., and Carbonell, R. G., *J. Colloid Interface Sci.* **158**, 259 (1993a); 274 (1993b).
- Rios, G., Pazos, C., and Coca, J., *J. Dispersion Sci. Tech.* **19**, 661 (1998).
- Roache, P. J., "Computational Fluid Dynamics." Hermosa Publisher, Albuquerque, New York, 1972.
- Ruckenstein, E., and Prieve, D. C., *J. Chem. Soc. Faraday II* **69**, 1522 (1973).
- Ruckenstein, E., *J Colloid Interface Sci.* **66**, 531 (1978).

- Sanders, R. S., Chow, R. S., and Masliyah, J. H., *J. Colloid Interface Sci.* **174**, 230 (1995).
- Sanders, S., Ph.D. dissertation, The University of Alberta, Edmonton, AB, 1996.
- Sanfeld, A., Thermodynamics of Charged and Polarized Layers, Monographs in Statistical Physics and Thermodynamics, Vol.10, Wiley, London, 1968.
- Saulnier, P., Lachaise, J., Morel, G., and Graciaa, A., *Colloid Polym. Sci.* **273**, 1060 (1995b).
- Saulnier, P., Lachaise, J., Morel, G., and Graciaa, A., *J. Colloid Interface Sci.* **182**, 395 (1996).
- Saulner, P., Bouriati, P., Morel, G., Lachaise, J., and Graciaa, A., *J. Colloid Interface Sci.* **200**, 81 (1998).
- Schechter, R. S., Graciaa, A., and Lachaise, J., *J. Colloid Interface Sci.* **204**, 398 (1998).
- Schultz, H. J., "Physico-Chemical Elementary Processes in Flotation, Developments in Mineral Processing." (Fuerstenau, D. Ed.), Vol. 4, Elsevier, New York, 1984.
- Sharma, A., and Ruckenstein, E., *J. Colloid Interface Sci.* **137**, 433 (1991).
- Sharma, A., and Jameel, A., *J. Colloid Interface Sci.* **161**, 190 (1993).
- Sherwood, J. D., *J. Fluid. Mech.* **162**, 129 (1986).
- Sirois, L. L., and Millar, G., *Can. Metallurgical Quart.* **12**, 281 (1973).
- Sjollema, J., Busscher, H.J., and Weerkamp, A.H., *Biofouling* **1**, 101 (1988).
- Sjostrom, L., and Akesson, T., *J. Colloid Interface Sci.* **181**, 645 (1996).
- Schlichting, H., "Boundary-Layer Theory." (Kestin, J. Trans.). McGraw-Hill, New York, 1979.
- Smoluchowski, M., *Z. Phys. Chem.* **92**, 129 (1917).
- Song, L., Johnson, P. R., and Elimelech, M., *Environ. Sci. Technol.*, **28**, 1164 (1994).
- Song, L., and Elimelech, M., *J. Colloid Interface Sci.* **173**, 165 (1995).
- Spielman, L. A., *J. Colloid Interface Sci.* **33**, 562 (1970).
- Spielman, L. A., and Goren, S. L., *Environ. Sci. Technol.* **4**, 135 (1970).



- Spielman, L. A., and Fitzpatrick, J. A., *J. Colloid Interface Sci.* **42**, 607 (1973).
- Spielman, L. A., and Cukor, P. M., *J. Colloid Interface Sci.* **43**, 51 (1973).
- Spielman, L. A., and Fitzpatrick, J. A., *J. Colloid and Interface Sci.* **46**, 22 (1974).
- Spielman, L. A., *Ann. Rev. Fluid Mech.* **9**, 297 (1977).
- Suzuki, A., Ho, N. F. H., and Higuchi, W. I., *J. Colloid Interface Sci.* **29**, 552 (1969).
- Swanton, S. W., *Adv. Colloid Interface Sci.* **54**, 129 (1995).
- Tien, C., "Granular Filtration of Aerosols and Hydrosols." Butterworths, 1989.
- Tobiason, J., *Colloids Surf.* **39**, 53 (1989).
- Usui, S., and Sasaki, H., *J. Colloid Interface Sci.* **65**, 36 (1978).
- Usui, S., and Barouch, E., *J. Colloid Interface Sci.* **137**, 281 (1990).
- van de Ven, T. G. M., and Kelemen, S. J., *J. Colloid Interface Sci.* **181**, 118 (1996).
- van de Ven, T. G. M., "Colloidal Hydrodynamics." Academic Press, San Diego, 1989.
- van Oss, C. J., *J. Dispersion Sci. Tech.* **11**, 491 (1990).
- Varenes, S., and van de Ven, T. G. M., *Physicochem. Hydrodyn.* **9**, 537 (1987).
- Varenes, S., and van de Ven, T. G. M., *Physicochem. Hydrodyn.* **10**, 415 (1988).
- Varenes, S., and van de Ven, T. G. M., *Colloids Surf* **33**, 63 (1988).
- Voncent, B., *J. Colloid Interface Sci.* **42**, 270 (1973).
- Visser, J., *Adv. Colloid Interface Sci.* **15**, 157 (1981).
- Walz, J.Y., *Adv. Colloid Interface Sci.* **74**, 119 (1998).
- Wang, Y. G., and Wen, C. S., *J. Fluid Mech.* **214**, 599 (1990).
- Warszynski, P., and Czarnecki, J., *J. Colloid Interface Sci.* **128**, 137 (1989).
- Warszynski, P., and van de Ven, T. G. M., *Faraday Discuss Chem. Soc.* **90**, 313 (1990).
- Warszynski, P., and van de Ven, T. G. M., *Adv. Colloid Interface Sci.* **36**, 33 (1991).

- Warszynski, P., and Adamczyk, Z., *J. Colloid Interface Sci.* **187**, 283 (1997).
- Wiersema, P. H., and Overbeek, J. Th. G., *J. Colloid Interface Sci.* **22**, 78 (1966).
- Wnek, W. J., Gidaspow, D., and Wasan, D. T., *J. Colloid Interface Sci.* **59**, 1 (1977).
- Yang, C., and Li, D., *J. Colloid Interface Sci.* **194**, 95 (1997).
- Yang, C., and Li, D., *Colloid Surf.* **143**, 339 (1998a).
- Yang, C., Li, D., and Masliyah, J. H., *Int. J. Heat Mass Transfer* **41**, 4229 (1998b).
- Yang, C., Dabros, T., Li, D., Czarnecki, J., and Masliyah, J. H., *J. Colloid Interface Sci.* **208**, 226 (1998c).
- Yang, C., Dabros, T., Li, D., Czarnecki, J., and Masliyah, J. H., *J. Colloid Interface Sci.* (in press, 1999a).
- Yang, C., Dabros, T., Li, D., Czarnecki, J., and Masliyah, J. H., *Colloid Surf.* (accepted, 1999b).
- Yoon, R. H., and Yordan, J. L., *J. Colloid Interface Sci.* **113**, 430 (1986).
- Yoon, R. H., and Luttrell, G. H., *Mineral Process. Extract. Metall. Rev.* **5**, 101 (1989).
- Yoon, R. H., in "Proceedings, XVII Int. Mineral Processing Congr., Dresden, Germany." Vol II, "Fine Particle Processing (Flotation)"p.17, 1991.
- Yoon, R. H., and Mao, L. Q., *J. Colloid Interface Sci.* **181**, 613 (1996).
- Zebel, G., *J. Colloid Interface Sci.* **20**, 522 (1965).
- Zhou, Z.A., Hussein, H., Xu, Z., Czarnecki, J., and Masliyah, J.H., *J. Colloid Interface Sci.* **197**, 242 (1998).

## APPENDIX 1

### NUMERICAL SCHEMES FOR SOLVING FLOW FIELDS IN THE IMPINGING JET FLOW REGION USING THE STREAM FUNCTION – VORTICITY METHOD

The finite difference analysis based control volume method is used to derive partial differential equations into finite difference ones. For convenience, equations (2.11) and (2.12) are represented by a general form of differential equations in the cylindrical coordinate system as

$$A_1 \left[ \frac{\partial}{\partial z} \left( \frac{-\partial \bar{\psi}}{\partial r} \right) - \frac{\partial}{\partial r} \left( \frac{-\partial \bar{\psi}}{\partial z} \right) \right] - \left[ \frac{\partial}{\partial z} \left( A_2 \frac{\partial \bar{\varphi}}{\partial z} \right) + \frac{\partial}{\partial r} \left( A_2 \frac{\partial \bar{\varphi}}{\partial r} \right) \right] + \bar{r} A_3 = 0 \quad (\text{A1.1})$$

The general dependent variables  $\bar{\varphi}$  and corresponding coefficients  $A_1$ ,  $A_2$  and  $A_3$  are listed in Table A-1, where  $\bar{\varphi}$  represents either the modified vorticity  $\bar{\omega}^* = \frac{\bar{\omega}}{r}$  or the stream function  $\bar{\psi}$ . Physically, the first term in the left hand of equation represents convection. The second term in the left hand of equation is related to diffusion. The third term in the left hand of equation is source term. For the purpose of derivation of the finite – difference equation, integration of the differential equations is performed over a control volume (surrounding a typical grid point P) that is enclosed by the small rectangle shown by the dashed lines in Figure 2.3. The upwind scheme is employed to approximate the convection terms. Central differences are used to deal with the diffusion terms. Details of derivation are given as below.

#### A1.1 Stream Function Equation (2.11)

Double integrating equation (2.11) gives

$$\int_{\bar{z},s}^{\bar{z},n} \int_{\bar{r},w}^{\bar{r},e} \frac{\partial}{\partial \bar{r}} \left( \frac{1}{\bar{r}} \frac{\partial \bar{\psi}}{\partial \bar{r}} \right) d\bar{r} d\bar{z} + \int_{\bar{r},w}^{\bar{r},e} \int_{\bar{z},s}^{\bar{z},n} \frac{\partial}{\partial \bar{z}} \left( \frac{1}{\bar{r}} \frac{\partial \bar{\psi}}{\partial \bar{z}} \right) d\bar{z} d\bar{r} + \int_{\bar{z},s}^{\bar{z},n} \int_{\bar{r},w}^{\bar{r},e} \bar{r} \bar{\omega}^* d\bar{r} d\bar{z} = 0 \quad (\text{A1.2})$$

where the integration limits are boundaries of the small rectangle.

Inspection of this equation reveals only diffusion  $I_D$  and source  $I_S$  terms included. When solving the stream function equation, the source term is the modified vorticity  $\bar{\omega}^*$  that is numerically treated as independent of  $\bar{\psi}$ , i.e., a constant. Hence, the source term integral is straightforward to obtain

$$I_S = \int_{\bar{z},s}^{\bar{z},n} \int_{\bar{r},w}^{\bar{r},e} \bar{r} \bar{\omega}^* d\bar{r} d\bar{z} = \bar{\omega}^* \bar{r}_P \frac{\bar{r}_E - \bar{r}_W}{2} \frac{\bar{z}_N - \bar{z}_S}{2} \quad (\text{A1.3})$$

The first part of the diffusion term integral is expressed as

$$I_{D1} = \int_{\bar{z},s}^{\bar{z},n} \int_{\bar{r},w}^{\bar{r},e} \frac{\partial}{\partial \bar{r}} \left( \frac{1}{\bar{r}} \frac{\partial \bar{\psi}}{\partial \bar{r}} \right) d\bar{r} d\bar{z} = \int_{\bar{z},s}^{\bar{z},n} \left( \frac{1}{\bar{r}} \right)_e \left( \frac{\partial \bar{\psi}}{\partial \bar{r}} \right)_e d\bar{z} - \int_{\bar{z},s}^{\bar{z},n} \left( \frac{1}{\bar{r}} \right)_w \left( \frac{\partial \bar{\psi}}{\partial \bar{r}} \right)_w d\bar{z} \quad (\text{A1.4})$$

By using central difference scheme, one may have

$$\left( \frac{1}{\bar{r}} \right)_e = \frac{2}{\bar{r}_E + \bar{r}_P} \quad \left( \frac{1}{\bar{r}} \right)_w = \frac{2}{\bar{r}_W + \bar{r}_P} \quad (\text{A1.5a})$$

$$\left( \frac{\partial \bar{\psi}}{\partial \bar{r}} \right)_e = \frac{\bar{\psi}_E - \bar{\psi}_P}{\bar{r}_E - \bar{r}_P} \quad \left( \frac{\partial \bar{\psi}}{\partial \bar{r}} \right)_w = \frac{\bar{\psi}_P - \bar{\psi}_W}{\bar{r}_P - \bar{r}_W} \quad (\text{A1.5b})$$

The substitution of equations (A1.5a) and (A1.5b) into equation (A1.4) gives

$$I_{D1} = \frac{2}{\bar{r}_E + \bar{r}_P} \frac{\bar{\psi}_E - \bar{\psi}_P}{\bar{r}_E - \bar{r}_P} \frac{\bar{z}_N - \bar{z}_S}{2} - \frac{2}{\bar{r}_W + \bar{r}_P} \frac{\bar{\psi}_P - \bar{\psi}_W}{\bar{r}_P - \bar{r}_W} \frac{\bar{z}_N - \bar{z}_S}{2} \quad (\text{A1.6})$$

Similarly, the second part of the diffusion term integral can be evaluated as

$$\begin{aligned} I_{D2} &= \int_{\bar{r},w}^{\bar{r},e} \int_{\bar{z},s}^{\bar{z},n} \frac{\partial}{\partial \bar{z}} \left( \frac{1}{\bar{r}} \frac{\partial \bar{\psi}}{\partial \bar{z}} \right) d\bar{z} d\bar{r} = \int_{\bar{r},w}^{\bar{r},e} \left( \frac{1}{\bar{r}} \right)_n \left( \frac{\partial \bar{\psi}}{\partial \bar{z}} \right)_n d\bar{r} - \int_{\bar{r},w}^{\bar{r},e} \left( \frac{1}{\bar{r}} \right)_s \left( \frac{\partial \bar{\psi}}{\partial \bar{z}} \right)_s d\bar{r} \\ &= \frac{2}{\bar{r}_N + \bar{r}_P} \frac{\bar{\psi}_N - \bar{\psi}_P}{\bar{z}_N - \bar{z}_P} \frac{\bar{r}_E - \bar{r}_W}{2} - \frac{2}{\bar{r}_S + \bar{r}_P} \frac{\bar{\psi}_P - \bar{\psi}_S}{\bar{z}_P - \bar{z}_S} \frac{\bar{r}_E - \bar{r}_W}{2} \end{aligned} \quad (\text{A1.7})$$

Then the final difference equation for the stream function is obtained by substituting equations (A1.6) and (A1.7) into equation (A1.2)

$$b_{P\bar{\psi}} \bar{\psi}_P = b_{E\bar{\psi}} \bar{\psi}_E + b_{W\bar{\psi}} \bar{\psi}_W + b_{N\bar{\psi}} \bar{\psi}_N + b_{S\bar{\psi}} \bar{\psi}_S + D_{\bar{\psi}} \quad (\text{A1.8})$$

where the coefficients shown in the above equation are expressed as

$$b_{E\bar{\psi}} = \frac{\bar{z}_N - \bar{z}_S}{(\bar{r}_E + \bar{r}_P)(\bar{r}_E - \bar{r}_P)} = \frac{\bar{z}_{i+1} - \bar{z}_{i-1}}{(\bar{r}_{j+1} + \bar{r}_j)(\bar{r}_{j+1} - \bar{r}_j)} \quad (\text{A1.9a})$$

$$b_{W\bar{\psi}} = \frac{\bar{z}_N - \bar{z}_S}{(\bar{r}_W + \bar{r}_P)(\bar{r}_P - \bar{r}_W)} = \frac{\bar{z}_{i+1} - \bar{z}_{i-1}}{(\bar{r}_{j-1} + \bar{r}_j)(\bar{r}_j - \bar{r}_{j-1})} \quad (\text{A1.9b})$$

$$b_{N\bar{\psi}} = \frac{\bar{r}_E - \bar{r}_W}{(\bar{r}_N + \bar{r}_P)(\bar{z}_N - \bar{z}_P)} = \frac{\bar{r}_{j+1} - \bar{r}_{j-1}}{2 \bar{r}_j (\bar{z}_{i+1} - \bar{z}_i)} \quad (\text{A1.9c})$$

$$b_{S\bar{\psi}} = \frac{\bar{r}_E - \bar{r}_W}{(\bar{r}_S + \bar{r}_P)(\bar{z}_P - \bar{z}_S)} = \frac{\bar{r}_{j+1} - \bar{r}_{j-1}}{2 \bar{r}_j (\bar{z}_i - \bar{z}_{i-1})} \quad (\text{A1.9d})$$

$$b_{P\bar{\psi}} = b_{E\bar{\psi}} + b_{W\bar{\psi}} + b_{N\bar{\psi}} + b_{S\bar{\psi}} \quad (\text{A1.9e})$$

$$D_{\bar{\psi}} = \bar{r}_P \frac{\bar{r}_E - \bar{r}_W}{2} \frac{\bar{z}_N - \bar{z}_S}{2} \omega_P = \frac{\bar{r}_j (\bar{r}_{j+1} - \bar{r}_{j-1}) (\bar{z}_{i+1} - \bar{z}_{i-1})}{4} \omega_{i,j} \quad (\text{A1.9f})$$

## A1.2 Vorticity Equation (2.12)

Applying double integration to the vorticity equation leads to

$$\int_{\bar{r},w}^{\bar{r},e} \int_{\bar{z},s}^{\bar{z},n} r^{-2} \left[ \frac{\partial}{\partial \bar{z}} \left( \bar{\omega} \frac{\partial \bar{\psi}}{\partial \bar{r}} \right) - \frac{\partial}{\partial \bar{r}} \left( \bar{\omega} \frac{\partial \bar{\psi}}{\partial \bar{z}} \right) \right] d\bar{z} d\bar{r} - \int_{\bar{r},w}^{\bar{r},e} \int_{\bar{z},s}^{\bar{z},n} \left\{ \frac{\partial}{\partial \bar{z}} \left[ r^{-3} \frac{\partial}{\partial \bar{z}} \left( \frac{1}{\text{Re}} \bar{\omega} \right) \right] + \frac{\partial}{\partial \bar{r}} \left[ r^{-3} \frac{\partial}{\partial \bar{r}} \left( \frac{1}{\text{Re}} \bar{\omega} \right) \right] \right\} d\bar{z} d\bar{r} = 0 \quad (\text{A1.10})$$

A comparison of the above equation with the general equation indicates that the first and the second integral in the vorticity equation represent convection and diffusion, respectively. Each of integral is evaluated as below.

The first part of the convection term integral is evaluated as

$$\begin{aligned}
I_{C1} &= \int_{\bar{r},w}^{\bar{r},e} \int_{\bar{z},s}^{\bar{z},n} r^{-2} \frac{\partial}{\partial \bar{z}} \left( \bar{\omega} \frac{\partial \bar{\psi}}{\partial \bar{r}} \right) d\bar{z} d\bar{r} = \int_{\bar{r},w}^{\bar{r},e} (r^{-2})_n (\bar{\omega})_n \left( \frac{\partial \bar{\psi}}{\partial \bar{r}} \right)_n d\bar{r} - \int_{\bar{r},w}^{\bar{r},e} (r^{-2})_s (\bar{\omega})_s \left( \frac{\partial \bar{\psi}}{\partial \bar{r}} \right)_s d\bar{r} \\
&\approx \bar{r}_P^{-2} (\bar{\omega})_n \frac{\bar{\psi}_{ne} - \bar{\psi}_{nw}}{\bar{r}_e - \bar{r}_w} (\bar{r}_e - \bar{r}_w) - \bar{r}_P^{-2} (\bar{\omega})_s \frac{\bar{\psi}_{se} - \bar{\psi}_{sw}}{\bar{r}_e - \bar{r}_w} (\bar{r}_e - \bar{r}_w)
\end{aligned} \tag{A1.11}$$

Introducing the upwind scheme and using the definition of the stream function, equation (A1.11) can be rewritten as

$$\begin{aligned}
I_{C1} &\approx \bar{r}_P^{-2} \left[ \bar{\omega}_N \frac{(\bar{\psi}_{ne} - \bar{\psi}_{nw}) - |\bar{\psi}_{ne} - \bar{\psi}_{nw}|}{2} + \bar{\omega}_P \frac{(\bar{\psi}_{ne} - \bar{\psi}_{nw}) + |\bar{\psi}_{ne} - \bar{\psi}_{nw}|}{2} \right] - \\
&\quad - \bar{r}_P^{-2} \left[ \bar{\omega}_P \frac{(\bar{\psi}_{se} - \bar{\psi}_{sw}) - |\bar{\psi}_{se} - \bar{\psi}_{sw}|}{2} + \bar{\omega}_S \frac{(\bar{\psi}_{se} - \bar{\psi}_{sw}) + |\bar{\psi}_{se} - \bar{\psi}_{sw}|}{2} \right]
\end{aligned} \tag{A1.12}$$

where numerically, we can assume

$$\bar{\psi}_{ne} \approx \frac{\bar{\psi}_{NE} + \bar{\psi}_E + \bar{\psi}_N + \bar{\psi}_P}{4} \quad \bar{\psi}_{nw} \approx \frac{\bar{\psi}_{NW} + \bar{\psi}_W + \bar{\psi}_N + \bar{\psi}_P}{4} \tag{A1.13a}$$

$$\bar{\psi}_{se} \approx \frac{\bar{\psi}_{SE} + \bar{\psi}_E + \bar{\psi}_S + \bar{\psi}_P}{4} \quad \bar{\psi}_{sw} \approx \frac{\bar{\psi}_{SW} + \bar{\psi}_W + \bar{\psi}_S + \bar{\psi}_P}{4} \tag{A1.13b}$$

Similarly, the second part of the convection term integral can be formulated as

$$\begin{aligned}
I_{C2} &= \int_{\bar{z},s}^{\bar{z},n} \int_{\bar{r},w}^{\bar{r},e} r^{-2} \frac{\partial}{\partial \bar{r}} \left( \bar{\omega} \frac{\partial \bar{\psi}}{\partial \bar{z}} \right) d\bar{r} d\bar{z} \\
&= \bar{r}_P^{-2} \left[ \bar{\omega}_E \frac{(\bar{\psi}_{ne} - \bar{\psi}_{se}) + |\bar{\psi}_{ne} - \bar{\psi}_{se}|}{2} + \bar{\omega}_P \frac{(\bar{\psi}_{ne} - \bar{\psi}_{se}) - |\bar{\psi}_{ne} - \bar{\psi}_{se}|}{2} \right] - \\
&\quad - \bar{r}_P^{-2} \left[ \bar{\omega}_P \frac{(\bar{\psi}_{nw} - \bar{\psi}_{sw}) + |\bar{\psi}_{nw} - \bar{\psi}_{sw}|}{2} + \bar{\omega}_W \frac{(\bar{\psi}_{nw} - \bar{\psi}_{sw}) - |\bar{\psi}_{nw} - \bar{\psi}_{sw}|}{2} \right]
\end{aligned} \tag{A1.14}$$

Therefore, the convection term in equation (A1.10) can be expressed as

$$\begin{aligned}
I_C &= I_{C1} - I_{C2} \\
&= \left( \bar{a}_{PN\bar{\omega}} \bar{\omega}_P - \bar{a}_{N\bar{\omega}} \bar{\omega}_N \right) + \left( \bar{a}_{PS\bar{\omega}} \bar{\omega}_P - \bar{a}_{S\bar{\omega}} \bar{\omega}_S \right) + \left( \bar{a}_{PE\bar{\omega}} \bar{\omega}_P - \bar{a}_{E\bar{\omega}} \bar{\omega}_E \right) + \left( \bar{a}_{PW\bar{\omega}} \bar{\omega}_P - \bar{a}_{W\bar{\omega}} \bar{\omega}_W \right)
\end{aligned} \tag{A1.15}$$

where

$$a_{PN\bar{\omega}} = r_P^{-2} \frac{(\bar{\psi}_{ne} - \bar{\psi}_{nw}) + |\bar{\psi}_{ne} - \bar{\psi}_{nw}|}{2} \quad (\text{A1.16a})$$

$$a_{N\bar{\omega}} = r_P^{-2} \frac{(\bar{\psi}_{nw} - \bar{\psi}_{ne}) + |\bar{\psi}_{nw} - \bar{\psi}_{ne}|}{2} \quad (\text{A1.16b})$$

$$a_{PS\bar{\omega}} = r_P^{-2} \frac{(\bar{\psi}_{sw} - \bar{\psi}_{se}) + |\bar{\psi}_{sw} - \bar{\psi}_{se}|}{2} \quad (\text{A1.16c})$$

$$a_{S\bar{\omega}} = r_P^{-2} \frac{(\bar{\psi}_{se} - \bar{\psi}_{sw}) + |\bar{\psi}_{se} - \bar{\psi}_{sw}|}{2} \quad (\text{A1.16d})$$

$$a_{PE\bar{\omega}} = r_P^{-2} \frac{(\bar{\psi}_{se} - \bar{\psi}_{ne}) + |\bar{\psi}_{se} - \bar{\psi}_{ne}|}{2} \quad (\text{A1.16e})$$

$$a_{E\bar{\omega}} = r_P^{-2} \frac{(\bar{\psi}_{ne} - \bar{\psi}_{se}) + |\bar{\psi}_{ne} - \bar{\psi}_{se}|}{2} \quad (\text{A1.16f})$$

$$a_{PW\bar{\omega}} = r_P^{-2} \frac{(\bar{\psi}_{nw} - \bar{\psi}_{sw}) + |\bar{\psi}_{nw} - \bar{\psi}_{sw}|}{2} \quad (\text{A1.16g})$$

$$a_{W\bar{\omega}} = r_P^{-2} \frac{(\bar{\psi}_{sw} - \bar{\psi}_{nw}) + |\bar{\psi}_{sw} - \bar{\psi}_{nw}|}{2} \quad (\text{A1.16h})$$

Using the same approach as for derivation of diffusion terms in stream function equation, the first diffusion term in equation (A1.10) is evaluated as

$$\begin{aligned} I_{D1} &= \int_{r,w}^{\bar{r},e} \int_{z,s}^{\bar{z},n} \frac{\partial}{\partial z} \left[ r^{-3} \frac{\partial}{\partial z} \left( \frac{1}{\text{Re}} \bar{\omega}^* \right) \right] d\bar{z} d\bar{r} = \int_{r,w}^{\bar{r},e} \left( \frac{r^{-3}}{\text{Re}} \right)_n \left( \frac{\partial \bar{\omega}^*}{\partial z} \right)_n d\bar{r} - \int_{r,w}^{\bar{r},e} \left( \frac{r^{-3}}{\text{Re}} \right)_s \left( \frac{\partial \bar{\omega}^*}{\partial z} \right)_s d\bar{r} \\ &= \frac{r_P^{-3} + r_N^{-3}}{2 \text{Re}} \frac{\bar{\omega}_N^* - \bar{\omega}_P^*}{\bar{z}_N - \bar{z}_P} \frac{\bar{r}_E - \bar{r}_W}{2} - \frac{r_P^{-3} + r_S^{-3}}{2 \text{Re}} \frac{\bar{\omega}_P^* - \bar{\omega}_S^*}{\bar{z}_P - \bar{z}_S} \frac{\bar{r}_E - \bar{r}_W}{2} \end{aligned} \quad (\text{A1.17})$$

and the second diffusion term in equation (A1.10) is

$$\begin{aligned} I_{D2} &= \int_{z,s}^{\bar{z},n} \int_{r,w}^{\bar{r},e} \frac{\partial}{\partial r} \left[ r^{-3} \frac{\partial}{\partial r} \left( \frac{1}{\text{Re}} \bar{\omega}^* \right) \right] d\bar{r} d\bar{z} = \int_{z,s}^{\bar{z},n} \left( \frac{r^{-3}}{\text{Re}} \right)_e \left( \frac{\partial \bar{\omega}^*}{\partial r} \right)_e d\bar{z} - \int_{z,s}^{\bar{z},n} \left( \frac{r^{-3}}{\text{Re}} \right)_w \left( \frac{\partial \bar{\omega}^*}{\partial r} \right)_w d\bar{z} \\ &= \frac{r_P^{-3} + r_E^{-3}}{2 \text{Re}} \frac{\bar{\omega}_E^* - \bar{\omega}_P^*}{\bar{r}_E - \bar{r}_P} \frac{\bar{z}_N - \bar{z}_S}{2} - \frac{r_P^{-3} + r_W^{-3}}{2 \text{Re}} \frac{\bar{\omega}_P^* - \bar{\omega}_W^*}{\bar{r}_P - \bar{r}_W} \frac{\bar{z}_N - \bar{z}_S}{2} \end{aligned} \quad (\text{A1.18})$$

Then the whole diffusion term can be expressed as

$$I_D = I_{D1} + I_{D2} = b_{E\bar{\omega}} \bar{\omega}_E + b_{W\bar{\omega}} \bar{\omega}_W + b_{N\bar{\omega}} \bar{\omega}_N + b_{S\bar{\omega}} \bar{\omega}_S - b_{P\bar{\omega}} \bar{\omega}_P \quad (\text{A1.19})$$

where

$$b_{E\bar{\omega}} = \frac{\bar{r}_P + \bar{r}_E}{2 \text{Re}} \frac{1}{\bar{r}_E - \bar{r}_P} \frac{\bar{z}_N - \bar{z}_S}{2} = \frac{(\bar{r}_j + \bar{r}_{j+1})(\bar{z}_{i+1} - \bar{z}_{i-1})}{4 \text{Re}(\bar{r}_{j+1} - \bar{r}_j)} \quad (\text{A1.20a})$$

$$b_{W\bar{\omega}} = \frac{\bar{r}_P + \bar{r}_W}{2 \text{Re}} \frac{1}{\bar{r}_P - \bar{r}_W} \frac{\bar{z}_N - \bar{z}_S}{2} = \frac{(\bar{r}_j + \bar{r}_{j-1})(\bar{z}_{i+1} - \bar{z}_{i-1})}{4 \text{Re}(\bar{r}_j - \bar{r}_{j-1})} \quad (\text{A1.20b})$$

$$b_{N\bar{\omega}} = \frac{\bar{r}_P + \bar{r}_N}{2 \text{Re}} \frac{1}{\bar{z}_N - \bar{z}_P} \frac{\bar{r}_E - \bar{r}_W}{2} = \frac{\bar{r}_j (\bar{r}_{j+1} - \bar{r}_{j-1})}{2 \text{Re}(\bar{z}_{i+1} - \bar{z}_i)} \quad (\text{A1.20c})$$

$$b_{S\bar{\omega}} = \frac{\bar{r}_P + \bar{r}_S}{2 \text{Re}} \frac{1}{\bar{z}_P - \bar{z}_S} \frac{\bar{r}_E - \bar{r}_W}{2} = \frac{\bar{r}_j (\bar{r}_{j+1} - \bar{r}_{j-1})}{2 \text{Re}(\bar{z}_i - \bar{z}_{i-1})} \quad (\text{A1.20d})$$

When equations (A1.15) and (A1.19) are substituted into equation (A1.10), it can be seen

$$\begin{aligned} I_C - I_D = & (a_{PN\bar{\omega}} + a_{PS\bar{\omega}} + a_{PE\bar{\omega}} + a_{PW\bar{\omega}}) \bar{\omega}_P - a_{N\bar{\omega}} \bar{\omega}_N - a_{S\bar{\omega}} \bar{\omega}_S - a_{E\bar{\omega}} \bar{\omega}_E - a_{W\bar{\omega}} \bar{\omega}_W \\ & + b_{P\bar{\omega}} \bar{\omega}_P - b_{E\bar{\omega}} \bar{\omega}_E - b_{W\bar{\omega}} \bar{\omega}_W - b_{N\bar{\omega}} \bar{\omega}_N - b_{S\bar{\omega}} \bar{\omega}_S = 0 \end{aligned} \quad (\text{A1.21})$$

Thus the final difference equation for the vorticity is obtained by rewriting the above equation

$$c_{P\bar{\omega}} \bar{\omega}_P = c_{E\bar{\omega}} \bar{\omega}_E + c_{W\bar{\omega}} \bar{\omega}_W + c_{N\bar{\omega}} \bar{\omega}_N + c_{S\bar{\omega}} \bar{\omega}_S \quad (\text{A1.22})$$

where the coefficients are

$$c_{E\bar{\omega}} = a_{E\bar{\omega}} + b_{E\bar{\omega}} \quad (\text{A1.23a})$$

$$c_{W\bar{\omega}} = a_{W\bar{\omega}} + b_{W\bar{\omega}} \quad (\text{A1.23b})$$

$$c_{N\bar{\omega}} = a_{N\bar{\omega}} + b_{N\bar{\omega}} \quad (\text{A1.23c})$$

$$c_{S\bar{\omega}} = a_{S\bar{\omega}} + b_{S\bar{\omega}} \quad (\text{A1.23d})$$

$$c_{P\bar{\omega}} = a_{PN\bar{\omega}} + a_{PS\bar{\omega}} + a_{PE\bar{\omega}} + a_{PW\bar{\omega}} + b_{E\bar{\omega}} + b_{W\bar{\omega}} + b_{N\bar{\omega}} + b_{S\bar{\omega}} \quad (\text{A1.23e})$$

Once algebraic equations are derived, a Gauss-Seidel method based iterative procedure is employed to solve these equations.



Table A1.1 Coefficients expressed in general equation (A1.1)

$\bar{\varphi}$	$A_1$	$A_2$	$A_3$
$\bar{\omega}$	$r^{-2}$	$r^{-3}/\text{Re}$	0
$\bar{\psi}$	0	$1/r$	$-\bar{\omega}$

## APPENDIX 2

### THICKNESS OF VISCOUS BOUNDARY LAYER IN THE IMPINGING JET FLOW REGION

In the following, a detailed procedure for derivation of equation (3.35) will be presented (Yang et al., 1999a). This equation can be used to approximately estimate the hydrodynamic boundary layer thickness in the impinging jet flow. To begin, it is assumed that the bubble concentration is very dilute so that the Navier-Stokes equations can be applied to describe the undisturbed fluid flow field. According to Schlichting (1968), the governing equations and boundary conditions, based on boundary-layer approximation, are expressed as

Continuity equation

$$\frac{1}{r} \frac{\partial}{\partial r} (r v_r) + \frac{\partial v_z}{\partial z} = 0 \quad (\text{A2.1})$$

Momentum balance in the boundary layer leading to

$$v_r \frac{\partial v_r}{\partial r} + v_z \frac{\partial v_r}{\partial z} = -\frac{1}{\rho_f} \frac{\partial P}{\partial r} + \nu_f \frac{\partial^2 v_r}{\partial z^2} \quad (\text{A2.2})$$

Boundary conditions

$$z=0 \quad v_r=0 \quad v_z=0 \quad (\text{A2.3a})$$

$$z \rightarrow \infty \quad v_r = U \quad (\text{A2.3b})$$

Assume that the velocity variation of the potential flow outside the boundary-layer region is

$$U = \beta r \quad (\text{A2.4})$$

where  $\beta$  is a constant representing the flow intensity.

According to Bernoulli equation, the hydrodynamic pressure is expressed by

$$-\frac{1}{\rho_f} \frac{\partial p}{\partial r} = U \frac{dU}{dr} = \beta^2 r = \beta U \quad (\text{A2.5})$$

By introducing new parameters,  $\eta = \sqrt{\frac{\beta}{\nu_f}} z$  and  $f(\eta) = \sqrt{\frac{1}{\beta \nu_f}} \frac{\psi}{r^2}$  ( $\psi$  being the stream function of the viscous boundary-layer flow) and doing a similarity transformation, the boundary-layer equation (A2.2) can be simplified to an ordinary differential equation

$$\frac{d^3 f}{d\eta^3} + 2f \frac{d^2 f}{d\eta^2} - \left(\frac{df}{d\eta}\right)^2 + 1 = 0 \quad (\text{A2.6})$$

which is subjected to the following boundary conditions:

$$\eta=0 \quad f=0 \quad \frac{df}{d\eta}=0 \quad (\text{A2.7a})$$

$$\eta \rightarrow \infty \quad \frac{df}{d\eta} = 1 \quad (\text{A2.7b})$$

One may obtain the solution to equation (A2.6) in the form of a power series, from which the boundary-layer thickness is given by

$$\delta_v = 2.4 \sqrt{\frac{\nu_f}{\beta}} \quad (\text{A2.8})$$

To determine the flow intensity  $\beta$ , one should recall that the potential flow pattern outside the viscous boundary-layer region is given by equation (A2.4), from which the stream function  $\varphi$  of the potential flow can be determined,

$$\varphi = \beta z r^2 \quad (\text{A2.9})$$

Applying the equation (A2.9) to the exit of the capillary in the impinging jet system, one can write

$$\text{at } r_1 = 0 \quad \text{and} \quad z_1 = 2R \quad \varphi_1 = 0 \quad (\text{A2.10a})$$

$$\text{at } r_2 = R \quad \text{and} \quad z_2 = 2R \quad \varphi_2 = 2\beta R^3 \quad (\text{A2.10b})$$

Noting that by definition the stream function can be related to the volumetric flow rate, for the impinging jet system, it can be shown that

$$2\pi(\varphi_2 - \varphi_1) = Q_v = \pi v_f R Re \quad (\text{A2.11})$$

Substituting equations (A2.10a) and (A2.10b) into equation (A2.11) yields

$$\beta = \frac{v_f Re}{4 R^2} \quad (\text{A.12})$$

Finally, the hydrodynamic boundary-layer thickness can be obtained by putting equation (A2.12) into equation (A2.8),

$$\delta_v = 4.8 R Re^{-0.5} \quad (\text{A2.13})$$

Based on this equation, the hydrodynamic boundary-layer thickness is plotted as a function of the Reynolds number in Figure A2.1. It is interesting to note that for a fixed  $Re$ , the hydrodynamic boundary-layer thickness in the impinging jet geometry is constant. It also should be pointed out that the hydrodynamic boundary-layer thickness estimated from equation (A2.13) is based on an assumption of hyperbolic flow distribution (Schlichting, 1968) outside the boundary layer, i.e., equation (A2.4) which may not be always true in the practical impinging jet system.

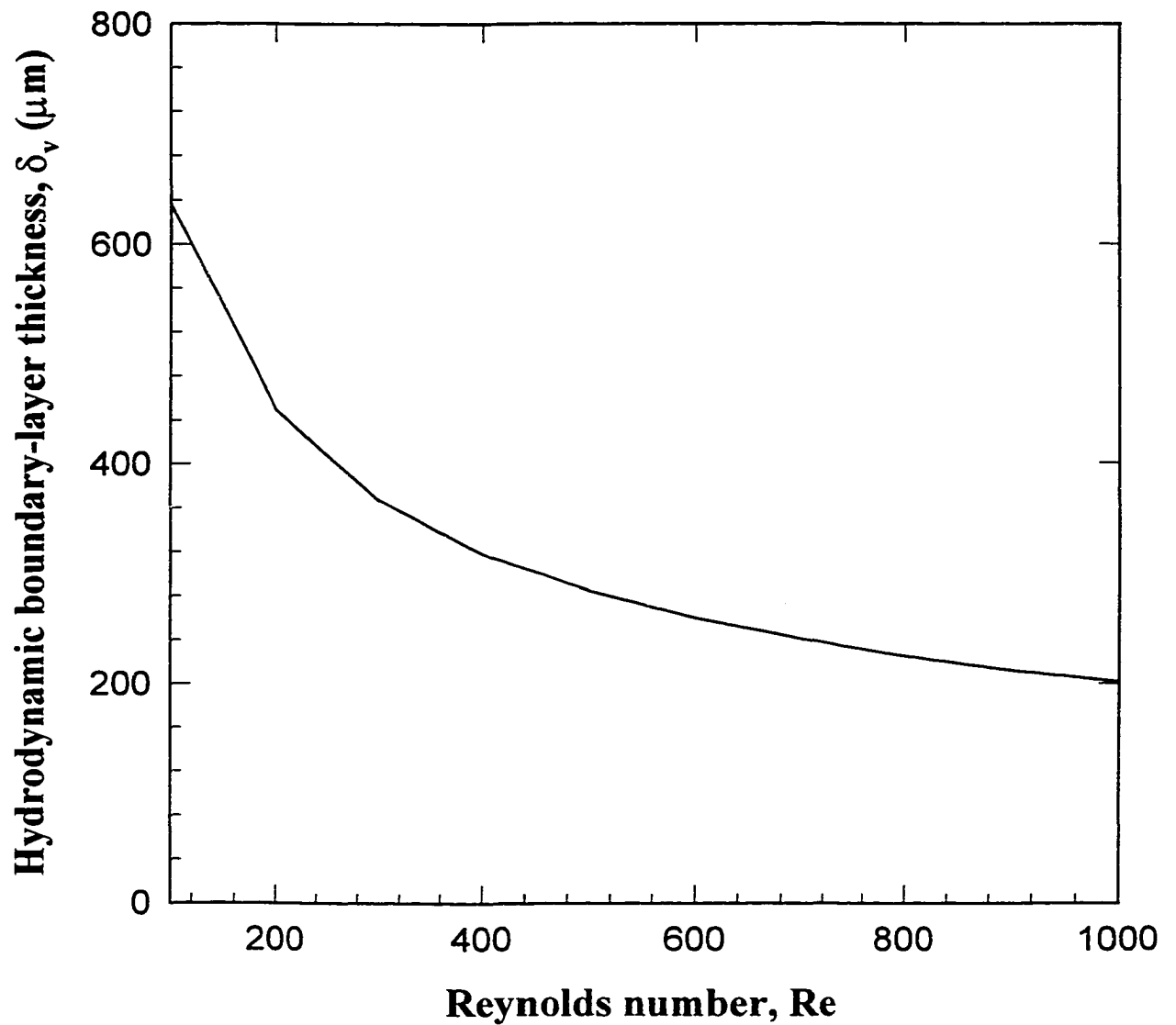


**Figure A2.1** Dependence of the hydrodynamic boundary-layer thickness,  $\delta_v$ , in the impinging jet flow on the Reynolds number,  $\text{Re}$ . (the radius of the capillary tube is chosen as  $R=1325 \mu\text{m}$ )

## APPENDIX 3

### AN EXPRESSION FOR THE DEPENDENCE OF THE SHERWOOD NUMBER, $Sh$ , ON THE PECLET NUMBER, $Pe$ , IN THE IMPINGING JET FLOW REGION

As shown in Figure 4.1, for small Peclet numbers, the dependence of  $Sh$  on  $Pe$  exhibits unexpected trends; i.e., the Sherwood number,  $Sh$ , unusually decreases when the Peclet number,  $Pe$ , increases. In the literature, these abnormal phenomena are attributed to the effects of the radial flow (Dabros and Adamczyk, 1979). Ruckenstein (1978) suggested a modification to the interaction force boundary layer method to account for radial flow effects. Following this suggestion, Prieve and Lin (1980) derived an algebraic formula for the rotating disc by using surface force boundary approximation. In the following, a simple expression will be derived to relate  $Sh$  to particle convection, diffusion, and migration (Yang et al., 1998c). The expression shows that other than hydrodynamic and physicochemical parameters, the Sherwood number is strongly dependent on the particle concentration distribution. This expression together with the particle concentration distributions can be used to explain the above mention abnormal phenomenon.

For particle deposition in the impinging jet system, the mass conservation equation is expressed as

$$\frac{1}{r} \frac{\partial(r \bar{j}_r)}{\partial r} + \frac{\partial \bar{j}_z}{\partial h} = 0 \quad (\text{A3.1})$$

Integrating equation (A3.1) from  $\bar{h}_o = \bar{\delta}$  to an arbitrarily chosen  $\bar{h}$  (here,  $\bar{h}$  is between  $\bar{\delta}$  and the position where the particle concentration maximum occurs, normally  $\bar{\delta} < \bar{h} \leq 0.4$ ), one obtains

$$-\bar{j}_z|_{\bar{\delta}} = -\bar{j}_z|_{\bar{h}} - \int_{\bar{\delta}}^{\bar{h}} \frac{1}{r} \frac{\partial(r\bar{j}_r)}{\partial r} dZ \quad (\text{A3.2})$$

Physically, the term on the left of equation (A3.2) is the nondimensional particle deposition flux at the PEM, which coincides with the expression for the Sherwood number,  $Sh$ . The second term on the right of equation (A3.2) represents the radial loss of particles in the gap width  $(\bar{h} - \bar{\delta})$ .

It was shown in Chapter 3 (equations (3.31a) and (3.31b)) that the dimensionless particle mass flux components in the impinging jet flow along the direction of two cylindrical coordinates,  $r$  and  $z$ , are expressed as

$$\bar{j}_r = \frac{1}{2} f_3 Pe \bar{n} \bar{r} \bar{z} \quad (\text{A3.3a})$$

$$\bar{j}_z = -\frac{1}{2} f_1 f_2 Pe \bar{n} \bar{z}^2 - f_1 \frac{d\bar{n}}{dZ} + f_1 \bar{F}_z \bar{n} \quad (\text{A3.3b})$$

Substituting equations (A3.3a) and (A3.3b) into equation (A3.2) gives

$$Sh = \frac{1}{2} (1 + \bar{h})^2 f_1(\bar{h}) f_2(\bar{h}) Pe \bar{n} + f_1(\bar{h}) \frac{d\bar{n}}{d\bar{h}} + f_1(\bar{h}) (-\bar{F}_{colloid} + Gr) \bar{n} - Pe \int_{\bar{\delta}}^{\bar{h}} (1 + Z) f_3(Z) \bar{n} dZ \quad (\text{A3.4})$$

Note that in the integration range  $[\bar{\delta}, \bar{h}]$ , both  $f_3(\bar{h})$  and  $\bar{n}(\bar{h})$  are monotonically increasing. It can be shown that a value  $\bar{h}_c$  exists within the range  $[\bar{\delta}, \bar{h}]$ , which fulfills the following relationship

$$Pe \int_{\bar{\delta}}^{\bar{h}} (1 + Z) f_3(Z) \bar{n}(Z) dZ = Pe f_3(\bar{h}) \bar{n}(\bar{h}) \int_{\bar{h}_c}^{\bar{h}} (1 + Z) dZ \quad (\text{A3.5})$$

Adding the first term on the right of equation (A3.4) to equation (A3.5) yields a new function  $I(Pe, \bar{h})$  expressed as

$$I(Pe, \bar{h}) = g(\bar{h}) Pe = \left\{ -\frac{1}{2} (1 + \bar{h})^2 [f_3(\bar{h}) - f_1(\bar{h}) f_2(\bar{h})] + \frac{1}{2} (1 + \bar{h}_c)^2 f_3(\bar{h}) \right\} Pe \quad (\text{A3.6})$$

where  $g(\bar{h}) = -\frac{1}{2}(1 + \bar{h})^2 [f_3(\bar{h}) - f_1(\bar{h})f_2(\bar{h})] + \frac{1}{2}(1 + \bar{h}_c)^2 f_3(\bar{h})$ .

Putting equation (A3.6) back into equation (A3.5) gives

$$Sh = f_1(\bar{h}) \frac{d\bar{n}}{d\bar{h}} + f_1(\bar{h}) (-\bar{F}_{colloid} + Gr) \bar{n} + g(\bar{h}) Pe \bar{n} \quad (A3.7)$$

Equation (A3.7) can be used to estimate contributions due to the diffusion,  $f_1(\bar{h}) \frac{d\bar{n}}{d\bar{h}}$ , the migration driven by colloidal and gravity forces,  $f_1(\bar{h}) (-\bar{F}_{colloid} + Gr) \bar{n}$ , and the hydrodynamic convection,  $g(\bar{h}) Pe \bar{n}$ . Equation (A3.7) shows that for fixed physiochemical parameters, the Sherwood number,  $Sh$ , directly depends upon the Peclet number,  $Pe$ , the particle concentration gradient,  $\frac{d\bar{n}}{d\bar{h}}$ , and the particle concentration,  $\bar{n}$ . While both  $\frac{d\bar{n}}{d\bar{h}}$  and  $\bar{n}$ , in turn, are determined by the  $Pe$  number. This formula can be applied to anywhere in the range  $[\bar{\delta}, \bar{h}]$  as long as the condition that the function  $\bar{n}(\bar{h})$  is monotonically increasing is fulfilled. In this range, the functions of  $\frac{d\bar{n}}{d\bar{h}}$  and  $Gr$  are quite simple:  $\frac{d\bar{n}}{d\bar{h}} \geq 0$  and  $Gr = \text{constant}$ .  $\bar{F}_{colloid}$ , however, is very complicated and it can be positive, negative, or zero, depending on the interaction energy profiles (Yang et al., 1998c). Based on the values for  $f_1, f_2, f_3$  given in the literature, one can show that in the range  $\bar{\delta} < \bar{h} \leq 0.4$ ,  $f_1, f_2, f_3$  are bounded by  $0.002 < f_1 \leq 0.26$ ,  $0.34 < f_3 \leq 0.94$ , and  $0.006 < f_1 f_2 \leq 0.64$ . A simple calculation for  $g(\bar{h})$  shows that  $g(\bar{h})$  is always positive in such a range of  $[\bar{\delta}, \bar{h}]$ . This implies that normally the contribution of convection is positive, namely,  $Sh$  is supposed to increase as  $Pe$  increases. However, abnormal dependence of  $Sh$  on  $Pe$  may occur if unusual particle concentration distributions are present, for instance, if the particle concentration distribution decreases as  $Pe$  increases.



As mentioned above, for  $Gr > 10$  in Figure 4.1, there is the prediction of an unusual minimum in  $Sh$ . The existence of such a minimum can be better understood by plotting the corresponding particle concentration distribution, which is given in Figure A3.1 ( $Gr = 10$  and  $Pe=10^{-2}, 1, 100$ ). As can be seen, for a positive  $Gr$ , the particles are facilitated towards the collector. At the same time, the influence of retarding hydrodynamic drag forces results in a particle collection close to the collector, i.e., a relatively large particle concentration  $\bar{n}$  exists at this location. Moreover, in the low Peclet number regime (i.e.,  $Pe \leq 10$ ), the concentration maximum of each curve even drops when  $Pe$  increases, i.e.,  $\bar{n}_{\max}|_{Pe=10^{-2}} > \bar{n}_{\max}|_{Pe=1}$ . By applying equation (A3.7) to the concentration maximum of each curve, one can approximately estimate all terms in equation (A3.7). The results are summarized in Table A3.1 (Note: In calculation,  $\bar{h}_c$  was chosen as  $\bar{\delta}$ , which is a conservative estimate. The actual value of  $\bar{h}_c$  is dependent on the shape of particle concentration distribution). From Table A3.1, it can be shown that  $Sh|_{Pe=10^{-2}} > Sh|_{Pe=1}$ . However, with a further increase in  $Pe$ , for example  $Pe = 10^2$ , one may find that not only the diffusion boundary layer is compressed, leading to stronger colloidal interaction forces, but also the contribution of hydrodynamic convection rapidly increases so that a much larger value of Sherwood number,  $Sh$ , can be expected.

**Table A3.1** Application of equation (A3.7) to the particle concentration maximum (shown in Figure A3.1) in the presence of gravity and van der Waals forces only

$Pe$	$H_{n_{\max}}$	$\bar{n}_{\max}$	$f_1 \frac{d\bar{n}}{dH}$	$f_1(-\bar{F}_{coll} + Gr)$	$g(H)Pe$	$Sh_1^*$	$Sh_2^*$
$10^{-2}$	0.2640	4.4431	0.0	2.216	0.00138	9.85	9.88
1	0.2400	3.0960	0.0	2.141	0.1329	7.04	7.28
$10^2$	0.0720	2.1890	0.0	4.069	6.7624	23.71	25.95

\*  $Sh_1$  is the Sherwood number calculated from equation [27];

$Sh_2$  is the Sherwood number calculated from equation [15]

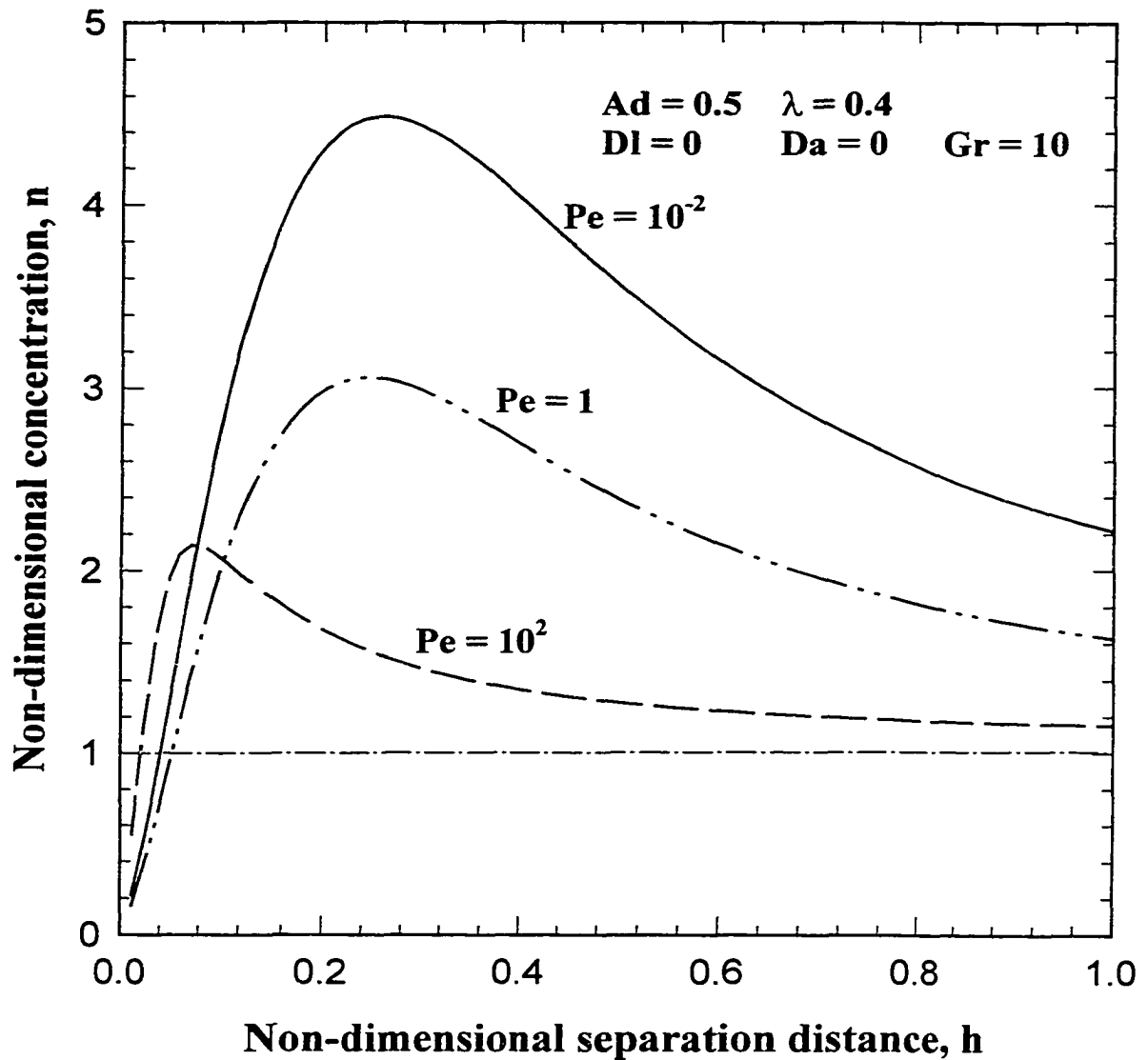


**Figure A3.1** Effect of the Peclet number,  $Pe$ , on Computational particle concentration distributions under positive gravity force ( $Gr > 0$ ) in the absence of the *EDL* interaction

## APPENDIX 4

### ELECTROSMOTIC FLOW INSIDE RECTANGULAR ELECTROPHORESIS CELLS

As pointed out in Chapter 6, in the Komagata approach the electroosmotic flow near the cell wall is considered in such a way that it appears to move at a constant velocity  $u_{os}$ . In other words, the variation of hydrodynamic velocity, charge density, and electric potential inside the *EDL* region is ignored. This, on the one hand, is obviously against the widely accepted no-slip hydrodynamic boundary condition. On the other hand, from a physical mechanism point of view, it is contradictory to the fact that the electroosmotic flow in a closed cell is induced by the presence of the charge density and profile inside the *EDL* region. Recently, electrokinetic phenomena in a rectangular geometry have been re-examined by Yang and Li (1997, 1998a, 1998b). Following their approach, first a more rigorous expression for the electroosmotic flow is developed, and then the position of the stationary level inside a rectangular cell is located.

#### A4.1 Electrostatic Double Layer Field in Rectangular Geometry

In order to evaluate the electroosmotic flow, one first must obtain the distributions of electrical potentials and net charge density in a rectangular geometry. Consider a rectangular cell of height  $2b$ , depth  $2a$ , and length  $l$  as illustrated in Figure 6.3b. According to the theory of electrostatics, the relationship between the local electrical potential,  $\psi$ , and the net charge density per unit volume,  $\rho_e$ , at any point in the solution is governed by the two-dimensional Poisson equation (Yang and Li, 1997, 1998a, 1998b; Mala et al., 1998)

$$\frac{\partial^2 \psi}{\partial x^2} + \frac{\partial^2 \psi}{\partial y^2} = -\frac{\rho_e}{\epsilon_r \epsilon_0} \quad (\text{A4.1})$$

where  $\varepsilon_r$  is the relative dielectric permittivity of the solution and  $\varepsilon_o$  is the dielectric permittivity of vacuum.

Assuming the Boltzmann distribution equation is applicable, the number concentration of the type-i ion in a symmetric electrolyte solution is of the form,

$$n_i = n_{i_o} \exp\left(-\frac{z_i e \psi}{k_b T}\right) \quad (\text{A4.2})$$

where  $n_{i_o}$  and  $z_i$  are the bulk number concentration and the valence of the type-i ion, respectively,  $e$  is the elementary charge,  $k_b$  is the Boltzmann constant, and  $T$  is the absolute temperature. Strictly speaking, the Boltzmann distribution is applicable only when the system is in an equilibrium state. If there exists a liquid flow, the ionic concentration distribution may be distorted by the presence of the flow and hence should be described by the general Fokker-Planck (i.e., the convection – diffusion mass transfer) equation (van de Ven, 1989). In such a case, the problem may become more difficult to deal with since the Poisson equation, the Fokker-Planck equation, and the equation of motion are coupled. However, in the literature many previous studies simply assumed that the Boltzmann distribution is applicable without giving any proof. As such, the validity of Boltzmann distribution applicable to the electroosmotic flow has been examined in this study. It was found that only for a flow with a very small Peclet number or in a fully-developed hydrodynamic state, the Boltzmann distribution can be safely applied. The detailed proof is given in Appendix 5 (Yang et al., 1998b).

The net volume charge density,  $\rho_e$ , is proportional to the concentration difference between symmetric cations and anions, via.

$$\rho_e = ze(n_+ - n_-) = -2zen_o \sinh\left(\frac{ze\psi}{k_b T}\right) \quad (\text{A4.3})$$

Substituting equation (A4.3) into the Poisson equation leads to the well-known Poisson-Boltzmann equation,

$$\frac{\partial^2 \psi}{\partial x^2} + \frac{\partial^2 \psi}{\partial y^2} = \frac{2zen_o}{\varepsilon_r \varepsilon_o} \sinh\left(\frac{ze\psi}{k_b T}\right) \quad (\text{A4.4})$$

By defining the Debye-Huckel length  $\kappa = \sqrt{2z^2 e^2 n_o / \epsilon_r \epsilon_o k_b T}$  ( $1/\kappa$  is normally referred to as the *EDL* thickness) and the hydraulic diameter of the rectangular cell

$$D_h = 4ab / (a + b) \text{ and introducing the dimensionless groups: } X = x / D_h, Y = y / D_h,$$

$K = \kappa D_h$ , and  $\Psi = ze\psi / k_b T$ , the above equation can be nondimensionlized as

$$\frac{\partial^2 \Psi}{\partial X^2} + \frac{\partial^2 \Psi}{\partial Y^2} = K^2 \sinh \Psi \quad (\text{A4.5})$$

Due to symmetry of a rectangular geometry, equation (A4.5) is subjected to the following boundary conditions in a quarter of the rectangular cross section:

$$X = 0 \quad \frac{\partial \Psi}{\partial X} = 0 \quad X = \frac{b}{D_h} \quad \Psi = \bar{\zeta} \quad (\text{A4.6a})$$

$$Y = 0 \quad \frac{\partial \Psi}{\partial Y} = 0 \quad Y = \frac{a}{D_h} \quad \Psi = \bar{\zeta} \quad (\text{A4.6b})$$

where  $\bar{\zeta}$ , defined by  $\bar{\zeta} = ze\zeta / k_b T$ , is a non-dimensional zeta potential of the channel wall (here  $\zeta$  is the zeta potential of the channel wall). The zeta potential is a measurable electric potential at the shear plane, i.e. the boundary between the compact (Steric) layer and the diffuse layer, as defined in the *EDL* theory (Hunter, 1981).

For small values of  $\psi$ , the Debye-Huckel approximation, which physically means that the electrical potential is small in comparison with the thermal energy of ions (i.e.  $|ze\psi| < \kappa_b T$ ), is applicable. Hence, the Poisson-Boltzmann equation can be linearized as

$$\frac{\partial^2 \Psi}{\partial X^2} + \frac{\partial^2 \Psi}{\partial Y^2} = K^2 \Psi \quad (\text{A4.7})$$

By using the separation of variables method, the solution to the linearized P-B equation, equation (A4.7), can be obtained. Therefore, the electrical potential distribution in the rectangular cell is of the form,

$$\begin{aligned}
\Psi(X, Y) = & 4\bar{\zeta} \sum_{m=1}^{\infty} \frac{(-1)^{m+1} \cosh\left[\sqrt{1 + \frac{(2m-1)^2 \pi^2 D_h^2}{4K^2 a^2}} KX\right]}{(2m-1)\pi \cosh\left[\sqrt{1 + \frac{(2m-1)^2 \pi^2 D_h^2}{4K^2 a^2}} \frac{Kb}{D_h}\right]} \cos\left[\frac{(2m-1)\pi D_h}{2a} Y\right] \\
& + 4\bar{\zeta} \sum_{n=1}^{\infty} \frac{(-1)^{n+1} \cosh\left[\sqrt{1 + \frac{(2n-1)^2 \pi^2 D_h^2}{4K^2 b^2}} KY\right]}{(2n-1)\pi \cosh\left[\sqrt{1 + \frac{(2n-1)^2 \pi^2 D_h^2}{4K^2 b^2}} \frac{Ka}{D_h}\right]} \cos\left[\frac{(2n-1)\pi D_h}{2b} X\right]
\end{aligned} \tag{A4.8}$$

In order to completely solve the non-linear, two-dimensional, elliptic, differential equation (A4.5), a numerical finite-difference scheme is introduced to derive this differential equation into the discrete, algebraic equation by integrating the governing differential equation over a control volume surrounding a typical grid point. The non-linear source term is linearized as

$$\sinh \Psi_{n+1} = \sinh \Psi_n + (\Psi_{n+1} - \Psi_n) \cosh \Psi_n \tag{A4.9}$$

where the subscript (n+1) and n represent the (n+1)th and the nth iterative value, respectively. The derived discrete, algebraic equations are solved by using the Gauss-Seidel iterative procedure. The solution of the linearized P-B equation with the same boundary conditions, i.e., equation (A4.8), is chosen as the first guess value for the iterative calculation. The under-relaxation technique is employed to make this iterative process converge quickly. The criterion of numerical convergence is chosen as  $10^{-4}$ , which is the relative desired accuracy (given as  $\left| \frac{\Psi_{n+1} - \Psi_n}{\Psi_n} \right| \leq 10^{-4}$ ) for the calculated dimensionless potential values at each grid point on two successive iterations.

After the electrical potential distributions inside the rectangular cell are computed, the local net charge density can be obtained from equation (A4.3) as

$$\rho_c(X, Y) = -2ze n_0 \sinh \Psi(X, Y) \tag{A4.10}$$

This local net charge density is required to determine electrostatic force caused by the presence of the *EDL* field. Such an electrostatic force is considered as an additional body force in the Navier-Stokes equation, which will be discussed in the next section.

#### A4.2 Electroosmotic Flow Field in a Rectangular Cell

Consider the case of a forced, laminar flow through a rectangular cell as illustrated in Figure A4.1. The equation of motion for an incompressible liquid is given by

$$\rho_f \frac{\partial \underline{V}}{\partial t} + \rho_f (\underline{V} \cdot \nabla) \underline{V} = -\nabla P + \underline{F} + \mu_f \nabla^2 \underline{V} \quad (\text{A4.11})$$

In this equation,  $\rho_f$  and  $\mu_f$  are the density and viscosity of the liquid, respectively. For a steady-state, fully-developed flow, the components of velocity  $\underline{V}$  satisfy  $u = u(x, y)$  and  $v = w = 0$  in terms of Cartesian coordinates. Thus both the time-related term  $\frac{\partial \underline{V}}{\partial t}$  and the inertia term  $(\underline{V} \cdot \nabla) \underline{V}$  vanish. Also, the hydraulic pressure  $P$  is a function of  $z$  only and the pressure gradient  $\frac{dP}{dz}$  is constant. If the gravity effect is negligible, the body force  $\underline{F}$  is only caused by the action of an applied electrical field  $E$  on the net charge density  $\rho_c(X, Y)$  in the *EDL* region, i.e.  $F_x = E \rho_c$ . With these considerations, equation (A4.11) is reduced to

$$\frac{\partial^2 u}{\partial x^2} + \frac{\partial^2 u}{\partial y^2} = \frac{1}{\mu_f} \frac{dP}{dz} - \frac{1}{\mu_f} E \rho_c(x, y) \quad (\text{A4.12})$$

Defining the reference Reynolds number  $Re_o = \frac{\rho_f D_h U}{\mu_f}$  and non-dimensionalizing equation (A4.12) via the following dimensionless parameters

$$X = \frac{x}{D_h} \quad Y = \frac{y}{D_h} \quad Z = \frac{z}{D_h Re_o} \quad (\text{A4.13a})$$

$$\bar{u} = \frac{u}{U} \quad \bar{P} = \frac{P - P_o}{\rho_f U^2} \quad (\text{A4.13b})$$



$$\frac{d\bar{P}}{dZ} = \frac{D_h \text{Re}_o}{\rho_f U^2} \frac{dP}{dx} \quad \bar{E} = \frac{E D_h \text{Re}_o}{\zeta_o} \quad (\text{A4.13c})$$

(where  $U$  is a reference velocity,  $P_o$  is a reference pressure, and  $\zeta_o$  is a reference electrical potential), one can obtain dimensionless form of the equation of motion,

$$\frac{\partial^2 \bar{u}}{\partial X^2} + \frac{\partial^2 \bar{u}}{\partial Y^2} = \frac{d\bar{P}}{dZ} - \frac{\psi_c}{\rho_f U^2} \bar{E} \rho_e(X, Y) \quad (\text{A4.14})$$

Substituting  $\rho_e(Y, Z)$  by equation (A4.10) and defining a new dimensionless number

$\bar{G} = \frac{2ze n_o \zeta_o}{\rho_f U^2}$ , the equation of motion may, therefore, be written as

$$\frac{\partial^2 \bar{u}}{\partial X^2} + \frac{\partial^2 \bar{u}}{\partial Y^2} = \frac{d\bar{P}}{dZ} + \bar{G} \bar{E} \sinh \Psi(Y, Z) \quad (\text{A4.15})$$

The boundary conditions that apply for the velocity  $\bar{u}$  are

$$X = 0 \quad \frac{\partial \bar{u}}{\partial X} = 0 \quad Y = 0 \quad \frac{\partial \bar{u}}{\partial Y} = 0 \quad (\text{A4.16a})$$

$$X = \frac{b}{D_h} \quad \bar{u} = 0 \quad Y = \frac{a}{D_h} \quad \bar{u} = 0 \quad (\text{A4.16b})$$

Here, equation (A4.16a) is the symmetric condition and equation (A4.16b) is the no-slip condition at the walls of the cell.

By using the Green's function formulation, the solution of equation (A4.15) subjecting to the above boundary conditions is

$$\bar{u}(X, Y) = -\lim_{t \rightarrow \infty} \int_{\tau=0}^t d\tau \int_{X'=0}^{b/D_h} \int_{Y'=0}^{a/D_h} G(X, Y, t | X', Y', \tau) \left[ \frac{d\bar{P}}{dZ} + \bar{G} \bar{E} \sinh \Psi(X', Y') \right] dX' dY' \quad (\text{A4.17})$$

Here  $G(X, Y, t | X', Y', \tau)$  is the Green's function which can be found by using the separation of variables method (Beck, 1984). The expression for  $G(X, Y, t | X', Y', \tau)$  is

$$\begin{aligned}
G(X, Y, t | X', Y', \tau) &= \frac{4D_h^2}{ab} \sum_{m=1}^{\infty} \sum_{n=1}^{\infty} \exp \left\{ \frac{-\pi^2 D_h^2}{4} \left[ \frac{(2m-1)^2}{b^2} + \frac{(2n-1)^2}{a^2} \right] (t - \tau) \right\} \\
&\times \cos \left[ \frac{(2m-1)\pi D_h}{2b} X \right] \cos \left[ \frac{(2m-1)\pi D_h}{2b} X' \right] \\
&\times \cos \left[ \frac{(2n-1)\pi D_h}{2a} Y \right] \cos \left[ \frac{(2n-1)\pi D_h}{2a} Y' \right]
\end{aligned} \tag{A4.18}$$

Substituting equation (A4.18) into equation (A4.17) and rearranging it, one can obtain the non-dimensional fluid velocity profile in the cell as follows:

$$\begin{aligned}
\bar{u}(X, Y) &= -\frac{64}{\pi^4 D_h^2} \frac{d\bar{P}}{dZ} \sum_{m=1}^{\infty} \sum_{n=1}^{\infty} \frac{(-1)^{m+n} \cos \left[ \frac{(2m-1)\pi D_h}{2b} X \right] \cos \left[ \frac{(2n-1)\pi D_h}{2a} Y \right]}{(2m-1)(2n-1) \left[ \frac{(2m-1)^2}{b^2} + \frac{(2n-1)^2}{a^2} \right]} \\
&\quad - \frac{16}{\pi^2 ab} \bar{G} \bar{E} \sum_{m=1}^{\infty} \sum_{n=1}^{\infty} \frac{\cos \left[ \frac{(2m-1)\pi D_h}{2b} X \right] \cos \left[ \frac{(2n-1)\pi D_h}{2a} Y \right]}{\frac{(2m-1)^2}{b^2} + \frac{(2n-1)^2}{a^2}} \\
&\quad \times \int_{X'=0}^{b/D_h} \int_{Y'=0}^{a/D_h} \cos \left[ \frac{(2m-1)\pi D_h}{2b} X' \right] \cos \left[ \frac{(2n-1)\pi D_h}{2a} Y' \right] \sinh \Psi(X', Y') dX' dY'
\end{aligned} \tag{A4.19}$$

If there is no electrostatic interaction, the second term on the right hand side of the above equation drops off. The fluid velocity reduces to

$$\bar{u}_o(X, Y) = -\frac{64}{\pi^4 D_h^2} \frac{d\bar{P}}{dZ} \sum_{m=1}^{\infty} \sum_{n=1}^{\infty} \frac{(-1)^{m+n} \cos \left[ \frac{(2m-1)\pi D_h}{2b} X \right] \cos \left[ \frac{(2n-1)\pi D_h}{2a} Y \right]}{(2m-1)(2n-1) \left[ \frac{(2m-1)^2}{b^2} + \frac{(2n-1)^2}{a^2} \right]} \tag{A4.20}$$

which is the well-known Poiseuille flow velocity profile through the rectangular geometry.

For a closed system,  $\bar{u}(X, Y)$  should fulfill the following condition,

$$\int_{b/D_h}^{b/D_h} \int_{a/D_h}^{a/D_h} \bar{u}(X, Y) dY dX = 0 \tag{A4.21}$$

or

$$\frac{d\bar{P}}{dZ} = \frac{\pi^2 D_h^2 \bar{G} \bar{E}}{4ab} \frac{\sum_{m=1}^{\infty} \sum_{n=1}^{\infty} \frac{(-1)^{m+n} C_{mn}}{(2m-1)(2n-1) \left[ \frac{(2m-1)^2}{b^2} + \frac{(2n-1)^2}{a^2} \right]}}{\sum_{m=1}^{\infty} \sum_{n=1}^{\infty} \frac{1}{(2m-1)^2 (2n-1)^2 \left[ \frac{(2m-1)^2}{b^2} + \frac{(2n-1)^2}{a^2} \right]}} \quad (\text{A4.22})$$

where  $C_{mn} = \int_{X'=0}^{b/D_h} \int_{Y'=0}^{a/D_h} \cos\left[\frac{(2m-1)\pi D_h}{2b} X'\right] \cos\left[\frac{(2n-1)\pi D_h}{2a} Y'\right] \sinh \Psi(X', Y') dX' dY' .$

Submitting the expression for  $\frac{d\bar{P}}{dZ}$  into the velocity equation (A4.19) gives the

electroosmotic flow field inside the cell,

$$\begin{aligned} \bar{u}(X, Y) = & \frac{16}{\pi^2 ab} \bar{G} \bar{E} \frac{\sum_{m=1}^{\infty} \sum_{n=1}^{\infty} \frac{(-1)^{m+n} C_{mn}}{(2m-1)(2n-1) \left[ \frac{(2m-1)^2}{b^2} + \frac{(2n-1)^2}{a^2} \right]}}{\sum_{m=1}^{\infty} \sum_{n=1}^{\infty} \frac{1}{(2m-1)^2 (2n-1)^2 \left[ \frac{(2m-1)^2}{b^2} + \frac{(2n-1)^2}{a^2} \right]}} \\ & \times \sum_{m=1}^{\infty} \sum_{n=1}^{\infty} \frac{(-1)^{m+n} \cos\left[\frac{(2m-1)\pi D_h}{2b} X\right] \cos\left[\frac{(2n-1)\pi D_h}{2a} Y\right]}{(2m-1)(2n-1) \left[ \frac{(2m-1)^2}{b^2} + \frac{(2n-1)^2}{a^2} \right]} \\ & - \frac{16}{\pi^2 ab} \bar{G} \bar{E} \sum_{m=1}^{\infty} \sum_{n=1}^{\infty} C_{mn} \frac{\cos\left[\frac{(2m-1)\pi D_h}{2b} X\right] \cos\left[\frac{(2n-1)\pi D_h}{2a} Y\right]}{\frac{(2m-1)^2}{b^2} + \frac{(2n-1)^2}{a^2}} \end{aligned} \quad (\text{A4.23})$$

Then the position of the stationary level  $Y_0$  can be determined from solving the following equation, which is resulted from setting the electroosmotic flow velocity to be zero in the median plane of the cell, i.e.,  $\bar{u}(0, Y_0) = 0$ .

$$\begin{aligned}
& \frac{\sum_{m=1}^{\infty} \sum_{n=1}^{\infty} \frac{(-1)^{m+n} C_{mn}}{(2m-1)(2n-1) \left[ \frac{(2m-1)^2}{b^2} + \frac{(2n-1)^2}{a^2} \right]}}{\sum_{m=1}^{\infty} \sum_{n=1}^{\infty} \frac{1}{(2m-1)^2 (2n-1)^2 \left[ \frac{(2m-1)^2}{b^2} + \frac{(2n-1)^2}{a^2} \right]}} \\
& \times \sum_{m=1}^{\infty} \sum_{n=1}^{\infty} \frac{(-1)^{m+n} \cos\left[\frac{(2n-1)\pi D_h}{2a} Y_o\right]}{(2m-1)(2n-1) \left[ \frac{(2m-1)^2}{b^2} + \frac{(2n-1)^2}{a^2} \right]} = \sum_{m=1}^{\infty} \sum_{n=1}^{\infty} C_{mn} \frac{\cos\left[\frac{(2n-1)\pi D_h}{2a} Y_o\right]}{\left[ \frac{(2m-1)^2}{b^2} + \frac{(2n-1)^2}{a^2} \right]}
\end{aligned} \tag{A4.24}$$

It is interesting to note that compared with the Komagata correction (see equation (6.14)), the position of the stationary level  $Y_o$  not only depends on the geometric dimension of the cell but also is related to the potential distribution (implicitly expressed by  $C_{mn}$ ), which, in turn, is a function of the zeta-potential of the cell wall and the solution condition. However, it is not a trivial task to obtain the “real” value for  $Y_o$  because of mathematical complexity.

## APPENDIX 5

### PROOF OF VALIDITY OF THE POISSON – BOLTZMANN EQUATION FOR THE ELECTROSMOTIC FLOW IN A RECTANGULAR ELECTROPHORESIS CELL

In the following, the validity of the Boltzmann distribution in the case of the fluid flow inside the cell will be discussed (Yang and Li, 1998b).

Generally, the ionic concentration distribution  $n_i$  is described by the Fokker-Planck equation (van de Ven, 1989), which under steady-state conditions and in the absence of source terms can be expressed in the convection-diffusion form

$$\nabla \cdot (D_i \nabla n_i) - \nabla \cdot (\underline{V}_i n_i) = 0 \quad (\text{A5.1})$$

where  $D_i$  is the diffusion coefficient of the type- $i$  ion and  $\underline{V}_i$  is the velocity of the type- $i$  ion. Under such a situation, the ion velocity,  $\underline{V}_i$ , can be decomposed into contributions from hydrodynamic velocity,  $\underline{V}$ , and a velocity,  $\underline{u}_i$ , due to the electrostatic field acting on the ion (caused by the presence of the  $EDL$  field). Then one can write

$$\underline{V}_i = \underline{V} + \underline{u}_i \quad (\text{A5.2})$$

The velocity,  $\underline{u}_i$ , is related to the electrostatic force exerting on the ions by the following equation

$$\underline{F}_{ei} = z_i e \underline{E}_{Edl} = f_i \underline{u}_i \quad (\text{A5.3})$$

where  $z_i$  is the valence of the type- $i$  ion,  $e$  is the elementary charge,  $\underline{E}_{Edl}$  is the strength of the  $EDL$  field, and  $f_i$  is the hydrodynamic resistance coefficient. Noting that  $\underline{E}_{Edl}$  is given by

$$\underline{E}_{Edl} = -\nabla \psi \quad (\text{A5.4})$$

(here  $\psi$  is the electrical potential) and the hydrodynamic resistance coefficient,  $f_i$ , can be determined from the Stokes-Einstein equation

$$f_i = \frac{k_b T}{D_i} \quad (\text{A5.5})$$

(here  $k_b$  is the Boltzmann constant), one can readily show that the velocity,  $\underline{u}_i$ , can be expressed as

$$\underline{u}_i = -\frac{z_i e D_i \nabla \psi}{k_b T} \quad (\text{A5.6})$$

Substituting equations (A5.6) and (A5.2) into equation (A5.1), and using  $\nabla \cdot \underline{V} = 0$ , yields

$$\nabla^2 n_i - \frac{\underline{V}}{D_i} \cdot \nabla n_i + \nabla \cdot \left( \frac{z_i e n_i}{k_b T} \nabla \psi \right) = 0 \quad (\text{A5.7})$$

The equation (A5.7) then can be normalized as

$$\nabla^2 \bar{n}_i - Pe \underline{e}_{\underline{V}} \cdot \nabla \bar{n}_i + \nabla \cdot \left( \frac{z_i e \bar{n}_i}{k_b T} \nabla \psi \right) = 0 \quad (\text{A5.8})$$

where  $\bar{n}_i$  is the non-dimensional ionic concentration,  $\bar{n}_i = \frac{n_i}{n_{io}}$  (here  $n_{io}$  is the bulk concentration of the type-i ion),  $Pe$  is the Peclet number,  $Pe = \frac{|\underline{V}| D_h}{D_i}$ ,  $\underline{e}_{\underline{V}}$  is the unit vector along the hydrodynamic velocity  $\underline{V}$  direction.

With equation (A5.8), two cases are discussed as below:

(i) Considering a flow with a very small Peclet number, i.e.  $Pe \approx 0$ , the second term in the equation (A5.8) drops out and then equation (A5.8) becomes

$$\nabla^2 \bar{n}_i + \nabla \cdot \left( \frac{z_i e \bar{n}_i}{k_b T} \nabla \psi \right) = 0 \quad (\text{A5.9})$$

(ii) If the microchannel flow is fully-developed, the components of hydrodynamic velocity  $\underline{V}$  satisfy  $u = u(x, y)$  and  $v = w = 0$  in terms of Cartesian coordinates. Under such conditions, equation (A5.8) is reduced to

$$\nabla^2 \bar{n}_i - Pe_z \frac{\partial \bar{n}_i}{\partial Z} + \nabla \cdot \left( \frac{z_i e \bar{n}_i}{k_b T} \nabla \psi \right) = 0 \quad (\text{A5.10})$$

Note that under steady-state situations, no mass exchange occurs at the channel wall. This implies that there is no appreciable ionic concentration gradient along the axial direction, i.e.,  $\frac{\partial \bar{n}_i}{\partial Z} = 0$ . Accordingly, the equation (A5.10) is also reduced to equation (A5.9).

In either case (i) or case (ii), one can readily solve equation (A5.9) and obtain its solution, which is

$$\bar{n}_i = \exp\left(-\frac{z_i e \psi}{k_b T}\right) \quad \text{or} \quad n_i = n_{io} \exp\left(-\frac{z_i e \psi}{k_b T}\right) \quad (\text{A5.11})$$

This is the well-known Boltzmann distribution. Therefore, it can be concluded that for a flow with a very small Peclet number or in a fully-developed hydrodynamic state, the Boltzmann distribution equation is still valid.